Titel

Mechanical and electrochemical behavior of Fe_3Al-xCr intermetallics

Dissertation

zur Erlangung des Grades

des Doktor der Ingenieurwissenschaften (Dr.-Ing.)

der Naturwissenschaftlich-Technischen Fakultät III

Chemie, Pharmazie, Bio- und Werkstoffwissenschaften

der Universität des Saarlandes

von

Mohammad Zamanzade, M.Sc.

Saarbrücken

2014

Tag des Kolloquiums:	17.11.2014
Dekan:	Prof. Dr.-Ing. Dirk Bähre
Berichterstatter:	Prof. Dr. Horst Vehoff
	Prof. Dr. Ralf Busch
	Prof. Dr. Gerhard Dehm
Vorsitz:	Prof. Dr.-Ing. Christian Boller
Akad. Mitarbeiter:	Dr.-Ing. Zhaoyu Chen

Preface

This dissertation is being submitted for the degree of Doctor of Philosophy at the Saarland University. The work described in this document was carried out between December 2008 and April 2014 under the supervision of Prof. Dr. Horst Vehoff in the Department of Materials Science and Methods.

To the best of my knowledge the work described in this dissertation is original, except where reference has been made to the work of others, and has not been submitted, in part or entirety, for any degree or qualification at any other university.

Mohammad Zamanzade
Saarland University
May 2014

Contents

List of figures

List of tablets

List of equations

Acknowledgment

I am most indebted to Prof. Dr. rer. nat. Horst Vehoff for giving me an opportunity to start with my graduation. I am very grateful for his endless support and guidance for both technical and non-technical issues.

I would like to gratefully acknowledge my supervisor Prof. Dr. Afrooz Barnoush for his enthusiastic supervision, consistent support, advice, and managing to read the entire thesis and papers so thoroughly and legibly.

I acknowledge the help of Prof. Dr. Christian Motz for his technical support, relevant discussion, and general advice.

Special thanks to Dr. M. Palm, Dr. M. Rohwerder and Dr. S. Merzlikin for supporting materials and also performing the XPS measurements.

I appreciate Prof. Dr. Busch and Prof. Dr. Dehm for serving on my review committee.

Furthermore, I would like to thank my colleagues and friends at the department of Materials Science and Methods of Saarland University, especially Stefan Schmitz, Peter Limbach, Andreas Kirsch, Jorge Rafael Velayarce, Atef Zekri, Michael Nackas, Jonathan Holst, Kerstin Schüler, Andrea Bachmaier, Diana Born and Rita Maron for creating such a splendid atmosphere for carrying on my PhD.

I want to appreciate Mr. Oscar Torrents Abad from Leibniz Institute for new Materials (INM) and Mr. Georg Hasemann from the Institute of Materials and Joining Technology, Otto-von-Guericke University Magdeburg.

My heartfelt thanks to my wife Maryam Manavipour, I greatly appreciate her continual encouragement, love and harp editorial pencil. Finally, I am always indebted to my parents for their blessing, encouraging and inspiration.

Danksagung

Die vorliegende Arbeit entstand am Lehrstuhl für Werkstoffwissenschaft und Methodik der Universität des Saarlandes unter der wissenschaftlichen Betreuung von Herrn Prof. Dr. rer. nat. Horst Vehoff. Für seine Anregungen, sein Vertrauen und seine ständige Unterstützung bin ich ihm sehr dankbar.

Ich bin Herrn Prof. Dr. Afrooz Barnoush für die Vermittlung seiner unfassbaren theoretischen und praktischen Kenntnisse zu besonderem Dank verpflichtet.

Mein besonderer Dank gilt auch Herrn Prof. Dr. Christian Motz für die fruchtbare Arbeit im Team und seine Freundschaft und wertvolle Anmerkungen.

Dr. M. Palm, Dr. M. Rohwerder and Dr. S. Merzlikin von MPIE möchte ich für ihre Hilfe danken.

Herrn Prof. Dr. Busch danke ich für die Übernahme des Zweitgutachtens, Herrn Prof. Dr. Dehm für die Erstellung des Drittgutachtens.

Zum erfolgreichen Abschluss dieser Arbeit haben auch alle Mitarbeiter und ehemalige Mitarbeiter des Lehrstuhls für Werkstoffwissenschaft und Methodik beigetragen, ihnen möchte ich danken, insbesondere jedoch:

• meinen lieben Kollegen den Herren Stefan Schmitz, Peter Limbach und Andreas Kirsch für viele nützliche Ideen.

• Herren Jorge Rafael Velayarce, Georg Hasemann, Atef Zekri, Frau Kerstin Schüler, Diana Born und Rita Maron für ihre Hilfsbereitschaft, Freundschaft und Unterstützung; Michael Nackas, Andrea Bachmaier und Jonathan Holst für das Korrekturlesen.

• Herrn Dr. Ing. Michael Marx, für seine fachlichen Diskussionen und Anmerkungen.

Aus tiefstem Herzen möchte ich meinen Eltern für ihren grenzenlosen Beistand danken. Ohne moralische Unterstützung von meiner Familie wäre ein Gelingen der vorliegenden Dissertation kaum möglich gewesen.

Schließlich gilt mein allergrößter Dank meiner Frau Maryam Manavipour für ihre Liebe, Geduld und ihr Verständnis.

Abstract

Different concentrations of Cr were added to the binary Fe_3Al intermetallics, in order to enhance the ductility and pitting resistance of alloys. The results of nanoindentation in air show the influence of Cr on various mechanical properties like Young's modulus, Gibbs free energy needed for homogeneous dislocation nucleation, and hardness. The increase of the Young's modulus and Gibbs free energy after addition of Cr is due to the enhancement of the strength of interatomic bonds. Moreover, Cr decreases the flow stress and eases the cross slipping of dislocations.

Furthermore, the results of nanoindentation under cathodic and anodic charging show the impact of hydrogen on the reduction of Young's moduli of alloys; whereas measurements of the pop-in load indicate a drastic decrease after cathodic charging in samples with low Cr content. This is thought to be due to the decrease of the dislocation line energy based on the defect acting agents concept. Based on our results, the mechanism of dislocation shielding should be considered for analyzing the fracture characteristics of Fe_3Al in aqueous solutions, and in atmospheres containing hydrogen.

Finally, the effect of Cr on electrochemical properties of passive layer, and susceptibility of alloys to pitting and crevice corrosion in solutions with different concentrations of Cl^- ions, was studied using various methods like cyclic polarization, cyclic voltammetry, impedance spectroscopy and the Mott-Schottky.

Kurzzusammenfassung

Um die Duktilität und den Widerstand gegen Lochkorrosion zu verbessern, wurde in einer intermetallischen Fe_3Al- Legierung die Konzentrationen an Cr variiert. Durch Nanoindentations-Messungen an Luft konnte gezeigt werden, dass Cr die mechanischen Eigenschaften wie z.B. den E-Modul, die Gibbs-Energie für homogene Versetzungsbildung und die Härte beeinflusst. Der Anstieg des E-Moduls und der Gibbs-Energie durch die Zugabe von Cr kann auf die Verstärkung der interatomaren zurückgeführt werden. Außerdem verringert Cr die Fließspannung und erleichtert das Quergleiten von Versetzungen.

Die Ergebnisse der Nanoindentation mit kathodischer und anodischer Beladung zeigten, dass Wasserstoff den E-Moduls der Legierung verringert; Bei geringem Cr-Gehalt kam es hingegen zu einem drastischen Abfall der „pop-in load“ bei kathodischer Beladung, was durch die Verringerung der Versetzungslinienenergie aufgrund des „defect acting agents“ Konzepts erklärt werden kann. Unsere Ergebnisse zeigen, dass der shielding-Effekt der Versetzungen für die Analyse des Bruchverhaltens von Fe_3Al Legierungen in wässrigen Lösungen und wasserstoffhaltigen Umgebungen berücksichtigt werden sollte.

Des Weiteren wurde die Wirkung von Cr auf passive Oxidschichten, elektrochemische Eigenschaften und die Neigung zu Loch- und Spaltkorrosion in Lösungen mit verschiedenen Cl^- Ionen Konzentrationen mit Hilfe verschiedener Methoden u.a. Polarisation, zyklische Voltammetrie, Impedanz Spektroskopie und Mott-Schottky untersucht.

List of appended papers

Paper A — Effect of substitutional solid solution on dislocation nucleation in Fe_3Al intermetallic alloys, Afrooz Barnoush, Mohammad Zamanzade, Philosophical Magazine 92 (2012), 3257-3268.

Paper B — Effect of chromium on elastic and plastic deformation of Fe_3Al intermetallics, Mohammd Zamanzade, Horst Vehoff, Afrooz Barnoush, Intermetallics 41(2013), 28-34.

Paper C — Effect of the chromium on the electrochemical properties of iron aluminide intermetallics, Mohammad Zamanzade, Afrooz Barnoush, Corrosion Science 78 (2014), 223-232.

Paper D — Cr effect on hydrogen embrittlement of Fe_3Al-based iron aluminide intermetallics: Surface or bulk effect, Mohammd Zamanzade, Horst Vehoff, Afrooz Barnoush, Acta Materialia 69 (2014), 210-223.

Paper E — Direct observation of hydrogen-enhanced plasticity in super duplex stainless steel by means of in situ electrochemical methods, Afrooz Barnoush, Mohammad Zamanzade, Horst Vehoff, Scripta Materialia 62 (2010), 242-245

Statement of contribution of co-Authors

Paper A:

Contributor	Statement of contribution*
Afrooz Barnoush	aided data analysis and wrote the main part of manuscript
Mohammad Zamanzade	aided experimental design, conducted experiments, and data analysis; wrote some part of the manuscript (experimental portion, introduction and also some parts of results and discussion).

Paper B:

Contributor	Statement of contribution*
Mohammad Zamanzade	aided experimental design, conducted experiments, and data analysis; wrote the manuscript.
Horst Vehoff	aided experimental design
Afrooz Barnoush	aided experimental design

Paper C:

Contributor	Statement of contribution*
Mohammad Zamanzade	aided experimental design, conducted experiments, and data analysis; wrote the manuscript.
Afrooz Barnoush	aided experimental design

Paper D:

Contributor	Statement of contribution*
Mohammad Zamanzade	aided experimental design, conducted experiments, and data analysis; wrote the manuscript.
Horst Vehoff	aided experimental design

Afrooz Barnoush	aided experimental design

Paper E:

Contributor	Statement of contribution*
Afrooz Barnoush	aided experimental design, and wrote the main part of manuscript.
Mohammad Zamanzade	conducted experiments, and data analysis and wrote some part of the manuscript (experimental part, introduction and also some parts of results and discussion).
Horst Vehoff	aided experimental design

Name	Signature	Date
Mohammad Zamanzade		08-04-2014

1 - Introduction

Transition metal (TM) – aluminide intermetallics like TiAl, NiAl, FeAl and Fe_3Al, have attracted considerable interest due to their unique properties such as high melting points, enhanced corrosion resistance, relatively low density, and utility as soft magnetic materials [1-3]. These ordered intermetallics have stoichiometry due to their strongly attractive chemical bonding between the bi-metallic species of the alloys. However, the energy of interatomic bonds differs from the early TM (TiAl, VAl) to the late TM alloys (CoAl, NiAl and FeAl). The calculated heats of formation for aluminides with equiatomic composition are plotted in Fig. 1-1 [4].

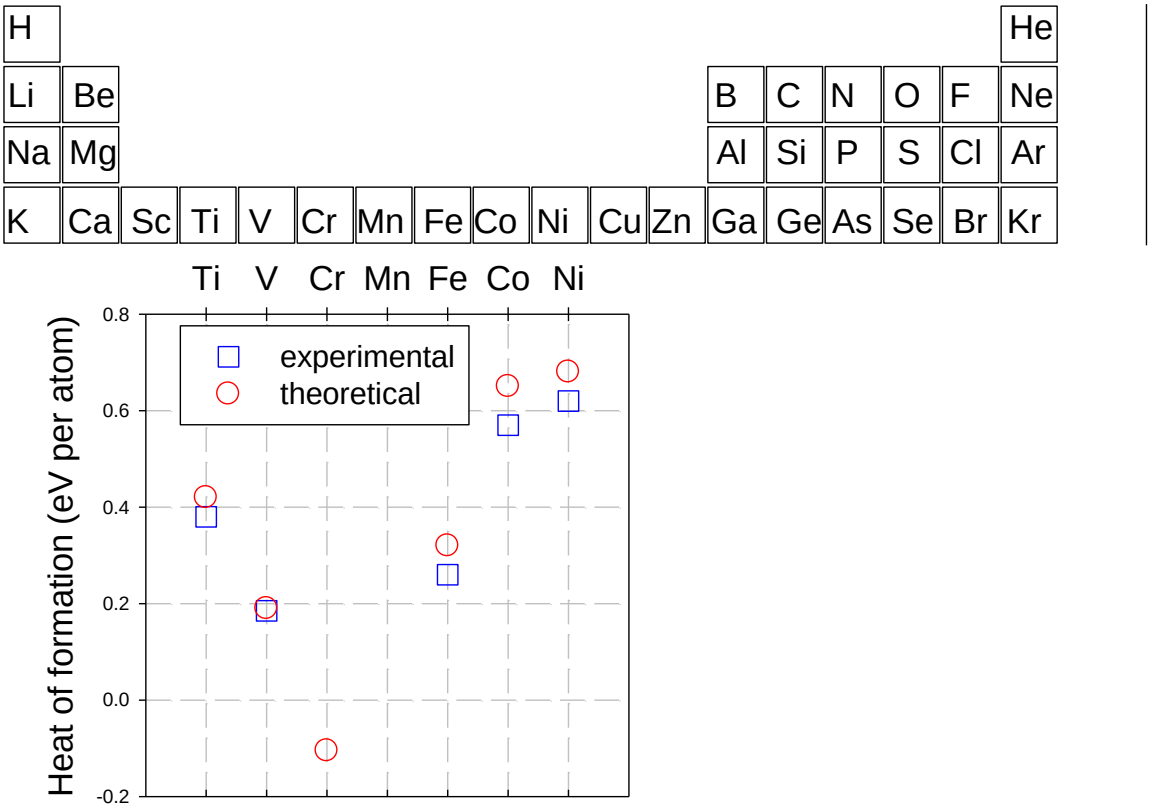

Fig. 1-1. Heats of formation for transition-metal aluminides (with equiatomic composition). Square and circle symbols are experimental and theoretical values, respectively [4].

The middle TM aluminides are shown to have the lowest degrees of ordering. For early TM intermetallics, the interatomic bonds between nearest transition metal neighbors are strong and

directional. For the case of late transition metal alloys, charge transfer from Al to the transition metal, and hybridization between Al sp and transition metal d-states is the driving force in bonding. It is the reason that in iron aluminides, for example, Fe-Al neighbors are energetically favored and, in contrary, Al-Al neighbors are avoided. These differences in bonding give rise to an FCC based crystal structure for early transition metal alloys and a BCC based crystal structure for late transition metal alloys.

Aluminides were first aimed to be used at high temperatures instead of Ni-based super alloys. Hence, some of the thermo-mechanical properties of the aluminides have been reviewed and compared with the routine Ni-base super alloys in Fig. 1-2. The aluminides show six major advantages for high temperature structural applications over the Ni based super alloys. These advantages include: a) higher melting temperatures[1], b) lower densities[2], c) better oxidation resistance[3], d) lower ductile to brittle transition temperature (DBTT), e) similar thermal expansion coefficient with the metals and f) the components are relatively inexpensive since they do not generally incorporate rare and strategic elements [5-8]. Three negative features of the intermetallics at elevated temperatures are: low strength and creep resistance, in addition to their high thermal conductivity. For example, the thermal conductivity of NiAl is about 4 to 8 times greater than the Ni base super alloys, depending on temperature and composition. More information about the mechanical properties of intermetallics at high temperature exist in Appendix A.

At low to moderate temperatures, most of the intermetallics suffer from poor ductility and fracture toughness (Fig. 1-2c) [9]. This feature impedes the wide usage of intermetallics significantly because the machining of alloys (at low temperature) becomes very difficult. In the B2 compounds, two slip directions were observed while the slip plane remains $\{110\}$. $\langle 100 \rangle$ is the slip direction for NiAl and CoAl [10] while the slip direction for FeAl and Fe_3Al is $\langle 111 \rangle$.

[1] The melting temperatures define the upper limit of use temperature and are indicators of the temperature range at which diffusion controlled processes start to dominate.

[2] The lower densities (especially in the case of γ-TiAl intermetallics) result in lower operating stresses that make it possible to fabricate smaller and lighter components which, in turn, result in better engine accelerations due to the lower inertial mass of the rotating parts.

[3] The high aluminum content of intermetallics makes it highly resistant to oxidation and burning; ideal properties for the high temperature applications it has been targeted for.

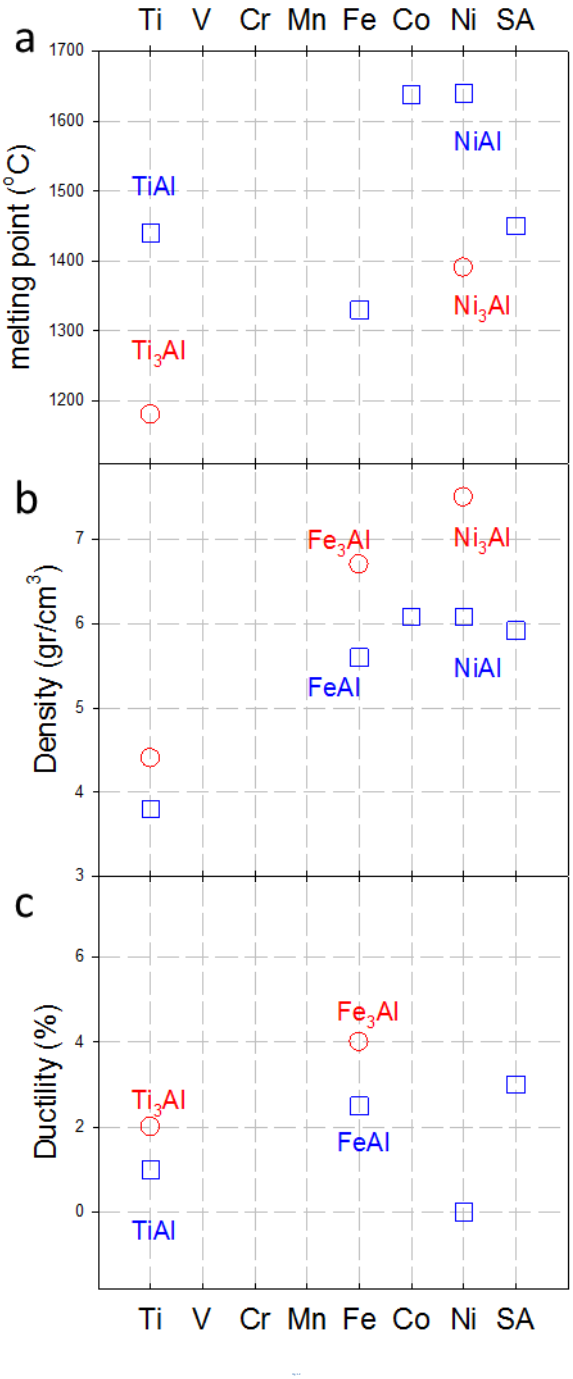

Fig. 1-2. Mechanical properties of transition-metal aluminides [5-8]. Equiatomic composition (1 Fe:1 Al) are plotted in blue rectangles and 3 Fe: 1 Al compositions are plotted in red circles

This difference influences the ductility of intermetallics significantly. NiAl and CoAl only have three independent slip systems, which is less than the minimum number of slip systems needed

for plastic flow of material in the polycrystalline materials base of the Von Mises criterion [11]. Therefore, no ductility is expected for these alloys.

Since the number of slip systems in the Fe-Al intermetallics is more than the required five independent slip systems, iron aluminides are more ductile. Liu et. al. [12] showed that FeAl is intrinsically ductile, since 36.5 at.% Al FeAl was shown to have ductility of 17.6% in dry oxygen. Afterward, the iron aluminides attract a huge interest for substitution with the routine stainless steels. In Fig. 1-3a, it is shown that the iron aluminides have much higher yield stress for a wide range of temperatures and the cost of production of alloys (Fig. 1-3b) is much less for such a low-density material. Furthermore, iron aluminides allow for the conservation of less accessible elements such as nickel and molybdenum. These advantages have led to the consideration of many applications, such as brake disks for windmills and trucks [13], filtration systems in refineries and fossil power plants [14], transfer rolls for hot rolled steel strips, and ethylene crackers and air deflectors for burning high-sulfur coal [15]. In general, increasing the Al concentration decreases the density of materials and enhances the protective oxide layer at high temperatures [16 and 17]. Fig. 1-3c shows extremely better resistance of iron aluminide against high temperature oxidation in comparison with 304 stainless steel. However, existence of high aluminum concentration has negative side effects. The reaction of reactive Al atoms with water results in production of hydrogen atoms which are responsible for the low ductility of Fe-Al based intermetallic alloys [18 and 19] (Fig. 1-4), especially those with higher concentrations of Al [20 and 21]. Furthermore, high sensitivity of the alloys to localized (pitting and crevice) corrosion in Cl^- containing solutions is another shortcoming of the alloys.

Numerous methods to enhance ductility have been proposed and implemented, for example including the formation of protective oxide layers on surfaces by pre-oxidizing the samples and grain structure refinement by either thermo-mechanical treatment or second-phase particles (alloying with Zr, B and C to form zirconium borides and carbides). The other, more popular, method to increase the ductility of alloys is the addition of ternary alloying elements like chromium. McKamey et. al [22] observed an approximate 8-10% increase in ductility at room temperature with the addition of 6 at.% chromium. In general, the reasons for the increased ductility are thought to be caused by: i) the influence of Cr on the bulk properties of binary alloys, like facilitating the dislocation cross slipping, solid solution softening and an increment in cleavage strength of alloys, and/ or ii) the effect of Cr on the surface properties through the

contribution of chromium oxide into the passive layers and the decrement of the kinetics of water reduction reactions, which leads to the reduction of hydrogen formation/adsorption [23-25]. The constructive effect of chromium on the physico-chemical properties of the passive oxide layer was shown in iron base alloys [26 and 27] and also Fe-Al-Cr intermetallics [28 and 29].

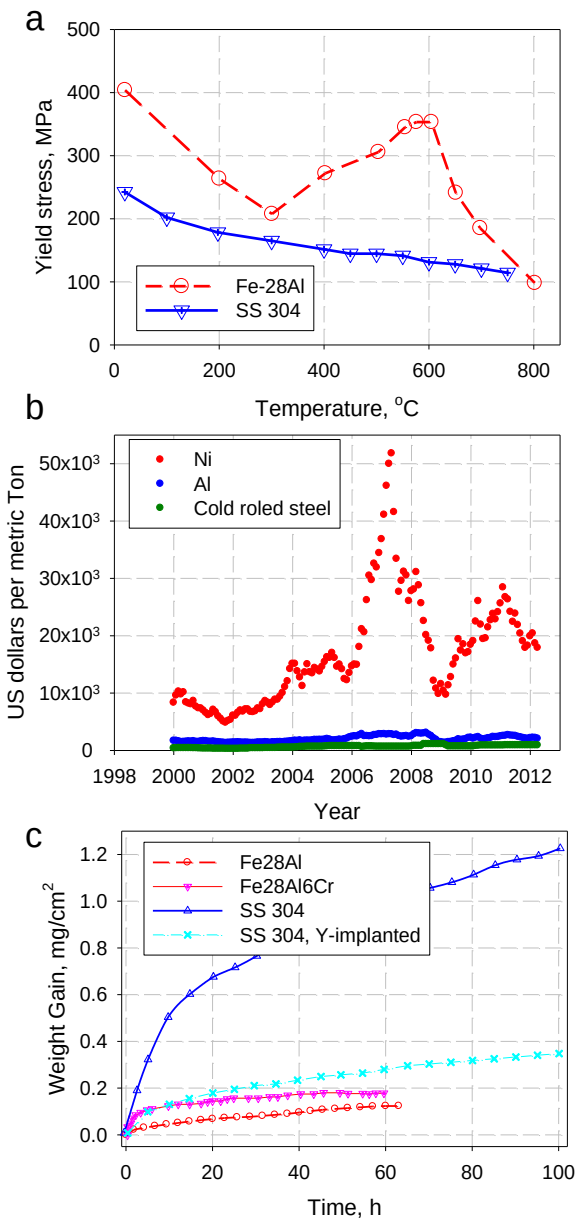

Fig. 1-3. a) Yield stress of Fe_3Al in comparison with SS304 at 25-800 °C [30]. b) Prices of different alloying elements [31] c) Oxidation rate of Fe_3Al [32] in comparison with SS304 at 1000 °C [33].

However, successful application of Fe_3Al– xCr alloys in industry strictly depends on our fundamental understanding of the effect of alloying elements on their mechanical and

electrochemical properties, in different environments. Hence, we added different concentrations of Cr to the Fe_3Al intermetallics where the Al concentration was held constant. Our target is a more in-depth analysis of the effect of chromium on:

1) different mechanical properties consisting of Young's modulus, Gibbs free energy needs for homogeneous dislocation nucleation, hardness and dislocations mobility.
2) mechanism of hydrogen embrittlement based on fundamental mechanics.
3) electrochemical characteristics of the passive layer, such as the electronic behavior, thickness and effective capacitance of passive layer, protectivity of oxide layers and their resistance to pitting corrosion.

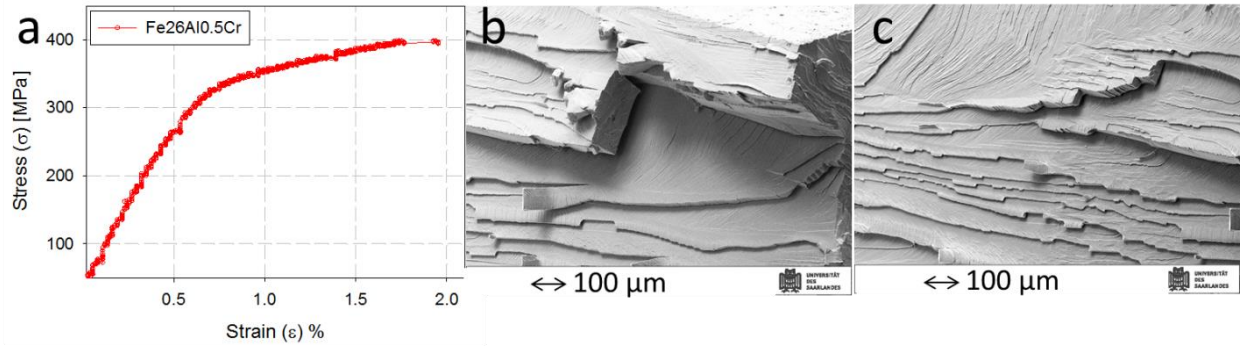

Fig. 1-4. a) Shows low ductility of Fe-Al aluminides. b and c) Cleavage like fracture surface of a Fe26Al0.5Cr intermetallic after doing tensile test in air.

2 - Literature review

2.1. Characteristics of Fe-Al intermetallics

2.1.1. Phase diagram

Iron aluminides have been widely studied since the 1930's, when the excellent oxidation resistance was first noticed [34 and 35]. Afterward, numbers of papers have been published to determine the Fe-Al phase diagram using different methods like dilatometric measurement [36], electrical resistivity and specific heat measurement [37 and 38], X-ray diffraction methods [39], Elastic modulus and magnetic properties of alloys [39-41]. The first well accepted binary Fe–Al phase diagram was reported in the 90th [42]. Afterwards, the phase diagram was intensively studied with the TEM [43]. The phase diagrams essentially have a common form (Fig. 2-1), though the phase boundaries and transitional temperatures differ slightly in various literatures. The different phases and transitional temperatures are listed in Table 2-1 and Table 2-2 respectively. In the phase diagram some of the solubility lines are plotted with dashed lines like $A2|A2+D0_3$ and $D0_3|B2$ boundaries (known as K_1[4]and K_2 respectively), because they are still not well determined.

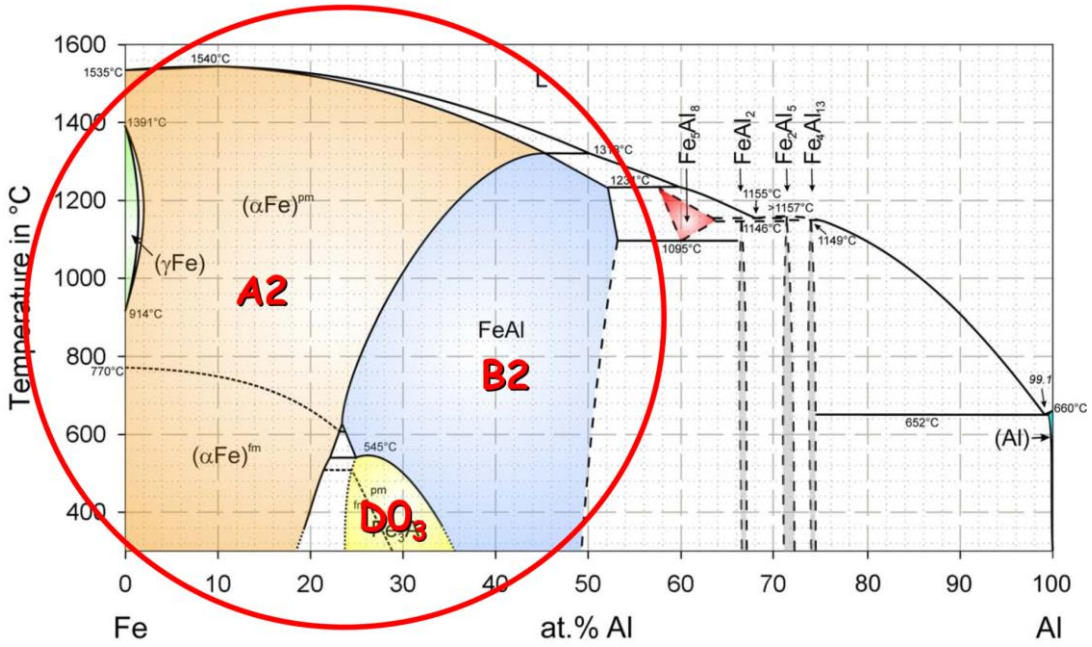

Fig. 2-1. Fe-Al phase diagram [44].

[4] K state for German combination of Komplex-Zustand.

Table 2-1. Different Fe-Al phases

Phase	Label in Fig. 2-1	Pearson symbol	Space group	Prototype	Lattice parameters	Ref.
Liquid	L					
Al	Al	$cF4$	$Fm\bar{3}m$	Cu	$a_0=b_0=c_0=4.0500$	
$FCC(\gamma Fe)$	γFe	$cF4$	$Fm\bar{3}m$	Cu	$a_0=b_0=c_0=3.6599$	[45]
$BCC(\alpha Fe)$	$A2(pm)$[5]- $A2(fm)$[6]	$cI2$	$Im\bar{3}m$	W	$a_0=b_0=c_0=0.28665$	[45]
Fe_3Al	$D0_3$	$cF16$	$Fm\bar{3}m$	BiF_3	$a_0=b_0=c_0=2*0.2895$	[46]
$FeAl$	$B2(pm)$	$cP8$	$Pm\bar{3}m$	$CsCl$	$a_0=b_0=c_0=0.29100$	[45]
Fe_5Al_8	$\varepsilon(D8_2)$	$cI52$	$I4\bar{3}m$	Cu_5Zn_8	n.a.	[47]
$FeAl_2$	$FeAl_2$	$aP18$	$P1$	$FeAl_2$	$a_0=0.4872$ $b_0=0.6459$ $c_0=0.8794$ $\alpha=91.76$ $\beta=73.35$ $\gamma=96.89$	[45]
Fe_2Al_5	Fe_2Al_5	$oC?$	$Cmcm$		$a_0=0.7652$ $b_0=0.6463$ $c_0=0.4229$	[45]
Fe_4Al_{13}	Fe_4Al_{13}	$mC102$	$C2/m$		n.a.	[45]

Table 2-2. Phase transitional temperatures of different iron aluminides [48-51].

$L+B2\rightarrow\varepsilon$	1232	1222	1231	1222	1226
$L\rightarrow\varepsilon+Fe_2Al_5$	1169	1157	1155	1155	1154
$\varepsilon+Fe_2Al_5\rightarrow FeAl_2$	1165	1155	1146	1155	1153
$L+Fe_2Al_5\rightarrow Fe_4Al_{13}$	1160	1151	1149	1153	1151
$\varepsilon\rightarrow B2+FeAl_2$	1102	1115	1092	1094	1089
$L\rightarrow Al+Fe_4Al_{13}$	655	654		654	654

The reason for this uncertainty is the anomaly in the physical properties like Young's modulus, thermal expansion and electrical resistance in this range of concentrations. The origin of the irregularity is not yet clear. However, possible explanations including other long-range ordered

[5] paramagnetic

[6] ferromagnetic

states, short-range ordering, two-phase structure, carbide precipitation and quenched-in vacancies are proposed [41, 52-54].

Fig. 2-1 shows the extension of the solid solution of aluminum in iron from 0 to 45 at.% Al at high temperatures. At low temperatures, this region is subdivided into three separate parts. The first part consists of disordered alloys up to 18.75 at.% aluminum at room temperature. The $FeAl$ (B2) and Fe_3Al ($D0_3$) phases are ordered forms on the body-centered cubic (BCC) lattice and are separated from the disordered A2 phase by first- or second-order transitions. Al reach intermetallics like $FeAl_2$, Fe_2Al_5 and Fe_4Al_{13} have lower density in comparison with $FeAl$ and Fe_3Al but are not good candidates for structural applications because of their small homogeneity ranges, complex crystal structures and brittle behavior. Therefore, we will not focus on them in this text.

X-Ray diffraction method was used for studying the distribution of iron and aluminum atoms in the crystal lattice of $FeAl$ (B2) and Fe_3Al ($D0_3$) phases [39, 55 and 56]. The lattice sites in a unit cell are classified into three kinds: α, β and γ as illustrated in Fig. 2-2a. The probability for each one of these lattice sites to be occupied by an aluminum atom at room temperature has been plotted against the aluminum composition, as seen in Fig. 2-2b. In the $FeAl$ (B2) crystal lattice, in the stoichiometric composition, the Fe atoms occupy the γ sub lattice, whereas the Al atoms occupy α and β sublattices. In the Fe_3Al ($D0_3$) structures, the Fe atoms occupy both α and γ sublattices, while the Al atoms occupy the β sublattice. In a $D0_3$ structure, each Fe atom on the γ sublattice is surrounded with four Fe and four Al atoms as nearest neighbors (NN), but the Fe atoms on the α sublattice and the Al atoms on the β sublattice have eight Fe atoms as NNs. This difference causes a significant influence in the defects' formation energies [57].

2.1.2. Point defects in the super cells

The B2 structure has the ideal stoichiometry of 50 at.% Fe- 50 at.% Al and the $D0_3$ super structure has the ideal stoichiometry of 25 at.% Fe- 75 at.% Al. However, a deviation in the concentration of FeAl and Fe_3Al was seen in the phase diagram. It could be accomplished by the existence of vacancies and/or formation of anti-site defects. The type and concentration of the point defects are important issues in Fe-Al intermetallics because the constitutional

vacancies, or anti-sites, influence thermo-mechanical, magnetic and electrical properties of the intermetallics. The point defects controlled the diffusion-assisted processes, such as creep. The effect of quenched-in thermal vacancies on solid solution strengthening and hardness of alloys was studied in detail in references [1, 58-62]. It was shown that vacancies could act as obstacles to dislocation movement. Additionally, strong interactions between structural defect and hydrogen could significantly influence the hydrogen concentration and penetration rates in the iron aluminides and causes severe mechanical degradation. Furthermore, the knowledge of point defect energetics is essential for the proper estimation of the formation (excess) energy of extended 1D or 2D defects, such as dislocations or grain boundaries, with local off-stoichiometry.

Point defect structure in intermetallics has been studied extensively by various theoretical methods like nearest-neighbor pair-wise interactions [63], embedded atom potentials [64] and local-density-functional (LDF) model [65]. Fu et. al. [65] used the LDF model to estimate the formation energy of different defects. With consideration of non-interacting defects in the B2 FeAl, the energy of a Fe and Al mono-vacancy ($[V_{Fe}]$ and $[V_{Al}]$) was calculated to be 0.97 eV and 4.00 respectively. The anti-site defect formation energy at the Fe and Al ($[Fe_{Al}]$ and $[Al_{Fe}]$) was calculated to be 1.04 eV and 0.95 eV respectively.

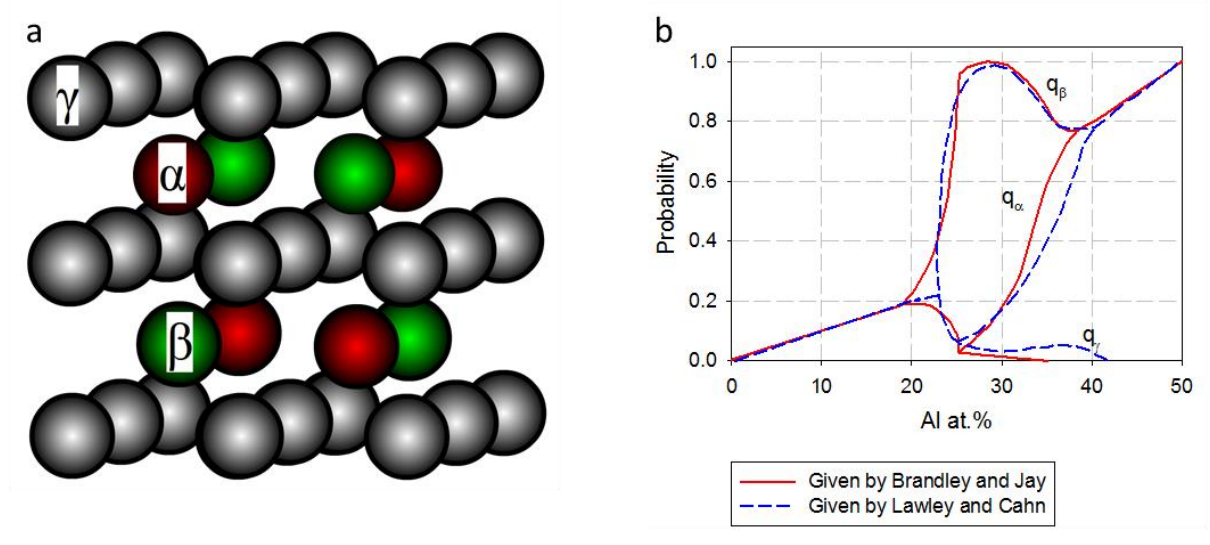

Fig. 2-2. a) Atomic arrangement in a B2 super lattice. b) Occupation probabilities of the lattice sites by Al atoms in the Fe-Al system [55 and 56].

The low formation energies of anti-sites and also $[V_{Fe}]$ cause high concentration of these forms of defects. In fact, $[V_{Fe}]$ and $[Al_{Fe}]$ are dominant defect types for Al rich FeAl. For Fe-rich FeAl, on the other hand, the constitutional $[Fe_{Al}]$ sites are the main defect type. However, the presence of $[V_{Al}]$ is not thermodynamically favored due to its very high energy of formation.

Based on the defect formation energies (DFE), four various forms of point defects could exist on the $D0_3$ sublattices; Fe atoms on the β sublattice (anti-site Fe atoms), Al atoms on the α sublattice (anti-site Al atoms) and vacancies on the α or β sublattice. The effective formation energies of all different local defects including vacancies and antisite atoms vary only slightly with composition in $D0_3$ structures, and it is in contrast with the DFEs in B2 structures. However, due to the lower vacancy formation energies in the $[V_{Fe-\alpha}]$ in comparison with $[V_{Fe-\gamma}]$ (1.25 and 2.27 eV respectively), the probability of the $[V_{Fe-\alpha}]$ is much higher. Additionally the calculated formation energy of $[V_{Al}]$ is around 1.4 eV, therefore, formation of $[V_{Al}]$ along with $[V_{Fe-\alpha}]$ is possible.

Along with studying the thermodynamically stable types of defects, the kinetic of defect formation or annihilation is also important. The A2 crystal structure has a much larger vacancy formation enthalpy[7], which leads to a much lower vacancy concentration in comparison to the ordered structures (Fig. 2-3a). The lowest enthalpy and, therefore, the highest concentration of thermal vacancies can be found for the B2 crystal structure [54]. The $D0_3$ structure will have a lower thermal vacancy concentration (in compare with B2 structure); it is what we could expect based on the DFE calculations. In reality, however, the vacancy concentrations are well above the predicted values based on the theoretical calculations. This is due to the interaction of different vacancies and sub-lattices, which form defect clusters. The higher effective formation volume of the defects in the B2 phases (1.4Ω), in comparison with one atomic volume Ω, was observed in reference [66]. In the ordered B2 phase, the main defect types are changing from triple defects at low temperature to double vacancies at higher temperature and Al content [66].

[7] According to Morris [54] the effective vacancy formation enthalpy could be obtained from a logarithmic plot of measured vacancy concentrations vs. the inverse of the absolute temperature (Fig. 2-3b).

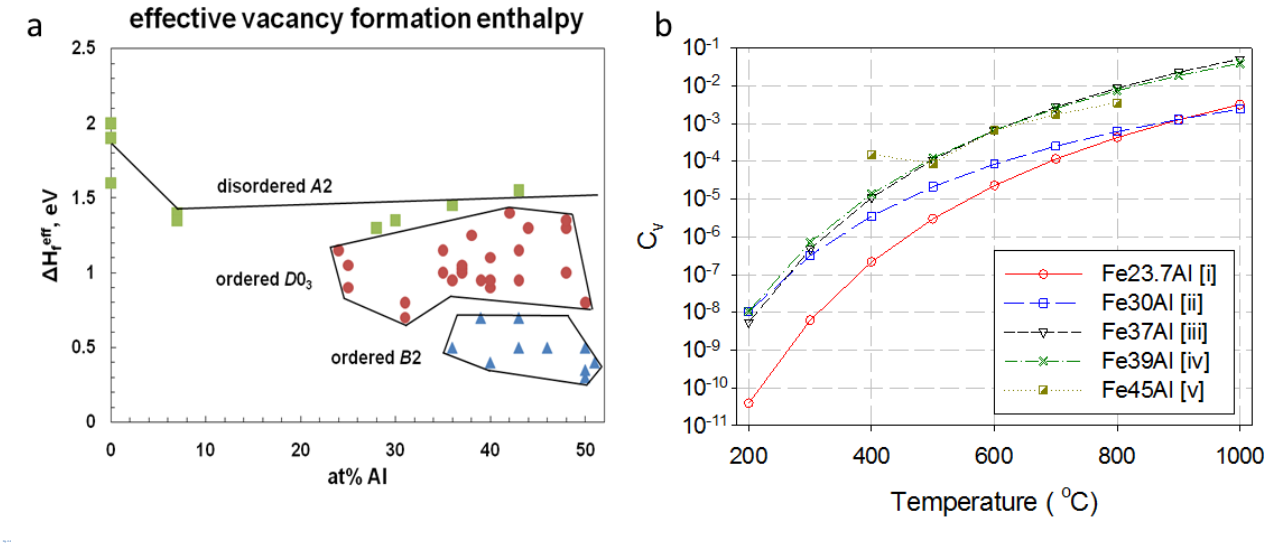

Fig. 2-3. Vacancy concentration of Fe-Al alloys based on the experimental approaches [54], b) Vacancy formation enthalpy for Fe-Al alloys as a function of Al concentration and according to the state of order of the materials (i) [67], (ii) [68], (iii) [69], (iv) [69] and (v) [70].

At aluminides with less than 35 at.% Al the type of defects at low temperatures are mostly mono-vacancies. Fig. 2-3b shows the variation of the equilibrium vacancy concentration (C_v) of samples with different concentrations of Al at various temperatures based on the experimental approaches. The C_v in the materials can be evaluated as follows [71]:

$$C_v = \exp\left[-\frac{\left(E_v^f + pV_v^f - TS_v^f\right)}{k_B T}\right] \qquad \text{Eq. 2-1}$$

where p is the pressure, E_v^f, V_v^f and S_v^f are the energy, volume and entropy of formation of a vacancy, respectively. Clearly, the increase of either temperature or aluminum content will increase the C_v.

The migration enthalpy of the defects increases with increasing Al concentration, at a constant temperature, and the migration of vacancies seems to be very slow especially for the high Al content alloys. Because, in ordered alloys, unlike pure metals in which self-diffusion occurs by random vacancy motion, self-diffusion is not possible since it would disrupt the ordering.

Therefore, diffusion occurs mostly via nearest neighbor jumps into vacant sites[8]. However, both high migration enthalpy and low formation energy of vacancies dictate the existence of large concentrations of thermal vacancies at high temperatures and quenching of these thermal vacancies is easy.

2.1.3. Dislocations in Fe-Al

Yielding in B2 Fe-Al intermetallics at room temperature occurs due to slip along $\langle 111 \rangle$ slip planes. The Burgers vector of the B2 superlattice dislocation is two times longer than that of an ordinary dislocation in the BCC structure. The super lattice dislocation splits into two super-partials, each with a $a/2\langle 111 \rangle$ burgers vector (b) and separated with an anti-phase boundary (APB) [72].

In Fe_3Al with $D0_3$ structure, a superlattice dislocation with burgers vector of $\langle 111 \rangle$ is known to be dissociated into four superpartial dislocations with $b = a/4\langle 111 \rangle$, bound by two types of antiphase boundaries (APBs): the nearest-neighbor APB (NNAPB) and the next-nearest neighbor APB (NNNAPB) [51] (Fig. 2-4). As it is clearly shown in Fig. 2-4a, after initiation of the forth super partial, no APB will be left behind. However, uncoupled and paired superpartials glide trailing the NNAPB and NNNAPB, respectively. Saburi et. al. [72] observed that the dislocations in this $D0_3$ type of order were found to glide as single $a/2\langle 111 \rangle$ dislocation leaving NNNAPB behind, additionally Yasuda and Umakoshi [73] observed the movement of the uncoupled $a/4\langle 111 \rangle$ superpartials, which will leave an NNAPB behind. This was attributed to the relatively low energy of these APBs in Fe_3Al. With an Al concentration above 25at% the APB energies increase as long as a homogeneous $D0_3$ structure is present in Fe-Al alloys [73]. The preferred slip plane for both B2 and $D0_3$ is {101}. The frequent short distance double cross-slip processes onto {112}-planes and back onto {110}-planes was observed as well [74 and 75]. It produces wide slip bands in localized areas at temperatures below 350 K, while adjacent areas remain free

[8] The possible diffusion mechanisms in the B2 structures are single vacancy transport, triple defects mechanism and the six-jump cycle. The six-jump vacancy model allows diffusion to occur exclusively by nearest neighbor vacancy jumps. The most probable mechanism of diffusion depends on temperature, stoichiometry and ordering energy of the compound.

of mobile dislocations. The prominent screw character of dislocations was seen, as well as a great number of dipoles in the deformed areas, which resulted from frequent cross-slip events.

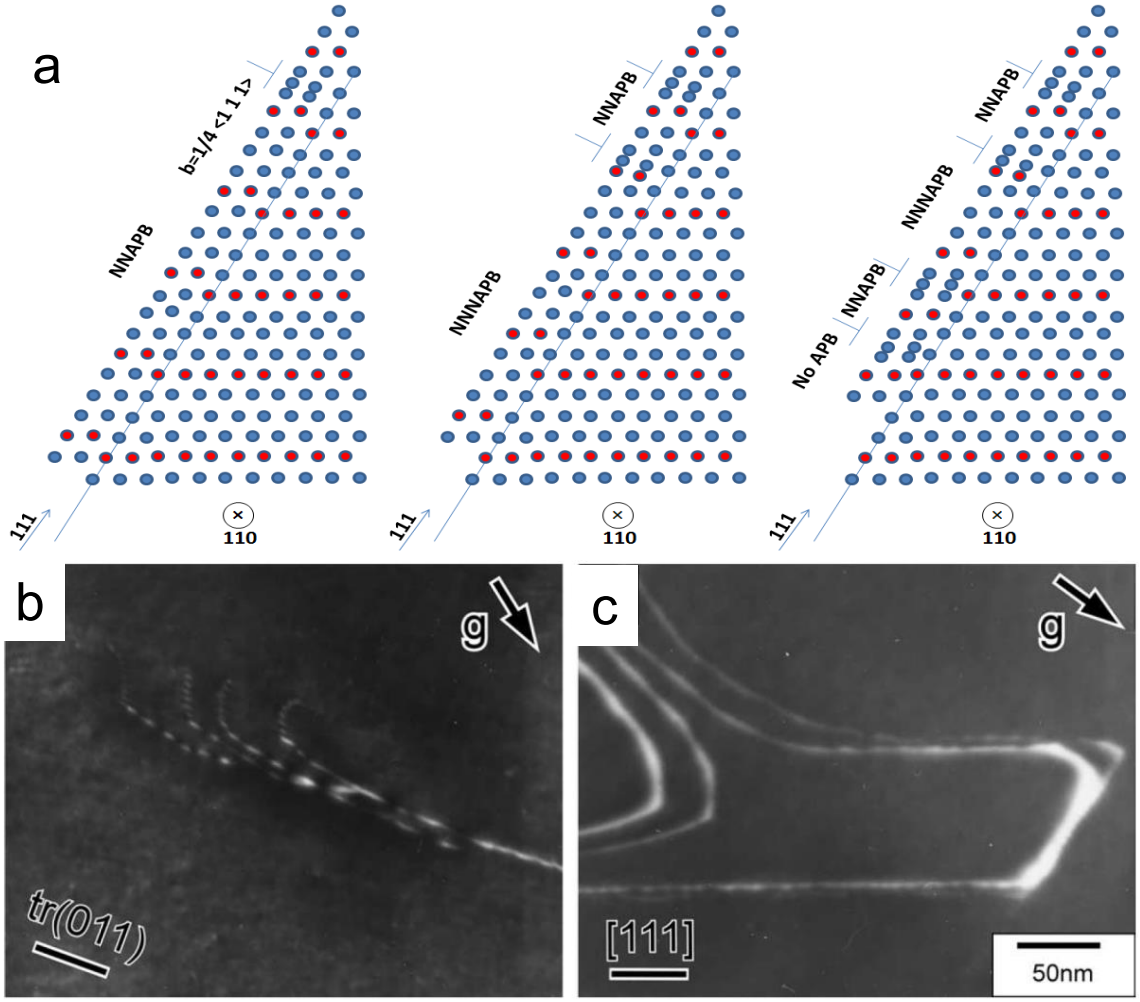

Fig. 2-4. a) shows, schematically, the initiation of partial dislocation and formation of anti-phase boundaries. Dislocation structure in b) Fe25.0Al and c) Fe28.0Al [51].

2.1.4. Alloying elements

To improve the mechanical, thermal or electrochemical properties of binary Fe-Al intermetallics, we can add some different selected alloying elements to the binary alloys. Some metallic alloys like Si, V, Cr, Mn, Co, Ni, Cu and Zn have large solid solubility [52 and 76] and some others like Zr, Nb and Ta have restricted solid solubility in Fe-Al [77]. The effect of metallic substitutional atoms, and interstitials, like boron [78] and carbon [79-81], on the mechanical and corrosion properties of Fe-Al alloys were studied at different temperatures. However, a summary

about the effects of various alloying elements on the mechanical behavior of Fe–Al based alloys is presented in the appendix A.

Here we will limit our discussion to the highly soluble Cr atoms with maximum concentrations less than the solubility limits, in other words, those which make solid solutions. It is generally accepted that addition of Cr could increase the ductility of alloys in humid atmospheres [22]. Additionally, beneficial effect of Cr on the chemical and mechanical properties of the passive layer in iron base alloys was shown earlier [26 and 27]. The passive layer formation on Fe–Cr alloys, under electrolytic conditions, arises by simultaneous oxidation of the Fe and Cr, coupled with selective dissolution of Fe. The enrichment of chromium on the surface significantly influences the electrochemical behavior of alloys. Cr doped iron aluminides have the tendency to broaden the passivation region and reduce the sensitivity of alloys to pitting corrosion in the Cl^- containing solutions [28 and 29].

Palm determined, experimentally, an isothermal section for the Fe–Al–Cr system at 1000 $^\circ$C [76]. He did not find any ternary intermetallic phases, because the binary phases can dissolve considerable amounts of the third component and the substitution does not make any changes in the crystallographic structures.

Addition of the Cr as a ternary element significantly increases the complexity of the super lattice. To have just one Cr atom in a single super cell consisting of 16 atoms, there should be more than 6 at.% Cr in the material. And in the case of samples with 0.5 at.% Cr, we should define a super cell with more than 128 atoms to have just one atomic Cr in the cell. Friak et. al. [46] calculated the site preferences of the chromium atoms in the $D0_3$ structures based on the formation energies. It was shown that the formation energies are -185, -175 and -156 (meV per atom) for the γ, α and β sub-lattices, respectively. It shows that the γ sub-lattice sites are preferred by Cr. This is in agreement with experimental neutron-measurement data [82]. The addition of Cr to lattice influences the lattice constants. Some experimental measurements [83] and theoretical calculations show a linear reduction of the lattice constant with increments of Cr concentrations, while other experiments show very slight increments [82]. The addition of Cr on ordering kinetics and dislocation configurations is not very significant [84]. The effect of Cr on the APBs is also still a matter of debate. When Kral et. al. [85] found increased APB energy with Cr addition, McKamey et. al. [22] found that Cr addition reduce the APB energy. Morris et. al. [74]

did not observed differences in the APB energies with Cr addition. Therefore, more experiments and simulations are needed for precise conclusion about the Cr effect on APB energies.

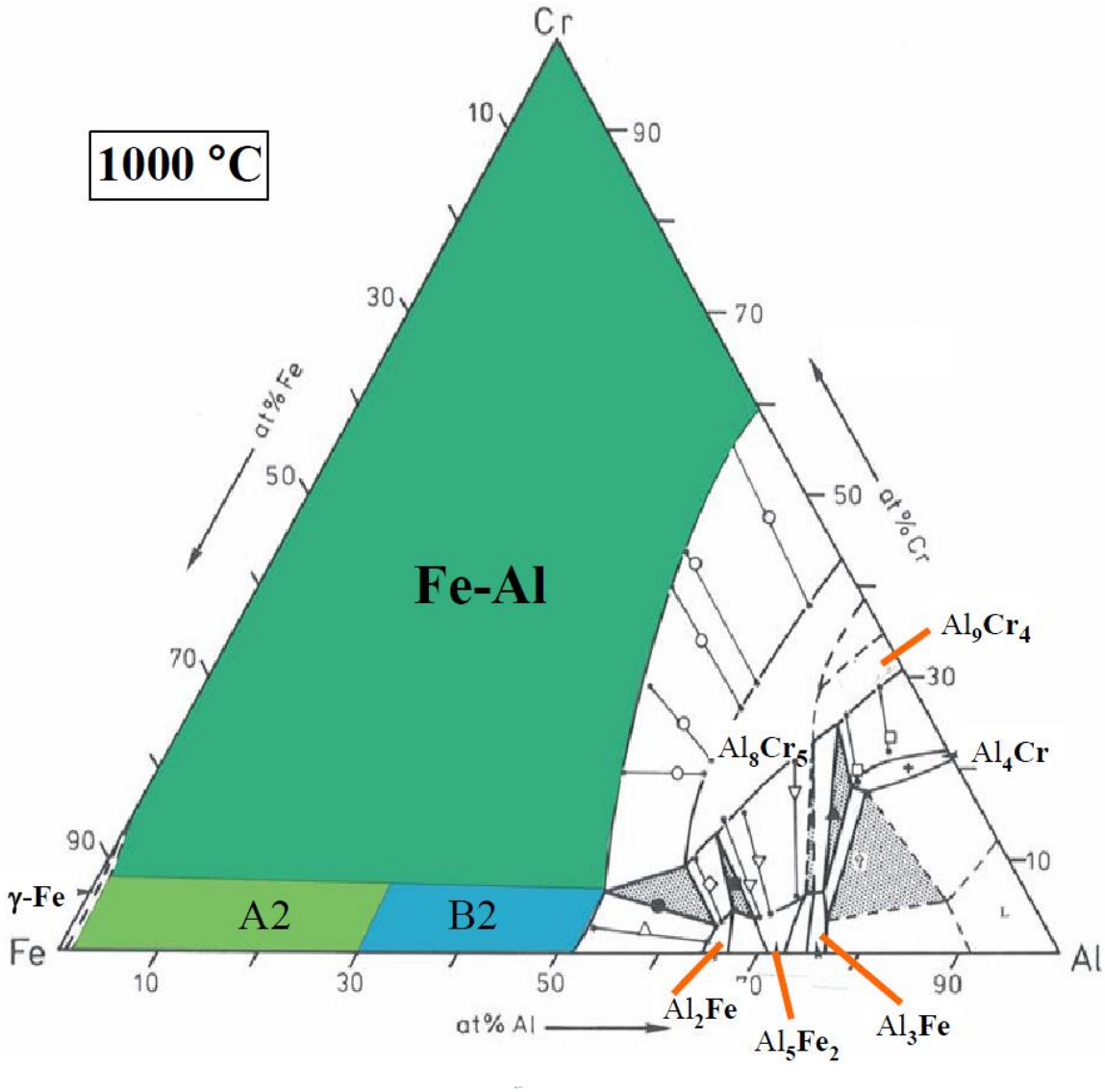

Fig. 2-5. Shows solid solubility of Cr in Fe-Al at 1000 ^{o}C [76].

2.2. Hydrogen Embrittlement (HE)

Hydrogen embrittlement causes severe mechanical degradation of various materials [86] and especially aluminides [12, 22, 87]. In iron-aluminides, the environmental embrittlement was considered as a major cause for the low ductility at ambient temperatures and in air. High reactivity of Al atoms with the moisture in air creates hydrogen, and it is the resulting hydrogen atoms that are then responsible for the lowered ductility. At the crack tips, this reaction results in embrittlement due to the formation of the atomic hydrogen, which penetrates the crack tips.

2.2.1. Mechanism of Hydrogen Ingress

Although there are many promising results with the effects of hydrogen on the mechanical properties of iron-aluminides, the mechanism by which hydrogen enters the metal and assists cleavage, and how far ahead of the crack tip it needs to be transported, is not yet completely understood [88]. In the following, we will explain the sequences of hydrogen formation/ penetration in more detail.

First, the corrosion of aluminum causes water reduction reaction in aqueous environments or moist atmospheres. The consequence of the electro-chemical reactions can be written as follows:

$$Al \rightarrow 3\bar{e} + Al^{3+} \qquad \text{Eq. 2-2}$$

$$3\times\left[H_2O + Al + \bar{e} \rightarrow AlH_{ads} + OH^-\right] \qquad \text{Eq. 2-3}$$

Next, Hydrogen is adsorbed (H_{ads}) at the metallic surface as atomic hydrogen. Then, a part of atomic hydrogen recombines chemically (Tafel reaction Eq. 2-4), or electrochemically (Heyrovsky mechanism Eq. 2-5) to form molecular hydrogen, H_2, which leaves the metallic surface [89]. The molecular hydrogen does not cause severe embrittlement, possibly as a result of its lower activity in comparison to the atomic hydrogen.

$$AlH_{ads} + AlH_{ads} \rightarrow 2Al + H_2$$ Eq. 2-4

$$AlH_{ads} + H_2O + e^- \rightarrow Al + H_2 + OH^-$$ Eq. 2-5

A part of H_{ads} will undergo an absorption (H_{abs}) reaction inside the material ($H_{ads} \leftrightarrow H_{abs}$). The passage of atomic hydrogen through the alloy/solution interface depends on the surface coverage (θ) and also the number of available sites in the subsurface that the hydrogen can occupy. The consequence is the accumulation of hydrogen under the interface, leading to a concentration C_0. Density functional theory-local density approximation calculations [90] in addition to periodic density functional theory calculations within the generalized gradient approximation [91] predicted that hydrogen sits at tetrahedral sites in the bulk FeAl lattice, like its interstitial sites in bulk Fe [92]. Hydrogen diffusivity in iron-aluminides is lower than in pure Fe [93-95]; and the activation barrier varies from 0.42 eV [93], 0.22 eV [96] and 0.26 eV [91] for Fe25Al, Fe40Al and Fe50Al, respectively. Electrochemical permeation tests [97-99] found that H diffusivity in Fe-Al alloys decreases with increasing Al content. The diffusion coefficient at room temperature was measured to be $10^{-8}\, m^2/s$ [100] for Fe, $10^{-11}\, m^2/s$ [94 and 97] for Fe18Al, $1.45\times10^{-13}\, m^2/s$ [94] for Fe25Al and $4.4\times10^{-13}\, m^2/s$ [95] for Fe40Al. More recent measurements at room temperature show an effective diffusion constant of $|5.57, 5.07, 4{,}46, 3{,}62\& 2.25|\times10^{-10}\, m^2/s$ for Fe-[37, 40, 43, 46& 50] Al $Fe-|37, 40, 43, 46\& 50|Al$ respectively [98]. Reported new experimental diffusivity data for Fe-Al alloys vary significantly from the older data, presumably due to experimental uncertainties, varying Al concentration, impurities and microstructural differences [91]. Additionally, increasing the chromium content of iron [101] or iron aluminum [94] decreases the diffusion coefficient and increases the solubility of hydrogen. Since the heat of absorption decreases and d-vacancies increase with substitution of iron with chromium [101].

For the passivated materials, the transport of hydrogen through the passive layer is driven by the electric potential gradient and the hydrogen concentration gradient [102] in contrast to the transport of hydrogen in bulk materials, which is controlled mainly by the concentration gradients. The ionic characteristic of hydrogen atoms (protons) in oxides [103] makes a strong columbic interaction between hydrogen- oxygen ions. It may cause a very high concentration of hydrogen in the oxide in comparison with bulk metal or the metal /oxide interface. For iron, the

ratio of hydrogen concentration in oxide to bulk is measured to be ca. 10^6 [102]. The transport of hydrogen within the oxide must occur by the activated jumping of a proton from one oxygen ion to another [104], and the necessary breaking of the coulombic bond with the initial oxygen ion causes the mobility of hydrogen in an oxide to be considerably lower than that in the metal phase. Therefore, in the case of Fe, for example, the hydrogen diffusivity in the iron oxide layer is much less than that in iron (around 10^{-14} m^2/s [102 and 105]). Based on the density functional theory simulation [106], existence of an Al_2O_3 layer on the FeAl bulk material suppresses the mobility of hydrogen atoms. Diffusion of the adsorbed hydrogen atoms from the outer part of solution/oxide layer into the α - Al_2O_3 layer is thermodynamically unfavorable, endothermic and rate controlling. In contrary, the H diffusion from the inner part of α - Al_2O_3 to the oxide/bulk interface, as well as from the interface into the bulk of the FeAl, is a thermodynamically spontaneous, and exothermic process [106]. It should be mentioned here that the diffusion mechanism through the passive layer and also the passive layer/ bulk metal interface is still largely unknown and has, so far, not been completely explored in published papers. Due to the existence of high donor densities in the passive layers [107], it has semiconductive behavior and the real thermodynamics and kinetics of hydrogen diffusion may be far from the predicted values based on simulations or the measurements performed on aluminum-reach coatings [108]. Though, the semiconductive properties of the oxide layer result in a rectification effect which is the easy movement of current carriers (i.e. electron and protons, H^+) from the oxide/electrolyte towards the metal/oxide interface. It eases the reaction of the absorbed H^+ ions with the Al substrate at defect sites, which follows with the oxidization of the Al and reduction of H^+ [109]. Therefore, an increase in hydrogen diffusivity can be expected with an increase in the density of defects and distortion of the long-range order of oxide film.

2.2.2. Hydrogen interaction with defects

Earlier we studied different types of defects, which may exist in the intermetallics. However, any kind of lattice defect inside the material could work as a trap for hydrogen atoms and consequently a greater number of hydrogen atoms can be introduced into the metal. It was shown earlier [110] that along with the conventional hydrogen solubility in the lattice matrix, there are trap sites for hydrogen atoms on the surface, in subsurface sites, at dislocations (especially edge

dislocations), grain boundaries and vacancies. The binding energies between hydrogen atoms and each of the mention sites vary. Accordingly, the traps are divided into reversible and irreversible, or low and high energies, respectively. Table 2-3 lists different defects and their energies.

Table 2-3. Binding energies of various traps in Fe and Al

Host material	Type of trap	Binding energy (eV)	Reference (s)
$\alpha-$Fe	Vacancy	0.63, 0.48	[111 and 112]
	substitutional (Ti)	0.19	[111]
	interstitional (C)	0.03	[111]
	interstitional (N)	> 0.13	[111]
	Grain boundary	0.10	[112]
	Dislocation elastic stress field	0.21	[112]
	Dislocation core	0.61	[112]
	Free surface	0.73	[112]
BCC carbon steel	Fe_3C phase interface	0.11	[111]
Al	Vacancy	0.52, 0.53	[111, 113-115]
	Grain boundary	0.15	[111]
	Al_2O_3-Al phase interface	0.7,1.0-1.4	[111]

The total hydrogen content in a metal at a defined temperature (C_T^H) is the sum of the solute hydrogen atoms (C_L^H) and the trapped atoms at different defects [92].

$$C_T^H = C_L^H + \sum_j k^H n_j^H N_j^H \qquad \text{Eq. 2-6}$$

Where k^H is a constant, n_j^H and N_j^H are the fraction of trap sites filled with hydrogen and the total number of trap sites per unit volume, respectively. For the dislocations $N_{dis}^H \approx \pi b^{-1}\rho$, here b and ρ are the burgers vector and dislocation density, respectively. For the grain boundaries, the total number of trap sites per unit volume could be estimated as $N_{gb}^H \approx b^{-2}L_{gb}$, where L_{gb} is the

length of grain boundaries per unit area of observation. According to Hirth [92], the trapping effect is measureable for a trap density of 10^{23} m^{-3} or more, and is negligible for smaller trap densities at temperatures below 550 K. Dislocation trap densities can exceed this value at room temperature, while recovery reduces the dislocation and trap densities.

The presence of traps also influences the hydrogen diffusion coefficient in different ways. Substitutionally dissolved impurities accelerate the hydrogen diffusion [111], which relates to reduced vacancy formation energy in the excess volume of the boundary. In contrast, the hydrogen diffusion does not rely on vacancies [111]. The effect of interphase and grain boundaries on the hydrogen transport was studied in different materials and especially in Pd [110 and 111]. At moderate hydrogen concentrations ($10^{-3} < C_H < 10^{-2}$), it was shown that the hydrogen diffusion coefficient in the α phase of nano-crystalline Pd is close to that in the α phase of single-crystalline Pd. The diffusion coefficient seems to be constant in the single-crystal, while it increases with the enhancement of hydrogen concentration in nano crystalline sample. Close to the solubility limit ($C_H > 10^{-2}$), the diffusion coefficient is increased by approximately one order of magnitude, but at small hydrogen concentrations ($C_H < 10^{-3}$) the hydrogen diffusivity is decreased by approximately one order of magnitude [111]. Lower grain-boundary hydrogen diffusivity was related to the trapping effect of low-energy sites at grain boundaries [111].

However, for high purity single-phase single crystals the diffusion paths are either bulk diffusion or pipe diffusion along dislocations [88]. It is possible that the hydrogen does not enter the lattice by diffusion, but is transported into the lattice by gliding dislocations that originate at the surface. The “Cottrell atmosphere”, formed around dislocations, could simultaneously move with the dislocation during deformation and improve the transport of hydrogen, if the velocity of the dislocations is less than a critical value [116-118]. The critical velocity (v_c) could be analytically calculated based on the following equation [119]:

$$v_c = \frac{\sigma b l D_{ok}}{RT} \exp\left(-\frac{Q_k + 2F_k^*}{RT}\right) \qquad \text{Eq. 2-7}$$

Here R, T, D_{ok}, Q_k and $2F_k^*$ are gas constant, absolute temperature, pre-exponential term for kink diffusion, activation energy for kink diffusion and free energy of formation of a double – kink on a dislocation, respectively.

2.2.3. Mechanisms of hydrogen embrittlement

HE has been recognized and researched for many of different materials as early as 1875 [120]. Since then, various mechanisms of HE were introduced. Though, it is highly unlikely that just one mechanism is capable of explaining hydrogen embrittlement. Different mechanisms may operate in different scales and the HE may be influenced by many variables such as environmental situation (like hydrogen concentration, existence of promoters[9] and temperature), mechanical characteristics (e.g. level and type of applied or residual stresses) and material aspects (like microstructural stability of alloys, the strength of material and microstructural constituents and surface conditions).

In some materials, marriage of the hydrogen and stress induce phase transition or make hydride, which follows with a cleavage-like fracture. The most sensitive alloys to the phase transition in the hydrogen environments are the Ti, Zr, Hf at the IVb column of the periodic table and V, Nb and Ta at the Vb column of the periodic table.

Furthermore, the recombination of solute atomic hydrogen could produce gaseous hydrogen (H_2) at the internal pores. The high pressure developed in the voids by formation of molecular hydrogen causes blister formation and crack propagation. Additionally, hydrogen itself could ease the creation and agglomeration of vacancies (especially under strain field of the crack front side), and promote formation and linking of microvoids [121].

However, the solute atomic hydrogen could also induce embrittlement in different ways. Some of the most cited mechanisms of the hydrogen embrittlement are listed below [122-124]:

i) Hydrogen enhanced de-cohesion (HEDE).
ii) Hydrogen enhanced local plasticity (HELP)
iii) Adsorption induced dislocation emission (AIDE)
iv) DEFect ACTing AgeNTS (defactants) theory

In the following, the mentioned mechanisms will be explained shortly.

[9] promoters eases the hydrogen adsorption. Different types of promoters are listed below:
- Certain compounds of the following elements: phosphorus, arsenic, and antimony belonging to the V-A periodic Group, and sulfur, selenium, and tellurium belonging to the VI-A periodic group.
- Anions like: CN^- (cyanide), CNS^- (rhodanide), and I^- (iodide).
-Carbon compounds: CS_2 (carbon sulfide), CO (carbon monoxide),CON_2H_4 (urea), and CSN_2H_4 (thiourea).

HEDE: considers the reduction of cohesive bonding strength between metal atoms as a result of hydrogen accumulation within the crystal lattices [125-129]. This mechanism of embrittlement plays a role especially at the places with high tensile stress, like the crack tip. The effect of hydrogen on the de-cohesion could activate some other mechanisms of embrittlement, like internal hydrogen assisted cracking (IHAC) and hydrogen environment assisted cracking (HEAC), in high strength alloys.

HELP: considers the effect of hydrogen on facilitation of the movement of dislocations. It is due to the formation of a Cottrel atmosphere around the dislocations, which shield the stress field of the dislocations and reduce the interaction between dislocations and other elastic obstacles. It also could lessen the stacking-fault energy, which enhances the tendency for slip planarity by increasing the separation distances between partials [123, 124 and 130-132].

AIDE: is facilitation of the emission of dislocations from crack tips. Here, the term "dislocation emission" covers both the nucleation and the following movement of dislocation away from the crack tip. Based on the AIDE mechanism, crack growth under constant or monotonically increasing stresses occurs. This method does not only cover the dislocation emission from crack tip, but also nucleation and growth of microvoids ahead of crack tips. Nucleation and growth of voids at second phase particles and slip band intersections or other sites in the plastic zone occur because stresses required for dislocation emission are sufficiently high. Void formation contribution to crack growth serves to sharpen crack tips and results in small crack tip opening angles. However, crack growth occurs primarily by dislocation emission from crack tips [133].

DEFACTANTS: the mechanism of DEFect ACTing AgeNTS shelters the interaction between atoms segregating to defects in solids (like hydrogen) and reducing their formation energy in the way that surfactants reduce surface energies in liquids. If surfaces and interfaces in solids and liquids are considered to be defects of the continuum, surfactants are a subgroup of defactants [134 and 135]. For example, segregation of hydrogen atoms to dislocations reduces their formation energy. Consequently, the solute energy is reduced, and this interaction can be described by relating the decrease in the overall free energy to a decrease in the defect formation energy. Therefore, in the presence of hydrogen, the line energy of the newly formed loop and, hence, the formation energy of dislocations is reduced. Additionally, the effect of hydrogen on the creation of a high density of strain-induced vacancies has already been theoretically and experimentally shown [136 and 137].

2.2.4. Hydrogen embrittlement of Fe-Al intermetallics

The marriage between the iron aluminides and hydrogen could be very problematic because of at least three reasons: i) High reactivity of Al atoms with the moisture in air creates high fugacity of hydrogen atoms; ii) Existence of a high concentration of point defects and especially vacancies (Fig. 2-3b) increases the solubility of hydrogen in the intermetallics, and enhances the influence of hydrogen on the mechanical properties; iii) The iron aluminides have a limited amount of ductility (and very high slip planarity) in comparison to metals, and an additional reduction with hydrogen charging will decrease the ductility of the binary iron-aluminums. Therefore, the effect of hydrogen on the ductility and crack initiation of iron aluminides was a subject of many of studies [138-141]. For single crystals of Fe‑40Al tested in air, crack initiation occurred at the surface, producing elongations less than 1%. Specimens tested in an O_2 atmosphere had internally initiated cracks, possibly at flaws, and elongations of ~10% [138 and 141]. More recently Wittmann et. al. [88] studied the ductility of single-slip-oriented single crystals of Fe–40Al. They also observed improved ductility when tested in vacuum versus air, but greater ductility in air (between 1.1-5.9%) compared with previously reported results for multiple slip-oriented specimens. The elongations and fracture strengths are shown in Table 2-4.

Table 2-4. Elongation and fracture strength of Fe-40Al in different environments after performing tensile test [88].

Sample	Elongation (%)		Fracture strength (MPa)	
Orientation	Air	Vacuum	Air	Vacuum
Edge	4.0	9.4	336	460
	3.3	5.7	335	425
	5.9	12.0	320	422
Screw	1.1	3.0	235	435
	2.6	10.8	335	495
	5.7	10.1	345	470

The scatter, shown in the results, is believed to be due to the small thickness of the tensile specimens. However, the ductility appears to be less in air than in a vacuum. Additionally, higher fracture strengths were seen in a vacuum. Wittmann et. al. [88] did not observe differences in environmental embrittlement of specimens oriented such that strain was predominately carried

by screw dislocations or edge dislocations. In contrary, results from tensile tests of Fe_3Al single crystals, oriented in a way that the main strain was produced either by screw dislocations, or by edge dislocations, showed considerable ductility for the screw orientation in both air and vacuum, whereas the edge-oriented specimens showed little ductility in air [140]. Saka and Nishizaki [140] related this difference to the role of edge dislocations in transporting hydrogen into the Fe_3Al lattice.

The fracture in FeAl propagates mainly along the {100} plane in air [138 and 139]. In contrast, in a vacuum, fracture has been shown to occur along {111} for stoichiometric FeAl, and {100} for Fe-40Al, and Fe-35Al [138 and 139]. Munroe and Baker [142] proposed that the {100} cleavage that results from the interaction of two $a/2\langle 111\rangle$ edge super partials may produce a sessile $\langle 100\rangle$ edge dislocation on {001}. This edge dislocation can then act as a crack nuclei. Moreover, formation of the $\langle 100\rangle$ edge dislocations may enhance absorption of hydrogen rather than two super partials [143].

The polycrystalline Fe-36.5Al was shown to have ductility of just 2.2% in air and 5.4% in vacuum while its ductility in dry oxygen could be as high as 17.6% [12] (Fig. 2-6). However, the fracture of Fe-Al polycrystalline materials seems to be dominated with the intergranular crack growth mechanism in moist environments, while the cracks will grow transgranularly in the Fe_3Al structures.

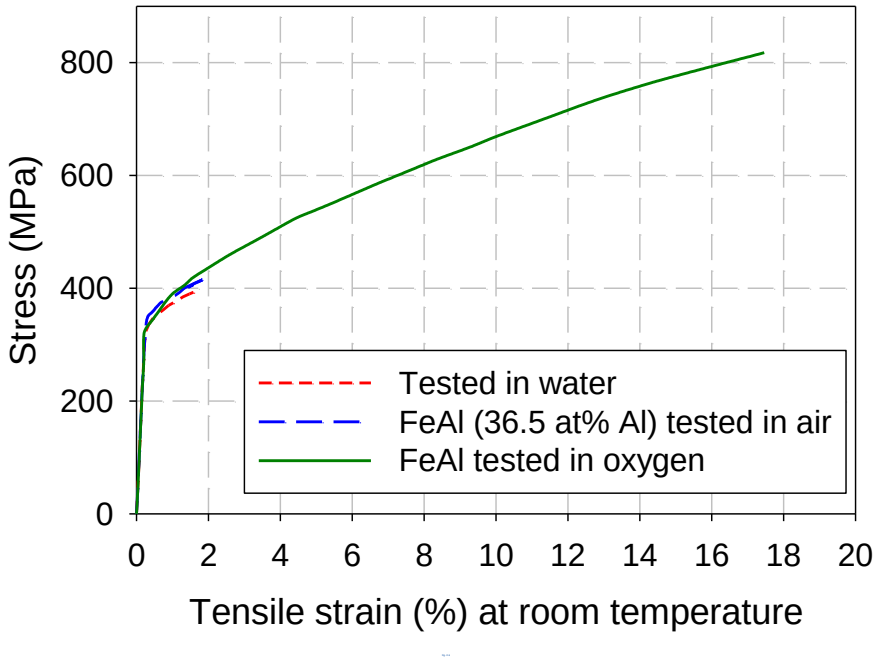

Fig. 2-6. Stress-strain curves of FeAl intermetallics in different environments at room temperature [12].

2.3. Oxidation and Corrosion of Iron-Aluminides

The applications of the Fe-Al intermetallics require use in hostile environments, which results in a resistance to oxidation, sulfidation, salt and air corrosion at high temperatures. Binary iron-aluminums containing almost 10 at.% Al could produce a homogeneous α-alumina layer [16 and 144]. This layer maintains its desirable oxidation resistance over a wide range of temperatures and in steam environments [145-149]. Increasing the Al concentration enhances the protectivity of oxide layer at high temperatures [16 and 17]. In the studies of the oxidation behavior of B2 aluminides, a parabolic oxide growth rate was observed at high temperatures [150]. It occurs by oxygen diffusing inward through the oxide, with oxide formation taking place at the metal/oxide interface. Oxidation resistance of aluminides can be improved by the additions of rare earth metals and transition metals like Cr[10], Ti, Nb [52], Y and Ce [151]. However, addition of high concentrations of Mo or Zr may increase the corrosion rate of iron aluminides (Fig. 2-7) [52].

Furthermore, resistance to aqueous corrosion at low temperatures is essential for the applicability of iron aluminides without compromising their structural integrity. Remarkable enrichment of aluminium within the passive film [152] plays a beneficial role on the passivation of iron-aluminium intermetallics. A Pourbaix diagram of aluminum [153] provides information about the thermodynamic stability of different species as a function of potential and pH (Fig. 2-8). At room temperatures and in near neutral and Cl^- free solutions, aluminum makes a protective insoluble oxide/hydroxide film [154-156]. However, the range of passivity varies with temperature, the specific form of oxide film present on surface, and with the presence of substances in the solution that can form soluble complexes or insoluble salts with aluminum [157 and 158]. According to the Pourbaix diagram, the corrosion rate increases as the pH moves away from the near-neutral condition. In alkaline environments, aluminum dissolves as AlO_2^-. Additionally, aluminum is not resistant to corrosion in many acidic solutions and dissolves as Al^{3+} ions.

Like other commercial Al reach alloys, iron-aluminum intermetallics have poor resistance to localized (pitting and crevice) corrosion in Cl^- containing solutions. The efforts of the

[10] At the temperatures more than 1000°C, Cr_2O_3 is no longer stable and its evaporation will increase the oxidation rate of alloys (see Fig. 1-3c).

production of "stainless" aluminum or aluminum reach alloys, with a high resistance to localized corrosion in a chloride solution, is still impaired.

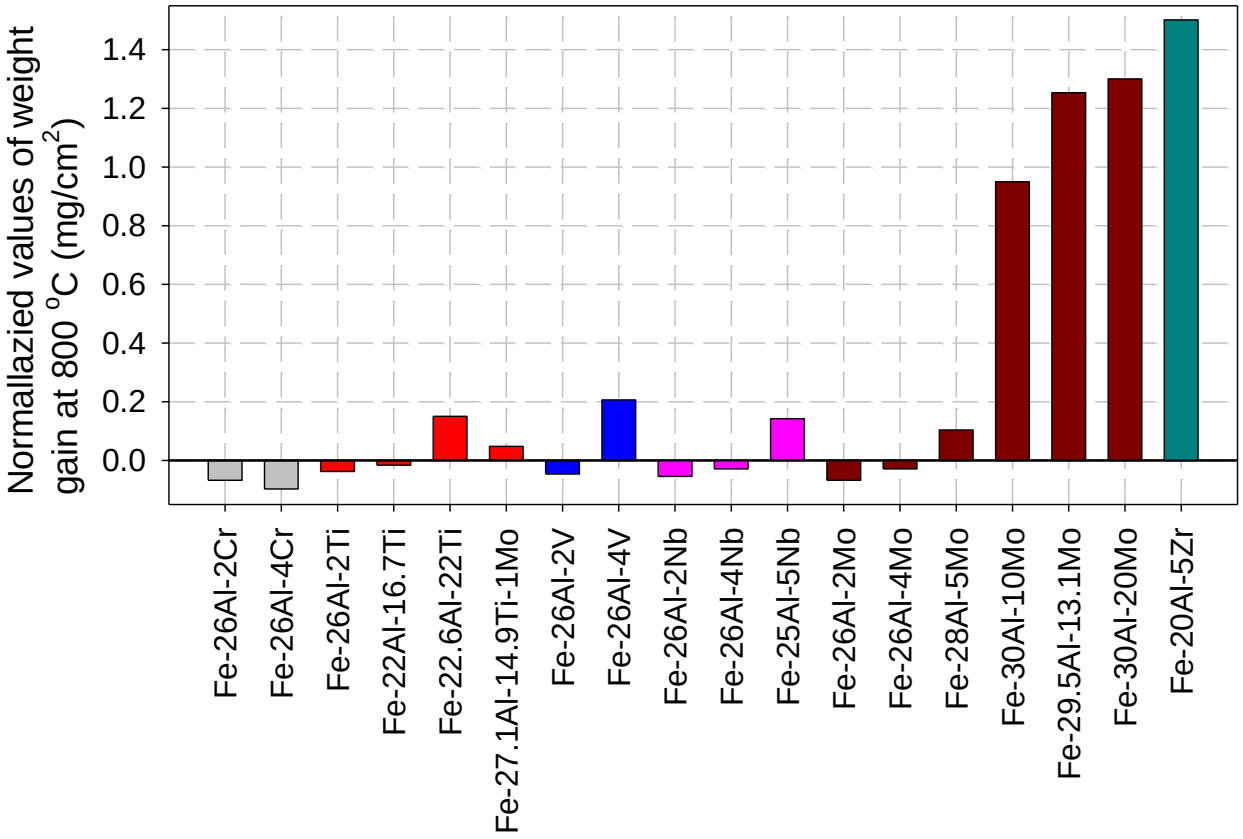

Fig. 2-7. Normalized values of weight gains of Fe-Al based intermetallics are air (zero line is the mass gain of Fe-26Al) [52].

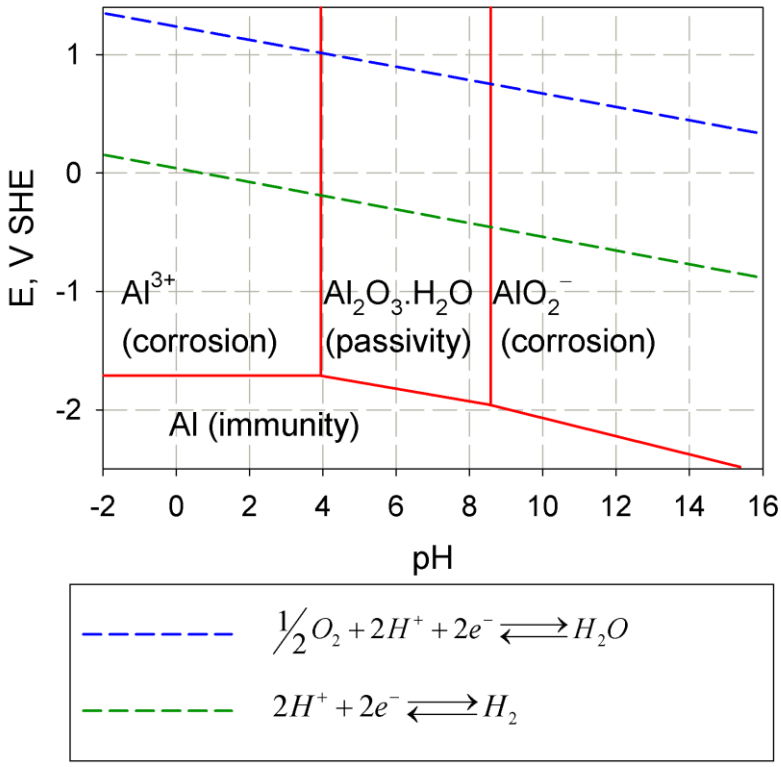

Fig. 2-8. Pourbaix diagram for aluminum at 25 °C [152].

2.4. Introduction to the nanoindentation technique

Recently instrumented-indentation technique or nanoindentation technique has gained enormous popularity because it represents the current-day version of the traditional hardness testing technique. Probing extremely small volumes during nanoindentation makes the technique, effectively, non-destructive. Furthermore, the small sample size simplifies the pre- and post-characterization of the sample. The technique was first applied for the investigation of size effects [159-163] and thin films [164 and 165]. Furthermore, there is considerable interest in further development to extend the capabilities of the technique, such as evaluation of the mechanical properties of viscoelastic materials [166] or indentation in a variety of environments, including immersion in liquids [18, 109, 135, 167 and 168], high and low temperatures [169-171] and etc.. This allows measurements to be performed in near natural/ industrial conditions.

Typical dislocation densities in an annealed metal are in the range 10^{10}–10^{12} m^{-2} with dislocations spaced between 1 and 10 µm apart. Therefore, it is very probable to indent a dislocation free region. In this case the collected load-displacement (L-D) curves start with a completely elastic deformation segment. Beyond the elastic limit of a crystal, plastic deformation occurs by nucleation, propagation and multiplication of dislocations. The displacement burst, or pop-in, which appears after the initial elastic loading sequence of a nanoindentation experiment, correlates to the homogenous dislocation nucleation (HDN). This shows the capability of the nanoindentation technique to resolve the dislocation nucleation in samples with low dislocation density [172 and 173] and also extracting the activation energies required for dislocation nucleation [18, 109, 167 and 168]. Additionally, Oliver and Pharr popularized nanoindentation as a technique to extract elastic properties along with hardness using the measured L-D data [174]. In the following, the most popular methods used for analyzing different mechanical properties based on the L-D curves are explained in detail.

2.4.1. Oliver-Pharr method for measurement of mechanical properties

During the 90th, Oliver and Pharr re-introduced the stiffness equation(s) and demonstrated that this equation works for all axisymmetric indenters with any infinitely smooth profile. Based on their model, during the unloading segment, it is assumed that the deformation is completely elastic and the reduced elastic modulus (E_r) can be measured by analyzing this part of the curve, according to Eq. 2-8 [175].

$$E_r = \mathrm{B}\frac{\sqrt{\pi}}{2\sqrt{A_c}}S$$ Eq. 2-8

Where $S = \partial P/\partial h$ is the slope of the load-displacement curve at the initial part of the unloading segment, A_c is the projected contact area evaluated from the contact depth (h_c), and the tip area function, B, is a correction factor depending on the tip geometry (1.034 for a Berkovich indenter). The calculated E_r according to Eq. 2-8, is the reduced elastic modulus and is related to the elastic modulus and Poisson's ratio of the sample (E and υ) and the indenter (E_T and υ_T) according to the following equation [174].

$$\frac{1}{E_r} = \frac{1-\upsilon^2}{E} + \frac{1-\upsilon_T^2}{E_T}$$ Eq. 2-9

The nanohardness (H) was measured according to Eq. 2-10:

$$H = \frac{P_{\max}}{A_c}$$ Eq. 2-10

where $P_{\max}$ is the maximum applied load.

2.4.2. Pile-up and sink-in Behavior

During nanoindentation, materials with limited elasticity accommodate the volume of the indenter by plastic flow of the material, eventually piling-up around the tip. It may cause over or under estimation of the contact area (A_c) and, hence, influence the precision of the measured values of hardness or elastic modulus. The Oliver and Pharr analysis assumes that the material deforms elastically around the contact impression. However, in reality, plastic deformation can also occur in the surrounding material. Bolshakov and Pharr [176] used finite element modeling to study the interaction between tip and material. They modeled the indenter as a rigid cone with the same area-to-depth ratio as a Berkovich indenter, and assumed a frictionless interface between the indenter and the sample. In materials with a high ratio of reduced Young's modulus to yield stress $\left(E_r/\sigma_y\right)$, the material surrounding the indent was found to pile-up around the indentation and increase the effective contact area. In materials with low E_r/σ_y ratio, the

surrounding material was sinking-in and, therefore, the effective contact area was less than expected. Work hardening favored sink-in behavior while the increment of dislocation (work hardening) does not influence the elastic modulus, but enhances the yield stress of materials. Pile-up (or sink-in) changes the real contact surface area and causes an over estimation of measured E or H. Based on the finite element simulation of nanoindents, a criterion was proposed for judging the probable under- or over-estimation of the contact area. According to this criterion, the pile-up effect becomes significant if the ratio of the final indentation depth (h_f) to the indentation depth at the maximum force ($h_{\max}$) is higher than the critical value of 0.7 for a conical tip. This ad-hoc approach provides a tool for a rapid judgment on the possible error in the nanoindentation hardness and Young's modulus measurements. However, it does not provide a solution for correction of the error in the case of the underestimation of the contact area due to a large pile up. The most appropriate methods for correcting the pile-up effect on contact area estimations are based on subsequent imaging of the indents with high spatial resolution.

2.4.3. Hertzian contact model

The initial elastic deformation before pop-in could be used to extract the E_r , according to the Hertzian contact theory. Hertz`s model is based on the linear theory of elasticity for frictionless contact surfaces. He first made his hypothesis that the contact area between two spheres is generally elliptical. Each body can be regarded as an elastic half space loaded over a small elliptical region of its plane surface. In his model, he ignores the existence of highly stressed regions beneath the contact area. However, it is shown that this model is promising for continuous surfaces at small strains or displacements [177]. Applicability of this technique is due to the fact that all indenters are approximately spherical at the tip, and hence the elastic interactions between tip and surface can be modeled with the Herzian contact theory. Using this model makes it possible to accurately analyze data without the influence of pile-ups. According to this model, the initial elastic loading segment prior to the displacement burst is predicted by the following equation [177]:

$$P = \frac{4}{3} E_r R^{1/2} h^{3/2}$$ Eq. 2-11

where h is the penetration depth and R is combined radius of tip (R_1) and surface ($R_2 \approx \infty$ for a flat surface). It can be calculated using Eq. 2-12.

$$\frac{1}{R} = \frac{1}{R_1} + \frac{1}{R_2}$$ Eq. 2-12

In this Equation, in order to be able to calculate the E_r, we need to know the tip radius R_1. One method for precise tip radius measurement is the direct measurement of this value by means of the SEM or AFM techniques.

2.4.4. Pop-in load analysis

It is shown in experiments as well as simulations that the measured maximum shear stress at the pop-in load in a dislocation free area approaches the theoretical shear strength [178]. Hence, nanoindentation, unlike other mechanical testing methods, also allows dislocation nucleation events to be detected on well-prepared surfaces [179-182]. Clearly, indentation of the samples with high dislocation densities mainly activates existing sources of dislocations, such as Frank-Read sources, where no pop-in occurs [168]. According to continuum mechanics and computer simulations, the maximum shear stress is applied on a point 0.48 times the contact radius, $\alpha_{contact}$, below the sample surface. The position of this maximum shear stress $Z_{r(\max)}$ and its value ($\tau_{\max}$) are calculated by Eq. 2-13 and Eq. 2-14 [135].

$$Z_{r(\max)} = 0.48 \times \alpha_{contact} = 0.48 \left(\frac{3PR}{4E_r}\right)^{\frac{1}{3}}$$ Eq. 2-13

$$\tau_{(\max)} = 0.31 \left(\frac{6E_r^2}{\pi^3 R^2} P\right)^{\frac{1}{3}}$$ Eq. 2-14

Based on classic dislocation nucleation theory [183], the free energy required for HDN can be calculated using the line energy of the newly formed loop W_{dis} and the work for extending the dislocation loop $\tau_{(\max)} b$ per loop area (πr^2) (i.e. the Peach–Köhler force [184]).

$$\Delta G = 2\pi r W_{dis} - \pi r^2 b \tau_{\max} \quad \text{Eq. 2-15}$$

The first term on the right-hand side of Eq. 2-15 describes the energy required to create a dislocation loop of radius r in a defect-free lattice and in the absence of any stress field. The second term represents the work done by the applied stress at the pop-in load ($\tau_{\max}$) to expand a dislocation loop, i.e. the activation area under the applied stress for a given loop radius. The elastic self-energy for a full circular dislocation loop in an infinite elastic solid is given by:

$$W_{dis} = \frac{2-\upsilon}{1-\upsilon}\frac{\mu b^2}{8\pi}\left(ln\frac{4r}{\psi} - 2\right) \quad \text{Eq. 2-16}$$

where ψ is the dislocation core radius. Considering Eq. 2-15 and Eq. 2-16, ΔG can be rewritten as follows:

$$\Delta G = \frac{2-\upsilon}{1-\upsilon}\frac{\mu r b^2}{4}\left(ln\frac{4r}{\psi} - 2\right) - \pi r^2 b \tau_{\max} \quad \text{Eq. 2-17}$$

Addition of interstitial hydrogen atoms or substantial atoms could influence the line energy of a dislocation with changing the μ, b and ψ. Accordingly, it may alter the shear stress ($\tau_{\max}$) we need for dislocation nucleation. Therefore, nanoindentation is a very powerful technique for studying the effect of substantial and interstitials on the mechanism of dislocation nucleation, and for the energy needed for dislocation nucleation. Its application was studied earlier on copper [168], nickel [167] and aluminum [109], 316 and PPN treated alloys [185-188].

3 - Experimental

3.1. Sample Preparation and Characterization

Different features of the studied materials, like iron-aluminides and super duplex stainless steels, will be considered in this section. However, this part will also cover the characteristics of the standard samples for performing different types of calibrations.

3.1.1. Fe-26Al-xCr

The investigated Fe-Al intermetallics where produced by the Max-Planck institute in Düsseldorf, with the induction melting method in argon inert gas. The nominal compositions of the binary and ternary intermetallics in addition to the measured impurity content of alloys are given in Table 3-1.

Table 3-1. Composition of Fe-26Al-xCr used in this study [41].

Fe at.%	Al at.%	Cr at.%	Si wt.ppm	S wt.ppm	C wt.ppm	N wt.ppm	O wt.ppm	P wt.ppm
74	26	0	⩽10	⩽4	⩽50	⩽20	⩽100	⩽20
73.5	26	0.5	⩽10	⩽4	⩽50	⩽20	⩽100	⩽20
70	26	4	⩽10	⩽4	⩽50	⩽20	⩽100	⩽20
69	26	5	⩽10	⩽4	⩽50	⩽20	⩽100	⩽20

In all samples, concentration of aluminum remains constant at 26 at.%. Ternary atoms were substituted for iron atoms. The chemical compositions of selected alloys were analyzed in the Max-Planck institute by electron-probe microanalysis (EPMA), using a Cameca SX 50 instrument [41]. It was shown that the compositions, determined by EPMA, are in good agreement with the nominal compositions within ±0.4 at.% [41].

Different samples have been cut using spark erosion on cylinders with a diameter of 12 mm. A part of the as-casted materials were heat treated first at 1200 °C for 24 h in a vacuum with subsequent furnace cooling for homogenization. Afterward, one part of the homogenized sample was annealed at 400 °C for 168 h in a vacuum to make a $D0_3$ structure. Another part was heat-treated in the B2 state at 750 °C for 72 h in air, and subsequently quenched in water.

3.1.2. Super duplex stainless steels

The SAF 2507® super duplex stainless steels (SDSS) were supported by OUTOKUMPU. The composition provided by the supplier is given in Table 3-2. The sample was in the solution annealed condition, having been heat treated at 1120 °C for 45 min and quenched in water. The ferrite content was 46% according to the supplier's test results. Cylindrical samples (Ø12 mm and 5 mm thickness) were cut from a slab by spark erosion method for performing in-situ hydrogen charging tests.

Table 3-2. Composition of SDSS used in this study as provided by the supplier

Element	C	Si	Mn	P	S	Cr	Ni	Mo	N
wt.%	0.016	0.23	0.79	0.021	0.001	25	6.98	3.82	0.27

3.1.3. Samples for calibrations

The nanoindenter's manufacturer, Hysitron Ltd, provided the calibration samples, which included high purity aluminum and fused silica. The mechanical properties of the samples in addition to the tips are listed in Table 3-3.

Table 3-3. Materials properties of commonly used calibration standard materials when coupled with a diamond indenter

Material	Reduced elastic modulus (GPa)	Elastic Modulus (GPa)	Hardness (GPa)	Poisson's Ratio
Diamond	1140	n.a	> 100 GPa	0.07
Fused Quartz	72	69.6	9.2	0.17
Tungsten	322	412	6.6	0.28
Aluminium	76	70.8	0.25	0.36

3.1.4. Metallographic Preparation

For all samples, the working surface was ground with 320, 600, 1200, 2500 and 4000 grit emery paper. For nanoindentation and AFM measurements, samples were polished with successively finer diamond paste from 3 µm to 0.25 µm using an Alogitech PM5 machine. Afterward, the samples were cleaned, first with ethanol and then by being submerged for ten minutes in a 50% ethanol-50% isopropanol ultrasonic bath. Finally, since a low- surface roughness and low-dislocation density is a prerequisite for AFM and nanoindenter measurement, samples were electropolished in order to remove the mechanically damaged layer on the surface after mechanical polishing. The parameters we used for the electropolishing are listed in Table 3-4.

3.1.5. Solution preparation

All solutions were made from analytical-grade reagents and double distilled water. A borate buffer $\left(H_3BO_3\left[0.3\ M\right], Na_2B_4O_7.10H_2O\left[0.075\ M\right]\right)$ with the pH of 8.4 was used for in-situ nanoindentation tests, cyclic-polarization, electrochemical impedance and capacitance measurements. Sodium chloride, of various concentrations, was added to the borate solutions for polarization and galvanostatic measurements. All tests were carried out at ambient conditions.

Table 3-4. Defined parameters for electropolishing of different samples.

Material	Voltage (V)	Solution	Temperature (°C)	Time (s)	Flow rate
Al	42	A2 solution	<10	10-20	15
SDSS	30	$1M\ H_2SO_4 - methanol$	10 < T <20	10	15
Fe-26Al, Fe-26Al-0.5	28	$1M\ H_2SO_4 - methanol$	10 < T <20	10-30	20
Fe-26Al-4Cr, Fe-26Al-5Cr	29	$1M\ H_2SO_4 - methanol$	10 < T <20	10-30	20

3.2. Characterization of samples

Quantitative and qualitative characterisations of the samples were conducted using a wide range of instruments. The methods are described briefly in this section.

Optical Microscopy: All optical microscopy of specimens were conducted using an Axiotech Zeiss optical microscope equipped with a differential interference contrast and an Olympus digital camera.

Scanning electron microscopy: Zeiss ΣIGMA™ -VP Field Emission Scanning Electron Microscope (FE-SEM), equipped with the energy dispersive X-ray (EDX) and EBSD detectors, was used to characterize the different samples. EDX analysis was performed with the brand new large area (20 mm^2) Silicon Drift Detectors X-Max 20 SDD with Inca Energy 450 software package from Oxford Instruments, UK. Spectral resolution of these detectors is better than 129 eV. Additionally, the Oxford Instruments AZtec® EBSD system combined with Nordlys hardware was used for performing EBSD measurements.

X-ray Diffraction (XRD): X-ray diffraction was performed in air, using a PANalytical X'Pert Pro MPD diffractometer. The x-rays were generated using a 40 keV accelerating voltage and a 40 mA current, with a copper target. The scan was run from 5° to 130° 2θ, with a step size of 0.05° 2θ

and a step time of 2 seconds.

X-ray photoelectron spectroscopy (XPS): A Physical Electronics Quantum 2000 Scanning ESCA Microprobe was used to perform XPS measurements and analyze the surface composition of the freshly electropolished samples. A penning source was operated with Ar^+ (2 keV) for XPS depth profiling. The sputter rate was calibrated by using an oxidized silicon wafer of known oxide thickness. Quantitative evaluation of spectra was carried out on the basis of standard spectra of oxygen and the alloying components.

3.3. Electrochemical measurement

A conventional three-electrode electrochemical flat cell inside a Faraday cage was used for performing the electrochemical tests. The surface area of specimens after installation in the cell was 0.92 cm^2. A saturated calomel electrode (SCE) or a saturated KCl, Ag/AgCl reference electrode was used for the measurement of the potential of the working electrode. All potentials were converted and are reported compared to the standard hydrogen electrode (SHE). A reference electrode was connected to the cell through a Luggin capillary to avoid chloride contamination. A platinum foil with the surface area of 4 cm^2 was used as the counter electrode. The working electrodes were left to stabilize at its free corrosion potential for at least one hour before starting the experiments. The DC and AC tests were performed using a Zahner IM6ex electrochemical testing system.

3.3.1. DC measurements

Cyclic voltammetry (CV): this technique is used to study the effect of Cr concentration on the electrochemical behavior of the Fe_3Al intermetallics. CV measurements were performed on mechanically and also electrochemically polished samples, in a borate buffer solution. It was performed with the scan rate of $20\ mV/s$.

Polarization tests: the tests were performed with the sweep rate of $1.5\ mV/s$. The measurements were conducted in borate buffer solution with and without different contents of NaCl.

Galvanostatic tests: an anodic current of $1\ mA/cm^2$ was applied to the samples submerged in the borate buffer + 0.01M NaCl solution in order to check the mechanism of pitting and density of pits in different crystal orientations. Slew rate of the start phase was driven by the $1\ mA/s$.

3.3.2. AC measurements

Electrochemical impedance spectroscopy (EIS): EIS measurements were performed at different potentials from 0.54, up to1.04 V_{SHE}, with 100 mV steps and frequencies from 20 kHz to 2 Hz, with voltage amplitude $\pm 10\ mV$. The EIS measurements were performed after reaching the steady-state current at each potential, i.e. after ca. one hour. The validity of all the EIS results was tested with the Kramers-Krönig transformation in order to check the three requirements formulated for the constraints of the linear system theory (LST), i.e. causality, linearity and stability.

Mott-Schottky (MS): MS tests were performed by stepping the potential in the positive direction, from 0.04 V_{SHE} to 1.04 V_{SHE}, in 50 mV increments. The impedance was measured at one particular frequency after each 50 mV change of potential. The potential was then stepped and held at the film formation potential until the steady-state current was achieved. A total of three different frequencies were employed: 1000, 700 and 500 Hz.

3.4. Atomic force microscopy (AFM):

AFM characterization was performed, using the Bruker dimension 3000® atomic force microscope (AFM). Ex-situ AFM was performed under contact and tapping modes and the in-situ measurements in fluid were performed using only contact mode. A gold-coated cantilever with an ultra-sharp tip was used in this work for in-situ measurements. We tried to improve the image quality carefully by adjusting the integral, proportional and derivative (PID) gains. The gains (especially integral gain) were increased in small increments until noise was observed in amplitude feedback oscillations. Then, perfect gains were set by reducing the integral gain by 10-15%, which significantly reduced the noise and also improved the quality of the images. Once all the parameters were properly adjusted, we started scanning the surface while the sample was covered with approximately 2 mm of electrolyte. During the scanning process, we applied cathodic potentials to the samples. The experimental setup was developed in our institute (Fig. 3-1) and consists of three electrodes, which are designed and produced to fit into

the AFM chamber. A platinum wire was used as a counter electrode and the reference electrode was an Ag/AgCl used to control the electrochemical potentials. Analysis of the data was accomplished using Gwyddion software.

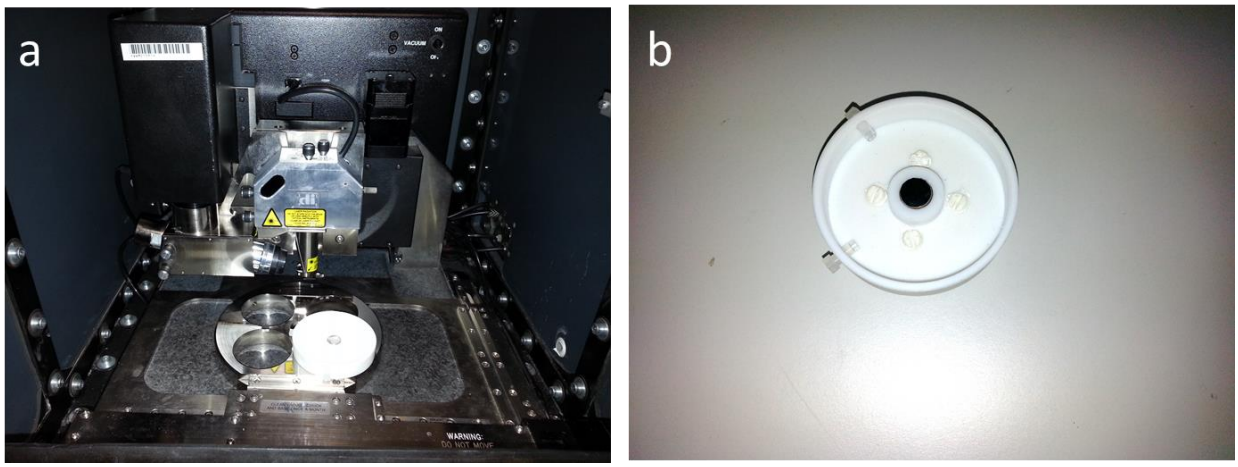

Fig. 3-1. a) Shows the experimental setup for in-situ AFM measurements. b) An AFM electrochemical cells with a sample installed at the center of the cell.

3.5. Nanoindentation

Nanoindentations were performed with a Hysitron TI 900 TriboIndenter equipped with a Performech controller, Stanford Research System (SRS) 830 DSP lock-in amplifier and National Instruments USB-GPIB adaptor. The internal digital feedback loop rate and data acquisition rates were up to 78 kHz and 38 kHz, respectively. Another important part of the TriboIndenter is the patented three-plate capacitive force/displacement transducer, developed by Hysitron. The maximum normal displacement of the tip was limited to 5 µm. During this work we used three different transducers for various reasons, as follows:

1- The 1D (normal force only) transducer. It consists of the force/displacement sensor, drive circuit board, and hardware used to mount the transducer to the TriboScanner. The features of the transducer are listed below:

   - maximum applied vertical load was 30 mN;

   -load Resolution was 1 nN;

   -displacement resolution was 0.04 nm;

   -thermal Drift was less than 0.05 nm/sec [189].

2- The 1D, nanoDMA III compatible transducer. With this transducer, performance of the dynamic measurements was possible. The features of the trasducer are listed below:

-maximum applied vertical load was 10 mN;

-load Resolution was 1 nN;

-displacement resolution was 0.04 nm;

-thermal Drift was less than 0.05 nm/sec [190].

3- The 2D (both normal and lateral force) transducer. It has the components of the 1D, plus two additional transducers mounted on opposite sides of the first, centered at a 90° angles. The features of the transducer are listed below:

-maximum applied loads in the vertical and horizontal directions were 10 mN and 2 mN respectively;

-lateral load Resolution was 3 µN;

-maximum lateral displacement was 15 µm;

-resolution of the lateral displacement was 4 nm;

-thermal Drift was less than 0.05 nm/sec [189].

Additionally, the TriboIndenter utilizes an active anti-vibration system, an acoustic enclosure, a stage controller and optic/ optic electronics. With the aid of the aforementioned parts, we could control the following items during nanoindentation:

1- Atmosphere, humidity and temperature variation[11] .

2- Environmental vibrations; vibrations less than 200 Hz could be dampened actively with the active anti-vibration system and vibrations over 200 Hz could be dampened passively [189].

3.5.1. Quasi-static and dynamic measurement

Different types of tests can be performed with the nanoindenter including quasi-static nanoindentation, NanoDMA Indents[12], bending and low cycle fatigue test of micro pillars, wear and nano-scratch. The focus of this work was on indentation and, hence, we will discuss only the first two methods in the following paragraphs.

Quasi-static nanoindentation was traditionally used to quantitatively measure the mechanical properties, like hardness and elastic modulus of materials. With the Quasi-static nanoindentation method, we can collect the applied load vs. displacement data and measure the hardness and

[11] Temperature variation during the measurement was less than 0.5 °C.

[12] The nanoDMA III interface software is compatible with the performech controller.

elastic modulus at one single depth of indentation[13], with the presumption that the material deformation is purely elastic/plastic [189]. However, any sample that can be characterized using the quasistatic nanoindentation method can be tested using nanoDMA to obtain much more information about the sample[14]. With the aid of dynamic measurement, a sinusoidal loading could be applied in addition to the quasi static loading (Fig. 3-2). With this technique, we can define the load amplitude, and frequency (0.1 Hz - 300 Hz) in addition to the routine controllable parameters for the Quasi-static, such as maximum load (displacement), loading (displacement) rate, number of segments, data acquisition rate and etc. [190].

In general, we can perform three different types of tests with the dynamic modus, which include continuous measurement test (CMX), sweep and creep tests. CMX has been used to perform continuous measurements of different mechanical properties, like hardness at different depths. With the variable dynamic load scaling option, we set the dynamic load to be scaled with respect to the quasistatic load. Based on this option, the dynamic load was proportional to the square root of the quasistatic load. This option results in constant dynamic displacement amplitudes between 1-2 nm, to ensure the validity of the model used for analysis of the results [190] (Fig. 3-2b). We performed our measurement with the fixed frequency of 220 Hz. More information about the sweep and creep tests exist in appendix B.

3.5.2. Methods of calibration

Like other high precision instruments, nanoindentation technique requires performing different types of calibrations. Three of the most important calibration methods include tip area function calibration, frame compliance measurement, and tip to optic calibration. Here, our main target is to explain the reasons and basic requirement for the calibration. More information about the methods of calibration is stated in the references [189 and 190].

[13] Depth profiling can be accomplished by performing a series of individual quasistatic tests, each at a different location, and different loads. This technique is time-consuming due to the fact that only one measurement of the material properties at a single depth is obtained from each test.

[14] The dynamic mechanical analysis, commonly referred to as DMA, was developed primarily in response to the insufficiencies of quasi-static testing for materials that display significant time-dependent deformation and recovery, such as viscoelastic materials [190].

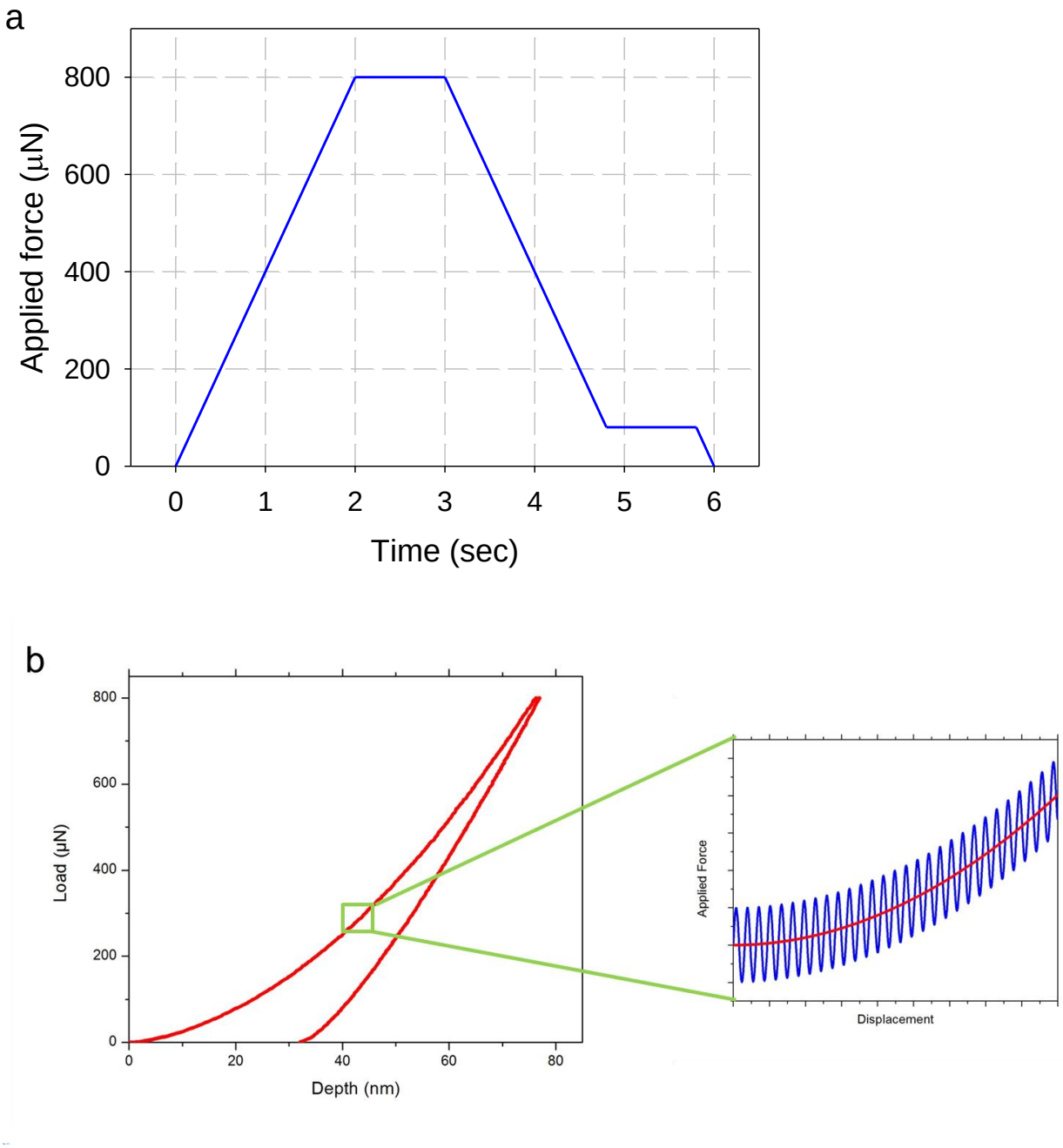

Fig. 3-2. a) Shows a typical quasi-static loading function with a holding segment at the maximum forces for checking the creep behavior of alloys and another holding segment during unloading at low forces to check the drift in the measurements. b) Shows a typical CMX Load-Displacement curve.

3.5.2.1. Tip area function calibration,

Brinell sphere, Rockwell cono-spheroids, Vickers and Knoop pyramids are some of the commonly used indenter geometries for macro-micro scale indentation. For the pyramids, this is

due to the unavoidable line of conjunction (chisel edge) formed across the tip of a four-sided pyramid whenever one side deviates from ideal geometry. Berkovich and cube corner indenters, however, are suited well to nano-scale testing, since they can be manufactured with very small tip radii by virtue of their three-sided pyramidal geometry. Parameters for common indenter shapes are shown in Table 3-5 [191].

Table 3-5. Geometric factors for commonly used indenter profiles [191].

Indenter	Projected area	Centerline-to Face angel, φ	Equivalent cone angle	Intercept factor	Correction factor B
Berkovich	$24.562\times h_c^2$	65.3°	70.32°	0.75	1.05
Cube Corner	$2.598\times h_c^2$	35.26°	42.28°	0.75	1.034
Cone	$\pi\left[h_c\tan(\varphi)\right]^2$	φ	φ	0.72	1
Sphere	$\pi\left[2Rh_c - h_c^2\right]$	-	-	0.75	1
Knoop	$65.438\times h_c^2$	86.25° & 65°		0.75	1.012
Vickers	$24.504\times h_c^2$	68°	70.2996°	0.75	1.012

Nanoindentation is the application of a defined load (in the µN-mN range), with concurrent depth measurement (in the nm-µm range). Hence, the correlation between the depth of indentation and the contact area is a key point for precise measurements of mechanical properties like elastic modulus and hardness (refer to Eq. 2-8 and Eq. 2-10). On the other hand, deterioration of the tip after usage causes a deviation between the nominal projected area function, which is listed in Table 3-3, and the actual value. This dictates the necessity of precise tip area function calibration, which defines the correlation between the contact depth and contact area. One indirect (standard) method for analyzing the indenter tip geometry is indentation of a well-defined material. Since the Young's modulus of fused quartz (and hardness) is clear, we can use the Oliver and Pharr method for correlating the dependency between the depth of indentation and the contact area [191].

The materials we use for this type of calibration should be relatively hard and stiff. This ensures that loads applied at very low penetration depths are still large enough to be well within the force resolution of the indentation system. Thus, both sapphire and fused silica are appropriate for this calibration; however, fused silica is superior on elastic isotropy, economy and creep criteria [191].

By the way, the tip calibration at very low depths is not possible due to the spherical form of the tip at the top part (Fig. 3-3c). Additionally, the tip may break and / or becomes dirty during installation or handling (Fig. 3-3d). This shows the importance of the direct imaging of the tip in addition to the traditional methods of tip area function calibration.

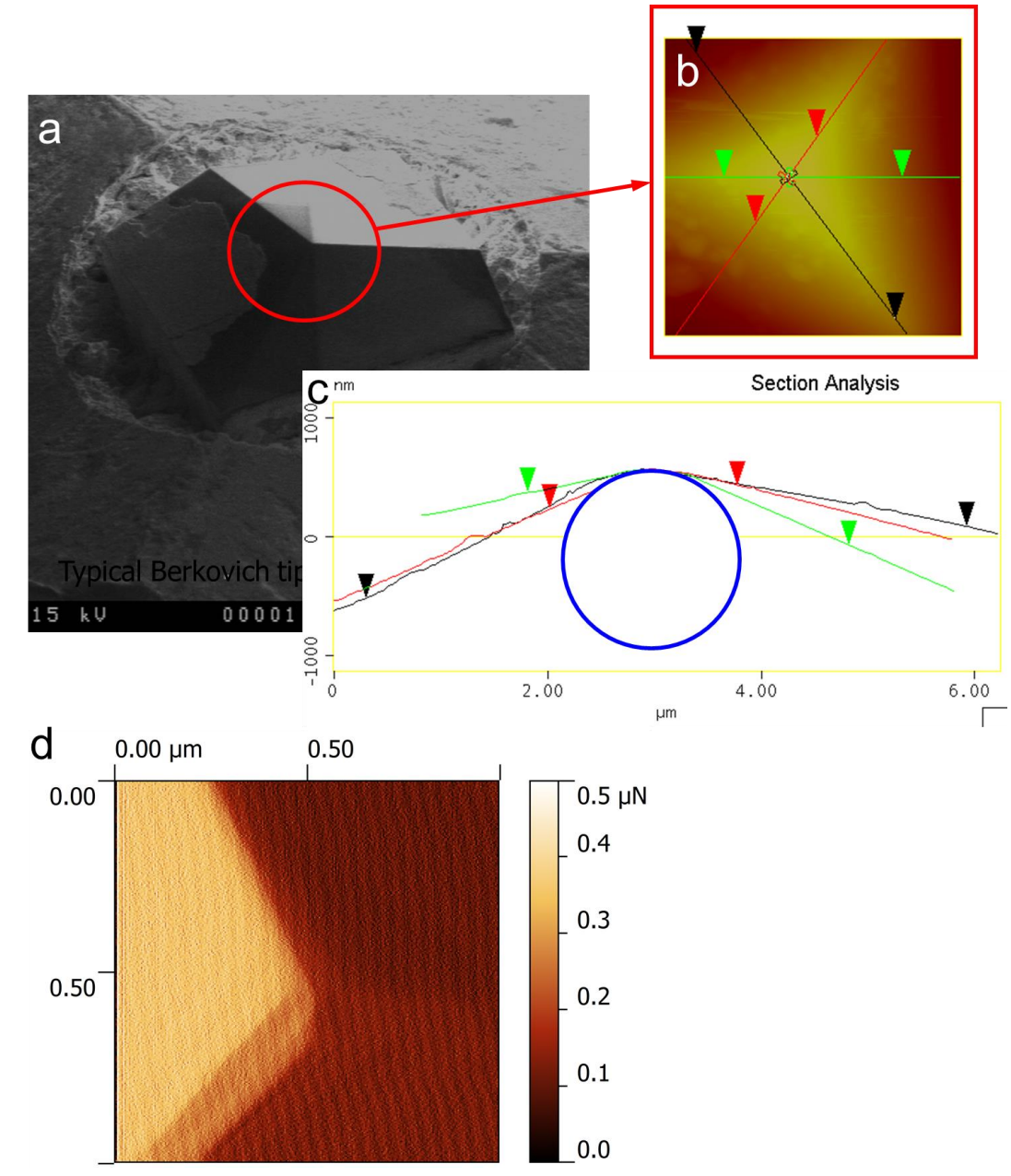

Fig. 3-3. a) An SEM image of a Berkovich tip. b and c) Show the spherical form of a tip at the most top part. d) An SPM image of a broken Berkovich tip.

The precise imaging of the tip with the scanning mode of the nanoindenter (Fig. 3 3b and d) [192] may give us the opportunity for the measurement of tip radius for calculation of the reduced elastic modulus based on Hertzian contact model (Eq. 2 11). Moreover, before we started the measurements, the tips were cleaned manually with very soft touching using an adhesive tape after installation on the transducer. This cleaning treatment removes most contamination of the indenter.

3.5.2.2. Frame compliance determination

The inverse of the stiffness ($C = S^{-1}$) is known as compliance. During the indentation, the deformation (elastic-elasto/plastic) is not only limited to the sample and the indenter tip, but also to the entire frame. In order to subtract its effect, we can use the following equation [191].

$$C_0 = C_F + C_s \qquad \text{Eq. 3-1}$$

Where C_0 is the uncorrected and C_s the real compliance of the sample. However, frame compliance (C_F) should be determined for precise calculation of the mechanical properties. Since the compliance of the sample and indenter are measured experimentally, we can re-write the Eq. 2-8 as follows:

$$C_0 = C_F + \frac{\sqrt{\pi}}{2\mathrm{B}E_r} \times \frac{1}{\sqrt{A_c}} \qquad \text{Eq. 3-2}$$

This shows the need of a priori knowledge of the indenter shape function for defining the frame compliance. However, sometimes it is the case that both the shape function and the frame compliance are initially unknown. In this case, an iterative procedure, achieving increasingly accurate approximations, can be used. First, it can be assumed that the shape function of the indenter is ideal for its geometry and a (preferably soft) sample can be indented at high loads, to create very large contact impressions. This minimizes the deviation from ideal geometry, and, by using a reference sample of known reduced modulus, an approximate value for the frame compliance can be determined. Additionally, using the frame compliance value in Eq. 3-2 allows the shape function to be estimated. By iterating this procedure, the values for the compliance and shape function can be refined for smaller indentations. Alternatively, the shape function can be determined directly by careful measurement of the shape of the tip using a

traceably calibrated, precision metrology device such as an AFM [191].

3.5.2.3. Tip to optic calibration,

For this reason a very soft material, such as high purity aluminum, that can easily be prepared with good surface quality or level of flatness, is desired. Since this test needs to be performed any time indenter tips are exchanged in the system, economy plays a large role. This calibration determines the offset between the location of the indenter tip and the location of the center of the focus of the microscope in the positioning stage of the nanoindentation system. Therefore, the only requirement of the material is that it readily holds a clear indentation impression [191].

3.5.2.4. Thermal Drift and Creep

Creep and thermal drift are completely different phenomena, but corrections are made for their occurrence using similar actions [191]. Thermal drift happens when the indenter system, as a whole, is not in thermal equilibrium. It results in displacements from thermal expansion/contraction being measured, instead of, or in addition to, indentation displacements [191]. This can be minimized by placing the system in a thermally controlled chamber, but experimental measurement of the drift rate during each indentation should be made for precise work. This is done by maintaining a fixed load, e.g. ~10% of maximum applied load, for a fixed period during the lower part of the unloading curve and measuring the displacement over time. Creep deformation may also occur during indentation. This is most easily observed during a hold period at maximum load (Fig. 3-2a). A dynamic reference creep test is a new method to clarify between the creep behaviors of alloys and drift in the measurements. It is a test with an initial reference frequency segment followed by a long constant force dynamic part. The first reference frequency segment will be used to calculate the contact area and the second (longer) reference frequency segment will be analyzed as the creep segment. For information about this technique, see appendix B.

3.5.3. In-situ measurement

For in-situ nanoindentation the whole sample was immersed in a borate buffer solution. Due to the remote force sensing method of nanoindentation technique (with transducer) and the sensitivity of the electronics, just a part of tip could be immersed in the solution and the

electronics were protected from the solution. For this reason we customized the form of the tip for in-situ nanoindentation measurement, and the Synton-MDP LTD produced the tips. The large length of the shaft (13.5 mm) made from Ti allows the end of the tip to be completely immersed in a fluid, while the tip holder and transducer remain in the air. The experimental setup developed for conducting in-situ electrochemical NI-AFM consists of three electrodes, which are designed and produced to fit into the nanoindenter chamber. Nanoindentation was conducted inside this electrochemical cell while the sample was covered with approximately 5 mm of electrolyte. A platinum plate was used as a counter electrode and the reference electrode was an Ag/AgCl used to control the electrochemical potentials. Special tubing was used to inject a deaerated solution into the electrochemical cell, as shown schematically in Fig. 3-4.

We implement ECNI in order to probe the bulk effect of the Cr addition to the Fe_3Al alloys in presence of the hydrogen. A very low depth of indentation assures hydrogen saturation after a few minutes, even though the diffusion rate is very low in iron aluminides. Since the ECNI measures the nanomechanical properties just below the surface, it is a surface sensitive technique. The XPS and electrochemical tests showed that the Cr addition to these alloys might alter some of the surface properties. Therefore, we were especially careful in keeping the surface condition of the samples, with different Cr content, as comparable as possible. Surface parameters were kept constant and unchanged with the following precautions:

(1) In all samples, the indents were performed in the grains with similar (001) normal orientation.

(2) The ex-situ and in-situ indents for each sample were performed in an identical grain.

(3) The surface roughness at different potentials was always checked before performing nanoindentation with the scanning probe microscope (SPM) mode of our nanoindenter, and checked for its consistency against the freshly electro-polished surface roughness values.

(4) By selecting the anodic polarization at 500 mV_{SHE}, the Al^{3+} enriched passive layer was stabilized for all samples and remained stable during the course of the ECNI tests.

(5) In order to have a similar hydrogen charging condition (HER and/or hydrogen uptake and transfer through the passive layer), the hydrogen charging was done in galvanostatic mode by application of 100 $\mu A/cm^2$ cathodic current density.

(6) Due to the importance of the cleanliness of different parts of the setup, the borate buffer solution was prepared from analytical grade compounds and double distilled water. Prior to the

tests, the electrochemical cell was cleaned in piranha acid, which is a warm mixture of three parts sulphuric acid (H_2SO_4) and one part hydrogen peroxide (H_2O_2). Because the mixture is a strong oxidizer, it will remove most organic matter, and it will also hydroxylate most surfaces, making them extremely hydrophilic and water compatible. The tip was also cleaned carefully before each test in an ultrasonic bath in a mixture of ethanol and isopropanol, and then in double distilled water.

(7) Controlling the current distribution and homogeneous charging of materials is highly important. A uniform current distribution in a miniature electrochemical cell, with small amounts of solution, is hard to achieve. Furthermore, inhomogeneous current distribution may cause overprotection (strong hydrogen bubbling) at places close to counter electrodes, while the potential of the area far from counter electrodes is less. This was the motivation behind optimizing the form of cells (Fig. 3-5), as well as the tips.

(8) Controlling the pH of the solution is essential. The buffer capability of borate solution prevents a rapid increase in local pH of the solution. It was also shown that Al^{3+} ions could form complex ions such as $Al\left[B(OH)_4\right]_6^{3-}$ which consume many OH^- ions. These factors probably suppress the alkalization and, thus, dissolution of the aluminum oxide film. Additionally, we decreased the applied cathodic current and, hence, the limit of the reduction reaction and the production of OH^-. Furthermore, we tried to pump solution in and out of the cell in order to have fresh conditions during the in-situ nanoindentation measurements. High-resolution SPM images show very homogeneous surface qualities after the application of low currents to the samples. Very small current density in both materials during the anodic scanning of the potential indicates that there is no active anodic oxidation reaction. In other words, the passive oxide layer cannot be reduced completely with the application of cathodic potential.

(9) Submersion of a part of the tip in solution may result in the formation of different variable forces, like meniscus buoyancy acting on the tip during the experiment [193]. We did not correct the effect of these forces on the measurements. However, because the depth of solution was the same at anodic and cathodic potentials the results in these situations should be comparable.

(10) Performing tests in a Cl^- free solution is important. The high susceptibility of iron-aluminum alloys to pitting corrosion in the Cl^- containing solutions was established earlier. Corrosion and/or re-deposition of the corrosion products could produce surface roughness, which would influence the quality of the results.

(11) Controlling the oxygen content of the solution is necessary. One problem during in-situ electrochemical nanoindentation is dissolved oxygen in the liquid, which can influence the electrochemical processes. In electrochemical experiments, the usual practice is to bubble an inert gas, e.g. argon or nitrogen, inside the solution to remove the oxygen and inhibit the dissolution of oxygen. In our experiments, this practice was not possible; therefore, we put the whole system inside a protective atmosphere, and the electrolytes were deaerated externally before each experiment.

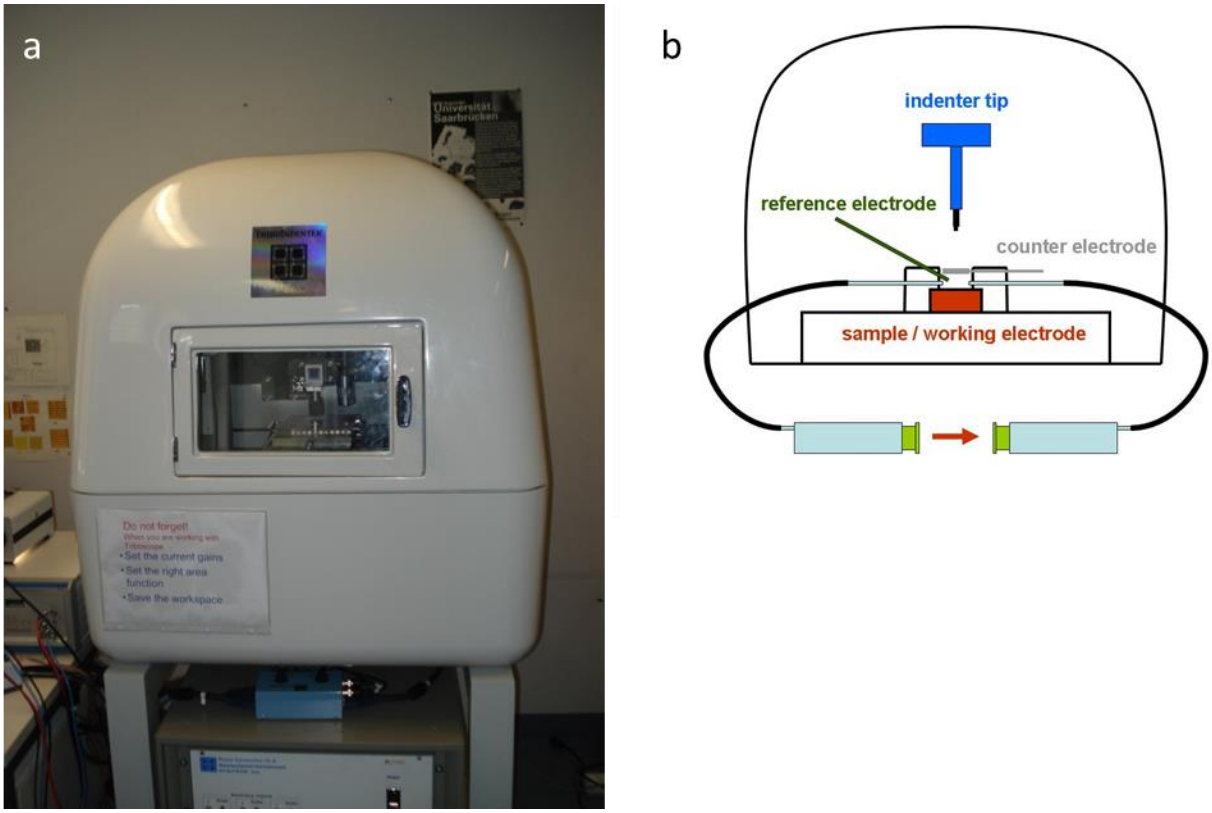

Fig. 3-4. a) Shows the Hysitron PI-900 nanoindenter, b) A schematic of the electrochemical measurement setup [193].

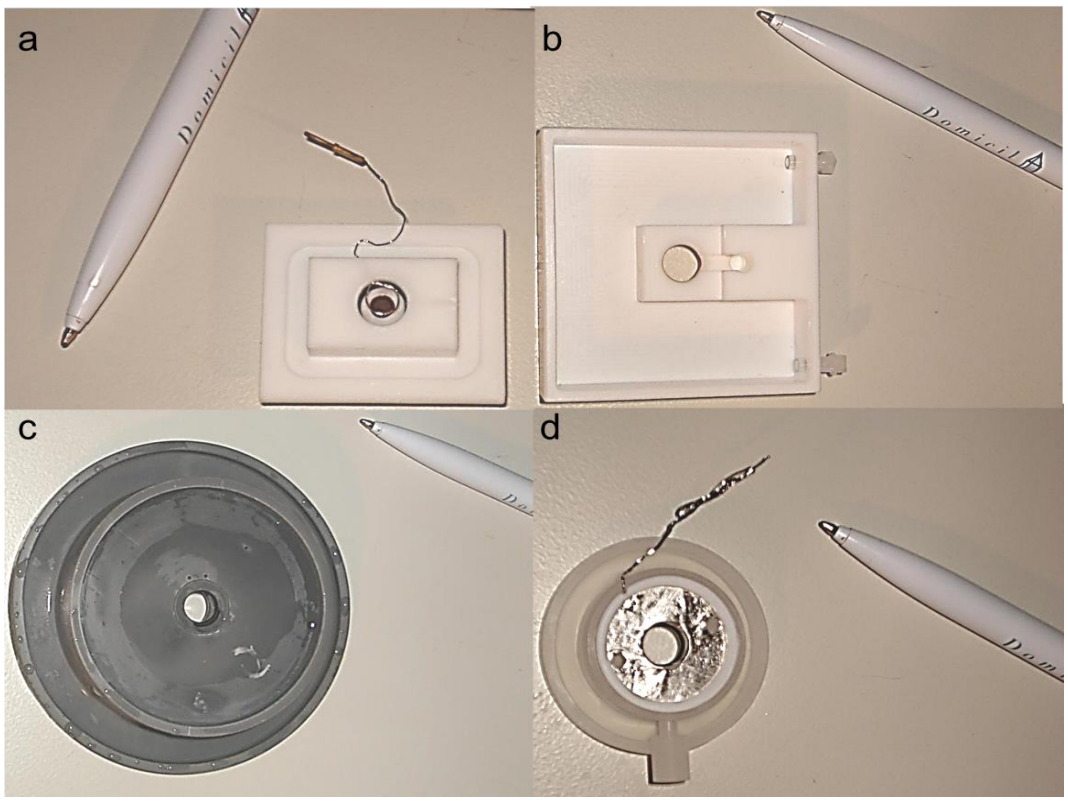

Fig. 3-5. Shows different generations of the electrochemical cells.

4 - Summaries of Appended Papers

Conventional mechanical tests are costly, time consuming, and due to their large scale, not very successful in obtaining mechanistic information. In contrast, a local method like nanoindentation has comprehensive ranges of possibilities to achieve an essential understanding about the influence of substantial (e.g. chromium) and/or interstitials (e.g. hydrogen) on the mechanical properties like Young´s modulus, Gibbs free energy for HDN, dislocation line energy and also friction stress. The method allows for measurement of mechanical behavior in simulated environments and atmospheres close to the routine industrial applications.

The effect of chromium concentration on the elastic modulus, incipient plasticity and post yielding behavior of the alloys was studied in details in papers A [178] and B [192]. It was shown in "paper A" [178] that the measured elastic and shear modulus will increase systematically with the increment of the Cr content in the alloys. The results were interpreted within the framework of the universal features of metallic bonding as a change in the interatomic potential, as proposed by Rose et. al. [194-196].

Strengthening of the interatomic bonds influences the dislocation line energy (Eq. 2-16), and hence the increase of elastic properties joins with the enhancement of the energy needed for dislocation nucleation. Therefore, by addition of Cr, the pop-load is increased, which means higher maximum shear stress beneath the nano-indenter tip is required in order to trigger the plastic deformation. In was shown in Table 1 Paper B [192] that the maximum shear stress at the pop-in load for each alloy is comparable with the theoretical shear strength $\tau_{max} \approx \frac{\mu}{20}$ predicted by Frenkel's model. It demonstrates the direct relationship between homogeneous dislocation nucleation (HDN) and onset of plasticity or pop-in in a dislocation free area beneath the tip. However, nucleation of a dislocation is a stress-assisted, thermally activated process. In other words, the energy barrier for dislocation nucleation could be overcome through the mechanical work of indentation and, simultaneously, by an appropriate thermal fluctuation. The observed scatter in the pop-in event (Fig. 3, paper A [178]) shows its unpredictable nature within a certain load range. The thermal noise sometimes favors yielding and sometimes works against it. Therefore, within the mentioned load range, we can talk about the probability of the pop-in

event[15]. Furthermore, by application of the classical dislocation and harmonic transition state theories, we were able to develop a simple relation to measure the effect of alloying elements on the shear modulus from the pop-in data (Fig. 5, paper A [178]).

In "paper B" [192], instrumented nanoindentation was used to investigate the hardness and mobility of dislocations via analysis of the load–displacement (L–D) curves. Surprisingly, the results show that alloys with 5at.% Cr have less micro-hardness, although the shear modulus increases; in contrary, with the decrease of the indentation depth, the nano-hardness of Cr containing samples will become more (Fig. 5 in paper B). The results show the slight increase of friction stress (τ_{P-N})[16], and strong decrease of flow stress (σ_{flow})[17], with Cr addition. The decrease of flow stress relates to the least strongly pinned segments in dislocations. Once these pinned segments become mobile, plastic deformation spreads by the mitigation of kinks. Another proof of the effect of Cr on the enhancement of the dislocations mobility was seen on the decrease of the height of pile-ups, and also wide spreading slip lines in the Cr-rich alloys (Fig. 3 and 4 in paper B). The reduction of average values of pile-ups after addition of Cr could be due to the increase of the capability of the material to include the plastic deformation, i.e. how far dislocations are capable of transferring the plasticity into the material. This can be explained by considering the ease of dislocation cross slipping in the Cr-rich samples.

After studying the influence of Cr on the bulk properties of alloys, we also tried to evaluate the effect of Cr on the passive layer in "paper C". Electrochemistry is of utmost importance for industrial production and application of different alloys. Hence, we studied the chemical properties of different alloys and electrochemical reactions at the solid/ solution interface in the presence of electric fields and currents. One typical starting point in exploring an electrochemical system is performing cyclic polarization. With the aid of this method, the potential is ramped linearly at a constant rate of potential change, and the current is measured as a function of

[15] The probability of overcoming the energy barrier by thermal fluctuations in a constant temperature increases if it takes longer to reach a certain critical stress. Thus, as the loading rate is increased the probability becomes lower and a higher stress is required to produce a critical thermal fluctuation to overcome, resulting in apparent higher yield strength. In our measurements, we kept the loading rate constant to be able to compare the average pop-in load.

[16] The increase of τ_{P-N} is mainly due to the influence of Cr on shear modulus.

[17] Here, σ_{flow} is considered without inclusion of intrinsic lattice resistance.

potential. For a single electrode reaction, the rate of electrochemical reactions[18] is proportional to the electric current. Though, corrosion of metals and alloys, especially in the presence of aggressive ions like Cl^-, often starts at local sites, and causes local material changes. Therefore, the susceptibility of alloys to pitting and crevice corrosion in solutions with different concentrations of Cl^- ions was studied. Considering Fig. 1, in paper C, the increase of current at high anodic potentials shows the enhancement of the amount of the electroactive reactions. In was shown that the incorporation of Cr as a ternary alloying element into the passive film increases the range of passivity and consequently resistance of the alloys to pitting corrosion and decreases the average density of pits. However, addition of 5 at. % Cr to the binary Fe_3Al intermetallics does not completely hinder the pitting and crevice corrosion of alloys. Furthermore, in a normal laboratory practice and especially in the routine industrial applications, polycrystalline materials are used, which are composed of grains with different surface orientations, and grain boundaries. Studies with single crystals have shown that exchange current densities and adsorption processes depend on surface orientation and electron density at the surface as well as on surface defects [197]. The same is true for the properties and electrochemical growth of oxide layers. Electrochemical measurements at polycrystalline surfaces, even of very pure materials, therefore, provide information averaged across the surface. Consequently, we tried to characterize the form and density of (meta) stable pits for different crystal orientations. It was shown in paper C that the pit facets have the {1 1 0} orientation. The grains with the {1 1 0} orientation have slightly higher pit density in comparison with other orientations, but the difference was not significant.

Electrochemical Impedance Spectroscopy (EIS) and the Mott–Schottky (MS) methods were also used to characterize the passive film. Contribution of Cr ions (Cr^{3+} and Cr^{6+}) to the increase of the effective capacitance and donor density of the passive layers was seen based on the electrochemical measurements. The effect of Cr on the polarization resistance was more obvious at high anodic potentials where the strong enrichment of the passivation layer with Cr^{3+} and Cr^{6+} could make a more protective p-type passive layer, instead of the n-type (Al^{3+} reach) layer, for example at lower potentials or in alloys without Cr. The reduction of the flat-band potential

[18] It controls by i) charge transfer reactions through the electrochemical double layer, ii) the mass transport of reactants to and products away from the electrode and, thus, concentration gradients at the electrode surface, iii) adsorption processes at the electrode surface, etc.

after the addition of 5 at.% Cr may reduce the sensitivity of alloys to the moist-induced hydrogen embrittlement. However, a complete characterization of passive layer requires methods with high spatial resolution to be applied, and requires information in addition to purely electrical data (current / potential / time). Therefore, the passive oxide film formed on the surface and the contribution of the Cr on the passive layer was characterized by means of X-ray photoelectron spectroscopy (XPS), in "paper D". With this technique the thickness of passive layer and contribution of Cr on its features was evaluated. In the sample with higher concentration of chromium, some part of iron oxide in the passive layer was replaced by Cr^{3+}. Additionally, aluminium and chromium enrichment, with respect to the bulk composition, was found at the passive layer.

Since Johnson [120] first reported on hydrogen embrittlement, various strong views on the mechanisms of hydrogen embrittlement have been vigorously discussed and thoroughly reviewed in the literature (see chapter 2.2.3). Because of the technological importance of hydrogen embrittlement, many people have explored the nature, causes and control of hydrogen-related degradation of metals. This has resulted in an enormous number of sometimes controversial findings and/or interpretations. This is mainly because of the ad-hoc approach used to tackle the hydrogen embrittlement within a specific alloy system. The lack of a systematic approach to the hydrogen embrittlement problem is mainly coupled with the time consuming and costly testing procedure based on the conventional mechanical tests with in-situ or ex-situ hydrogen charging. To get rid of these limitations, we developed a novel method called in-situ electrochemical nanoindentation (ECNI). Nanoindentation of the Fe_3Al-xCr alloys was preformed while the samples were electrochemically charged with hydrogen as it is shown in "paper D" [198]. Very low depth of indentation assures us that the hydrogen saturation, after a few minutes, ensues, although the diffusion rate is low in iron aluminides. Our results show that the hydrogen decreased i) the elastic and shear modulus of materials, due to the weakening of interatomic bonds (Fig. 8, in paper D); ii) the energy barrier for dislocation nucleation, caused by the increment of dislocation core radius (Fig. 9, in paper D); and iii) the mobility of dislocations by reason of the enhancement of friction stress (Fig. 11, in paper D). Now the question is

1) Which mechanism of HE is most likely to cause embrittlement?
2) How do the mentioned items relate to the low ductility of alloys?
3) How could we use our method for ranking different alloys based on their sensitivity to HE?

We tried to define a mechanism of HE based on fundamental mechanics. In general, at a constant temperature, and in the absence of any kind of phase transformation, the energy of the newly formed surfaces (due to the crack growth) is an intrinsic characteristic of material. The hydrogen ingress into the studied intermetallics can influence this new surface energy with the reduction of the strength of interatomic bonds (or shear modulus (μ)), as predicted by the HEDE mechanism. On the other hand, the presence of hydrogen controls the nucleation, multiplication, or movement of dislocations in agreement to the defactants, AIDE and HELP mechanisms. It shows that, even for materials with identical types of bonds, it is highly unlikely that there is just one conventional mechanism capable of explaining hydrogen embrittlement.

However, the magnitude of the influence of hydrogen on shear modulus, dislocation core radius and friction stress is different for various intermetallics. Therefore, different mechanisms may operate in different orders depending on the material, environmental and mechanical parameters. Incidentally, all the mentioned parameters (energy of the newly formed surfaces, multiplication or movement of dislocations) are key components of a ductile to brittle fracture transition [199]. In the classical theory of dislocation shielding of a singular crack, the effective stress intensity factor K_e at the crack tip is expressed as [199]:

$$K_e = K + K_D \qquad \text{Eq. 4-1}$$

where K and K_D are stress intensity factors induced by the externally imposed loading and dislocations, respectively. Fracture takes place when K_e reaches a critical value of K_C. The crack is said to be shielded by dislocations when $K_D < 0$, and anti-shielded when $K_D > 0$. Therefore, the growth rate of cracks will depend on the mobility of dislocations and the energy for dislocation nucleation. Binary alloys are very sensitive to hydrogen embrittlement because of the strong reduction of the energy needed for HDN after hydrogen charging. Additionally, all alloys exhibit higher friction stress after hydrogen charging. This shows that the absorption of hydrogen will ease nucleation of sessile dislocations and it decreases the shielding effect of dislocations. Finally, it favors the cleavage fracture of alloys. It demonstrates that the mechanism of dislocation shielding should be considered for analyzing the fracture characteristics of Fe_3Al in aqueous solutions and in atmospheres containing hydrogen. The power of the ECNI method results in quantitative information about the effect of hydrogen on the elastic properties,

dislocation nucleation and its' mobility. All these items could be used as criteria for ranking the susceptibility of different alloys to hydrogen embrittlement.

In "paper E" [200], we reported clear evidence for the effect of hydrogen on the ease of dislocation nucleation with in-situ AFM method. For this reason, a super duplex stainless steel was charged electrochemically. After a few seconds in the austenite grains of SDSS, the slip line traces were seen without application of any external stress (Figs. 1 and 2, in paper E). This happened under moderate H-charging, which could not trigger any phase transformation in austenite. This was proven by XRD and magnetic force microscope (MFM) techniques (Figs. 3 and 4, in paper E). Hydrogen reduces the required stress for activation of dislocation sources, which are already under tension due to residual stresses formed during quench annealing. This initiates dislocation punch out from the surface and relaxation of the microstructure. This shows how hydrogen, in combination with a complex microstructure, results in microstructural changes, which can play a crucial role in hydrogen embrittlement of industrially important alloys.

5 - Concluding remarks

There are two barriers for the wide usage of the Fe_3Al intermetallic at room temperature. One is for hydrogen embrittlement and the other is for localized corrosion of the alloys in the Cl^- containing solutions. In this thesis, we tried to shed more light on the reasons for each of the aforementioned problems; and also evaluate the possibility of overcoming the problems with the addition of different concentrations of chromium to the binary alloys.

The nanoindentation technique was used for studying the influence of Cr content on the elastic and plastic properties. The results show that chromium increases the Young's modulus, maximum shear stress for homogeneous dislocation nucleation and friction stresses in Fe_3Al intermetallics. Additionally, Cr decreases the σ_{flow} and facilities the cross slipping of dislocations. It was confirmed with the influence of Cr on the reduction of the pile-up heights.

This dissertation examines the further application of nanoindentation, investigates materials under different environments, and establishes some possibilities for obtaining new and unique information from Fe_3Al intermetallics with different Cr content. The novel method of in-situ nanoindentation was performed to detect the impact of hydrogen on mechanical properties and the sensitivity of intermetallics to hydrogen embrittlement. The decrement of Young's modulus and dislocation mobility was observed at cathodic potentials. Hydrogen also decreases the pop-in load and Gibbs free energy needs for homogeneous dislocation nucleation especially in samples with low Cr content, a sign of increased sensitivity to HE in Cr free alloys. This occurs because the addition of physically adsorbed hydrogen increases the dislocations core radius. However, among all different mechanisms of HE, it was shown that the dislocation shielding mechanism could be used for explaining the low ductility of Fe_3Al based intermetallics in a hydrogen containing environment.

Finally, with the XPS and electrochemical techniques we studied the incorporation of Cr as a ternary alloying element into the passive film. The resistance of alloys to pitting and crevice corrosion in Cl^- containing solutions was enhanced with the addition of Cr. The addition of 5 at. % Cr to the binary Fe_3Al intermetallics does not completely hinder the pitting and crevice corrosion of alloys, while it decreases the average density of pits. The effect of Cr on the polarization resistance was more obvious at high anodic potentials where the strong enrichment of the passive layer with Cr^{3+} and Cr^{6+} could make a more protective p-type layer, instead of the

n-type layer, such as at lower potentials, or alloys with lower Cr content. Additionally, it was shown that the addition of Cr also increases the effective capacitance and donor density of the passive layers.

6 - Outlook

6.1. Bending test of micro pillars in solution: A new approach to studying the hydrogen embrittlement of iron-aluminum intermetallics

The method of in-situ nanoindentation suffers from the complexity of the stress field below the nanoindenter. Therefore, a novel method was developed where miniaturized compression samples are machined using focused ion beam (FIB) milling and loaded in a nanoindenter system equipped with a flat diamond punch [18]. This method is able to probe mechanical properties on the micrometer and sub-micrometer scale under nominally uniaxial loading. Moreover, a very small volume of pillar guarantees a fast and homogeneous distribution of hydrogen. We continued our investigations of Fe_3Al-xCr pillars and reports on the hydrogen effect on the elastic properties and interaction of dislocations observed in various solid solution intermetallics using the in-situ bending test of micro pillars. The advantage of the bending test is the presence of high tensile stress in the pillar, during the test. It is in contrast to other techniques like in-situ nanoindentation or micropillar compression tests with the compressive stress field, which works as driving force for the hydrogen diffusion out of the highly stressed region.

To perform bending test, a new method was developed in our department. Bending tests of micro pillars were performed with a 2D (both normal and lateral force) transducer [189]. A conical tip with the semi angle of 90° was used for the tests. As it is shown schematically in Fig. 6-1, the bending test was performed in different sequences, as follows:

1- The pillar was positioned precisely using the imaging mode of the Triboindenter (step 1).
2- After positioning the pillar at the distance of 4.5-5 µm from the center, we disengaged the tip from the sample (step 2).
3- With the aid of air indentation mode, we measured exactly the distance between tip and surface using the load function, which is shown in Fig. 6-2a (step 3).
4- The bending test was performed with the lateral movement of tip using the load function shown in Fig. 6-2b (step 4-1 and 4-2).
5- Finally, the tip goes back to the initial position (step 5).

The deformed pillars and formation of slip traces at both sides of pillars is shown in Fig. 6-3. Our experimental results confirm that hydrogen decreases the Young´s modulus in samples with Cr and with 5 at.%Cr, but this reduction occurs more in the binary alloys.

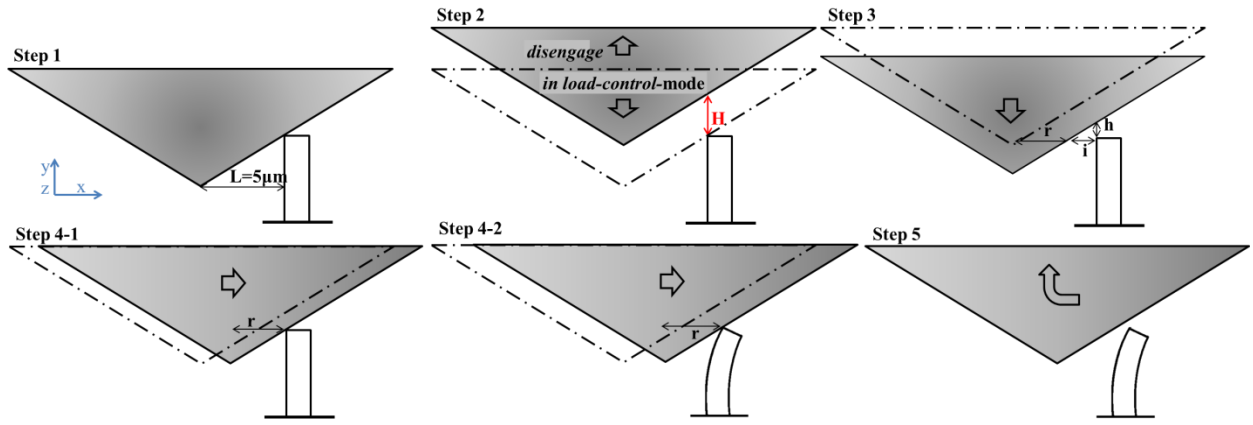

Fig. 6-1. Shows, schematically, the consequences of the bending test of micro pillars with a conical tip.

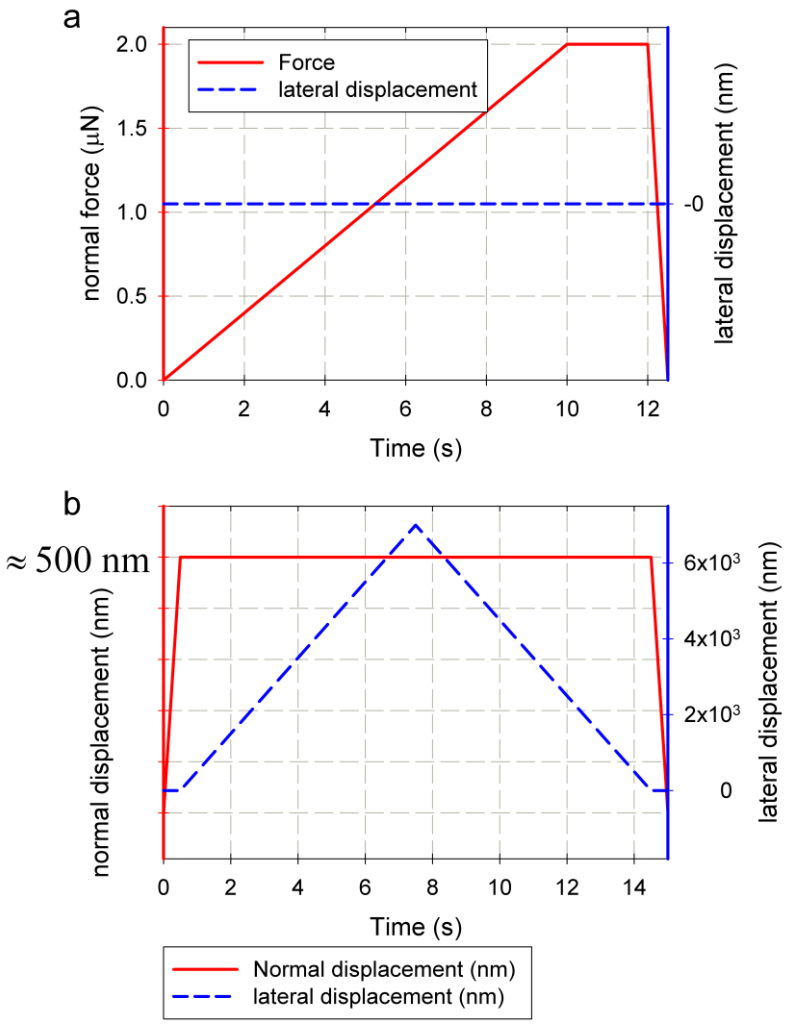

Fig. 6-2. Shows the loading functions for a) distance measurement and b) bending test.

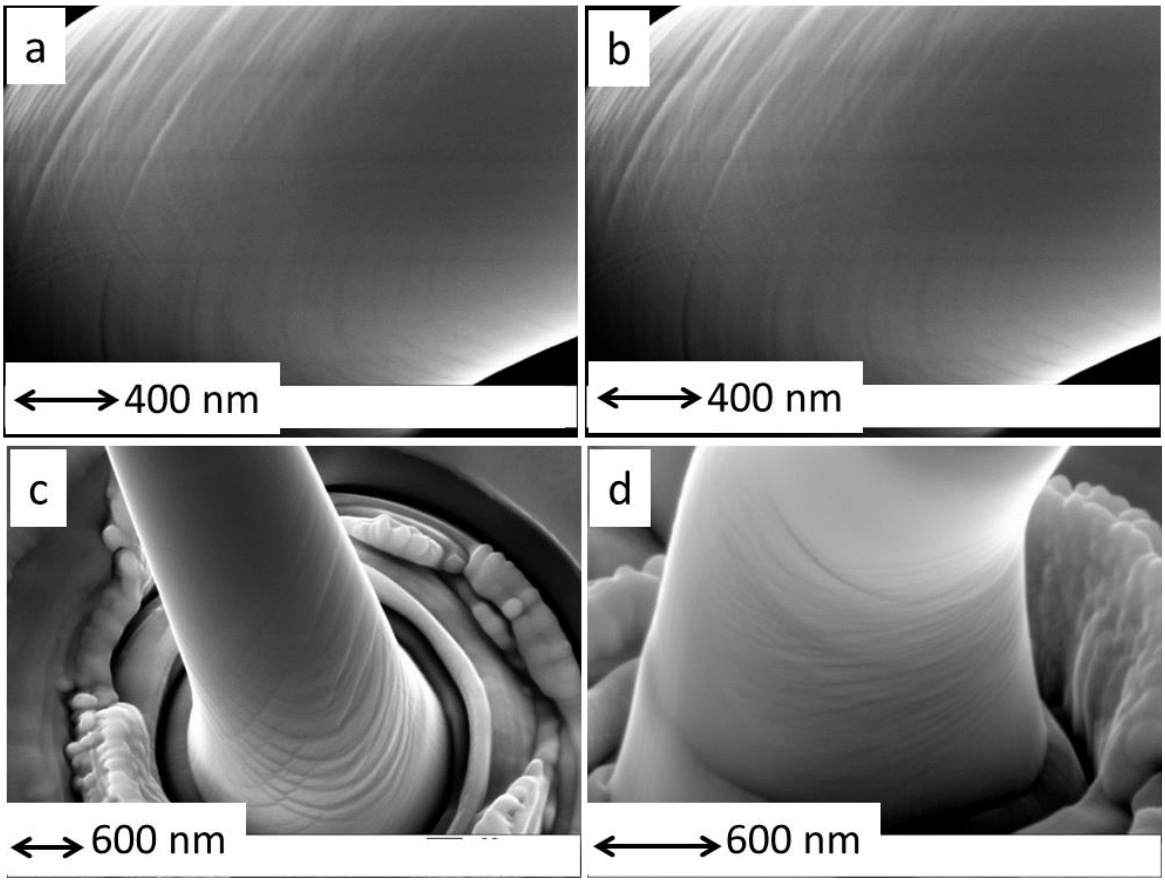

Fig. 6-3. Shows the slip traces at both sides of pillars (a and b)Fe26Al; (c and d) Fe26Al5Cr intermetallics.

6.2. Effect of vacancies on the mechanical behavior of iron aluminides

We attempted to study the effect of vacancies on the elastic and plastic behavior of iron aluminides with different Al content. We also evaluated the effect of vacancies on the dislocation nucleation, with the aid of the nanoindentation technique. For this reason, binary samples with various Al content were heat treated and quenched from different temperatures. Fig. 6-4a and c illustrates some typical load-displacement (L–D) curves with different histories of heat treatment. A statistical approach (cumulative distribution) is taken to clarify the effect of vacancy concentration on the elastic modulus of samples (Fig. 6-4b and d). The results show that the elastic behavior of samples reduces very slightly with the increase of the vacancy concentrations. The reduction is more in the samples with 45 at.% Al. The effect of vacancies is more highlighted on the incipient plasticity and post yielding behavior of the alloys. Cumulative distribution of the pop-in event is presented in Fig. 6-5.

Based on simulations, it was shown that the existence of vacancies can significantly facilitate the onset of plasticity, which results in a lower yield loads. The increase of the quench temperature promotes earlier displacement bursts in the Fe-45Al and, therefore, a significant shift in the population of pop-in loads (P_{pop-in}). In contrary, for the sample with 30 at.% Al the tendency was not clear. The volume of the material[19] ($V_{cylinder}$) beneath the indenter, where 99.9% of the maximum shear stress is acting (Fig. 6-6a), is shown in Fig. 6-6b. The total number of atoms in the volume with the maximum shear stress is also shown in Fig. 6-6b. Considering the average concentration of vacancies in the materials (Fig. 2-3b), the probability of encountering a preexisting equilibrium vacancy beneath the tip in a strained lattice is very high for Fe-45Al but very low for Fe-30Al. It may be the reason for the observed tendency of the pop-in load distribution.

[19] It has an elliptical cylinder form.

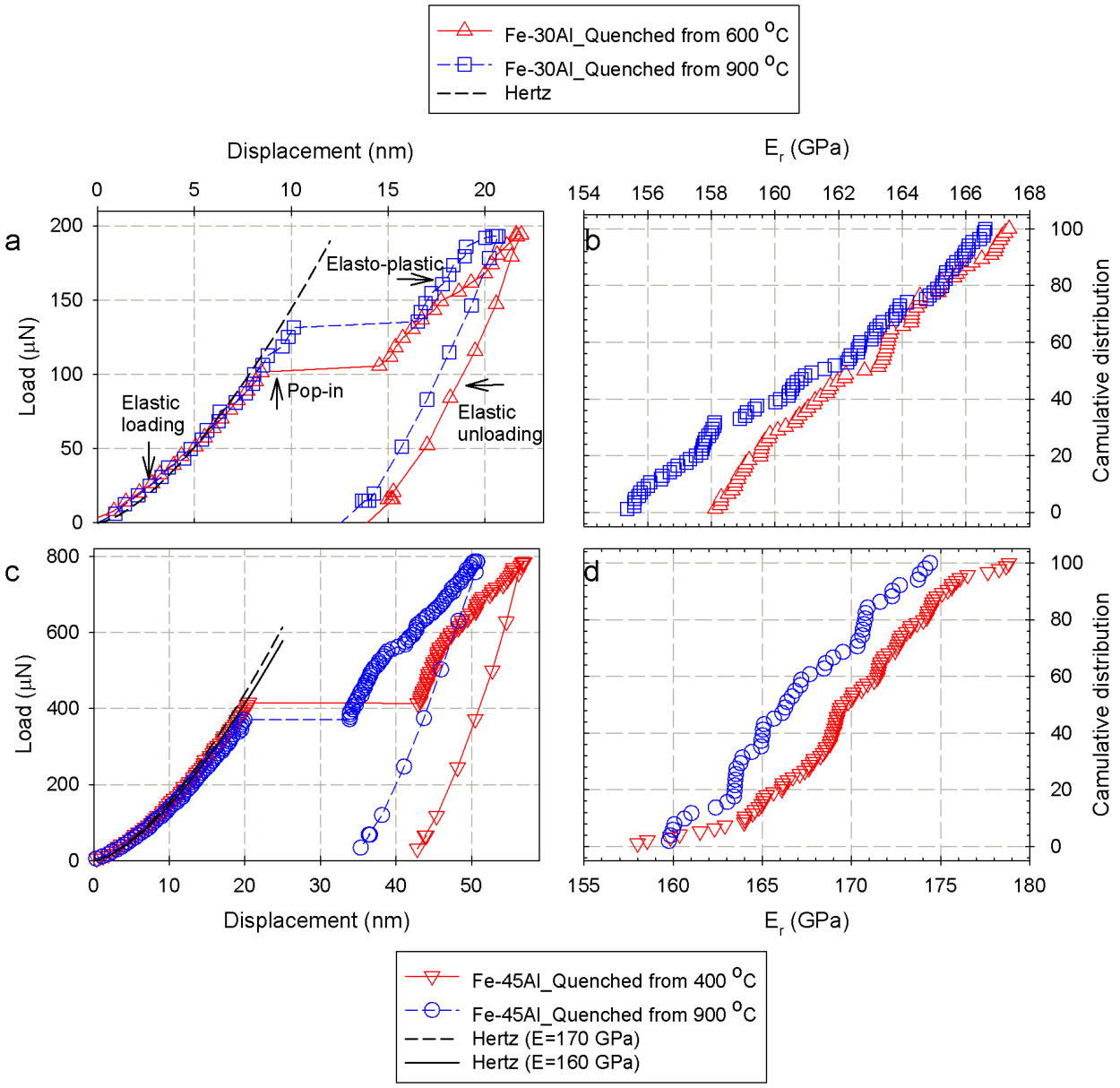

Fig. 6-4. a and c) show the L-D curves related to samples with 30 and 40 at% Al performed with a Berkovich tip on samples with different histories of heat treatment. b and d) show the effect of heat treatment (vacancy concentration) on the measured reduced elastic modulus.

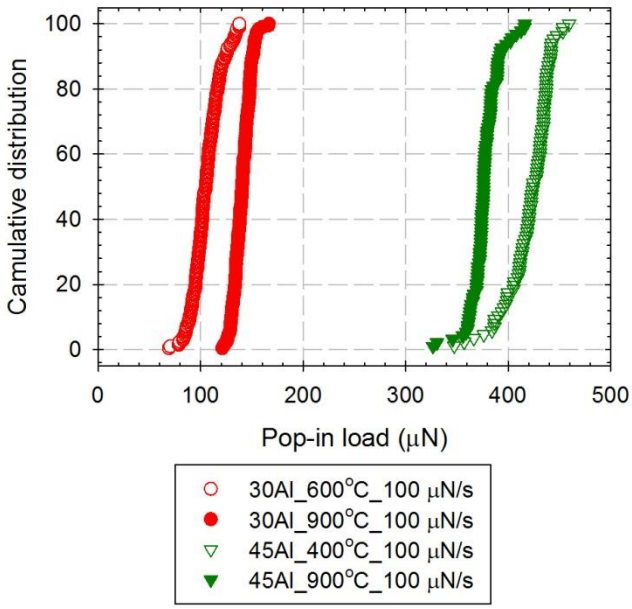

Fig. 6-5. Cumulative distribution of the pop-in event of samples with 30 and 45 at% Al performed with a Berkovich tip on samples with different histories of heat treatment.

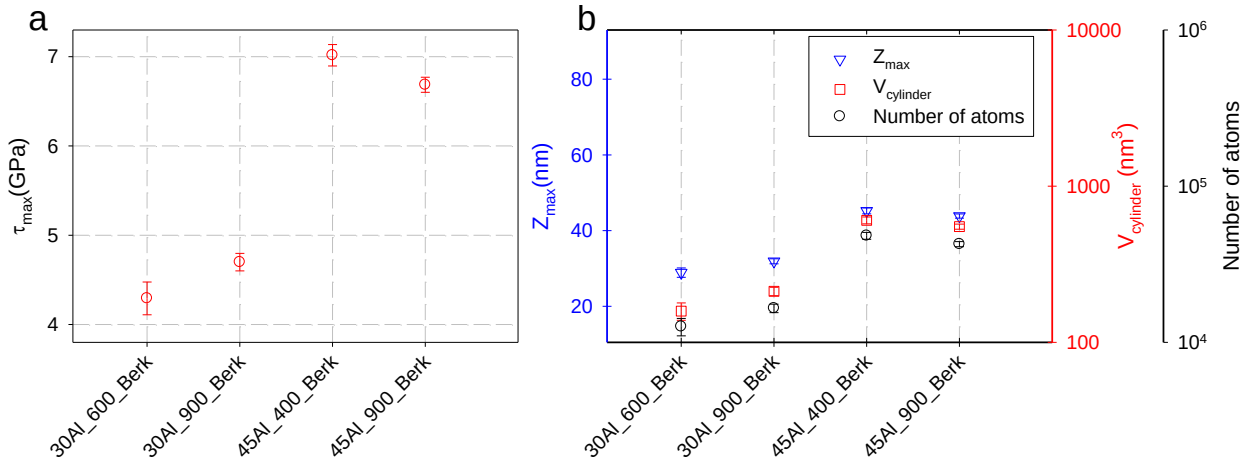

Fig. 6-6. a) Calculated maximum shear stress b) the depth of maximum shear stress, $V_{cylinder}$ and total number of atoms in the $V_{cylinder}$ of samples. The 30 and 40 at% Al iron aluminides with different histories of heat treatment were indented with a Berkovich tip.

6.3. Determining the effect of various substantial solute atoms on the mechanical properties of Fe_3Al intermetallics

In this work we focused mainly on ternary alloys with up to 5 at.% Cr. For improvement of the electrochemical properties and resistance of alloys against pitting corrosion, more Cr should be added to the binary alloys. Addition of other types of alloying elements, like Ti, may also have constructive influence on the pitting resistance of alloys. However, our experimental results show a significant enhancement of the elastic modulus and hardness of Ti reach alloys (Fig. 6-7a and b). The average values of the pop-in load will also increase with the addition of Ti (Fig. 6-7c).

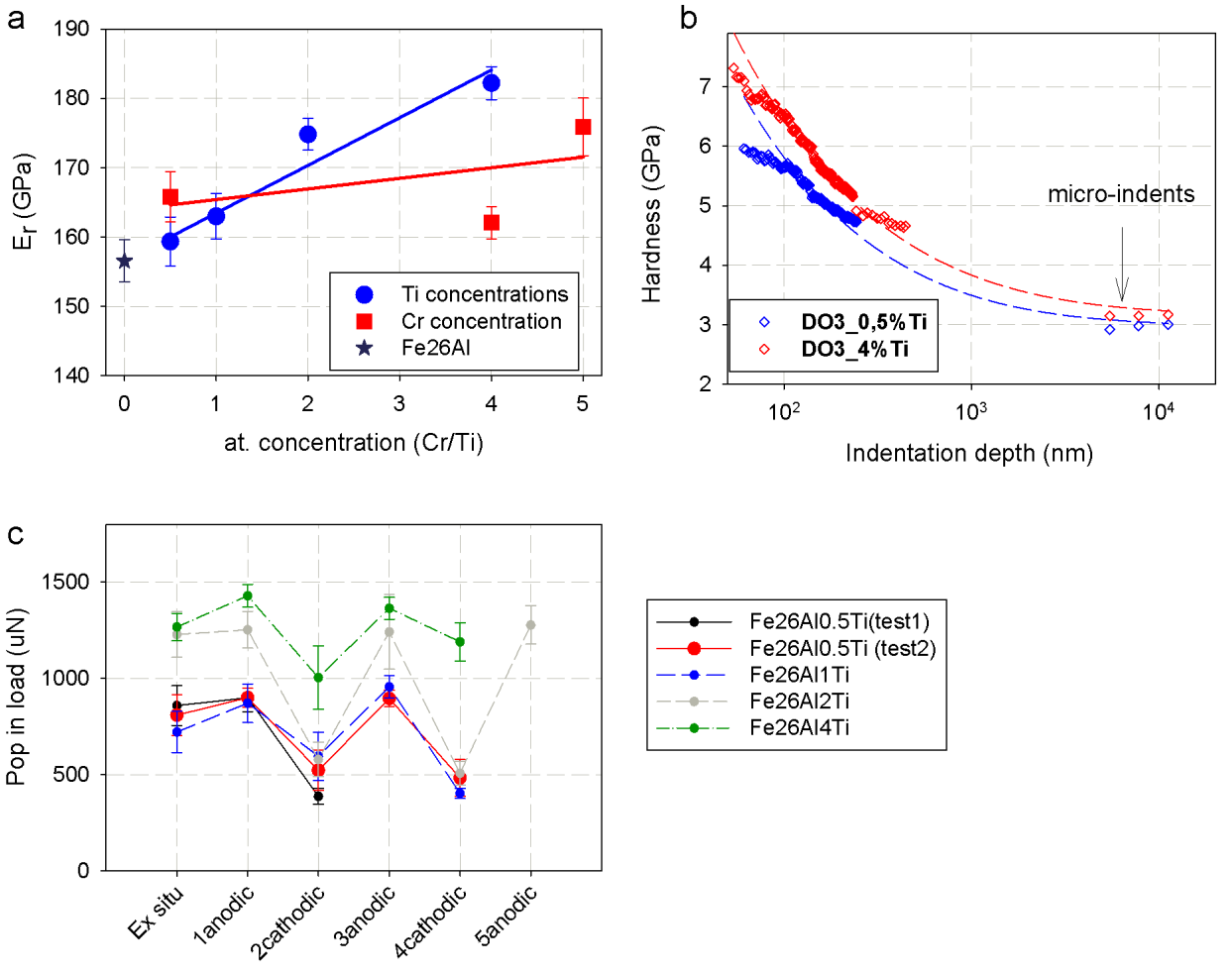

Fig. 6-7. a) Influence of Cr and Ti on the reduced elastic modulus, b) effect of Ti on the hardness of alloys and c) effect of hydrogen on the pop-in load of alloys with different Ti content.

The in-situ nano-indentation of 4 at.% Ti show a strong reduction of pop-in load after hydrogen charging (Fig. 6-7c). It shows the susceptibility of alloys to the hydrogen embrittlement, which is in contrast to the Cr-reach alloys where the reduction of pop-in load after hydrogen charging was significantly less than the binary alloys.

7 - Appendix

7.1. Appendix A

Effect of alloying elements on different properties of iron aluminides

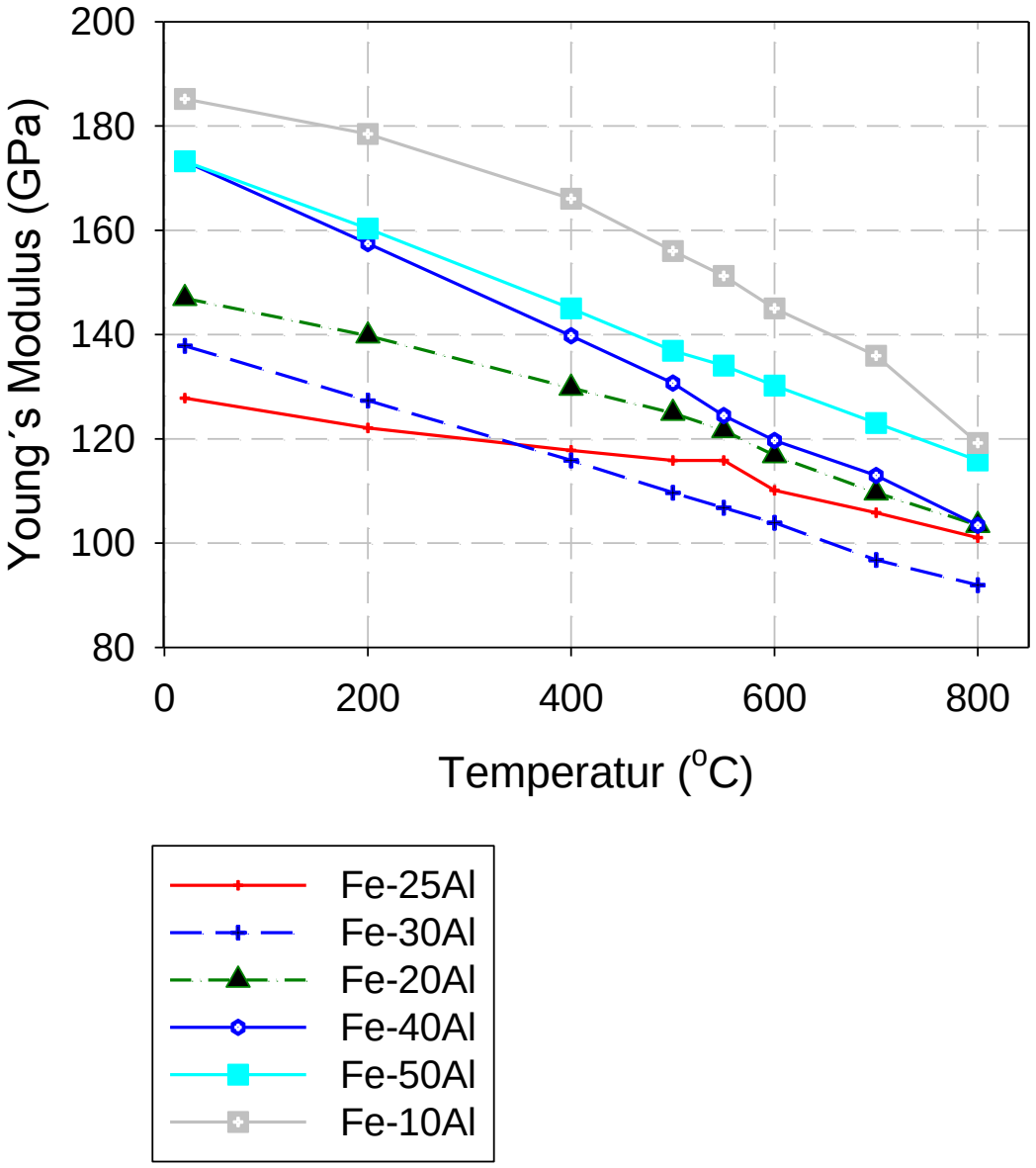

Fig. 7-1. Effect of Al concentration on the Young´s modulus at different temperatures [201 and 202].

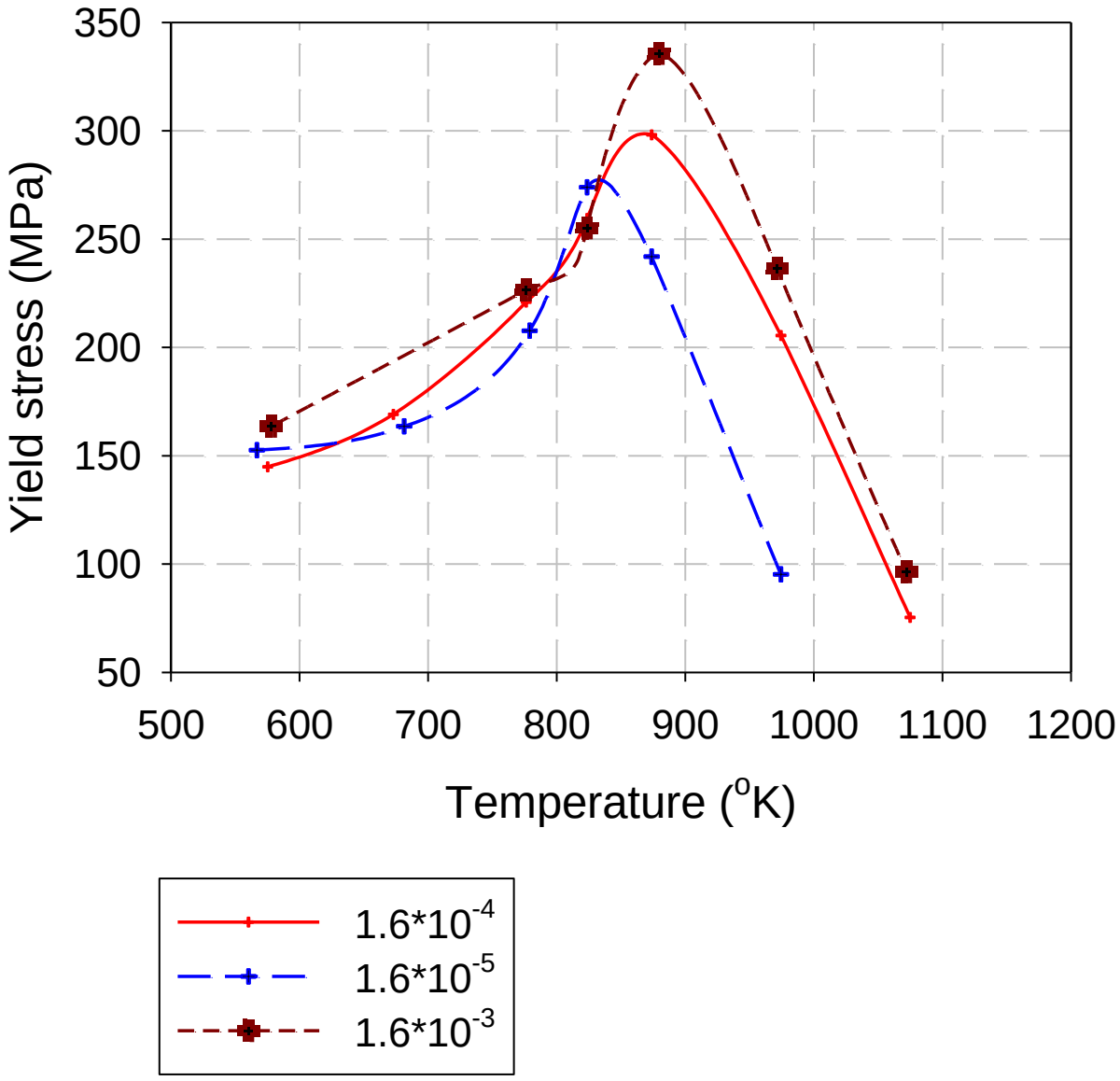

Fig. 7-2. Shows stress anomaly and strain rate sensitivity of Fe-Al intermetallics [203].

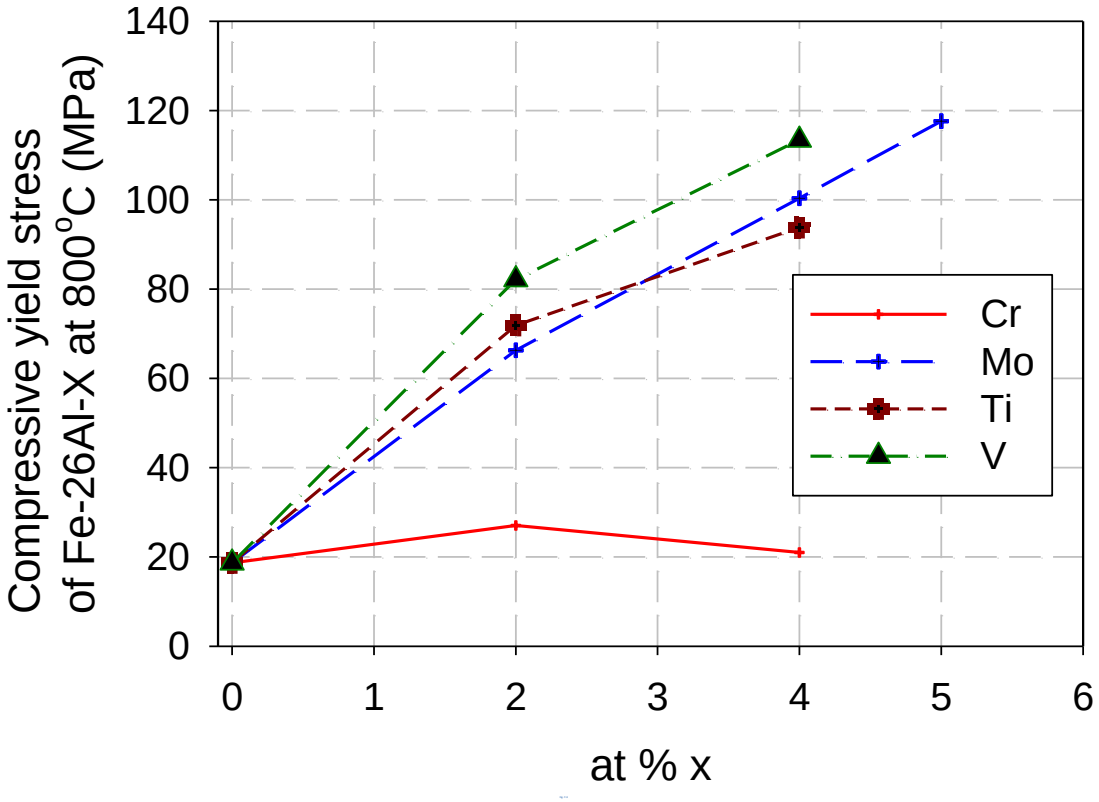

Fig. 7-3. Effect of various ternary alloying elements on the yield stress at 800 °C [52].

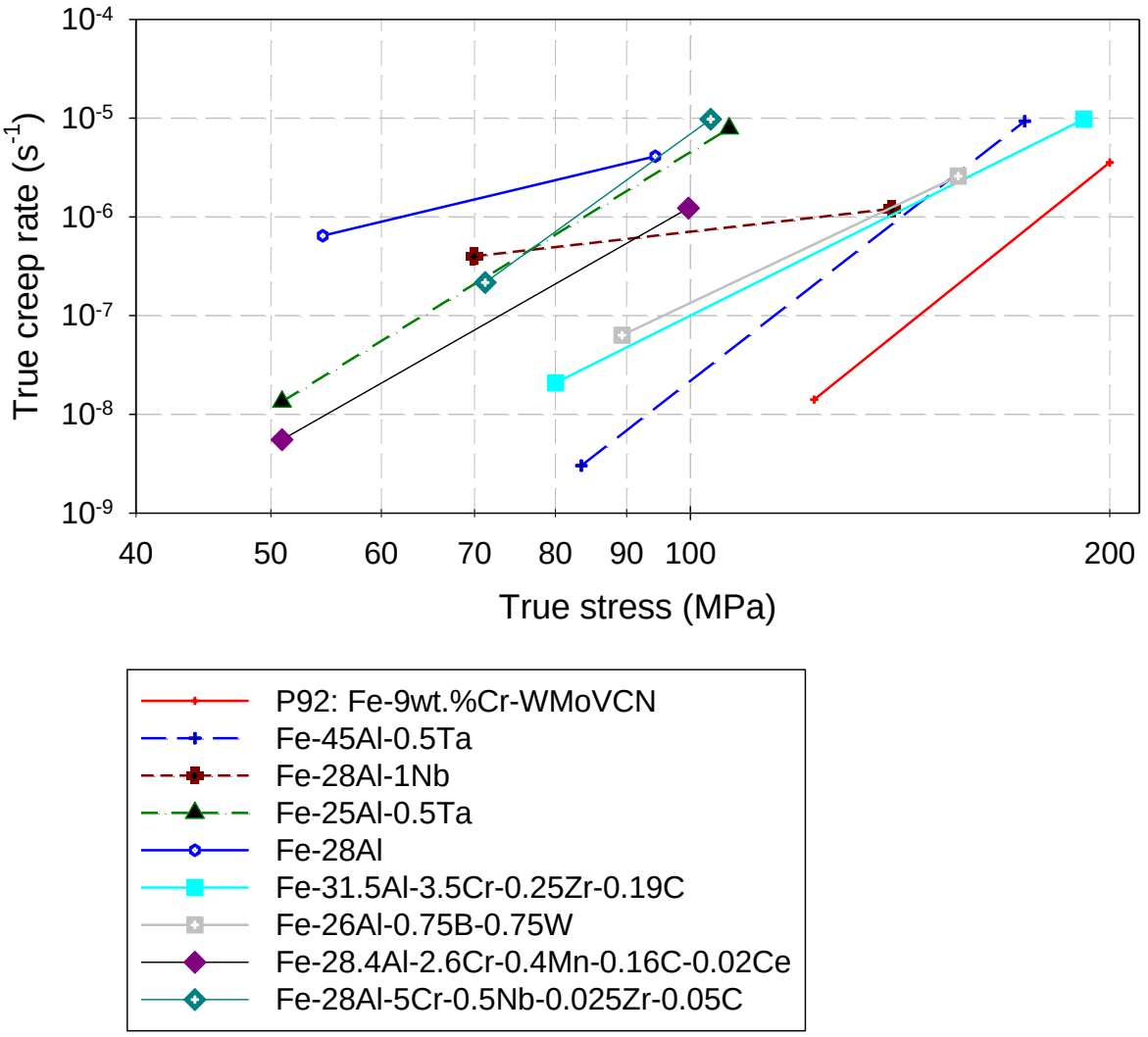

Fig. 7-4. Creep rate of various iron aluminides tested at 650°C [78].

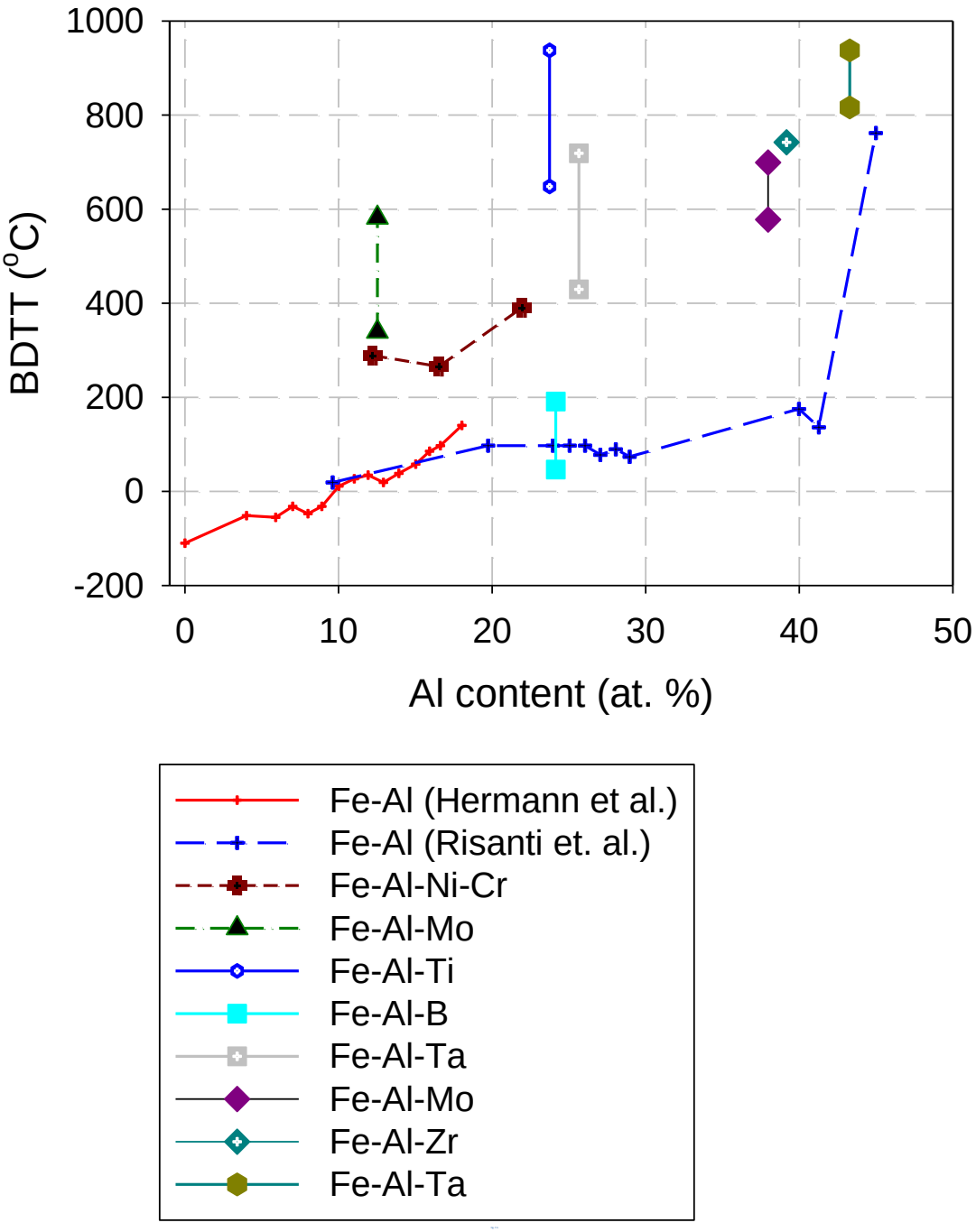

Fig. 7-5. Effect of various alloying elements on the brittle to ductile transition temperature (BDTT) [59, 204 and 205].

7.2. Appendix B

The methods of nanoDMA sweep and creep will explain very briefly in this part. However, these methods were not used for the characterization of iron aluminides and the results are not present in the text. For a sweep test, the frequency is varied in each progressive step. During this type of test, a fixed quasistatic load is chosen, as well as fixed dynamic load amplitude. Mechanical properties of viscoelastic materials often vary when tested at different frequencies. A ramping frequency test is used to determine mechanical properties as a function of frequency. This is the typical type of test performed by a DMA (dynamic mechanical analysis) instrument at macro scale. The frequencies may be ramped from 0.1 Hz up to 300 Hz. When testing at lower frequencies (below 10 Hz), the test can take a very long time, so it is recommended that lower frequency tests utilize the reference frequency functions to minimize drift effects. When testing is performed over 200 Hz, the amplitude can become quite small, and it may be difficult for the lock-in amplifier to measure the phase and amplitude of the displacement signal. The user must be sure that the amplitude is large enough at higher frequencies to ensure quality data.

A dynamic reference creep test is similar to a creep test performed with standard indentation, however, with the use of reference frequencies, the test time can be much longer and because of the dynamic components (in combination with the CMX capabilities). The test will continuously measure hardness, stiffness, modulus, etc. A reference creep test is a test with an initial reference frequency segment followed by a long constant force dynamic segment. The first reference frequency segment will be used to calculate the contact area and the second (longer) reference frequency segment will be analyzed as the creep segment.

CMX $\xrightarrow{\text{Fig. 3-2b}}$ { V̄eriable quasi static load; V̄ariable load amplitiude; C̲onstant oscillation frequency }

Sweep Test $\xrightarrow{\text{Fig. 7-6a}}$ { C̲onstant quasi static load; C̲onstant load amplitiude; V̄ariable oscillation frequency }

Creep Test $\xrightarrow{\text{Fig. 7-6b}}$ { C̲onstant quasi static load; C̲onstant load amplitiude; C̲onstant oscillation frequency }

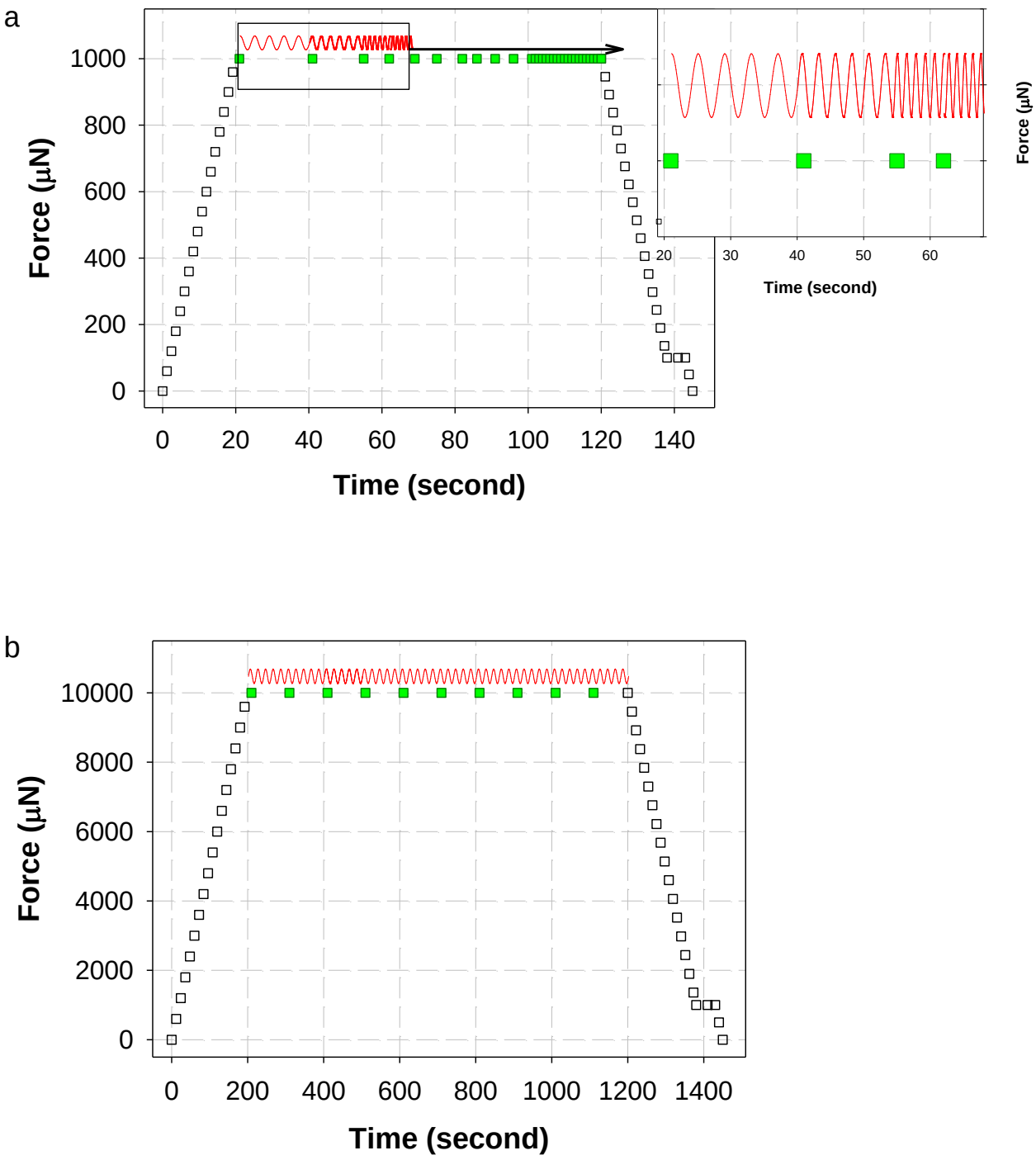

Fig. 7-6. a) Schematically shows the loading function for a sweep frequency test and b) the loading function for a creep test [190].

8 - References

[1] I. Baker and P. Munroe, "Mechanical properties of FeAl," *International materials reviews,* vol. 42, pp. 181-205, 1997.

[2] R. Noebe, R. Bowman and M. Natha, "Physical and mechanical properties of the B2 compound NiAl," *International materials reviews,* vol. 38, pp. 193-232, 1993.

[3] V. Sundararajan, B. Sahu, D. Kanhere, P. Panatt and G. Das, "Cohesive, electronic and magnetic properties of the transition metal aluminides FeAl CoAl and NiAl," *Journal of physics: condensed matter,* vol. 7, pp. 6019-6034, 1995.

[4] C. Fu and X. Wang, "The effect of electronic structure on the defect properties of FeAl," *Materials science and engineering:A,* vol. 239–240, pp. 761-768, 1997.

[5] D. Miracle and D. Pope, "NiAl and its alloys," in *Intermetallic compounds, vol. 3: structural applications of intermetallic compounds*, John Wiley & Sons, 1995, pp. 55-74.

[6] S. Huang and J. Chestnutt, "Gamma TiAl and its alloys," in *Intermetallic compounds, vol. 3: structural applications of intermetallic compounds*, John Wiley & Sons, 1995, pp. 75-90.

[7] K. Vedula, "FeAl and Fe3Al," in *Intermetallic compounds, vol. 3: structural applications of intermetallic compounds*, John Wiley & Sons, 1995.

[8] C. Briant, "Intergranular and cleavage fracture," in *Intermetallic compounds, vol.2: basic mechanical properties and lattice defects of intermetallic compounds*, John Wiley & Sons, 1995.

[9] C. McKamey, J. Devan, P. Tortorelli and V. Sikka, "A review of recent developments in Fe3Al-based alloys," *Journal of materials research,* vol. 6, pp. 1779-1805, 1991.

[10] A. Ball and R. Smallman, "The deformation properties and electron microscopy studies of the intermetallic compound NiAl," *Acta metallurgica,* vol. 14, pp. 1349-1355, 1966.

[11] R. Mises, "Mechanik der plastischen Formanderung von Kristallen," *Zeitschrift für Angewandte Mathematik und Mechanik,* vol. 8, pp. 161-185, 1928.

[12] C. Liu, E. Lee and C. McKamey, "An environmental effect as the major cause for room-temperature embrittlement in FeAl," *Scripta metallurgica,* vol. 23, pp. 875-880, 1989.

[13] P. Blau and H. Meyer, "Characteristics of wear particles produced during friction tests of conventional and unconventional disc brake materials," *Wear,* vol. 255, pp. 1261-1269, 2003.

[14] R. Judkins and U. Rao, "Fossil energy applications of intermetallic alloys," *Intermetallics,* vol. 8, pp. 1347-1354, 2000.

[15] N. Stoloff, C. Liu and S. Deevi, "Emerging applications of intermetallics," *Intermetallics,* vol. 8, pp. 1313-1320, 2000.

[16] R. Prescott and M. Graham, "The oxidation of iron-aluminum alloys," *Oxidation of metals,* vol. 38, pp. 73-87, 1992.

[17] P. Tortorelli and K. Natesan, "Critical factors affecting the high-temperature corrosion performance of iron aluminides," *Materials science and engineering:A,* vol. 258, pp. 115-125, 1998.

[18] A. Barnoush, J. Dake, N. Kheradmand and H. Vehoff, "Examination of hydrogen embrittlement in FeAl by means of in situ electrochemical micropillar compression and nanoindentation techniques," *Intermetallics,* vol. 18, pp. 1385-1389, 2010.

[19] R. Balasubramaniam, "Hydrogen in iron aluminides," *Journal of alloys and compounds,* Vols. 330-332, pp. 506-510, 2002.

[20] D. Alven and N. Stoloff, "The influence of composition on the environmental embrittlement of Fe3Al alloys," *Materials science and engineering:A,* vol. 239–240, pp. 362-368, 1997.

[21] A. Castagna and N. Stoloff, "Hydrogen embrittlement of Fe3Al alloys," *Materials science and engineering:A ,* Vols. 192-193, pp. 399-406, 1995.

[22] C. McKamey, J. Horton and C. Liu, "Effect of chromium on properties of Fe3Al," *Journal of materials research,* vol. 4, pp. 1156-1163, 1989.

[23] M. Keddam, O. Mattos and H. Takenouti, "Mechanism of anodic dissolution of iron–chromium alloys investigated by electrode impedances-I. Experimental results and reaction model," *Electrochimica acta,* vol. 31, pp. 1147-1158, 1986.

[24] M. Keddam, O. Mattos and H. Takenouti, "Mechanism of anodic dissolution of iron–chromium alloys investigated by electrode impedances-II. Elaboration of the reaction model," *Electrochimica acta,* vol. 31, pp. 1159-1165, 1986.

[25] I. Epelboin, M. Keddam, O. Mattos and H. Takenouti, "The dissolution and passivation of Fe and Fe-Cr alloys in acidified sulphate medium: Influences of pH and Cr content," *Corrosion science,* vol. 19, pp. 1105-1112, 1979.

[26] N. Hakiki, "Comparative study of structural and semiconducting properties of passive films and thermally grown oxides on AISI 304 stainless steel," *Corrosion science,* vol. 53, pp. 2688-2699,

2013.

[27] M. Salasi, G. Stachowiak, G. Stachowiak and M. Kilburn, "NanoSIMS investigation of passive oxide films on high-Cr cast iron," *Corrosion science,* vol. 67, pp. 298-303, 2013.

[28] V. Shankar Rao, "A review of the electrochemical corrosion behaviour of iron aluminides," *Electrochimica acta,* vol. 49, pp. 4533-4542, 2004.

[29] R. Balasubramaniam, "On the role of chromium in minimizing room temperature hydrogen embrittlement in iron aluminides," *Scripta materialia,* vol. 34, pp. 127-133, 1996.

[30] D. Morris and M. Morris, "Strengthening at intermediate temperatures in iron aluminides," *Materials science and engineering:A,* vol. 239, pp. 23-38, 1997.

[31] http://www.indexmundi.com/.

[32] D. Lee, G. Kim and J. Kim, "The oxidation of Fe3Al-(0, 2, 4, 6%) Cr alloys at 1000 °C," *Materials science and engineering:A,* vol. 339, pp. 109-114, 2003.

[33] F. Riffard, H. Buscail, E. Caudron, R. Cueff, C. Issartel and S. Perrier, "Effect of yttrium addition by sol–gel coating and ion implantation on the high temperature oxidation behaviour of the 304 steel," *Applied surface science,* vol. 199, pp. 107-122, 2002.

[34] N. Ziegler, "Resistance of iron-aluminum alloys to oxidation at high temperatures ," *Transactions of the american institute of mining, metallurgical, and petroleum engineers,* vol. 450, pp. 6-11, 1932.

[35] C. Sykes, J. Bampfylde and A. Jay, "Physical Properties of iron-aluminum alloys," *Journal iron steel institute,* vol. 130, pp. 389-428, 1932.

[36] H. McQueen and G. Kuczynski, "Order-disorder transformations in iron-aluminum alloys," *Transactions of the american institute of mining, metallurgical, and petroleum engineers,* vol. 215, pp. 619-622, 1959.

[37] R. Davies, "An X-ray and dilatometric study of order and the “K-state” in iron-aluminum alloys," *Journal of physics and chemistry of solids,* vol. 24, pp. 985-992, 1963.

[38] T. Eguchi, H. Matsuda, K. Oki and S. Y. K. Kiyoto, "Order-disorder transformation in Fe-Al alloys," *Materials transactions: the Japan institute of metals and materials,* vol. 8, pp. 174-179, 1967.

[39] A. Taylor and R. Jones, "Constitution and magnetic properties of iron-rich iron-aluminum alloys," *Journal of physics and chemistry of solids,* vol. 6, pp. 16-37, 1958.

[40] W. Köster and T. Gödecke, "Physical measurement on iron-aluminum alloys between 10 and 50 at% Al .1. confirmation of and additional contribution to the Iron and Aluminum phase-diagram," *Zeitschrift für Metallkunde,* vol. 71, pp. 765-769, 1980.

[41] F. Stein, A. Schneider and G. Frommeyer, "Flow stress anomaly and order-disorder transitions in Fe3Al-based Fe-Al-Ti-X alloys with X=V, Cr, Nb, or Mo," *Intermetallics,* vol. 11, pp. 71 - 82, 2003.

[42] O. Kubaschewski, Iron-binary phase diagrams, Springer, 1982.

[43] H. Warlimont, "Electron microscopic investigation of equilibria and transformations of alpha-Fe-Al-superlattice phases," *Zeitschrift für Metallkunde,* vol. 60, pp. 195-201, 1969.

[44] F. Stein, "The binary Fe-Al system:part1," Summer school on iron aluminides, Prague, 2009.

[45] M. Palm, G. Inden and N. Thomas, "The Fe-A1-Ti system," *Journal of phase equilibria,* vol. 16, pp. 209-222, 1995.

[46] Friák, M; Krein, R; Deges, J; Frommeyer, G; Neugebauer, J, "Combined ab initio and experimental study of structural and elastic properties of Fe3Al-based ternaries," *Intermetallics,* vol. 18, pp. 1310-1315, 2010.

[47] R. Ducher, F. Stein, B. Viguier, M. Palm and J. Lacaze, "A Re-examination of the liquidus surface of the Al–Fe–Ti system," *Zeitschrift für Metallkunde,* vol. 94, pp. 396-410, 2003.

[48] H. Okamoto and P. Beck, "Phase relationships in the iron-rich Fe-Al alloys," *Metallurgical and materials transactions,* vol. 2, pp. 569-574, 1971.

[49] P. Swann, W. Duff and R. Fisher, "The electron metallography of ordering reactions in Fe-Al alloys," *Metallurgical transactions,* vol. 3, pp. 409-419, 1972.

[50] K. Oki, M. Hasaka and T. Eguchi, "Process of order-disorder transformation in iron-aluminum alloys," *Japanese journal of applied physics,* vol. 12, pp. 1522-1530, 1973.

[51] H. Yasuda, T. Nakajima, K. Nakano, K. Yamaoka, M. Ueda and Y. Umakoshi, "Effect of Al concentration on pseudoelasticity in Fe3Al single crystals," *Acta materialia,* vol. 53, pp. 5343-5351, 2005.

[52] M. Palm, "Concepts derived from phase diagram studies for the strengthening of Fe–Al-based alloys," *Intermetallics,* vol. 13, pp. 1286-1295, 2005.

[53] D. Morris, C. Liu and E. George, "Pinning of dislocations and the origin of the stress anomaly in FeAl alloys," *Intermetallics,* vol. 7, pp. 1059-1068, 1999.

[54] D. Morris and M. Muñoz-Morris, "The stress anomaly in FeAl–Fe3Al alloys," *Intermetallics,* vol. 13, pp. 1269-1274, 2005.

[55] A. Bradley and A. Jay, "The formation of superlattices in alloys of iron and aluminium," *Proceedings of the royal society of London:A,* vol. 136, pp. 210-232, 1932.

[56] A. Lawley and R. Cahn, "A high temperature X-ray study of ordering in iron-aluminium alloys," *Journal of physics and chemistry of solids,* vol. 20, pp. 204-221, 1961.

[57] J. Mayer, B. Meyer, J. Oehrens, G. Bester, N. Bornsen and M. Fihnle, "Effective formation energies of atomic defects in DO3-Fe3Al: an ab-initio study," *Intemetallics,* vol. 5, pp. 597-600, 1997.

[58] J. Herrmann, G. Inden and G. Sauthoff, "Deformation behaviour of iron-rich iron-aluminium alloys at high temperatures," *Acta materialia,* vol. 51, pp. 3233-3242, 2003.

[59] J. Herrmann, G. Inden and G. Sauthoff, "Deformation behaviour of iron-rich iron-aluminum alloys at low temperatures," *Acta materialia,* vol. 53, pp. 2847-2857, 2003.

[60] P. Nagpal, I. Baker, “Effect of cooling rate on hardness of FeAl and NiAl”. *Metallurgical Transactions A*, Vol. 21, pp. 2281-2282, 1990.

[61] G. Hasemann, J.H. Schneibel, E.P. George, “Dependence of the yield stress of Fe3Al on heat treatment”, *Intermetallics*, Vol. 21, pp. 56-61, 2012.

[62] G. Hasemann, J.H. Schneibel, M. Krüger, E.P. George, “Vacancy strengthening in Fe3Al iron aluminides”, *Intermetallics*, Vol. 54, pp. 95-103, 2014.

[63] J. Neumann, Y. Chang and C. Lee, "Thermodynamics of intermetallic phases with the triple-defect B2 structure," *Acta metallurgica,* vol. 24, pp. 593-604, 1976.

[64] S. Foiles and M. Daw, "Application of the embedded atom method to Ni3Al," *Journal of materials research,* vol. 2, pp. 5-15, 1987.

[65] C. Fu, Y. Ye, M. Yoo and K. Ho, "Equilibrium point defects in intermetallics with the B2 structure: NiAl and FeAl," *Physical review:B,* vol. 48, pp. 6712-6715, 1993.

[66] F. Stain and M. Palm, "Re-determination of transition temperatures in the Fe–Al system by differential thermal analysis," *International journal of materials research,* vol. 98, pp. 580-588, 2007.

[67] H. E. Schaefer, K. Frenner and R. Würschum, "High-temperature atomic defect properties and diffusion processes in intermetallic compounds," *Intermetallics,* vol. 7, pp. 277-287, 1999.

[68] T. Hehenkamp, P. Scholz, B. Kohler and R. Kerl, "Vacancy formation and diffusion in FeAl-alloys," *Defect and diffusion forum,* Vols. 194-199, pp. 389-396, 2001.

[69] R. Würschum, C. Grupp and H. Schaefer, "Simultaneous study of vacancy formation and migration at high temperatures in B2- type Fe aluminides," *Physical review letters,* vol. 75, pp. 97-100, 1995.

[70] J. H. Schneibel, "Strengthening of iron aluminides by vacancies and/or nickel," *Materials science and engineering:A,* vol. 258, pp. 181-186, 1998.

[71] J. Wolff, M. Franz and T. Hehenkamp, "Defect analysis with positron annihilation-applications to Fe aluminides," *Microchimica acta,* vol. 125, pp. 263-268, 1997.

[72] T. Saburi, I. Yamauchi and S. Nenno, "Electron microscope observation of dislocations and antiphase boundaries in iron-aluminum alloys," *Journal of the physical society of Japan,* vol. 32, pp. 694-701, 1972.

[73] H. Yasuda and Y. Umakoshi, "Pseudoelastic behaviour of Fe3Al single crystals with D03 structure," *Intermetallics,* vol. 18, pp. 1273-1278, 2010.

[74] D. Morris, M. Dadras and M. Morris, "The influence of Cr addition on the ordered microstructure and deformation and fracture behaviour of a Fe-28%Al intermetallic," *Acta metallurgica et materialia,* vol. 41, pp. 97-111, 1993.

[75] A. Brinck, C. Engelke, H. Neuhäuser, G. Molénat, H. Rösner, E. Langmaack and E. Nembach, "Dislocation processes in Fe3Al investigated by transmission electron, scanning force and optical microscopy," *Materials science and engineering:A,* vol. 258, pp. 32-36, 1998.

[76] M. Palm, "The Al–Cr–Fe system–phases and phase equilibria in the Al-rich corner," *Journal of alloys and compounds,* vol. 252, pp. 192-200, 1997.

[77] F. Stein, G. Sauthoff and M. Palm, "Phases and phase equilibria in the Fe–Al–Zr system," *Zeitschrift für Metallkunde,* vol. 95, pp. 469-485, 2004.

[78] R. Krein, A. Schneider, G. Sauthoff and G. Frommeyer, "Microstructure and mechanical properties of Fe3Al-based alloys with strengthening boride precipitates," *Intermetallics,* vol. 15, pp. 1172-1182, 2007.

[79] D. Connetable, J. Lacaze, P. Maugis and B. Sundman, "A calphad assessment of Al–C–Fe system with the image carbide modelled as an ordered form of the fcc phase," *Calphad,* vol. 32, pp. 361-370, 2008.

[80] A. Schneider, L. Falat, G. Sauthoff and G. Frommeyer, "Constitution and microstructures of Fe–Al–M–C (M=Ti, V, Nb, Ta) alloys with carbides and Laves phase," *Intermetallics,* vol. 11, pp. 443-450,

2003.

[81] S. Kobayashi, S. Zaefferer and A. Schneider, "Carbide precipitation in an Fe3Al-Cr-Mo-C alloy," in *Proceedings of an international conference on solid - solid phase transformations in inorganic materials, vol.1:Diffusional transformations*, vol. 1, John Wiley & Sons, 2005.

[82] S. Zuqing, Y. Wangyue, S. Lizhen, H. Yuanding, Z. Baisheng and Y. Jilian, "Neutron diffraction study on site occupation of substitutional elements at sub lattices in Fe3Al intermetallics," *Materials science and engineering:A,* vol. 258, pp. 69-74, 1998.

[83] Y. Nishino, C. Kumada and S. Asano, "Phase stability of Fe3Al with addition of 3d transition elements," *Scripta materialia,* vol. 36, pp. 461-466, 1997.

[84] D. Morris, M. Dadras and M. Morris, "The influence of chromium additions on order and ductility in Fe3Al intermetallic," *Journal de physique IV,* vol. 3, pp. 429-434, 1993.

[85] F. Kral, P. Schwander and G. Kostorz, "Superdislocations and antiphase boundery energies in deformed Fe3Al single cristals with chromium," *Acta materialia,* vol. 45, pp. 675-682, 1997.

[86] R. Gangloff and B. Somerday, Gaseous hydrogen embrittlement of materials in energy technology, vol. 1, Cornwall, UK: Woodhead publishing, 2012.

[87] C. McKamey and C. Liu, "Chromium addition and environmental embrittlement in Fe3Al," *Scripta metallurgica et materialia,* vol. 24, pp. 2119-2122, 1990.

[88] M. Wittmann, D. Wu, I. Baker, E. George and L. Heatherly, "The role of edge and screw dislocations on hydrogen embrittlement of Fe–40Al," *Materials science and engineering:A,* Vols. 319-321, pp. 352-355, 2001.

[89] M. Stroe, Hydrogen embrittlement of ferrous materials, Bruxelles: Université Libre de Bruxelles, 2006.

[90] C. Fu and G. Painter, "First principles investigation of hydrogen embrittlement in FeAl," *Journal of materials research,* vol. 6, pp. 719-723, 1991.

[91] D. Johnson and E. Carter, "First principles assessment of hydrogen absorption into FeAl and Fe3Si: towards prevention of steel embrittlement," *Acta materialia,* vol. 58, pp. 638-648, 2010.

[92] J. Hirth, "Effects of hydrogen on the properties of iron and steel," *Metallurgical transactions:A,* vol. 11, pp. 861-890, 1980.

[93] X. Cheng and X. Wan, "Hydrogen diffusivity in a Fe3Al-based alloy," *Scripta materialia,* vol. 38, pp. 1505-1509, 1998.

[94] P. Banerjee and R. Balasubramaniam, "Hydrogen diffusivity in iron aluminides determined by subscale microhardness profiling," *Scripta materialia,* vol. 39, pp. 1215-1220, 1998.

[95] Y. Yang and S. Hanada, "Absorption and desorption of hydrogen in Fe-40Al intermetallic," *Scripta metallurgica et materialia,* vol. 32, pp. 1719-1724, 1995.

[96] M. Kupka and K. Stępień, "Hydrogen permeation in Fe-40 at.% Al alloy at different temperatures," *Corrosion science,* vol. 51, pp. 699-702, 2009.

[97] W. Luu and J. Wu, "Hydrogen transport and environmental embrittlement effects in iron aluminides," *Journal of materials science,* vol. 35, pp. 4121-4127, 2000.

[98] K. Stępień and M. Kupka, "Diffusivity of hydrogen in B2 iron aluminides," *Scripta materialia,* vol. 55, pp. 585-588, 2006.

[99] U. Prakash, N. Parvathavarthini and R. Dayal, "Effect of composition on hydrogen permeation in Fe–Al alloys," *Intermetallics,* vol. 15, pp. 17-19, 2007.

[100] H. Kimizuka, H. Mori and S. Ogata, "Effect of temperature on fast hydrogen diffusion in iron: A path-integral quantum dynamics approach," *Physical review:B,* vol. 83, pp. 094110–1-094110–7, 2011.

[101] J. Bockris, M. genshaw and M. Fullenwider, "The electro-permeation of hydrogen into metals," *Electrochimica acta,* vol. 15, pp. 47-60, 1970.

[102] R. Song, S.-l. P. and R. Oriani, "Hydrogen permeation through the passivation film on iron by time-lag method," *Journal of the electrochemical society,* vol. 137, pp. 1703-1706, 1990.

[103] P. Ruetschi and R. Giovanoli, "Cation vacancies in MnO2 and their influence on electrochemical reactivity," *The electrochemical society,* vol. 135, pp. 2663-2669, 1988.

[104] W. Lee, A. Nowick and L. Boatner, "Protonic conduction in acceptor-doped KTaO3 crystals," *Solid state ionics,* Vols. 18-19, pp. 989-993, 1986.

[105] R. Song, P. Su-ll and R. Oriani, "The hydrogen permeation through passivating film on iron by modulation method," *Electrochimica acta,* vol. 36, pp. 825-831, 1991.

[106] G. Zhang, X. Wang, F. Yang, Y. Shi, J. Song and X. Lai, "Energetics and diffusion of hydrogen in hydrogen permeation barrier of α-Al2O3/FeAl with two different interfaces," *International journal of hydrogen energy,* vol. 38, pp. 7550-7560, 2013.

[107] M. Zamanzade and A. Barnoush, "Effect of chromium on the electrochemical properties of iron aluminide intermetallics," *Corrosion science,* vol. 78, pp. 223-232, 2014.

[108] G. Hollenberg, E. Simonen, G. Kalinin and A. Terlain, "Tritium/hydrogen barrier development," *Fusion engineering and design,* vol. 28, pp. 190-208, 1995.

[109] A. Barnoush and H. Vehoff, "Hydrogen embrittlement of aluminum in aqueous environments examined by in situ electrochemical nanoindentation," *Scripta materialia,* vol. 58, pp. 747-750, 2008.

[110] A. Pundt and R. Kirchheim, "Hydrogen in metals:Microstructural aspects," *Annual review of materials research,* vol. 36, pp. 555-608, 2006.

[111] S. M. Myers, M. I. Baskes, J. W. Corbett, G. G. DeLeo, S. K. Estreicher, E. E. Haller, P. Jena, N. M. Johnson, R. Kirchheim, S. J. Pearton and M. J. Stavola, "Hydrogen interactions with defects in crystalline solids," *Reviews of modern physics,* vol. 64, pp. 559-617, 1992.

[112] J. Ryu, Hydrogen embrittlement in TRIP and TWIP steels, Department of ferrous technology: Pohang university of science and technology, 2012.

[113] S. Myers, F. Besenbacher and J. K. Nørskov, "Immobilization mechanisms for ion-implanted deuterium in aluminum," *Journal of applied physics,* vol. 58, pp. 1841-1850, 1985.

[114] H. Rajainmaki, S. Linderoth, R. Nieminen and H. Hansen, "Vacancies and interstitials in metals and alloys," *Materials science forum,* Vols. 15-18, pp. 611-616, 1987.

[115] S. Linderoth, H. Rajainmaki, B. Nielsen, H. E. Hansen, R. Nieminen and K. Petersen, "Hydrogen in vacancies in Mo and Ni," *Materials science forum,* Vols. 15-18, pp. 751-756, 1987.

[116] J. Tien, A. Thompson, I. Bernstein and R. Richards, "Hydrogen transport by dislocations," *Metallurgical transactions:A,* vol. 7, pp. 821-829, 1976.

[117] J. Donovan, "Accelerated evolution of hydrogen from metals during plastic deformation," *Metallurgical transactions:A,* vol. 7, pp. 1677-1683, 1976.

[118] M. Louthan, G. Caskey, J. Donovan and D. Rawl, "Hydrogen embrittlement of metals," *Materials science and engineering,* vol. 10, pp. 357-368, 1972.

[119] H. Johnson and J. Hirth, "Atomistics of fracture," in *NATO conference series, series VI: materials science*, 1983.

[120] W. Johnson, "On some remarkable change produced in iron and steel by the action of hydrogen and acids," in *Proceeding of the royal society of London*, 1875.

[121] M. Nagumo, "Hydrogen related failure of steels-a new aspect," *Materials science and technology,* vol. 20, pp. 940-950, 2004.

[122] I. M. Robertson, "The effect of hydrogen on dislocation dynamics," *Engineering fracture mechanics,* vol. 68, pp. 671-692, 2001.

[123] A. Windle and G. Smith, "The effect of hydrogen on the plastic deformation of nickel single crystals," *Metal science,* vol. 2, pp. 187-191, 1968.

[124] X. Tang and A. Thompson, "Hydrogen effects on slip character and ductility in Ni-Co alloys," *Materials science and engineering:A,* vol. 186, pp. 113-119, 1994.

[125] J. Morlet, H. Johnson and A. Troiano, "A new concept of hydrogen embrittlement in steel," *Journal of the iron and steel institute,* vol. 189, pp. 37-44, 1958.

[126] M. Whiteman and A. Troiano, "Hydrogen embrittlement of austenitic stainless steel," *Corrosion,* vol. 21, pp. 53-56, 1965.

[127] H. Wriedt and R. Oriani, "Effect of tensile and compressive elastic stress on equilibrium hydrogen solubility in a solid," *Acta metallurgica,* vol. 18, pp. 753-760, 1970.

[128] R. Oriani, "The diffusion and trapping of hydrogen in steel," *Acta metallurgica,* vol. 18, pp. 147-157, 1970.

[129] R. Oriani and P. Josephic, "Hydrogen-enhanced load relaxation in a deformed medium-carbon steel," *Acta metallurgica,* vol. 27, pp. 997-1005, 1979.

[130] P. Ferreira, I. Robertson and H. Birnbaum, "Hydrogen effect on the interaction between dislocations," *Acta materialia,* vol. 46, pp. 1749-1757, 1998.

[131] P. Ferreira, I. Robertson and H. Birnbaum, "Hydrogen effect on the character of dislocations in high purity aluminum," *Acta materialia,* vol. 47, pp. 2991-2998, 1999.

[132] M. Cornet, M. Trichet and S. Talbot Bernard, "Influence of hydrogen on plastic deformation and fracture of iron, studied by electron microscopy and Auger spectrography," *Memoires scientifiques de la revue de metallurgie,* vol. 74, pp. 307-316, 1977.

[133] S. Lynch, "Comments on ‘‘A unified model of environment-assisted cracking”," *Scripta materialia,* vol. 61, pp. 331-334, 2009.

[134] R. Kirchheim, "Revisiting hydrogen embrittlement models and hydrogen-induced homogeneous nucleation of dislocations," *Scripta materialia,* vol. 62, pp. 67-70, 2010.

[135] A. Barnoush and H. Vehoff, "Recent developments in the study of hydrogen embrittlement: Hydrogen effect on dislocation nucleation," *Acta materialia,* vol. 58, pp. 5274-5285, 2010.

[136] A. Cuitino and M. Ortiz, "Ductile fracture by vacancy condensation in f.c.c. single crystals," *Acta materialia,* vol. 44, pp. 427-436, 1996.

[137] K. Takai, H. Shoda, H. Suzuki and M. Nagumo, "Lattice defects dominating hydrogen-related failure of metals," *Acta materialia,* vol. 56, pp. 5158-5167, 2008.

[138] M. Nathal and C. Liu, "Intrinsic ductility of FeAl single crystals," *Intermetallics,* vol. 3, pp. 77-81, 1995.

[139] R. Lynch, K. Gee and L. Heldt, "Environmental embrittlement of single crystal and thermomechanically processed B2-ordered iron aluminides," *Scripta metallurgica et materialia,* vol. 30, pp. 945-950, 1994.

[140] H. Saka and T. Nishizaki, "Roles of edge and screw dislocations in the environmental embrittlement of an Fe-Al intermetallic compound," *Philosophical magazine:A,* vol. 73, pp. 1173-1179, 1996.

[141] Y. Yang, I. Baker and E. George, "Effect of vacancies on the tensile properties of Fe-40Al single crystals in air and vacuum," *Materials characterization,* vol. 42, pp. 161-167, 1999.

[142] P. Munroe and I. Baker, "Observation of 〈001〉 dislocations and a mechanism for transgranular fracture on {001} in FeAl," *Acta metallurgica et materialia,* vol. 39, pp. 1011-1017, 1991.

[143] J. Li and C. Liu, "Crack nucleation in hydrogen embrittlement," *Scripta metallurgica et materialia,* vol. 27, pp. 1701-1705, 1992.

[144] B. Pöter, F. Stein, R. Wirth and M. Spiegel, "Early stages of protective oxide layer growth of binary iron aluminides," *Zeitschrift für Physikalische Chemie,* vol. 219, pp. 1489-1503, 2005.

[145] I. O. Velon, "Oxidation Behavior of Ni3Al and Fe3Al:II. early stage of oxide growth," *Oxidation of metals,* vol. 56, pp. 425-452, 2001.

[146] A. Velon and D. Q. Yi, "Influence of Cr on the oxidation of Fe3Al and Ni3Al at 500°C," *Oxidation of metals,* vol. 57, pp. 13-31, 2002.

[147] W. Lee and R. Lin, "Oxidation, sulfidation and hot corrosion of intermetallic compound Fe3Al at 605°C and 800°C," *Materials chemistry and physics,* vol. 58, pp. 231-242, 1999.

[148] D. Vogel, A. Hotař, A. Vogel, M. Palm and F. Renner, "Corrosion behaviour of Fe–Al(–Ti) alloys in steam," *Intermetallics,* vol. 18, pp. 1375-1378, 2010.

[149] B. Pint and I. Wright, "The oxidation behavior of Fe-Al alloys," *Materials science forum,* Vols. 461-464, pp. 799-806, 2004.

[150] R. Hutchings and M. Loretto, "Compositional dependence of oxidation rates of NiAl and CoAl," *Metal science,* vol. 12, pp. 503-510, 1978.

[151] H. Grabke, "Oxidation of NiAl and FeAl," *Intermetallics,* vol. 7, pp. 1153-1158, 1999.

[152] S. Frangini, R. Giorgi, J. Lascovich and A. Mignone, "XPS Study of passive films formed on an iron-aluminium intermetallic Compound in acid solution," *Surface and interface analysis,* vol. 21, pp. 435-441, 1994.

[153] E. McCafferty, Thermodynamics of corrosion: pourbaix diagrams. In introduction to corrosion science, New York, NY, USA: Springer, 2010.

[154] N. De Cristofaro, S. Frangini and A. Mignone, "Passivity and passivity breakdown on a b-FeAl intermetallic compound in sulphate and chloride containing solutions," *Corrosion science,* vol. 38, pp. 307-315, 1996.

[155] S. Frangini, N. De Cristofaro, J. Lascovich and A. Mignone, "On the passivation characteristics of a b-FeAl intermetallics compound in sulphate solutions," *Corrosion science,* vol. 35, pp. 153-159, 1993.

[156] W. Moshier, G. Davis and J. Ahearn, "The corrosion and passivity of aluminium exposed to dilute sodium sulfate solutions," *Corrosion science,* vol. 27, pp. 785-801, 1987.

[157] J. Davis, "Corrosion of aluminium and aluminium alloys," in *ASM International*, 1999, pp. 1-43.

[158] G. Faith Olajumoke, Chromium-free conversion coating of aluminium-copper alloys, The university of manchester, 2010.

[159] B. Yang and H. Vehoff, "Grain size effects on the mechanical properties of nanonickel examined by nanoindentation," *Materials science and engineering:A,* vol. 400–401, pp. 467-470, 2005.

[160] B. Yang and H. Vehoff, "Dependence of nanohardness upon indentation size and grain size-A local examination of the interaction between dislocations and grain boundaries," *Acta materialia,* vol. 55, pp. 849-856, 2007.

[161] C. Motz, T. Schöberl and R. Pippan, "Mechanical properties of micro-sized copper bending beams machined by the focused ion beam technique," *Acta materialia,* vol. 53, pp. 4269-4279, 2005.

[162] Q. Ma and D. Clarke, "Size dependent hardness in silver single crystal," *Journal of materials research,* vol. 10, pp. 853-863, 1995.

[163] W. Nix and H. Gao, "Indentation size effects in crystalline materials: a law for strain gradient plasticity," *Journal of the mechanics and physics of solids,* vol. 46, pp. 411-425, 1998.

[164] S. Hainsworth, M. McGurk and T. Page, "The effect of coating cracking on the indentation response of thin hard-coated systems," *Surface and coatings technology,* vol. 102, pp. 97-107, 1998.

[165] A. Korsunsky, M. McGurk, S. Bull and T. Page, "On the hardness of coated systems," *Surface and coatings technology,* vol. 99, pp. 171-183, 1998.

[166] G. Constantinides, C. Tweedie, D. Holbrook, P. Barragan, J. Smith and K. Van Vliet, "Quantifying deformation and energy dissipation of polymeric surfaces under localized impact," *Materials science and engineering:A,* vol. 489, pp. 403-412, 2008.

[167] A. Barnoush and H. Vehoff, "In situ electrochemical nanoindentation of a nickel (111) single crystal: hydrogen effect on pop- in behaviour," *International journal of materials research,* vol. 97, pp. 1224-1229, 2006.

[168] A. Barnoush and H. Vehoff, "In situ electrochemical nanoindentation: a technique for local examination of hydrogen embrittlement," *Corrosion science,* vol. 50, pp. 259-267, 2008.

[169] B. Lucas and W. Oliver, "Indentation power-law creep of high-purity indium," *Metallurgical and materials transactions:A,* vol. 30, pp. 601-610, 1999.

[170] B. Beake, S. Goodes and J. Smith, "Nanoscale materials testing under industrially relevant conditions: high-temperature nanoindentation testing," *Zeitschrift für Metallkunde,* vol. 94, pp. 1-7, 2003.

[171] C. Schuh, J. Mason and A. Lund, "Quantitative insight into dislocation nucleation from high-temperature nanoindentation experiments," *Nature materials,* vol. 4, pp. 617-621, 2005.

[172] K. Durst, B. Backes, O. Franke and M. Göken, "Indentation size effect in metallic materials: modeling strength from pop-in to macroscopic hardness using geometrically necessary dislocations," *Acta materialia,* vol. 54, pp. 2547-2555, 2006.

[173] H. Vehoff, B. Yang, A. Barnoush, H. Natter and R. Hempelmann, "Mechanical properties of nanomaterials examined with a NI-AFM," *Zeitschrift für Physikalische Chemie,* vol. 222, pp. 499-525, 2008.

[174] W. Oliver and G. Pharr, "An improved technique for determining hardness and elastic modulus using load and displacement sensing indentation experiments," *Journal of materials research,* vol. 7, pp. 1564-1583, 1992.

[175] Y. Golovin, "Nanoindentation and mechanical properties of solids in submicrovolumes, thin near-surface layers, and films: A review," *Physics of the solid state,* vol. 50, pp. 2205-2236, 2008.

[176] A. Bolshakov and G. Pharr, "Influences of pileup on the measurement of mechanical properties by load and depth sensing indentation.," *Journal of materials research,* vol. 13, pp. 1049-1058, 1998.

[177] A. Fischer Cripps, The IBIS handbook of nanoindentation, Fischer-Cripps laboratories Pty Ltd, 2009.

[178] A. Barnoush and M. Zamanzade, "Effect of substitutional solid solution on dislocation nucleation in Fe3Al intermetallic alloys," *Philosophical magazine,* vol. 92, pp. 3257-3268, 2012.

[179] T. Li, Y. Gao, H. Bei and E. George, "Indentation Schmid factor and orientation dependence of nanoindentation pop-in behavior of NiAl single crystals," *Journal of the mechanics and physics of solids,* vol. 59, pp. 1147-1162, 2011.

[180] M. Lodes, A. Hartmaier, M. Göken and K. Durst, "Influence of dislocation density on the pop-in behavior and indentation size effect in CaF2 single crystals: experiments and molecular dynamics simulations," *Acta materialia,* vol. 59, pp. 4264-4273, 2011.

[181] A. Barnoush, "Correlation between dislocation density and nanomechanical response during nanoindentation," *Acta materialia,* vol. 60, pp. 1268-1277, 2012.

[182] I. Salehinia, S. Lawrence and D. Bahr, "The effect of crystal orientation on the stochastic behavior of dislocation nucleation and multiplication during nanoindentation," *Acta materialia,* vol. 61, pp. 1421-1431, 2013.

[183] J. Hirth and J. Lothe, Theory of dislocations, New York: John Wiley & Sons, 1981.

[184] M. Peach and J. Köhler, "The forces exerted on dislocations and the stress fields produced by them," *Physcal review,* vol. 80, pp. 436-439, 1950.

[185] M. Asgari, A. Barnoush, R. Johnsen and R. Hoel, "Nanomechanical evaluation of the protectiveness of nitrided layers against hydrogen embrittlement," *Corrosion science,* vol. 62, pp. 51-60, 2012.

[186] A. Barnoush, M. Asgari and R. Johnsen, "Resolving the hydrogen effect on dislocation nucleation and mobility by electrochemical nanoindentation," *Scripta materialia,* vol. 66, pp. 414-417, 2012.

[187] M. Asgari, A. Barnoush, R. Johnsen and R. Hoel, "Small-scale structural and mechanical characterization of the nitrided layer in martensitic steel," *Tribology international,* vol. 61, pp. 109-115, 2013.

[188] M. Asgari, A. Barnoush, R. Johnsen and R. Hoel, "Microstructural characterization of pulsed plasma nitrided 316L stainless steel," *Materials science and engineering:A,* vol. 529, pp. 425-434, 2011.

[189] TriboIndenter user manual, Minneapolis: Hysitron Incorporated, 2006.

[190] TriboIndenter user manual, Minneapolis: Hysitron Incorporated, 2011.

[191] J. Wheeler, Nanoindentation under Dynamic Conditions, University of Cambridge, 2009.

[192] M. Zamanzade, A. Barnoush and H. Vehoff, "Effect of chromium on elastic and plastic deformation of Fe3Al Intermetallics," *Intermetallics,* vol. 41, pp. 28-34, 2013.

[193] A. Barnoush, Hydrogen embrittlement, revisited by in situ electrochemical nanoindentation, Saarbrücken, 2007.

[194] J. Rose, J. Ferrante and J. Smith, "Universal binding energy curves for metals and bimetallic interfaces," *Physical review letters,* vol. 47, pp. 675-678, 1981.

[195] J. Rose, J. Smith and J. Ferrante, "Universal features of bonding in metals," *Physical review:B,* vol. 28, pp. 1835-1845, 1983.

[196] J. Rose, J. Smith, F. Guinea and J. Ferrante, "Universal features of the equation of state of metals," *Physical review:B,* vol. 29, pp. 2963-2969, 1984.

[197] F. U. Renner, A. Stierle, H. Dosch, D. M. Kolb, T. L. Lee and J. Zegenhagen, "Initial corrosion observed on the atomic scale," *Nature,* vol. 439, pp. 707-710, 2006.

[198] M. Zamanzade, A. Barnoush and H. Vehoff, "Cr effect on hydrogen embrittlement of Fe3Al-based iron aluminide intermetallics: Surface or bulk effect," *Acta materialia,* vol. 69, pp. 210-223, 2014.

[199] P. Hirsch and S. Roberts, "The brittle-ductile transition in silicon," *Philosophical magazine:A,* vol. 64, pp. 55-80, 1991.

[200] A. Barnoush, M. Zamanzade and H. Vehoff, "Direct observation of hydrogen-enhanced plasticity in super duplex stainless steel by means of in situ electrochemical methods," *Scripta Materialia,* vol. 62, pp. 242-245, 2010.

[201] W. Koster and T. Godecke, "Physical measurements on iron-aluminium-alloys between 10 at percent and 50 at percent Al .4. the modulus of elasticity of the alloys," *Zeitschrift für Metallkunde,* vol. 73, pp. 111-114, 1982.

[202] M. Yoo, M. Koeppe, C. Harting, H. Mecking, W. Hermann and H. Sockel, "Effect of temperature on elastic constants and dislocation properties of fesingle bond30% Al single crystals," *Acta materialia,* vol. 10, pp. 4323-4332, 1997.

[203] K. Yoshimi, S. Hanada and M. Yoo, "Yielding and plastic flow behavior of B2-type Fe-39.5 mol.% A1 single crystals in compression," *Acta metallurgica et materialia,* vol. 43, pp. 4141-4151, 1995.

[204] D. Risanti, J. Deges, L. Falat, S. Kobayashi, J. Konrad, M. Palm, B. Pöter, A. Schneider, C. Stallybrass and F. Stein, "Dependence of the brittle-to-ductile transition temperature (BDTT) on the Al content of Fe–Al alloys," *Intermetallics,* vol. 13, pp. 1337-1342, 2005.

[205] M. Palm, "Fe–Al materials for structural applications at high temperatures: current research at MPIE," *International journal of materials research,* vol. 100, pp. 277-287, 2009.

Paper A

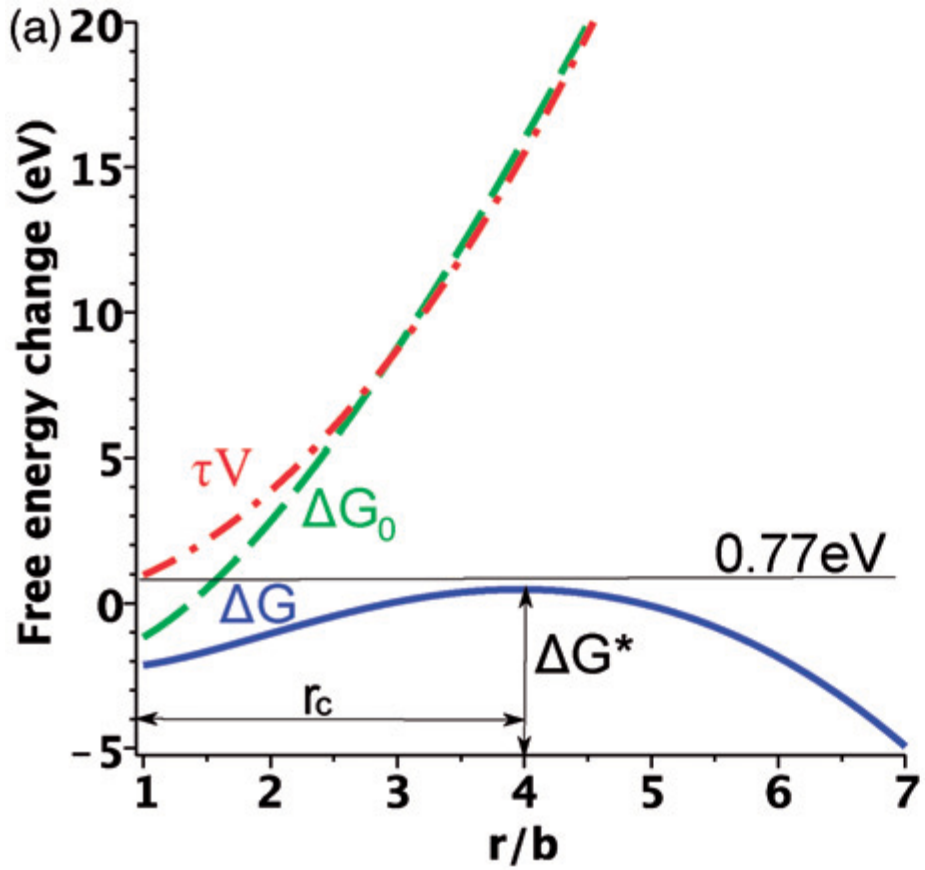
(a)
Free energy change (eV)
20
15
10
5
0
−5
τV
ΔG0
0.77eV
ΔG
ΔG*
rc
1
2
3
4
5
6
7
r/b

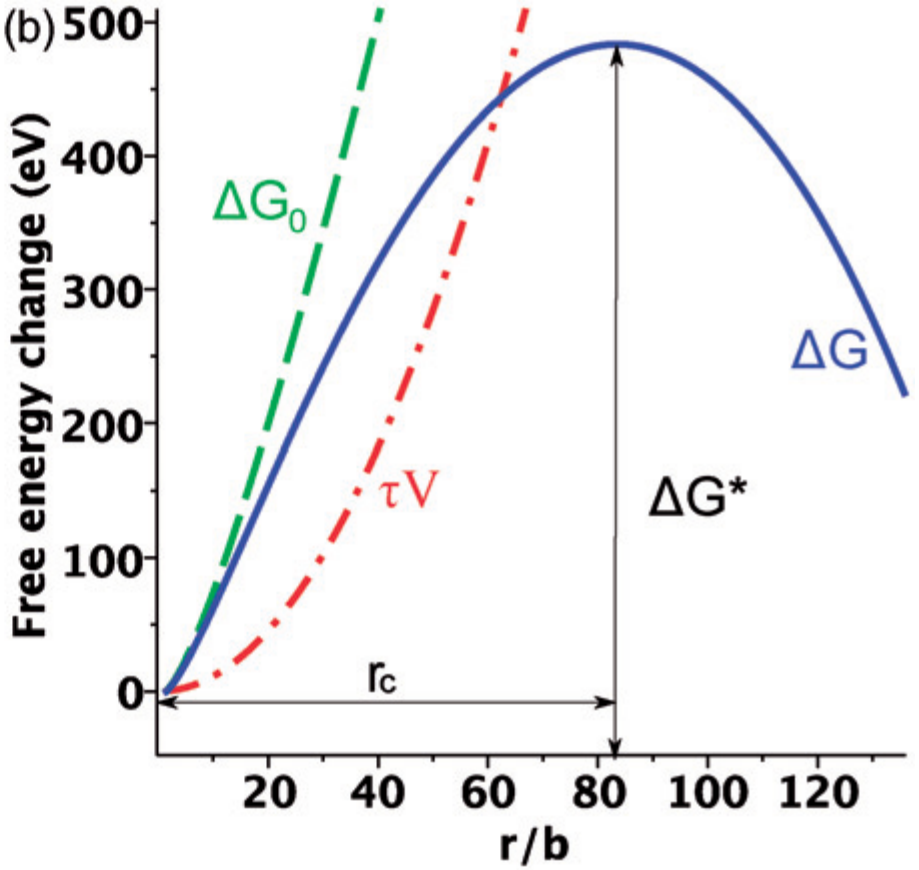
(b)
Free energy change (eV)
500
400
300
200
100
0
ΔG0
τV
ΔG
ΔG*
rc
20
40
60
80
100
120
r/b

Philosophical Magazine
Publication details, including instructions for authors and subscription information:
http://www.tandfonline.com/loi/tphm20

Effect of substitutional solid solution on dislocation nucleation in Fe_3Al intermetallic alloys

Afrooz Barnoush [a] & Mohammad Zamanzade [a]

[a] Department of Materials Science, Saarland University, Bldg. D22, P.O. Box 151150, D-66041 Saarbruecken, Germany

Available online: 20 Jun 2012

To cite this article: Afrooz Barnoush & Mohammad Zamanzade (2012): Effect of substitutional solid solution on dislocation nucleation in Fe_3Al intermetallic alloys, Philosophical Magazine, DOI:10.1080/14786435.2012.698759

To link to this article: http://dx.doi.org/10.1080/14786435.2012.698759

Philosophical Magazine
2012, 1–12, iFirst

Taylor & Francis
Taylor & Francis Group

Effect of substitutional solid solution on dislocation nucleation in Fe_3Al intermetallic alloys

Afrooz Barnoush* and Mohammad Zamanzade

Department of Materials Science, Saarland University, Bldg. D22, P.O. Box 151150, D-66041 Saarbruecken, Germany

(*Received 1 October 2011; final version received 8 May 2012*)

Dislocation nucleation in solid solutions of body-centered-cubic intermetallic Fe_3Al alloys was investigated by means of nanoindentation and measurement of the pop-in load of samples with different Cr content. It is clearly shown that the Cr solute element in the Fe_3Al intermetallic alloy increases the pop-in load, i.e. shear stress, required for dislocation nucleation in a previously dislocation-free region. Changes in pop-in load track closely with changes in elastic properties, which can be interpreted within the framework of the universal features of metallic bonding as a change in the interatomic potential, as proposed by Rose et al.

Keywords: nanoindentation; dislocations; mechanical properties; Fe_3Al

1. Introduction

Ordered intermetallics, which form long-range ordered crystal structures below their critical ordering temperatures, constitute an important emerging class of metallic materials. The Fe_3Al intermetallic alloys have been widely studied since the 1930s when their excellent oxidation resistance was first noted [1,2]. Their low cost, low density, good wear resistance, ease of fabrication, resistance to corrosion and sulfidation make them very attractive for industrial use. Additionally, they offer conservation of strategic elements like nickel, molybdenum and chromium by the replacement of stainless steels. They also have a lower density than stainless steels and potentially a better strength-to-weight ratio. Fe_3Al-based intermetallic alloys are one of the few structural intermetallics that pass through two ordered structures ($D0_3$ and B2) before becoming disordered. These structures ($D0_3$ and B2) are body-centered cubic (bcc) derivative structures with high crystal symmetries and slip behavior similar to bcc iron, indicating that Fe_3Al should be intrinsically ductile at ambient temperatures. These property advantages have led to the consideration of iron–aluminum alloys for many applications, such as brake disks for windmills and trucks [3], filtration systems in refineries and fossil power plants [4], transfer rolls for hot rolled steel strips, ethylene crackers and air deflectors for burning high-sulfur coal [5]. At present, the major issues that continue to delay further commercial viability of Fe_3Al intermetallic alloys are their low ductility and impact resistance at

*Corresponding author. Email: a.barnoush@matsci.uni-sb.de

ISSN 1478–6435 print/ISSN 1478–6443 online

http://dx.doi.org/10.1080/14786435.2012.698759
http://www.tandfonline.com

low temperatures due to moisture induced hydrogen embrittlement [6,7] and inadequate creep resistance at elevated temperatures [8–10].

There have been attempts to overcome these disadvantages by alloying Fe_3Al with different elements [11,12]. However, conventional mechanical tests are costly, time consuming, and due to their large scale, not very successful in obtaining mechanistic information. In contrast to conventional mechanical tests, an instrumented nanoindentation technique offers several advantages. First of all, the extremely small volume probed by this technique allows for easy pre- and post-characterization by means of non-destructive, high-resolution electron microscopy techniques like electron backscatter diffraction (EBSD), or electron channeling contrast [13–16]. Another advantage of the instrumented nanoindentation technique is its capability to resolve the homogeneous dislocation nucleation in annealed samples with very low surface roughness (electropolished) [17,18]. Typical dislocation densities in an annealed metal are within the range 10^{10}–$10^{12}\,m^{-2}$, with dislocations spaced between 1 and 10 μm apart. Depending on the tip radius [19,20], a relatively sharp nanoindenter tip in the elastic regime is able to probe a lateral region of at most a couple of hundred nanometers, to the point where the pop-in is noted. This suggests that the volume of material sampled by the indentation test at this depth is smaller than the average dislocation spacing, so that an indentation placed randomly on the surface would have a significant probability of sampling a region that contains no preexisting dislocations [21]. The absence of dislocations means the material continues to load elastically until the shear stress under the tip reaches a value near the theoretical shear strength of the material, well above what is necessary to activate an existing dislocation source. At this point dislocations are homogeneously nucleated [22] and are followed by subsequent glide and multiplication events. Homogeneous dislocation nucleation (HDN) should occur when the stress beneath the indenter tip approaches the theoretical shear strength of the material and is therefore directly related to the interatomic potential of the tested material [23]. The term HDN is used here to indicate that dislocations are nucleated from an otherwise dislocation-free material. For an indentation test, the applied shear stress that nucleates a dislocation can be assumed to be the maximum shear stress beneath the indenter during purely elastic loading. Lastly, instrumented nanoindentation, which probes the mechanical properties, i.e. hardness and elastic modulus of extremely small volumes of materials, can be used to investigate the mobility of dislocations via analysis of the load–displacement (L–D) curves [24]. Successful application of Fe_3Al–X alloys in industry strictly depends on our fundamental understanding of the effect of alloying elements on their mechanical properties. Nanaoindentation offers a comprehensive range of possibilities to achieve this understanding, along with the advantage of being a very resource conservative method. This paper reports the effect of the addition of Cr to the dislocation nucleation process in Fe_3Al examined by application of the nanoindentation technique.

2. Experimental procedure

The samples were received from the Max Plank Institute for Iron Research in Düsseldorf (MPIE) and were made by means of the vacuum induction

melting method. In all samples the concentration of aluminum remained constant at 26 atomic percent. Samples with different concentrations of Cr (see Table 1) were cut by spark erosion with a diameter of 12 mm and a thickness of 4 mm. After mechanically polishing the samples down to 1 μm using diamond paste, the samples were electropolished with a sulfuric acid methanol base solution [25]. One of the most critical issues during nanoindentation is the surface condition of the sample, specifically, when observation of pop-in and examination of the dislocation nucleation is the aim. Any step and inhomogeneity on the surface increases the scatter of the pop-in load [26]. Figure 1 shows the topography and surface quality

Table 1. Surface roughness of Fe_3Al–xCr samples after electropolishing with methanol-sulfuric acid base solution developed for these alloys.

	Surface roughness		Measurement area
Material	R_{RMS} (nm)	R_a (nm)	μm^2
Fe–26Al	1.06	0.87	27.363
Fe–26Al–0.5Cr	0.580	0.464	20.772
Fe–26Al–4Cr	0.65	0.52	51.521
Fe–26Al–5Cr	0.78	0.60	27.688

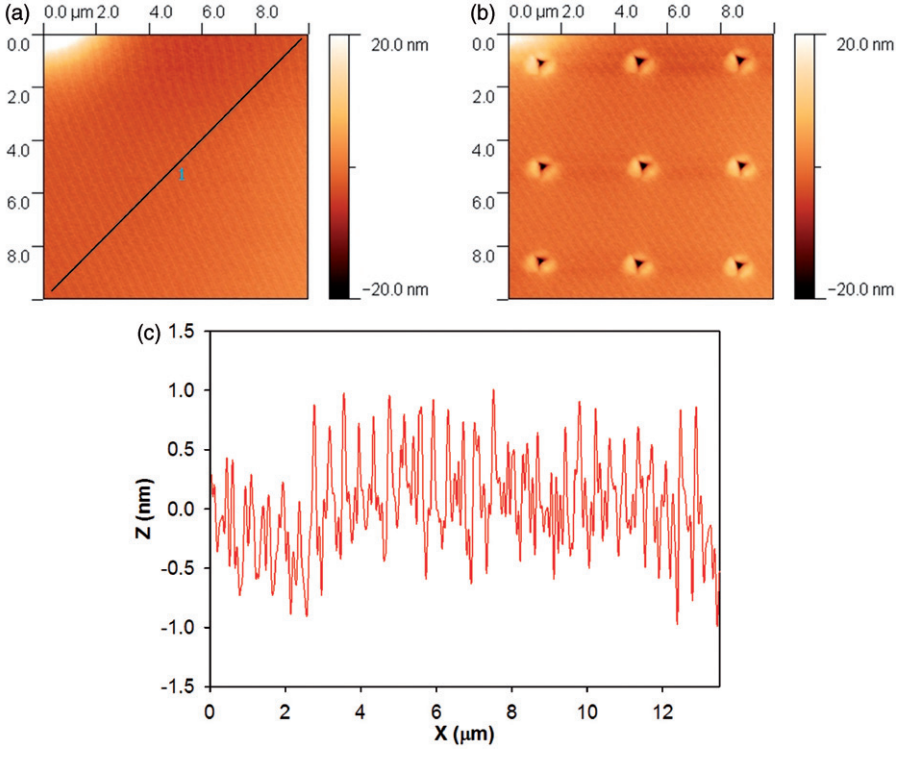

Figure 1. Surface topography of Fe_3Al–0.5Cr alloy before and after indentation. (a) Surface topography prior to indentation, (b) typical matrix of indents and (c) surface prole along the line 1 in Figure 1a.

after this surface preparation process for the Fe_3Al alloy. Table 1 summarizes the surface roughness of the different chromium Fe_3Al alloys after surface preparation. Another critical issue during the investigation of the pop-in and dislocation nucleation process is the orientation dependence of the pop-in load [27–29]. Therefore, in order to exclude the orientation effect from our measurement and to make the comparison of data from different samples possible, EBSD measurements were performed to characterize the different crystallographic orientations and grain sizes in all samples as shown in Figure 2. Then grains with orientation close to (1 0 0) are chosen for performing the nanoindentation tests. For indentations made on (1 0 0) plane the maximum shear stress calculated according to the Hertzian contact model lies on the (1 1 0) slip planes below the surface, i.e. the maximum shear stress is equal to the resolved shear stress on the slip plane.

In all the specimens the grains were larger than 500 μm. Considering the very small indentation depth, such a grain behaves like a single crystal during nanoindentation. Nanoindentations were performed with a Hysitron TriboIndenter® equipped with a Performech™ controller using a Berkovich diamond tip. In order to

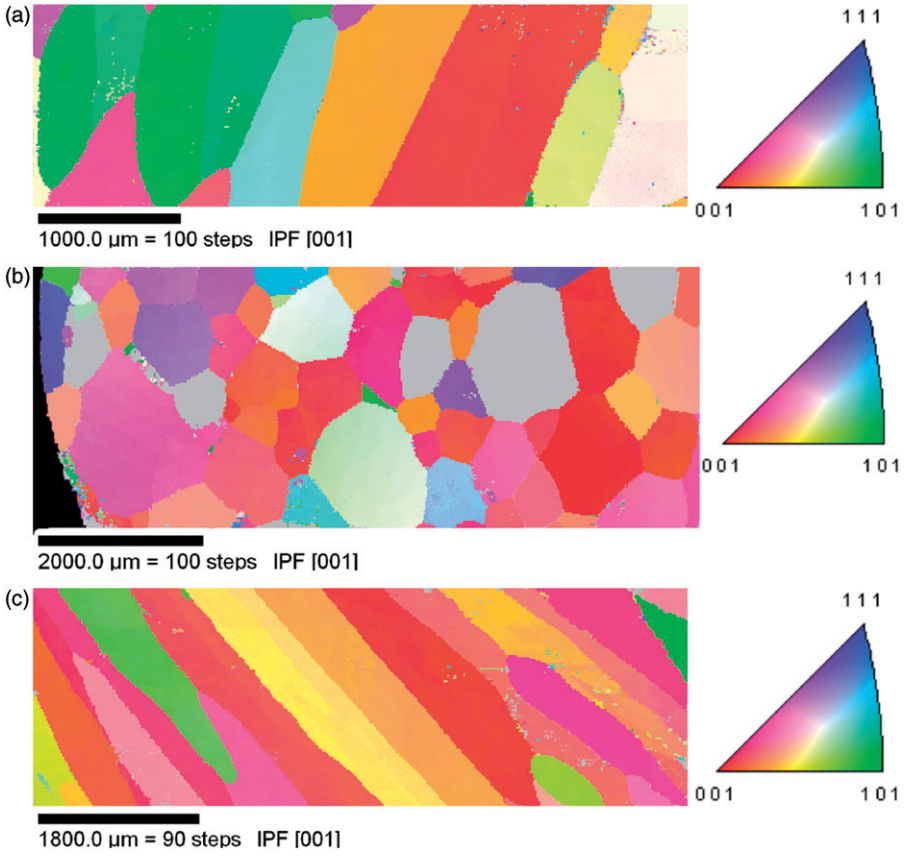

Figure 2. Orientation imaging maps resulting from EBSD measurements on different samples alloyed with. (a) 0.5 at.% Cr, (b) 4 at.% Cr and (c) 5 at.% Cr.

eliminate any scatter due to the change in the surface properties, the samples were directly nanoindented after electropolishing.

The load function used for the indentation consisted of a loading segment with a 500 μN/s loading rate and a 1 s holding time at peak value, with an additional 1 s holding time at 10% of the peak value during unloading for drift correction [30].

3. Results and discussion

The typical L–D curves for samples with different Cr content nanoindented on (1 0 0) oriented grains are presented in Figure 3. The L–D curves of Figure 3 show three stages: elastic loading, an excursion in depth (pop-in) at the onset of plasticity and continued elastoplastic loading. The initial elastic portion of the loading curves can be fitted with the Hertzian elastic response

$$P = \frac{4}{3} E_r \sqrt{Rh^3} \tag{1}$$

where P is the applied load, h is the indentation depth, R is the radius of the tip curvature, and E_r is the reduced modulus, given by the following [31].

$$\frac{1}{E_r} = \frac{1-\nu_1^2}{E_1} + \frac{1-\nu_2^2}{E_2} \tag{2}$$

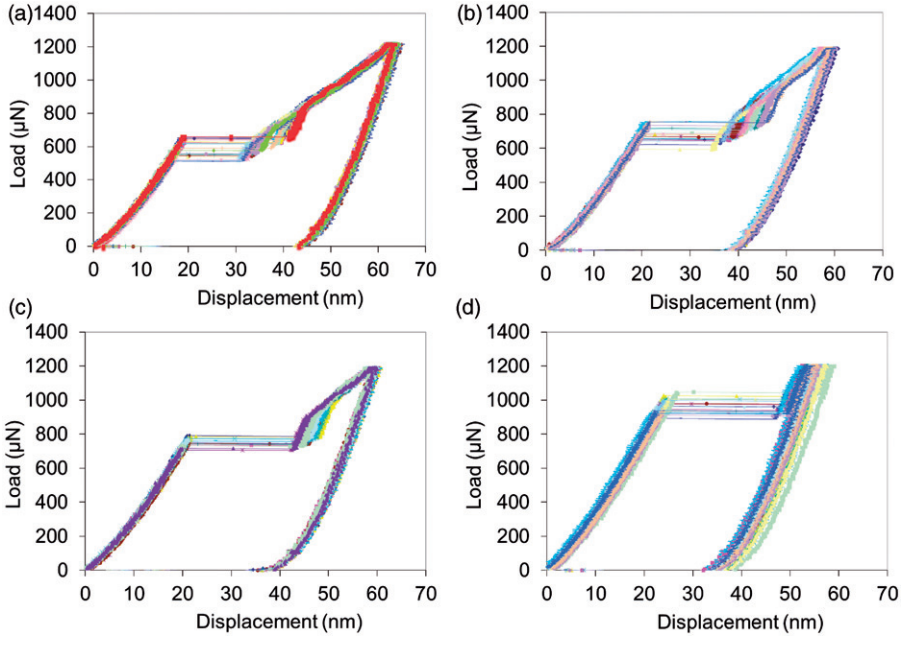

Figure 3. Typical load–displacement curves measured on the (1 0 0) oriented grains of samples with different chromium contents. The perfect surface preparation resulted in minimum scattering of the data. (a) Cr free sample, (b) 0.5% Cr alloyed, (c) 4% Cr alloyed and (d) 5% Cr alloyed.

Table 2. Parameters involved in Equation (7) and the mean pop-in load, $\bar{P}_{\text{pop-in}}$, experimentally observed during nanoindentation of the Fe_3Al alloys with different Cr content.

Samples	a (nm) [46]	b (nm)	ρ (nm)	E(GPa) [34]	$\bar{P}_{\text{pop-in}}$ (μN)
0.0 at.% Cr	0.2895	0.2507	0.1857	165.3	600
0.5 at.% Cr	0.2894	0.2506	0.1856	165.8	650
4.0 at.% Cr	0.2887	0.2500	0.1852	171.7	800
5.0 at.% Cr	0.2885	0.2498	0.1850	188.5	900

where E is the elastic modulus and ν is Poisson's ratio. The subscripts 1 and 2 indicate the tip and the sample, respectively. For a diamond tip $\nu = 0.07$ and $E = 1140$ GPa can be assumed. The reported values of elastic constants in ref. [32] are used to evaluate Young's modulus and Poisson's ratio of stoichiometric Fe_3Al following the Voigt–Reuss–Hill averaging method [33] as 162.2 GPa and 0.293, respectively. The value of 162.2 GPa is in good agreement with our measured value from nanoindentation tests [34] reported in Table 2. The value of $E_r = 153.65$ GPa is calculated according to Equation (2) for Fe_3Al. With the known value of E_r, it is now possible to estimate the radius of the Berkovich tip by fitting the elastic part of the L–D curves of the Fe_3Al (Cr free specimen) according to Equation (1). By this procedure the tip radius was found to be 1500 nm.

The initial elastic loading begins as soon as the tip contacts the material surface and continues until HDN occurs. For an indentation test, the applied shear stress that nucleates a dislocation can be assumed to be the maximum shear stress beneath the indenter at the onset of the pop-in. This maximum shear stress acts on a 45° inclined plane below the surface. For our (1 0 0) oriented grains the maximum shear stress lies on a (1 1 0) plane, which is a slip plane for Fe_3Al at room temperature [35]. According to continuum mechanics the position of the maximum shear stress is approximately 0.48 times the contact radius, a, below the sample surface. Computer simulations support this approximation [36]. The position and value of the maximum shear stress $z_{(\tau_{\max})}$, and $\tau_{\max}$, are given by the following [31].

$$z_{(\tau_{\max})} = 0.48\left(\frac{3PR}{4E_r}\right)^{\frac{1}{3}} \tag{3}$$

$$\tau_{\max} = 0.31\left(\frac{6E_r^2}{\pi^3 R^2}P\right)^{\frac{1}{3}}. \tag{4}$$

If we insert this tip radius into Equation (4), we obtain a maximum shear stress for each pop-in load. This maximum shear stress is responsible for the HDN below the tip at $z_{(\tau_{\max})}$. Classic dislocation nucleation theory, as summarized by Hirth and Lothe [37], suggests that the energy required to generate a dislocation loop depends on the shear stress. The free energy of a circular dislocation loop of radius r is given by:

$$\Delta G = 2\pi r W - \pi r^2 b\tau \tag{5}$$

where W is the line energy of the dislocation loop, b is the Burgers vector, and τ is the external shear stress acting on the loop (i.e. the Peach–Köhler force [38]). The first term on the right-hand side of Equation (5) describes the energy required to create a dislocation loop of radius r in a defect-free lattice and the absence of any stress field. The second term gives the work done by the applied stress τ as a result of the Burgers vector displacement and indicates the work done on the system to expand a dislocation loop of radius r, in another words, the area swept by the dislocation, i.e. the *activation area* under the applied stress for a given loop radius. However, within the classical concept of the thermally activated mechanisms in crystal plasticity, the activation energy of a given process is divided into the following two terms:

$$\Delta G = \Delta G_0 - \tau V \tag{6}$$

where V is the activation volume. For our process of HDN the activation volume for the formation of a dislocation loop, with a given radius r, is equal to $\pi r^2 b$ and the barrier activation energy at zero stress ΔG_0 is equal to $2\pi r W$. If we assume that the homogeneously forming dislocation loop within the region of the maximum shear stress below the tip is circular, then we can use the line energy W for a circular loop as given by [37]:

$$W = \frac{2-\nu}{1-\nu}\frac{\mu b^2}{8\pi}\left(\ln\frac{4r}{\rho} - 2\right) \tag{7}$$

to rewrite Equation (5) as follows:

$$\Delta G = \frac{2-\nu}{1-\nu}\frac{\mu r b^2}{4}\left(\ln\frac{4r}{\rho} - 2\right) - \pi r^2 b\tau \tag{8}$$

where μ is the shear modulus and ρ is the dislocation core radius. For a material with known values of μ, ν and ρ it is possible to calculate the changes in both barrier activation energy at zero stress ΔG_0, and activation volume V for the process of HDN as a function of the dislocation loop radius. For the given applied stress τ it is possible to draw ΔG_0, τV and ΔG as a function of loop radius. Figure 4 shows such a plot for Fe_3Al at two different applied shear stresses $\tau = \mu/20$ and $\tau = \mu/170$. The higher shear stress is comparable with the theoretical shear strength τ_{th} of Fe_3Al predicted by Frenkel's model [39]. The lower shear stress is comparable with the typical yield stress of a polycrystalline Fe_3Al [40].

Figure 4 shows that for a given shear stress, at small dislocation loop radii, the total increase in the lattice energy as a result of the dislocation loop formation (green dashed curve in Figure 4) is larger than the external work done by the applied shear stress (red dashed and dotted curve in Figure 4), and the total change in the free energy (blue solid curve in Figure 4) of the system is positive. This means any dislocation loop nucleus, formed within this range of radii is unstable and will vanish. This situation changes, however, as the radius grows in size, so that with larger radii, the free energy becomes negative. Therefore, the free energy for the formation of a dislocation loop, at a given applied stress τ, passes through a maximum (ΔG^*) at a critical loop radius r_c. ΔG^* defines the activation volume for the HDN process at the given stress, τ, and temperature, and $\pi r_c^2 b$ defines its activation volume. This means that the activation volume for HDN is in fact not

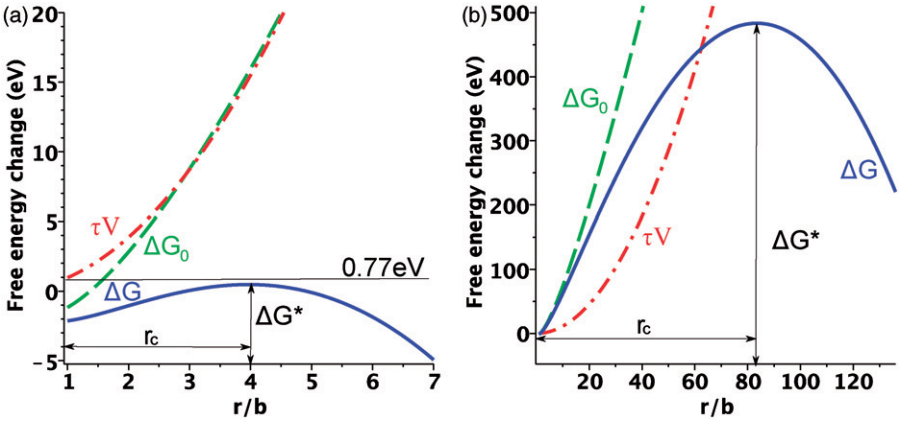

Figure 4. Change in free energy of homogeneous dislocation nucleation for Fe_3Al as a function of dislocation loop radius r. (a) $\tau = \mu/20 \approx \tau_{th}$ and (b) $\tau = \mu/170 \approx \sigma_y$.

constant as assumed by Mason et al. [41], but is dependent on the applied shear stress as shown in atomistic simulations [42,43]. This can be explained physically by considering that at the given stress and temperature, for thermally activated HDN, a certain volume of the material should be excited by the stress field. At a reduced stress level and the same temperature, a larger volume of the material should be excited in order to observe the thermally activated HDN. Now on the basis of the harmonic transition state theory [44], one can discuss the probability of a HDN under the given strain rate (indentation rate) and temperature [22]. This paper only focuses on the constant strain rate and temperature results. ΔG^* at a loop size r_c could be found by setting $\partial \Delta G/\partial r = 0$. The growth of any nucleus with a radius smaller than r_c requires an activation energy to overcome the ΔG^* energy barrier and form a stable dislocation loop. Rice and Beltz [45] estimated that the available thermal energy for thermal activation of dislocation nucleation at the crack tip is in the range of $\approx 30\,kT$ (0.77 eV at room temperature). We can assume the same thermal energy contribution for the HDN during nanoindentation. This means that pop-in is only observed for loads having a free-energy maximum, as typically shown for two different stresses in Figure 4, lower than the available thermal energy at room temperature (0.77 eV shown in Figure 4a).

This criterion ($\Delta G^* \leq 0.77$ eV), together with Equation (4), can be used in combination with the measured mean pop-in loads (Table 2) from different samples to calculate the effect of alloying elements on the process of HDN. The involved parameters in Equation (7) that can be influenced through alloying are b, ρ and μ. The change in b is coupled with a change in the lattice constant by addition of Cr. As a first approximation, we can assume that the change in ρ is also only coupled with the change in the lattice constant. These changes are given in Table 2 based on the change of the lattice constants as reported by Friák et al. based on *ab initio* calculations [46].

Two different methods were used to calculate the shear modulus, μ. The first method is based on the measured mean pop-in load and uses Equations (5) and (7). The other method is based on the measured E values according to the Oliver–Pharr

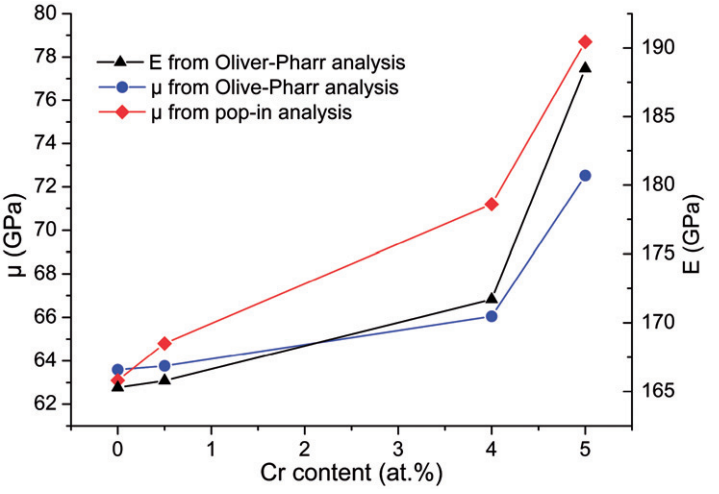

Figure 5. Change in the shear modulus, μ, and Young's modulus, E, of the Fe_3Al alloys with different Cr content as a function of the Cr content. The shear modulus is independently measured from the pop-in load dependence on the Cr concentration according to Equation (5), whereas Young's modulus, E, is calculated from unloading curves together with the correction for the pile-up [34].

method and uses the relation $\mu = E/2(1+\nu)$ to calculate μ. Figure 5 shows the change of both independently calculated shear moduli for samples with different Cr content and the changes in Young's modulus [34]. Both independently extracted values of μ (from the pop-in load) and E (from the Oliver–Pharr method) show a similar trend, which is in good qualitative agreement with the theoretical and experimental measurements reported by Friák et al. [46].

The elastic moduli (bulk, shear, Young's) are proportional to the second derivative of the crystal energy, U_c, with the displacement field. In other words, an elastic modulus is a measure of the increase of the crystal energy with dilatation (bulk modulus), normal strain (Young's modulus), or shear strain (shear modulus) imposed by an external stress. Rose et al. [47] have shown that metallic binding-energy distance curves can be approximately scaled into a single universal relation for adhesion [48] and cohesion of metals [49], as well as chemisorption on metal surfaces [48]. In each case the energy relation can be expressed as:

$$U_c(d) = \Delta U_c \; U_c^*(d^*) \tag{9}$$

where $U_c(d)$ is the total energy as a function of the interatomic separation distance d; ΔU_c is the equilibrium binding energy, while $U_c^*(d^*)$ is an approximately universal function which describes the shape of the binding-energy curve for metals. The coordinate d^* is a scaled length defined by:

$$d^* = \frac{(d - d_m)}{l} \tag{10}$$

where d_m is the equilibrium separation and l is a scaling length, which is to be determined.

The total-energy–distance curve for a given physical situation is determined from the two scaling parameters, ΔU_c and l, once the general form of $U_c^*(d^*)$ is established. All currently available *ab initio* calculations for the cohesion and adhesion of metals, as well as the chemisorption of gas atoms on metal surfaces, are shown to be determined by this single relation. These findings suggest a commonality of metallic bonding. From Equations (9) and (10), the following relation defines the second derivative of the crystal energy U_c:

$$\left[\frac{\partial^2 U_c(d)}{\partial d^2}\right]_{d=d_m} = \frac{\Delta U_c}{l^2}\left[\frac{\partial^2 U_c^*(d^*)}{\partial d^{*2}}\right]_{d^*=0}. \tag{11}$$

The total cohesive energy is a function of the separation between atoms for a uniformly dilated lattice. The separation between atoms can be characterized in terms of the Wigner–Seitz radius, r_{ws}, as suggested by Rose et al. [49]. The bulk modulus at equilibrium can be defined using the Wigner–Seitz radius as follows:

$$B = V^2\frac{\partial^2 U_c(d)}{\partial V^2} = \frac{1}{12\pi r_{ws}}\frac{\partial^2 U_c(d)}{\partial r_{ws}^2}. \tag{12}$$

Equation (11) can be rewritten using the relations $\mu = E/2(1+\nu)$ and $B = E/3(1-2\nu)$ and Equation (12) as follows:

$$\frac{U_{\text{Cohesive}}}{l^2}\left[\frac{\partial^2 U_c^*(d^*)}{\partial d^{*2}}\right]_{d^*=0} = \mu\frac{8\pi(1+\nu)}{(1-2\nu)}r_{ws}. \tag{13}$$

Because of the universality, the ratio of the second derivative in the large parentheses is independent of the considered metal.

Equation (13) has a simple physical meaning: The increase in the shear or Young's modulus is coupled with the increase of the strength of the interatomic bonds. Therefore, the increase of the shear and Young's moduli after addition of Cr as a ternary alloying element strengthen the interatomic bonds.

4. Conclusion

By application of the classical dislocation and harmonic transition state theories, we were able to develop a simple relation to measure the effect of alloying elements on the shear modulus from the pop-in data. Furthermore, we correlated the changes in the shear modulus with the interatomic bonds using the Rose potential. In this manner we provided direct evidence of the enhancing effect of Cr on interatomic bonds in Fe_3Al alloy. Improvement of the interatomic bonds strength can have an advantageous effect on resistance against HE as shown by *in situ* electrochemical nanoindentation studies [25,50]. Our results also show that the application of the nanoindentation method for development of new alloys in comparison to conventional macroscopic mechanical tests is advantageous since: (i) it requires a very limited volume of materials, i.e. a few cubic millimeters; (ii) it is possible to perform many tests on this small piece of sample and obtain a reasonable statistic; and (iii) the experimental results provide information on the intrinsic properties of the material

which are not influenced by microstructural features and the inhomogeneities usually present in macroscopic samples.

Acknowledgments

The authors thank Dr. Martin Palm from MPIE Düsseldorf for providing the samples and many valuable discussions, and the Hysitron and Physical Electronics GmbH for giving us the chance to use the Performech^{TM} controller.

References

[1] N. Ziegler, Am. Inst. Mining Met. Eng., Inst. Metals Division, Tech. Pub. 450 (1932) p.6.
[2] C. Sykes and J. Bampfylde, Iron Steel Inst. 130 (1934) p.389.
[3] P.J. Blau and H.M. Meyer III, Wear 255 (2003) p.1261.
[4] R. Judkins and U. Rao, Intermetallics 8 (2000) p.1347.
[5] N. Stoloff, C. Liu and S. Deevi, Intermetallics 8 (2000) p.1313.
[6] G. Chen and C. Liu, Int. Mater. Rev. 46 (2001) p.253.
[7] I. Baker, D. Wu, S.O. Kruijver and E.P. George, Mater. Sci. Eng. A 329–331 (2002) p.729.
[8] D. Morris, C. Liu and E. George, Intermetallics 7 (1999) p.1059.
[9] M. Palm, Int. J. Mater. Res. 100 (2009) p.277.
[10] D. Morris and M. Muñoz-Morris, Intermetallics 13 (2005) p.1269.
[11] C.G. McKamey, J.A. Horton and C.T. Liu, J. Mater. Res. 4 (1989) p.1156.
[12] C. McKamey, J. DeVan, P. Tortorelli and V. Sikka, J. Mater. Res. 6 (1991) p.1779.
[13] M. Asgari, A. Barnoush, R. Johnsen and R. Hoel, Mater. Sci. Eng. A 529 (2011) p.425.
[14] I. Gutierrez-Urrutia, S. Zaefferer and D. Raabe, Scr. Mater. 61 (2009) p.737.
[15] A. Barnoush, M.T. Welsch and H. Vehoff, Scr. Mater. 63 (2010) p.465.
[16] N. Zaafarani, D. Raabe, R. Singh, F. Roters and S. Zaefferer, Acta Mater. 54 (2006) p.1863.
[17] K. Durst, B. Backes, O. Franke and M. Göken, Acta Mater. 54 (2006) p.2547.
[18] H. Vehoff, B. Yang, A. Barnoush, H. Natter and R. Hempelmann, Zeitschrift für Physikalische Chemie 222 (2008) p.499.
[19] A. Barnoush, Acta Mater. 60 (2012) p.1268.
[20] S. Shim, H. Bei, E. George and G. Pharr, Scr. Mater. 59 (2008) p.1095.
[21] D. Lorenz, A. Zeckzer, U. Hilpert, P. Grau, H. Johansen and H.S. Leipner, Phys. Rev. B 67 (2003) p.172101.
[22] C. Schuh and A.C. Lund, J. Mater. Res. 19 (2004) p.2152.
[23] A. Barnoush and H. Vehoff, Scr. Mater. 55 (2006) p.195.
[24] A. Barnoush, M. Asgari and R. Johnsen, Scr. Mater. 66 (2012) p.414.
[25] A. Barnoush, C. Bies and H. Vehoff, J. Mater. Res. 24 (2009) p.1105.
[26] J. Zimmerman, C. Kelchner, P. Klein, J. Hamilton and S. Foiles, Phys. Rev. Lett. 87 (2001) p.165507.
[27] C. Begau, A. Hartmaier, E. George and G. Pharr, Acta Mater. 59 (2011) p.934.
[28] E.T. Lilleodden, J.A. Zimmerman, S.M. Foiles and W.D. Nix, J. Mech. Phys. Solids 51 (2003) p.901.
[29] T. Li, Y. Gao, H. Bei and E. George, J. Mech. Phys. Solids 59 (2011) p.1147.
[30] A. Barnoush and H. Vehoff, Corros. Sci. 50 (2008) p.259.
[31] K. Johnson, *Contact Mechanics*, Cambridge University Press, Cambridge, 2003.
[32] G. Kötter, K. Nembach, F. Wallow and E. Nembach, Mater. Sci. Eng. A 114 (1989) p.29.

[33] S. Danilkin, H. Fuess, T. Wieder and A. Hoser, J. Mater. Sci. 36 (2001) p.811.
[34] M. Zamanzade and A. Barnoush, Intermetallics (2012) submitted.
[35] S. Kobayashi, S. Zaefferer, A. Schneider, D. Raabe and G. Frommeyer, Mater. Sci. Eng. A 387–389 (2004) p.950.
[36] M. Wen, L. Zhang, B. An, S. Fukuyama and K. Yokogawa, Phys. Rev. B 80 (2009) p.094113.
[37] J.P. Hirth and J. Lothe, *Theory of Dislocations*, John Wiley, New York, 1981.
[38] M. Peach and J. Köhler, Phys. Rev. 80 (1950) p.436.
[39] J. Frenkel, Zeitschrift für Physik 37 (1926) p.572.
[40] J.H. Schneibel, H. Rühe, M. Heilmaier, H. Saage, M. Goncharenko and P. Loboda, Intermetallics 18 (2010) p.1369.
[41] J.K. Mason, A.C. Lund and C.A. Schuh, Phys. Rev. B 73 (2006) p.054102.
[42] M. Wen and Z. Li, Comput. Mater. Sci. 54 (2012) p.28.
[43] T. Zhu, J. Li, A. Samanta, A. Leach and K. Gall, Phys. Rev. Lett. 100 (2008) p.025502.
[44] J. Li, MRS Bull. 32 (2007) p.151.
[45] J.R. Rice and G.E. Beltz, J. Mech. Phys. Solids 42 (1994) p.333.
[46] M. Friák, J. Deges, R. Krein, G. Frommeyer and J. Neugebauer, Intermetallics 18 (2010) p.1310.
[47] J. Rose, J. Smith, F. Guinea and J. Ferrante, Phys. Rev. B 29 (1984) p.2963.
[48] J. Smith, J. Ferrante and J. Rose, Phys. Rev. B 25 (1982) p.1419.
[49] J. Rose, J. Smith and J. Ferrante, Phys. Rev. B 28 (1983) p.1835.
[50] A. Barnoush, J. Dake, N. Kheradmand and H. Vehoff, Intermetallics 18 (2010) p.1385.

Paper B

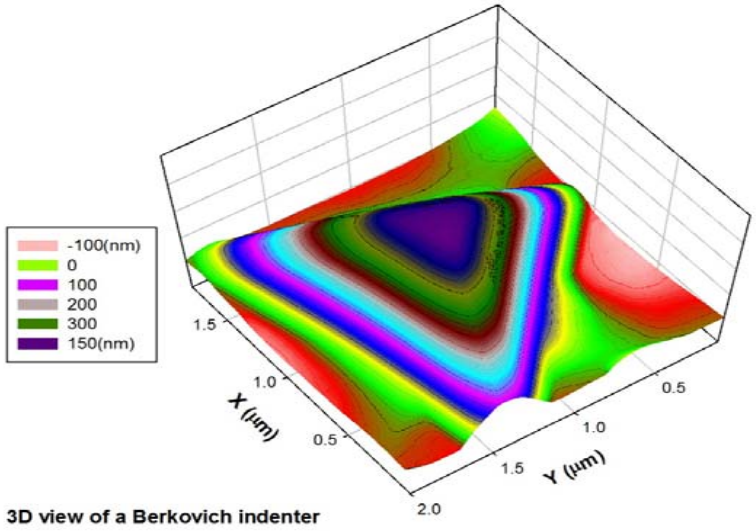

3D view of a Berkovich indenter

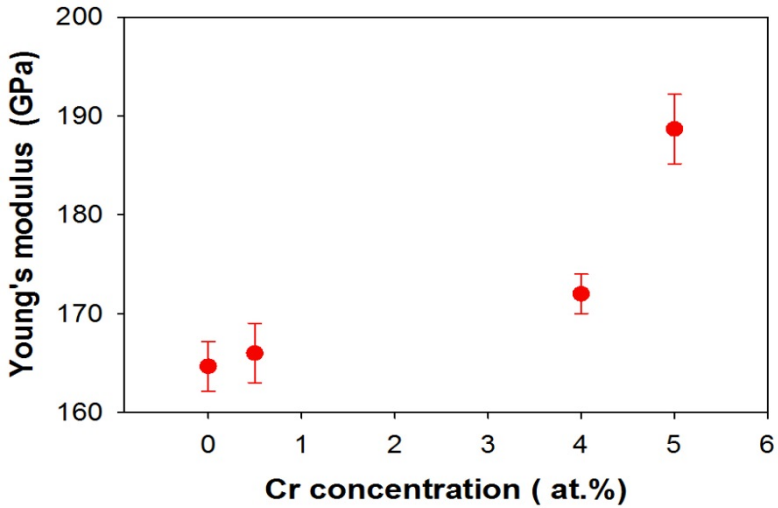

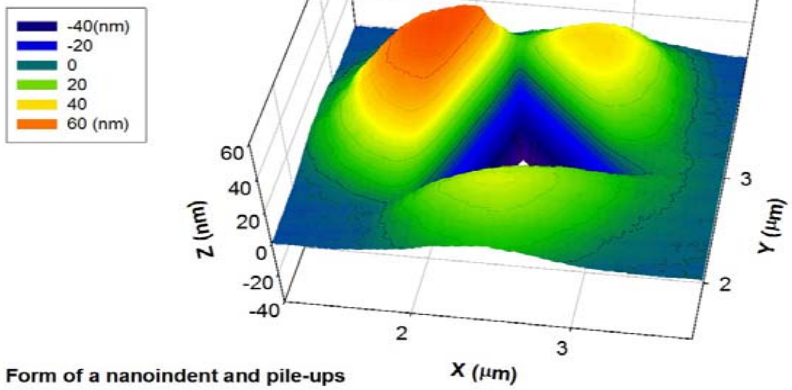

Form of a nanoindent and pile-ups

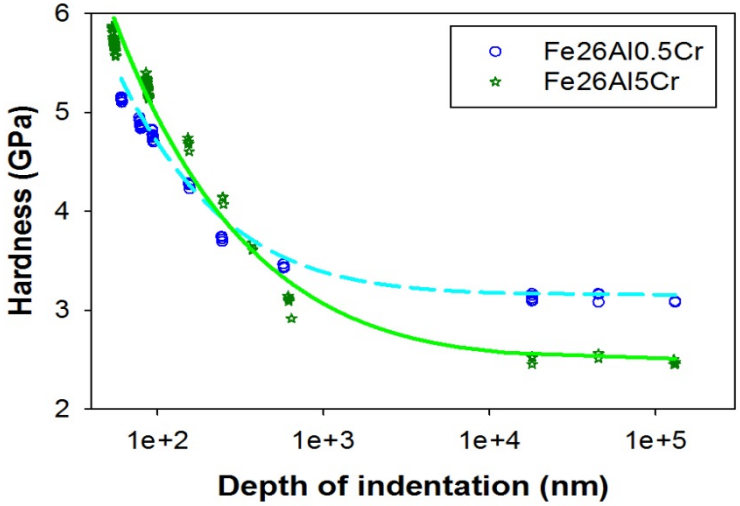

Materials Science and Methods

Intermetallics 41 (2013) 28–34

Contents lists available at SciVerse ScienceDirect

Intermetallics

journal homepage: www.elsevier.com/locate/intermet

Effect of chromium on elastic and plastic deformation of Fe_3Al intermetallics

Mohammad Zamanzade*, Horst Vehoff, Afrooz Barnoush

Saarland University, Department of Materials Science and Methods, Germany

ARTICLE INFO

Article history:
Received 1 March 2012
Received in revised form
18 April 2013
Accepted 19 April 2013
Available online 15 May 2013

Keywords:
A. Iron aluminides (based on Fe_3Al)
B. Alloy design
B. Work-hardening
B. Mechanical properties at ambient temperature
G. Environmental applications

ABSTRACT

In order to evaluate the effect of chromium concentration on the mechanical properties of single phase iron aluminum intermetallics, specifically those containing 26 at.% Al, a nano-indentation technique was used. The grain orientations of samples were revealed with the aid of Electron Backscatter Diffraction (EBSD) technique. Additionally, the surface roughness of each sample was checked after electropolishing with the aid of Atomic Force Microscopy (AFM). Finally, all nano- and micro-indents were performed within the (001) orientated grains, where the surface roughness was less than 1.06 nm on average, in all samples. The Oliver–Pharr method, with correction for pile up, was used to calculate the Young's modulus and nano-hardness for Fe_3Al–xCr alloys. Additionally, the effect of Cr on the shear stress needed for homogeneous dislocation nucleation, internal friction stress of dislocation motion (Peierls–Nabarro stress) and flow stress was studied.

1. Introduction

Among the different intermetallic alloys, iron aluminides have been widely studied since the 1930's, when their excellent oxidation resistance was first noticed [1 and 2]. The low cost, low density, good wear resistance, ease of fabrication, and resistance to corrosion and sulfidation of iron aluminides [1–6] make them very attractive as a substitute for routine stainless steels in industrial applications. Furthermore, they allow for the conservation of less accessible elements such as nickel and molybdenum, with the added benefit of a better strength to weight ratio than stainless steels.

One major limitation of Fe_3Al alloys is their poor ductility at ambient temperatures. It is now known to arise from the interaction of water vapor in the air with the aluminum on the surface of the specimen [5]. One possibility for overcoming this limitation is to alloy the Fe_3Al intermetallics with other elements. Chromium is one of the most studied elements added to the binary alloys to enhance the mechanical properties at room temperatures [6–8]. McKamey et al. [6] found that increasing the chromium concentration by up to 6 at.% improved room temperature ductility from approximately 4% to 8–10%. Moreover, they observed a difference in the character of dislocations with the addition of Cr. In order to discriminate between the effect of the microstructure and the effect of the composition, we used the Nano-Indentation (NI) technique which has opened up a new era in mechanical testing methods during the last decade. Small sample size, and an extremely small probed volume of sample during NI, allows for easy pre- and post-characterization of the samples [9 and 10]. It is now possible to nano-indent a selected crystallographic orientation to explore local plastic deformation characteristics of the sample. This technique was used earlier for calculation of different mechanical characteristics such as Young's modulus, nano-hardness [7 and 8] and also to resolve dislocation nucleation in Fe_3Al intermetallics [8]. Additionally, dislocation source activation energies [11–13], the mobility of dislocations [14] and their interactions with each other [15] can be probed by means of the NI technique.

In this paper, we present the results of nano- and micro-indentation tests on different Fe-26Al-xCr alloys to shed more light on the influence of chromium content on the interatomic bonds and characteristics of dislocations.

2. Experiments

The samples used in these experiments were made using the vacuum induction melting method. In all samples, the concentration of aluminum is kept constant at 26 at.%. The samples were cast,

* Corresponding author. Saarland University, Department of Materials Science and Methods, bldg. D2.2, Campus, D-66123 Saarbrücken, Saarland, Germany. Tel.: +49 681 302 5184; fax: +49 681 302 5015.
E-mail address: m.zamanzade@matsci.uni-sb.de (M. Zamanzade).

0966-9795/$ – see front matter © 2013 Elsevier Ltd. All rights reserved.
http://dx.doi.org/10.1016/j.intermet.2013.04.013

Symbols

A, A_c and A_{PU}	projection of the i) real contact area between tip and surface, ii) contact area determined by the Oliver–Pharr method and iii) the pile-up contact area
a_i	horizontal distance of the pile-up contact perimeter from the edge of indentation
B	bulk modulus
b	magnitude of the Burgers vector
C_{ij}	elastic constants
d_i	the vertical height of pile-up
E	young's modulus
E_r	the *reduced* Young's modulus measured by the Oliver–Pharr method
H and H_0	hardness at different depths and micro-hardness
h and h_c	measured displacement and contact depth determined by the Oliver–Pharr method
k	the distance between slip planes
L	the length of the side of the projected triangular area of Berkovich indenter
P	applied load
R	the tip radius
S	stiffness of material and relates to the slope of the load–displacement (L–D) curve at the initial unloading segment
$\alpha = 90 - \theta$	empirical constant depending on the tip shape and θ is the half angle of the tip
β	a correction factor depending on the tip geometry (1.034 for a Berkovich indenter)
φ	taylor coefficient which is between 0.1 and 0.5 depending on dislocation structures
μ and $\mu_{VRH\text{-}or\text{-}Her}$	experimentally measured and analytically calculated values of shear modulus
υ	poisson's ratio
σ_{flow}	flow stress in uniaxial tension
τ_{P-N}	friction stress
τ_{max}	maximum applied shear stress

and then cut by spark erosion, into sets of cylinders with a 12 mm diameter. Each set had a chromium concentration of 0.0, 0.5, 4.0 or 5.0 at.%. TEM measurements performed by Stein et al. [4] on several binary and ternary alloys with the same concentration of aluminum, and same history of heat treatment, show the existence of D03-ordered, single phase solid solutions at room temperature.

In order to observe homogenous dislocation nucleation (HDN) during NI, it is necessary to remove any potential heterogeneous nucleation site on the surface i.e. all surface steps had to be removed. Therefore, a surface with very low roughness was prepared by first polishing down to 1 μm with diamond slurry and then electro- polishing with a 1 M sulfuric acid-methanol solution [8] to remove mechanical damage on the surface. When examined with Atomic Force Microscopy (AFM), the average root-mean-square roughness of the samples was 1.06, 0.58, 0.65 and 0.78 nm for samples with 0.0, 0.5, 4.0 and 5.0 at.% chromium, respectively.

In order to exclude the orientation effect, Electron Backscatter Diffraction (EBSD) measurements were performed to characterize the different crystal orientations. Grains with orientations close to (001) were identified and marked by means of micro-indents. NI was performed on selected, freshly electropolished grains at room temperature. In all samples, the grain sizes were more than 500 μm in diameter, making it possible to perform tens of nano-indents on each grain. Considering the very small indentation depth, such a grain should act similar to a single crystal during nano-indentation.

We used a Hysitron TriboIndenter® with the Performech™ controller and a Berkovich and conical diamond tip to perform nano-indentation. The tip area function was defined with the conventional method of fused quartz calibrations. All nano-indents were performed with the same loading rate of 500 μN/s and unloading rate of −1000 μN/s.

3. Theory

According to the Oliver–Pharr method [16 and 17], the reduced Young's modulus can be measured by analyzing the elastic unloaded part of the Load Displacement curves as follows:

$$E_r = \beta \frac{\sqrt{\pi}}{2\sqrt{A_c}} S \tag{1}$$

The calculated E_r relates to the Young's modulus and Poisson's ratios of the sample (E and υ) and the indenter (E_T and υ_T) according to Eq. (2). For the diamond tip, one can use $E_T = 1140$ GPa and $\upsilon_T = 0.07$ based on the data supplied by the producer.

$$\frac{1}{E_r} = \frac{1-\upsilon^2}{E} + \frac{1-\upsilon_T^2}{E_T} \tag{2}$$

The nano-hardness (H) can also be measured according to Eq. (3):

$$H = \frac{P_{max}}{A_c} \tag{3}$$

where P_{max} is the maximum applied load. During NI, materials with limited elasticity accommodate the volume of the indenter by plastic flow of the material, eventually piling-up around the tip. Pile-ups change the real contact surface area and cause an over estimation of measured E or H [18]. Oliver and Pharr [19], based on the finite element simulation of nano-indents, proposed a criterion for judging the probable underestimation of the contact area due to pile-ups. According to their criterion, the pile-up effect becomes significant if the ratio of the final indentation depth (h_f) to the indentation depth at the maximum force (h_{max}) is higher than the critical value of 0.7 for a conical tip. This ad-hoc approach provides a tool for rapid judgment on the possible error in the nano-hardness and Young's modulus measurement. However, it does not provide a solution for correction of the error. The most appropriate methods to correct the pile-up effect on contact area estimation are based on imaging the indents with high spatial resolution. Kese et al. developed a method for correction of the contact area according to the topography images by aid of the following analytical formula [20 and 21].

$$A = A_c + A_{PU} = A_c + 5.915 h_c \sum a_i \tag{4}$$

According to this model, the pile-up contact area at each side of Berkovich tip is considered to have a semi-elliptical form with major axis L and minor axis a_i. a_i can be measured based on the indent's shape and L can be rewritten as a function of h_c for an "*ideal*" Berkovich tip, where $A_c = 24.56 h_c^2$ and $A_c = \sqrt{3}/4\, L^2$ for the equilateral triangle indents. This was used to find the semi-elliptical projected pile-up contact area ($\pi\, La_i/4$) for each side of the indent. Because the value of a_i varies from one side of an indent to the other, the summation of a_i for each indent side can be used to find the total pile up contact area as is stated in Eq. (4).

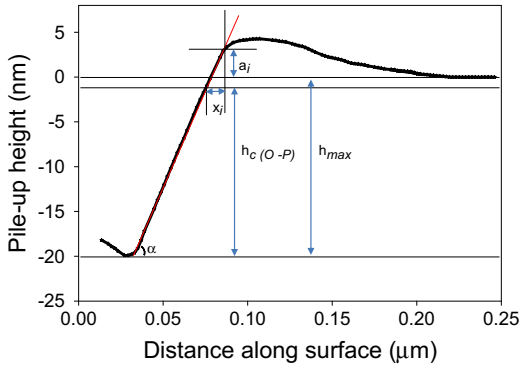

Fig. 1. The geometry of contact surface and pile-up after indentation with a Berkovich indenter.

This concept, with some optimizations, was used to correct the pile up effect in our NI data. We also assumed a semi-elliptical form for the pile-ups. The major axis L was calculated based on the A_c instead of h_c because no NI tip can be treated as an ideal Bekovich tip, and instead of a_i we used x_i, which is the projected part of pile-up, $x_i = [(h_{max} - h_c) + d_i]\cos\alpha$, where $\alpha = 90 - \theta$ was measured based on the method presented in Appendix A (Fig. 1);

$$A = A_c + 2.167\sqrt{A_c}\sum[(h_{max} - h_c) + d_i] \tag{5}$$

The experimentally measured values of Young's modulus were compared with the analytically calculated values for polycrystalline Fe_3Al samples based on the Voigt-Ruess-Hill and Hershey's homogenization methods [22]. Additionally, we calculated the material's resistance to uniform compression (B), $\mu_{VRH\text{-}or\text{-}Her}$ and υ using the following equations:

$$\mu_{VRH} = \left[\frac{1}{10}(C_{11} - C_{12} + 3C_{44}) + \frac{5C_{44}(C_{11} - C_{12})}{8C_{44} + 6(C_{11} - C_{12})}\right] \tag{6a}$$

$$64\mu_{Her}^4 + 16(4C_{11} + 5C_{12})\mu_{Her}^3 + [3(C_{11} + 2C_{12})(5C_{11} + 4C_{12}) - 8(7C_{11} - 4C_{12})C_{44}]\mu_{Her}^2 - (29C_{11} - 20C_{12})(C_{11} + 2C_{12}) \times C_{44}G_{Her} - 3(C_{11} + 2C_{12})^2(C_{11} - C_{12})C_{44} = 0 \tag{6b}$$

$$B = (C_{11} + 2C_{12})/3 \tag{6c}$$

$$E_{VRH-or-Her} = 9B\mu_{VRH-or-Her}/(3B + \mu_{VRH-or-Her}) \tag{6d}$$

$$\upsilon_{VRH-or-Her} = (3B - 2\mu_{VRH-or-Her})/[2(3B + \mu_{VRH-or-Her})] \tag{6e}$$

4. Results and discussion

Fig. 2 shows reproducible Load Displacement (L–D) curves related to the samples with different Cr concentrations. The curves start with a completely elastic deformation segment, which is followed by a displacement burst, called pop-in. The initial elastic loading begins as soon as the tip contacts the material surface and continues until Homogeneous Dislocation Nucleation (HDN) occurs [23]. The L–D curves show that an indentation test in the elastic regime probes a lateral region of, at most tens of nanometers, to the point where the pop-in is noted. Afterward, the elastoplastic deformation occurs in the rest of the loading segment.

4.1. Effect of Cr on the elastic properties

Table 1 summarizes the effect of Cr on increasing the mean values of E. Acceptable agreement is achieved between the measured and calculated (Table 2) values using the elastic constants of Fe28Al and Fe28Al6Cr single crystals reported in reference [24]. However, there is some small variation which could be due to a difference between the Al concentration in the tested sample (26 at.% with possibly slight variation) and the reference data

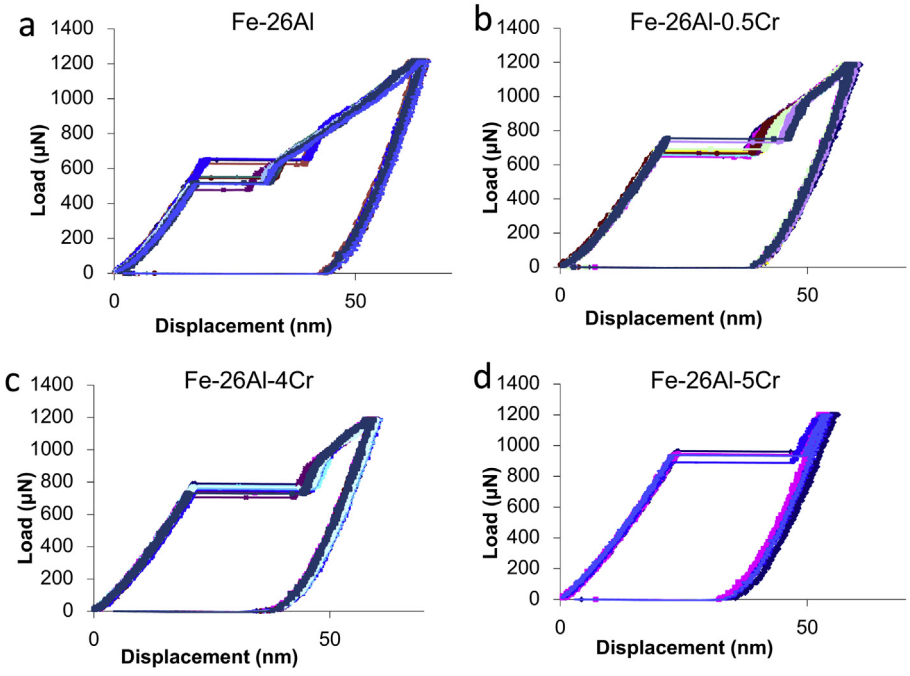

Fig. 2. Typical load-displacement curves of a) Fe26Al b) Fe26Al0.5Cr c) Fe26Al4Cr and d) Fe26Al5Cr.

Table 1
Effect of chromium on the experimentally measured values of Young's modulus, shear modulus, h_f/h_{max}, pop-in load and max shear stress (at $P_{pop\text{-}in}$).

Sample	E (GPa)	μ(GPa) $= E/2(1+\upsilon)$	h_f/h_{max}	$P_{pop\text{-}in}$ (μN)	τ_{max} (GPa)
0.0 at.% Cr	165 ± 3	63.59	0.68	567.48	3.55
0.5 at.% Cr	166 ± 3	63.77	0.65	684.33	3.80
4.0 at.% Cr	172 ± 2	66.05	0.66	750.89	4.01
5.0 at.% Cr	189 ± 4	72.52	0.62	963.28	4.64

Table 2
Effect of chromium on the analytically calculated values of bulk modulus, shear modulus, poisson's ratio and Young's modulus. The calculations were based on the elastic constants of $C_{11} = 166.36$, $C_{12} = 122.58$, $C_{44} = 130.97$ GPa for Fe28Al and $C_{11} = 188$, $C_{12} = 125.0$, $C_{44} = 126.3$ GPa for Fe28Al6Cr [24].

	Fe28Al				Fe28Al6Cr			
	B (GPa)	μ GPa)	υ	E (GPa)	B (GPa)	μ (GPa)	υ	E (GPa)
VRH	137.2	65.55	0.29	169.62	146	72.74	0.29	187.13
Hershey	137.2	66.66	0.29	172.10	146	73.94	0.28	189.78

and/or due to the anisotropy in elastic properties of Fe_3Al ($C_{11} - C_{12} \neq 2C_{44}$) [25].

As expected from the decrease in h_f/h_{max} ratios given in Table 1, with the addition of a chromium concentration, less pile-up form around the indents as shown in Fig. 3a–d. This behavior was identical after indentation with several different maximum loads. We also studied the effect of alloying element on the pile-up forms by indentation with an axisymmetric conospherical tip (Fig. 4). Here again the images show the strong effect of Cr on the reduction of pile-ups. The shapes of the emerging lobes relate to the shear direction in the material. Pile-ups generally form in the direction where glide of dislocations is easier [26 and 27]. The reduction of average values of pile-ups after addition of Cr could be due to the increase of the capability of the material to include plastic deformation i.e. how far dislocations are capable to transfer the plasticity into the material. This can be explained by considering the ease of dislocation cross slipping in the Cr enriched samples.

The effect of Cr on the E was coupled with the steadily increasing pop-in load ($P_{pop\text{-}in}$) (Table 1). The P within the elastic regime can be converted to the maximum shear stress (τ_{max}) acting below the tip inside the sample according to Eq. (7);

$$\tau_{(max)} = 0.31\left(\frac{6E_r^2}{\pi^3 R^2}P\right)^{\frac{1}{3}} \quad (7)$$

After precise measurement of the R (Appendix A), E_r, and with substitution of the $P_{pop\text{-}in}$ in Eq. (7), it is possible to calculate the maximum shear stress responsible for HDN for each alloy (Table 1). This maximum shear stress is comparable with the theoretical shear strength $\tau_{max} \approx \mu/20$ predicted by Frenkel's model [28]. By addition of Cr, the pop-load is increased, which means higher maximum shear stress beneath the nano-indenter tip is required in order to trigger the HDN process. Increase in the elastic modulus and critical shear stress with the addition of different Cr concentrations is due to the increase of the binding energy of atoms [29,30 and 8].

4.2. Effect of Cr on the hardness

The effect of Cr on the elasticity and dislocation nucleation has been discussed, but Cr also influences the hardness of the material. Hardness is defined as the resistance of a material to plastic deformation, and it is shown that the hardness is indentation depth

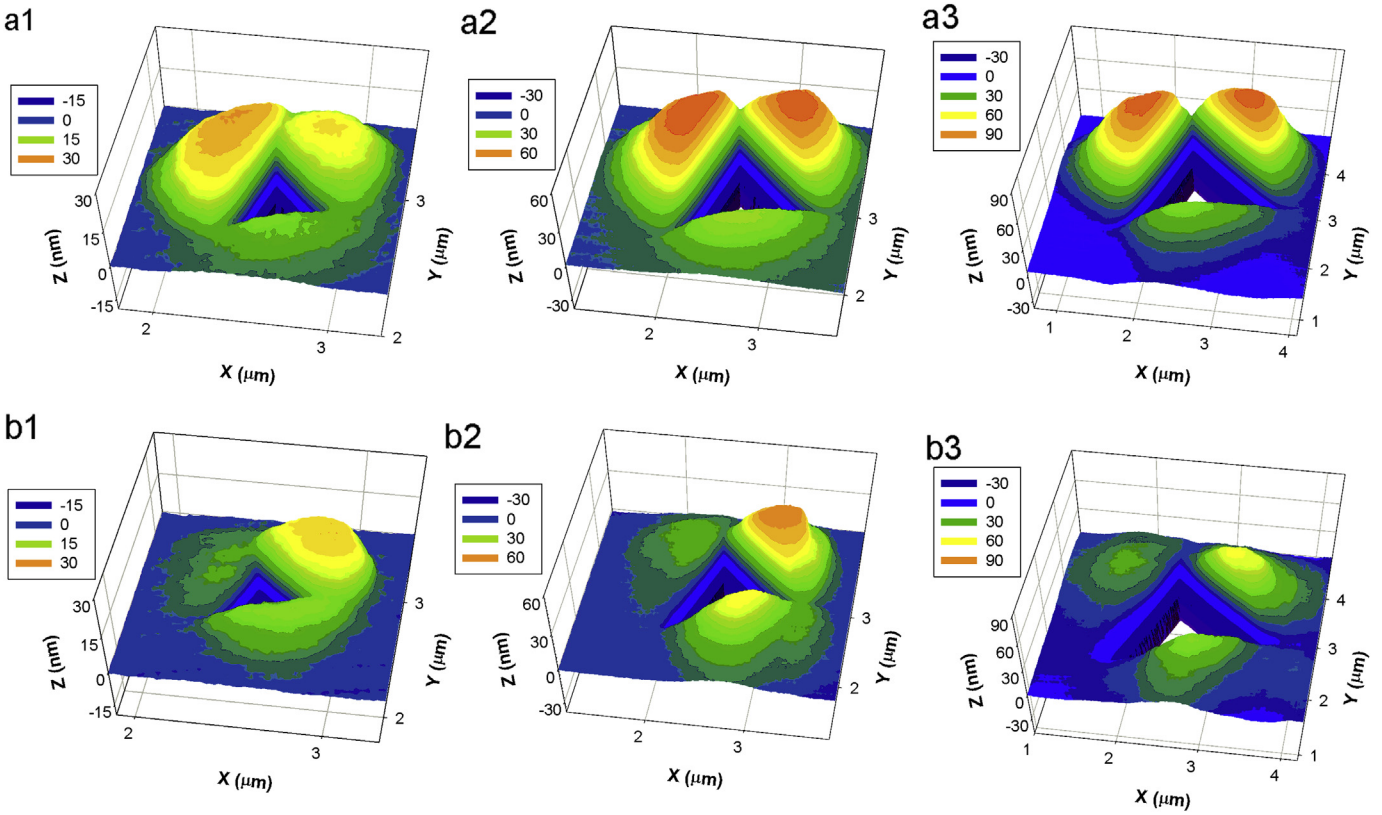

Fig. 3. The form of pile-ups in Fe26Al0.5Cr (a1–a3) and Fe26Al5Cr (b1–b3) samples. The indents were performed with a Berkovich indenter and the maximum applied load was 1200 (left), 5000 (center) and 10,000 μN (right).

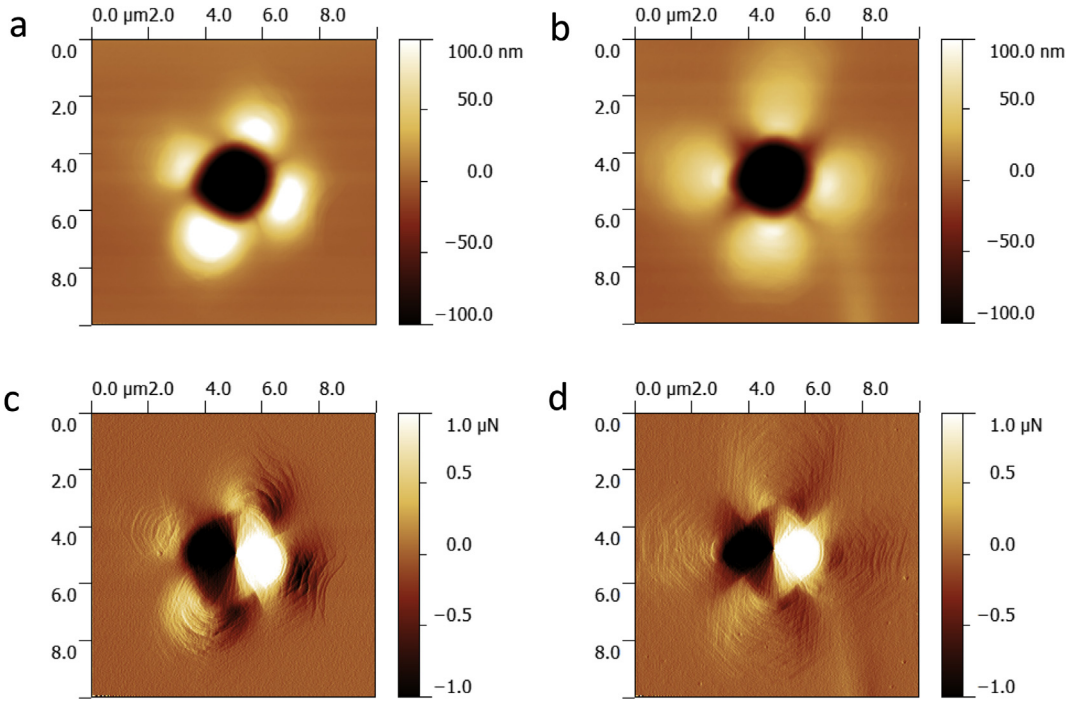

Fig. 4. Topography (above) and gradient (below) images of nano-indentations performed on Fe26Al0.5Cr (a and c) and Fe26Al5Cr (b and d) samples. The indentations were performed with a conical tip and the maximum applied load was 30 mN.

dependent i.e. the so called Indentation Size Effect (ISE) [31]. Based on Nix and Gao [31], the measured hardness relates to the indentation depth as follows:

$$H = \sqrt{9\sigma_{\text{flow}}^2 + \left[\frac{81}{2} b\mu^2\varphi^2 \tan^2\alpha\right]\frac{1}{h}} \tag{8}$$

Here, σ_{flow} is considered without inclusion of intrinsic lattice resistance. In the case of materials with high friction stress, like bcc metals or materials with covalent or ionic bonds, it is also necessary to include the effect of friction stress on the hardness (τ_{P-N}). Therefore, Eq. (8) could be modified to Eq. (9) [32 and 33].

$$H = \sqrt{9\sigma_{\text{flow}}^2 + \left[\frac{81}{2} b\mu^2\varphi^2 \tan^2\alpha\right]\frac{1}{h}} + 3\sqrt{3}\tau_{P-N} \tag{9}$$

At very large depths, where $1/h \rightarrow 0$, we will have $H_0 = 3\sigma_{\text{flow}} + 3\sqrt{3}\tau_{P-N}$and the hardness won't be depth dependent, as we can also observe in Fig. 5 where the hardness values are relatively constant. The dependency of the measured H, on the depth of indentation, in the sub-micrometer depths, up to 150 nm, fits very well with the modified Nix and Gao model when the $\tau_{P-N} = 289$ & 296 MPa is used for samples with 0.5 and 5 at.% Cr. Additionally, the flow stress of alloys can then be estimated as $\sigma_{\text{flow}} = 550$ & 360 MPa. The Taylor coefficient used was $\varphi = 0.3$, which indeed falls into the right range for φ. The τ_{P-N} could be also analytically calculated as follows [34]:

$$\tau_{P-N} = \frac{\mu(0.15 + 0.03(b/\xi k))}{(1-\upsilon)} \exp\left(\frac{-2\pi\xi k}{b}\right) \tag{10}$$

where $\xi = 1/(2(1-\upsilon))$. The calculated τ_{P-N} for the samples with 0, 0.5, 4 and 5 at.% Cr were 0.280, 0.280, 0.294 and 0.320 GPa, respectively, based on the values reported in reference [8] and are in agreement with the fitted values.

All in all, the results show the incremental increase of τ_{P-N} and a decrease of σ_{flow} with Cr addition. The increase of τ_{P-N} is mainly due to the influence of Cr on shear modulus and the strengthening of interatomic bonds after Cr addition, as discussed earlier. For the majority of materials, micro-hardness scales linearly with elastic shear modulus (or τ_{P-N}) for a given bonding type (covalent, ionic or metallic) [35]. However, as the results show, with addition of the Cr to the Fe26Al, the relationship no longer holds. Alloys with 5 at.% Cr have less micro-hardness, although the shear modulus increases. The reason could be the strong influence of Cr on the σ_{flow}. The decrease of flow stress relates to the least strongly pinned segments in dislocations. Once these pinned segments become mobile, plastic deformation spreads by the mitigation of kinks, which could

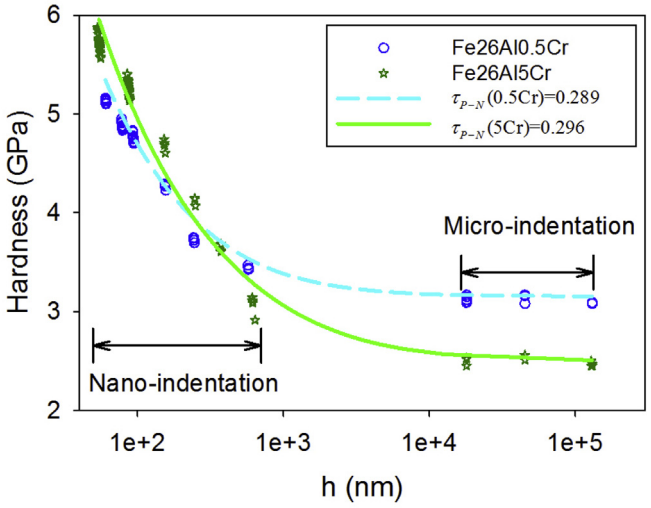

Fig. 5. a) The changes in hardness (H) at different indentation depths.

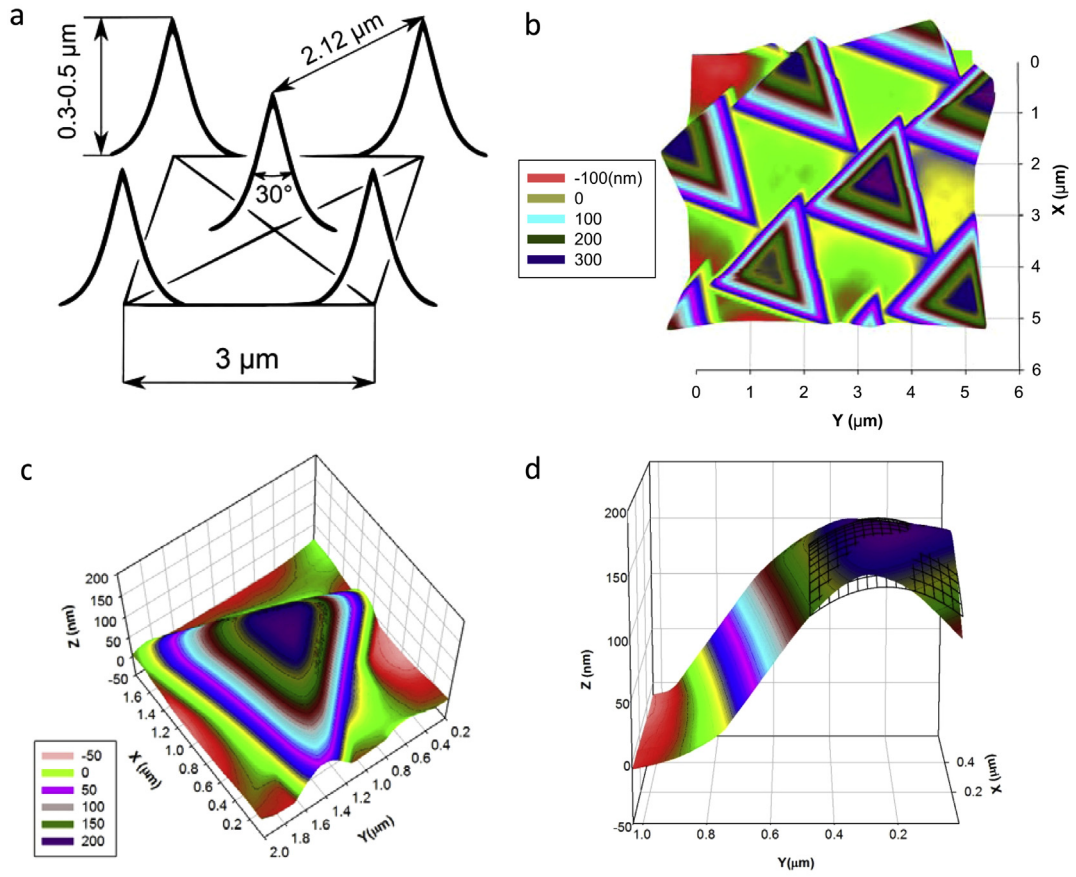

Fig. 6. a) The commercial calibration silicon grating (TGT01 from NT-MDT Inc.,) b and c) Typical 3D shape of a Berkochich tip. d) Spherical form of a Berkovich indenter at its tip which can be fitted with a sphere (grid structure). The standard error of estimation was 5.3449.

also be the reason for the decreased height of pile-ups and wide spreading slip lines in the Cr enriched alloys shown in Figs. 3 and 4.

5. Conclusion

In this paper, the effects of Cr addition on elastic and plastic properties of the Fe-26Al-*x*Cr intermetallic alloys were studied. For this, the nano-indentation technique was used due to: (i) small volume of the sample required to make indentation within the single grain. (ii) Fast and reproducible results in the case of the properly prepared samples. (iii) Imaging possibility of the system for pre- and post-indentation analysis of the surface. The results show the effect of chromium on the increase of the Young's modulus, maximum shear stress for homogeneous dislocation nucleation and friction stress in Fe_3Al intermetallics. All of which is due to the effect of chromium on the enhancement of interatomic bonds. Additionally, Cr decreases the σ_{flow} and eases the cross slipping of dislocations. This conclusion was confirmed with the influence of Cr on the reduction of the pile-up heights.

Future works are planned to evaluate the mechanical properties of the different crystallographical orientations as well as the influence of Cr on environmental embrittlement of iron-aluminums.

Acknowledgment

The authors wish to thank Dr. M. Palm of Max Planck Institute Eisenforsch GmbH. for supporting the materials, Prof. Christian Motz for his advice and help, Anna Lynn Maxfield for proofreading and DFG for financial supports.

Appendix A

In a completely new approach, we measured the real shape of our nano-indentation tip (R) using reverse tip imaging. A commercial calibration silicon grating, (TGT01 from NT-MDT Inc., Fig. 6a) having spikes with 10 nm radius, is imaged by a Hysitron Tribo-Indenter with in-situ imaging ability. The resulted image is shown in Fig. 6b and c. Scanning a nanoindenter tip over these structures provides an inverted image of the nanoindentor tip, yielding a mirror image of the tip shape, because the tip radius is almost 100 times larger than the spikes radius. An unwanted change in the shape of the tip could easily be observed as a consequence of tip deterioration or contamination.

A sphere was fitted to the Berkovich tip image at half of the total elastic displacement before pop-in, because, as it is shown in [36], "the depth of the circle of contact beneath the specimen's free surface is half of the total elastic displacement". The calculated tip radius with this method was 1.47 μm (Fig. 6d), which was used as the tip radius for the calculation of the maximum shear stress needed for HDN (Table 1).

References

[1] Ziegler NA. Resistance of iron-aluminum alloys to oxidation at high temperatures. Am Inst Mining Met Engr, Inst Metals Division 1932;6. Tech. Pub. No. 450.
[2] Sykes C, Bampfylde J. The physical properties of iron-aluminium alloys. J Iron Steel Inst 1934;130:389–410.
[3] Kimurat Y, Pope DP. Ductility and toughness in intermetallics. Intermetallics 1998;6:561–71.

[4] Stein F, Schneider A, Frommeyer G. Flow stress anomaly and order-disorder transitions in Fe_3Al-based Fe-Al-Ti-X alloys with X = V, Cr, Nb, or Mo. Intermetallics 2003;11:71–82.
[5] Alven DA, Stoloff NS. The influence of composition on the environmental embrittlement of Fe_3Al alloys. Mater Sci Eng A 1997;239–240:362–8.
[6] McKamey CG, Horton JA, Liu CT. Effect of chromium on properties of Fe_3Al. J Mater Res 1989;4:1156–63.
[7] Frutos E, Morris DG, Muñoz-Morris MA. Evaluation of elastic modulus and hardness of Fe–Al base intermetallics by nano-indentation techniques. Intermetallics 2013;38:1–3.
[8] Barnoush A, Zamanzade M. Effect of substitutional solid solution on dislocation nucleation in Fe_3Al intermetallic alloys. Philos Mag 2012;92:3257–68.
[9] Zaafarani N, Raabe D, Singh RN, Roters F, Zaefferer S. Three-dimensional investigation of the texture and microstructure below a nanoindent in a Cu single crystal using 3D EBSD and crystal plasticity finite element simulations. Acta Mater 2006;54:1863–76.
[10] Vehoff H, Yang B, Barnoush A, Natter H, Hempelmann R. Mechanical properties of nanomaterials examined with a NI-AFM. Phys Chem 2008;222:499–525.
[11] Barnoush A, Vehoff H. Hydrogen embrittlement of aluminum in aqueous environments examined by in situ electrochemical nanoindentation. Scripta Mater 2008;58:747–50.
[12] Barnoush A, Vehoff H. In situ electrochemical nanoindentation of a nickel (111) single crystal: hydrogen effect on pop- in behaviour. Int J Mat Res 2006;97:1224–9.
[13] Barnoush A, Dake J, Kheradmand N, Vehoff H. Examination of hydrogen embrittlement in FeAl by means of in situ electrochemical micropillar compression and nanoindentation techniques. Intermetallics 2010;18:1385–9.
[14] Barnoush A, Welsch MT, Vehoff H. Correlation between dislocation density and pop-in phenomena in aluminum studied by nanoindentation and electron channeling contrast imaging. Scripta Mater 2010;63:465–8.
[15] Barnoush A. Correlation between dislocation density and nanomechanical response during nanoindentation. Acta Mater 2012;60:1268–77.
[16] Golovin Y. Nanoindentation and mechanical properties of solids in submicrovolumes, thin near-surface layers, and films: a Review. Phys Solid State 2008;50:2205–36.
[17] Oliver WC, Pharr GM. An improved technique for determining hardness and elastic modulus using load and displacement sensing indentation experiments. J Mater Res 1992;7:1564–83.
[18] Fischer-Cripps AC. Critical review of analysis and interpretation of nanoindentation test data. Surf Coat Tech 2006;200:4153–65.
[19] Oliver WC, Pharr GM. Measurement of hardness and elastic modulus by instrumented indentation: advances in understanding and refinements to methodology. J Mater Res 2003;19:3–20.
[20] Kese K, Li ZC. Semi-ellipse method for accounting for the pile-up contact area during nanoindentation with the Berkovich indenter. Scripta Mater 2006;55:699–702.
[21] Kese KO, Li ZC, Bergman B. Method to account for true contact area in soda-lime glass during nanoindentation with the Berkovich tip. Mater Sci Eng A 2005;404:1–8.
[22] Friák M, Deges J, Krein R, Frommeyer G, Neugebauer J. Combined ab initio and experimental study of structural and elastic properties of Fe_3Al-based ternaries. Intermetallics 2010;18:1310–5.
[23] Barnoush A, Vehoff H. Recent developments in the study of hydrogen embrittlement: hydrogen effect on dislocation nucleation. Acta Mater 2010;58:5274–85.
[24] Kral F, Schwander P, Kostorz G. Superdislocations and antiphase boundry energies in deformed Fe_3Al single crystals with chromium. Acta Metall Mater 1997;45:675–82.
[25] Morris DG, Muñoz-Morris MA, Requejo LM. Work hardening in Fe-Al alloys. MSE 2007;A460-461:163–73.
[26] Zambaldi C, Roters F, Raabe D, Glatzel U. Modeling and experiments on the indentation deformation and recrystallization of a single-crystal nickel-base superalloy. Mater Sci Eng A 2007;454–455:433–40.
[27] Zambaldi C, Raabe D. Plastic anisotropy of c-TiAl revealed by axisymmetric indentation. Acta Mater 2010;58:3516–30.
[28] Frenkel J. Zur Theorie der Elastizitätsgrenze und der Festigkeit kristallinischer Körper. Z Phys 1926;37:572–609.
[29] Rose J, Smith J, Ferrante J. Universal features of bonding in metals. Phys Rev B 1983;28:1835–45.
[30] Rose J, Smith J, Guinea F, Ferrante J. Universal features of the equation of state of metals. Phys Rev B 1984;29:2963–9.
[31] Nix W, Gao H. Indentation size effects in crystalline materials: a law for strain gradient plasticity. J Mech Phys Solids 1998;46:411–25.
[32] Qiu X, Huang Y, Nix WD, Hwang KC, Gao H. Effect of intrinsic lattice resistance in strain gradient plasticity. Acta Mater 2001;49:3949–58.
[33] Feng G, Nix WD. Indentation size effect in MgO. Scripta Mater 2004;51:599–603.
[34] Nabarro FRN. Theoretical and experimental estimates of the Peierls stress. Philos Mag A 1997;75:703–11.
[35] Krenn CR. The ideal strength and mechanical hardness of solids. Ph.D. thesis. Ernest Orlando Lawrence Berkeley National Laboratory; 2000.
[36] Fischer-Cripps Anthony C. The IBIS handbook of nanoindentation. Fischer-Cripps Laboratories Pty Ltd; 2009.

Paper C

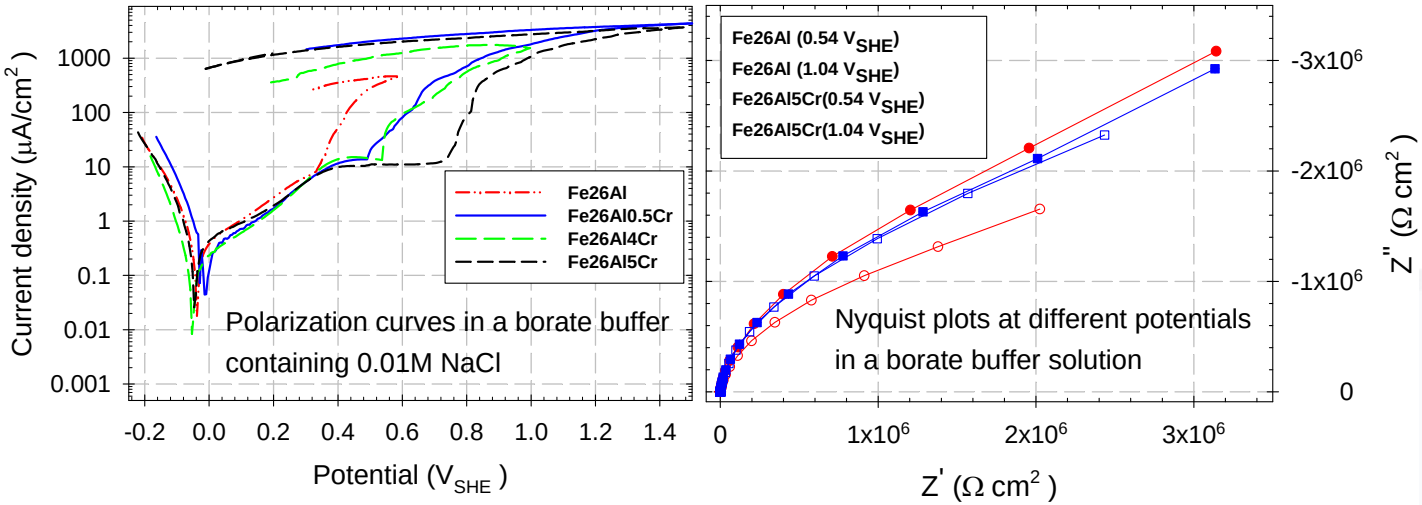

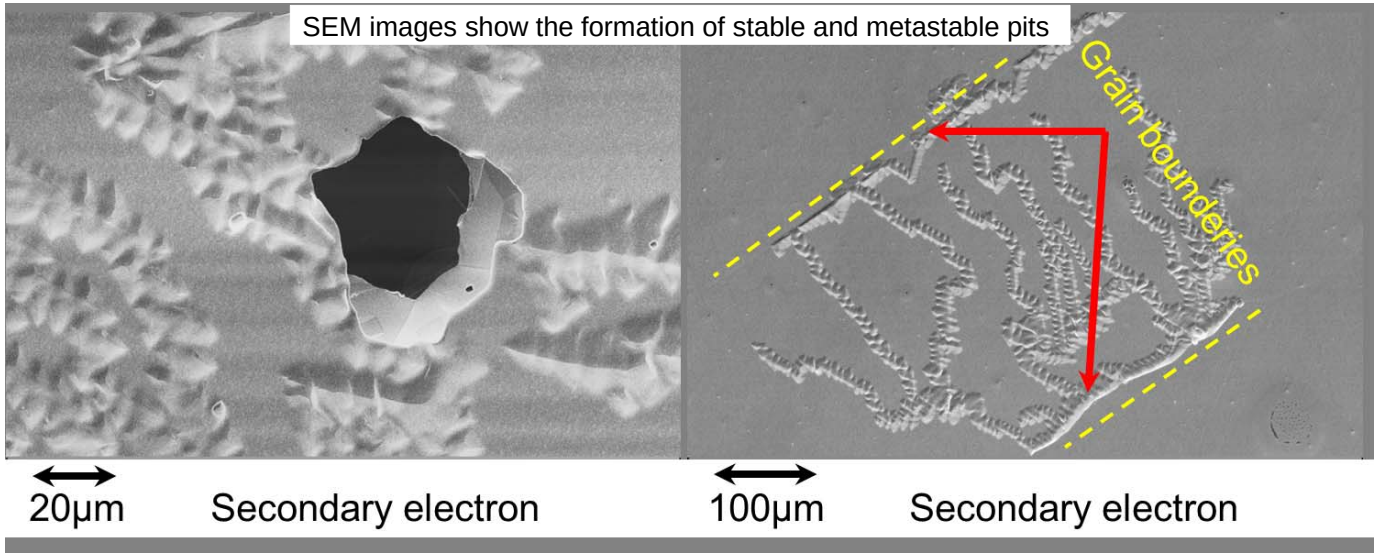

Materials Science and Methods

Corrosion Science 78 (2014) 223–232

Contents lists available at ScienceDirect

Corrosion Science

journal homepage: www.elsevier.com/locate/corsci

Effect of chromium on the electrochemical properties of iron aluminide intermetallics

Mohammad Zamanzade [a], Afrooz Barnoush [a,b,*]

[a] Department of Materials Science, Saarland University, D-66041 Saarbrücken, Germany
[b] Department of Engineering Design and Materials, Norwegian University of Science and Technology, No-7491 Trondheim, Norway

ARTICLE INFO

Article history:
Received 4 April 2013
Accepted 2 October 2013
Available online 15 October 2013

Keywords:
A. Intermetallics
B. EIS
B. SEM
C. Passivity
C. Pitting corrosion
C. Hydrogen embrittlement

ABSTRACT

The effect of chromium content on the electrochemical properties of Fe_3Al intermetallics is examined. The susceptibility of alloys to pitting and crevice corrosion in solutions with different concentrations of Cl^- ions was studied with the aid of cyclic polarization and galvanostatic methods. The form of the pits, and their concentration on different crystal orientations, was evaluated with the Scanning Electron Microscopy (SEM) and Electron Backscatter Diffraction (EBSD) techniques. Additionally, Electrochemical Impedance Spectroscopy (EIS) and the Mott–Schottky (MS) methods were used to characterize the passive film. The results show the beneficial effect of Cr for corrosion and hydrogen embrittlement resistance.

1. Introduction

Among the different possible ordered superstructures of aluminium and iron, Fe_3Al and FeAl with D03 and B2 structures attract the most interest due to their reasonable strength and toughness in vacuum and oxidizing atmospheres [1–9]. The other major driving force for the usage of Fe–Al intermetallics is the low cost of production for such a low-density material. Remarkable enrichment of aluminium within the passive film [6] plays a beneficial role on the passivation of iron–aluminium intermetallics. This layer is best in near neutral and Cl^- free solutions [1,2], and it maintains its desirable oxidation resistance at high temperatures [3–5]. However, there are barriers that limit the wide usage of binary alloys at room temperatures which are their low ductility in atmospheres containing H_2 or water vapour [10,11] and high sensitivity to localized (pitting and crevice) corrosion in Cl^- containing solutions [1].

One potential way to overcome these problems is the addition of alloying elements to the binary alloys. Chromium, in general, is a very good candidate for enhancement of the physico-chemical properties of the barrier oxide layer in iron base alloys [12,13]. The passive layer formation on Fe–Cr alloys under electrolytic conditions arises by simultaneous oxidation of the Fe and Cr. Coupled with selective dissolution of Fe, it enriches the chromium on the surface [14–16]. The constructive effect of Cr on the passive behaviour of Fe–Al–Cr intermetallics was shown earlier in [17,18]. Cr doped intermetallics have the tendency to broaden the passivation region and reduce the sensitivity of alloys to pitting corrosion in the Cl^- containing solutions. Additionally, the beneficial effect of Cr on the mechanical properties [19,20] and the reduction of hydrogen embrittlement of Fe_3Al intermetallics was observed [11]. In this study, we added different concentration of Cr to the Fe_3Al intermetallics where the Al concentrations remained constant at the 26 at.%. Our target is more an in-depth analysis of the effect of variation in the Cr content in order to gain a detailed understanding of the influence of Cr on corrosion processes. The electronic behaviour, thickness and effective capacitance of the passive layer were characterized with different electrochemical methods, and additionally the resistance of alloys to pitting and crevice corrosion was studied.

2. Experimental

2.1. Sample and solution preparation

The samples used in these experiments were made using the vacuum induction melting method. In all samples the concentration of aluminium remained constant at 26 at.%. The samples with different concentrations of chromium (0.0, 0.5, 4.0, and 5.0 at.%) were cut by spark erosion into cylinders with a 12 mm diameter. The working surface was ground with emery paper to 4000 grit.

* Corresponding author at: Department of Engineering Design and Materials, Norwegian University of Science and Technology, No-7491 Trondheim, Norway. Tel.: +47 735 93807; fax: +47 735 94129.
E-mail address: afrooz.barnoush@ntnu.no (A. Barnoush).

0010-938X/$ - see front matter © 2013 Elsevier Ltd. All rights reserved.
http://dx.doi.org/10.1016/j.corsci.2013.10.002

Afterward, the samples were cleaned first by double distilled water and then by being submerged for ten minutes in an ethanol ultrasonic bath prior to testing.

All solutions were made from analytical-grade reagents and double distilled water. A borate buffer (H_3BO_3[0.3 M], $Na_2B_4O_7 \cdot 10H_2O$[0.075 M]) with the pH of 8.4 was used for cyclic-polarization, electrochemical impedance and capacitance measurements. Sodium chloride of various concentrations was added to the borate solutions for polarization and galvanostatic measurements. All tests were carried out at ambient condition.

2.2. Electrochemical measurement

A conventional three-electrode electrochemical flat cell inside a Faraday cage was used for performing the electrochemical tests. The surface area of specimens after installation in the cell was 0.92 cm^2. A saturated KCl, Ag/AgCl reference electrode was connected to the cell through a Luggin capillary. All potentials are converted and reported in this paper vs standard hydrogen electrode (SHE). A platinum foil with the surface area of 4 cm^2 was used as the counter electrode. The DC and AC tests were performed using a Zahner IM6ex electrochemical testing system. In the case of DC tests, the working electrodes were left to stabilize at its free corrosion potential for one hour before starting experiments. We approximated the maximum allowed applied scan rate (υ_{max}) for polarization tests based on the method defined by Scully [21]:

$$\upsilon_{max} = \frac{\pi}{10}[\Delta E_{pp} f_{max}] \quad (1)$$

where ΔE_{pp} is the peak to peak voltage excitations in the EIS tests, $f_{max} = 1/[2\pi\, C_{dl}(R_s + R_P)]$, C_{dl} is the double layer capacitance, R_s is the solution resistance and R_P is the polarization resistance. All these parameters could be calculated through the concepts of impedance and the Bode-phase curves. At the scan rates below υ_{max} the capacitors remain fully charged and the current/voltage relationship reflects only the interfacial corrosion process. Here we applied the maximum allowed sweep rate of 1.5 mV/s. Additionally, galvanostatic anodic current of 1 mA/cm^2 was applied to the samples submerged in borate buffer +0.01 M NaCl solution in order to check the mechanism of pitting and density of pits in different crystal orientations. Slew rate of the start phase was driven by the 1 mA/s.

EIS measurements were performed at different potentials from 0.54 up to1.04 V_{SHE} with 100 mV steps and frequencies from 20 kHz to 2 Hz with voltage amplitude ±10 mV. The 0.54 V_{SHE} refers to the potential with the stable passive layer and 1.04 V_{SHE} is just below the oxygen evolution potential. The EIS measurements were performed after reaching the steady-state current at each potential i.e. after c.a. 1 h. The validity of all the EIS results were tested with the Kramers–Krönig transformation in order to check the three requirements formulated for the constraints of the linear system theory (LST) i.e. causality, linearity and stability [22–25].

Mott–Schottky (MS) tests were performed by stepping the potential in the positive direction from 0.04 V_{SHE} to 1.04 V_{SHE} in 50 mV increments. The impedance was measured at one particular frequency after each 50 mV change of potential. The potential was then stepped and held at the film formation potential until the steady-state current was achieved. A total of three different frequencies were employed: 1000, 700 and 500 Hz.

2.3. Surface characterization

After application of the defined anodic current for 10 and 600 s the morphology of metastable and stable pits, and their density, were studied with the aid of Zeiss ΣIGMA™-VP Field Emission Scanning Electron Microscopes (FE-SEM) equipped with an Energy Dispersive X-ray (EDX) and EBSD detectors. EDX analysis was performed with the brand new large area (20 mm^2) Silicon Drift Detectors X-Max 20 SDD with Inca Energy 450 software package from Oxford Instruments, UK. Spectral resolution for these detectors is better than 129 eV. Additionally, Oxford AZtec® EBSD system combined with Nordlys hardware was used for performing EBSD measurements.

Band contrast (BC) maps from the EBSD measurements were used to characterize the density of the pits. BC is an electron backscatter patterns (EBSP) quality factor derived from the Hough transformation that describes the average intensity of the Kikuchi bands with respect to the overall intensity within the EBSP [26]. Since EBSPs along the topographical features, like grain boundaries and pits on the surface, tend to show poor BC, therefore they can be easily distinguished in the BC map.

The samples were prepared for EBSD with electropolishing of samples with 1 M sulphuric acid in a methanol solution for 10 s. This is to remove damage imparted to the specimen surface by the grinding and polishing and corrosion products after performing electrochemical tests. Electropolishing, however, changes the form of pits and removes the sharp edges of the pits. Hence, to correlate between the crystallographic characteristics of pits and their form, some pits were characterized first with SEM directly after galvanostatic measurements and then the crystallographical plane of the pits were studied with EBSD after electropolishing of the corroded samples.

3. Results and discussion

3.1. Passivity break down and pitting corrosion

3.1.1. Electrochemical DC measurements

Representative polarization curves are displayed in Fig. 1 for different intermetallics in solutions with various concentrations of Cl^-. In the borate solution with the pH of 8.4, the surface of all alloys apparently passivated. The corrosion potential was located at approximately −0.1 V_{SHE} and the transpassive potentials began around 1.1 V_{SHE}. The strong increase of the current at higher potentials correlates with the oxidation of the water and evolution of the oxygen on the surface. The current that we measured during the polarization in the passive range was less than 10 μA/cm^2 and is due to the presence of defects in the oxide film. Existence of defects makes the composition of the passive layer nonstoichiometric and increases its conductivity [22]. However, the low electrical conductivity of the passive layer indicates that the redox reactions seem to be almost blocked. The measured current density in the passive region is in the same range as passivation current densities for pure iron or aluminium in a similar electrolyte [1,27–29]. The small deviation from the pure metals is due to the coexistence of iron, aluminium and chromium oxides on the intermetallic alloys. Existence of a mixture of Fe–Al [2] and Fe–Al–Cr [11] oxide was observed on the passive layer formed on binary and ternary intermetallics using the XPS technique.

Increasing the Cl^- concentration to 0.001 M did not change the corrosion potential of the air formed passive layer, the current density in the passive range and the transpassive potential. Although, at higher potentials, where oxygen evolution was taking place on the surface, the local destruction of the passive layer happened independent of the Cr concentration and the alloys failed to repassivate again after reversing the polarization. The breakdown of the passive film can occur by either mechanical or electrical forces. The chloride ions are not necessary for damage to the passive film to occur [30]. However, the initiation of pits requires Cl^- ions, in addition to the application of a potential higher than pitting potential. As was shown here, the role of Cl^- may be to prevent the repassivation of the intermetallics after transpassive potential.

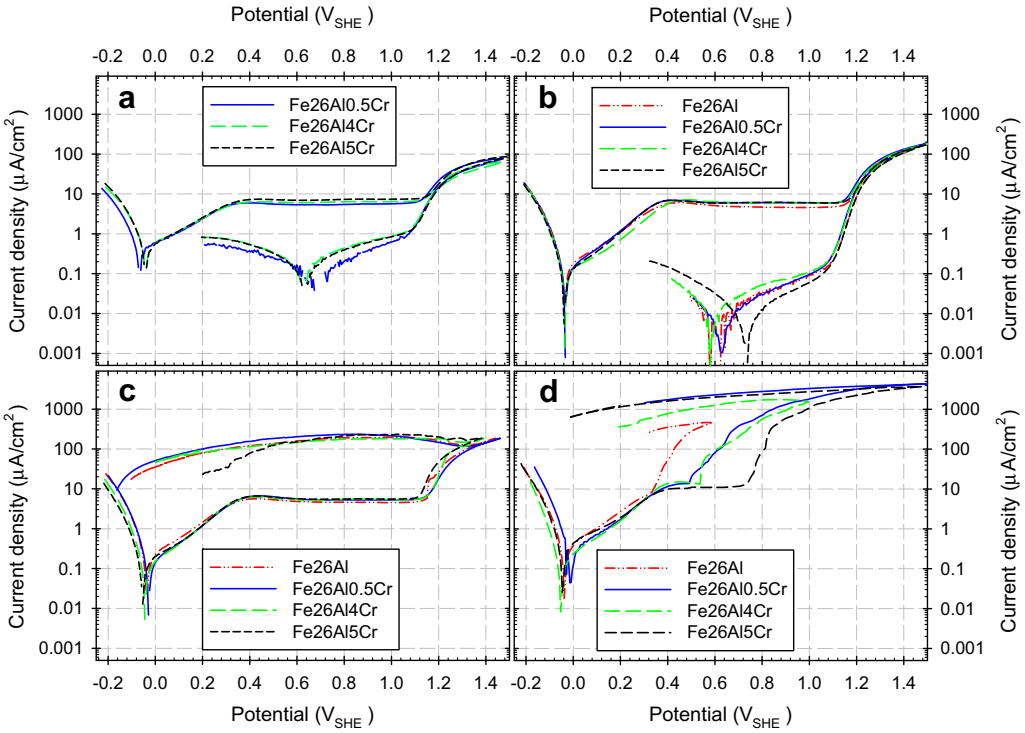

Fig. 1. Potentiodynamic polarization curves of Fe–26Al alloys with different concentration of Cr in borate buffer (a) without Cl^-, (b) with 0.0001 M NaCl, (c) with 0.001 M NaCl and (d) with 0.01 M NaCl.

In the borate buffer +0.01 M NaCl, we observed a steep current increase and passivity breakdown for all alloys at the potentials below the occurrence of oxygen evolution. The passive range achieved was only about 300 mV in the sample with 5 at.% of Cr, and decreased with any reduction of the chromium content in the intermetallics.

Polarization curves performed in solutions with 0.001 and 0.01 M NaCl (Fig. 1 c and d) show that after reversing the scanning potential, the materials fail to obtain repassivation; the anodic current remained very high and the hysteresis loops closed at low potentials. It is the polarization characteristics for electrodes susceptible to crevice and pitting simultaneously, since crevices are more difficult to passivate than pits. Crevice corrosion, which develops in shielded areas at specimen/holder interface during potentiodynamic measurements, was clearly identified in the SEM images (Fig. 2).

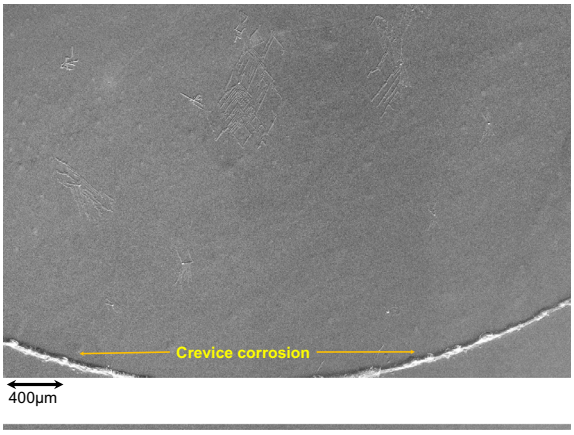

Fig. 2. (a) Secondary electron SEM image shows existence of crevice corrosion in the Fe26Al4Cr intermetallic after polarization measurement.

3.1.2. Surface characterization

Because of the very high sensitivity of all Fe_3Al–xCr intermetallics to crevice corrosion, it makes it very difficult to differentiate between two samples or conditions with only a minor difference in the expected pit resistance. As was proposed by Frangini and De Cristofaro [31], to limit crevice corrosion, and study more carefully the effect of chromium concentration on pitting behaviour, we used the galvanostatic polarization method. On the basis of the results, we observed significant reduction in crevices and more homogeneous distribution of pits in the samples but, unfortunately, it did not hinder it completely. The process of pitting corrosion, in general, acidifies the pit solution due to hydrolysis of dissolving metal ions [32,33]. However, the buffer capability of the borate solution prevents a rapid change in local pH of the solution but it does not hinder it completely [34,35]. Ions like Cl^- are carriers of current flow and hence will concentrate around the pits. This establishes the gradients in solution composition and electrode potential, which maintains the metal surface inside the pit in an active state in contrast to the passive state outside. As it is shown in Fig. 3, this process makes the pits deeper and deeper.

The pits formed on all samples had crystallographic characteristics. The sides of the pits were composed of sharply defined facets and steps (Fig. 4). With the aid of the EBSD technique, it is shown that the pit's growth direction is parallel with the {1 1 0} crystallographic direction. In the D03 structure of Fe_3Al intermetallics, the {1 1 0} close packed planes have thermodynamically lower surface energy because fewer bonds would be broken per unit area when the new surface is formed. This is the reason for the ease of pit nucleation in these planes, in comparison with the other low indices planes.

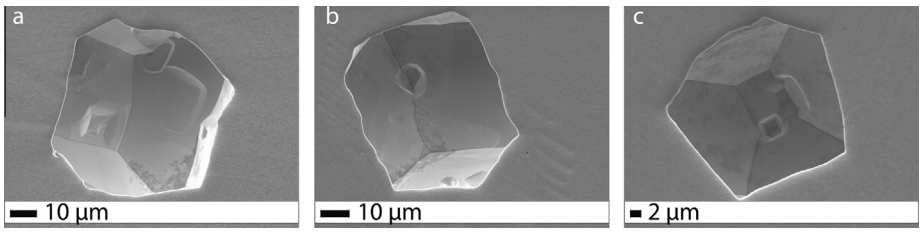

Fig. 3. Secondary electron SEM image show initiation of new pits inside the pre-exciting pits due to the gradients in solution composition and/or electrode potential.

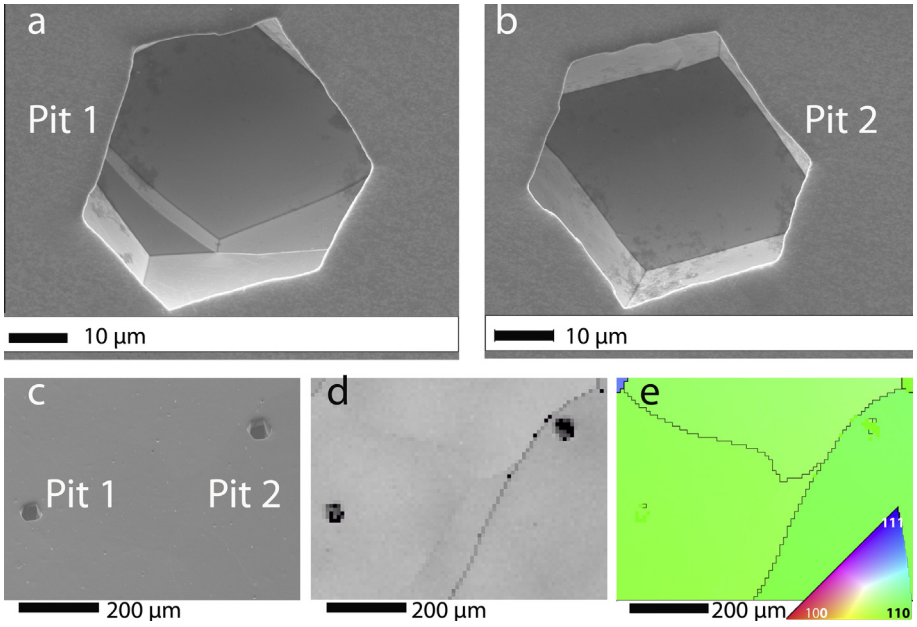

Fig. 4. Secondary electron SEM image of two different pits with sharp edges in the Fe26Al0.5Cr intermetallic before electropolishing (a and b) and after electropolishing (c). Band contrast (d) and EBSD (e) images show the grain boundaries and grain orientations.

Based on the EBSD measurement (Fig. 5), strong localization of pits in special orientation or grain boundaries was not seen in any of the samples. However, it seems that the {1 1 0} oriented grains have slightly more pit density than other orientations. Therefore, the easy nucleation of pits in the {1 1 0} plane does not guarantee localization of pits in the {1 1 0} orientation, due to the influence of some other parameters like (i) misorientation between the oxide film and metal substrate, (ii) the competitive rate of film dissolution and formation, in different crystal orientations and (iii) chloride content in the passive film; more detailed information about the density of pits in different materials is presented in Refs. [36–38].

However, the effect of Cr on the reduction of the density of pits is clearly shown in Fig. 6. In addition to faceted holes, metastable

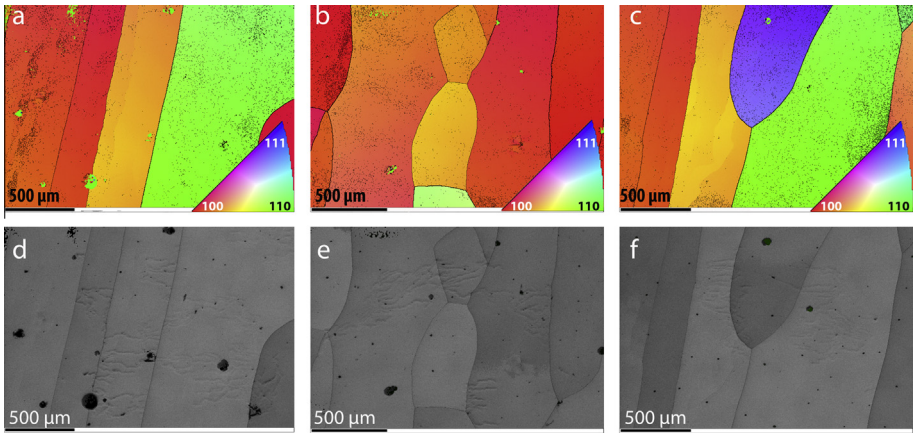

Fig. 5. EBSD (a–c) and band contrast (d–f) images in the Fe26Al5Cr intermetallic show the initiation of pits in both inter- and trans-granular sites. The corrosion pits are the black circles in the images (d–f).

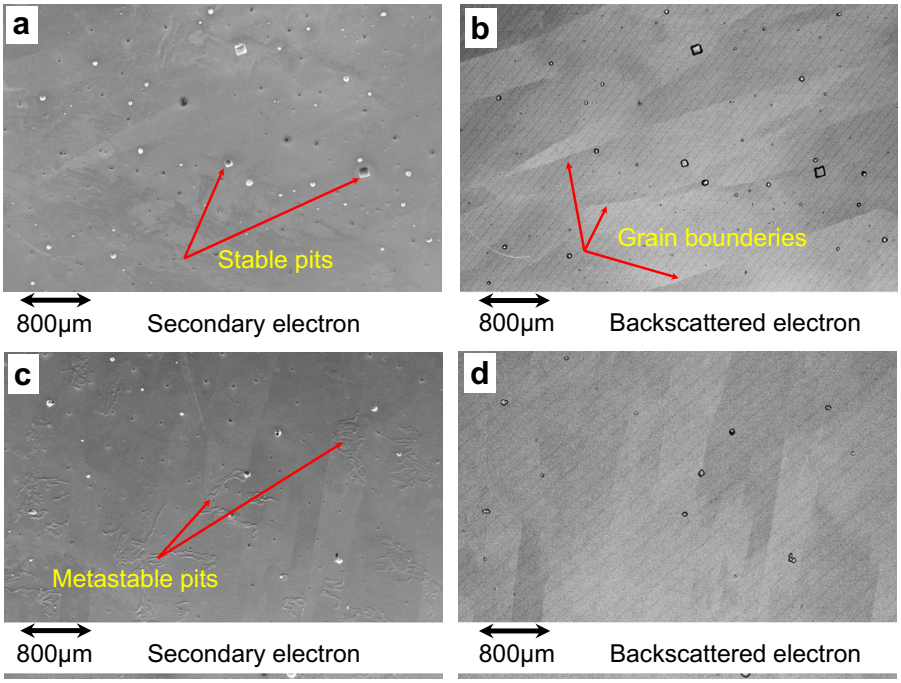

Fig. 6. Secondary electron (left) and Backscattered electron (right) SEM images after 600 s, application of galvanostatic anodic current of 1 mA/cm^2. The images show the reduction of the density of pits with increment of Cr concentration from 0.5 at.% Cr (a and b) to 5 at.% Cr (c and d).

pits with percolation-cluster-like patterns were also observed (Fig. 7). We observed higher density of the percolation patterns in samples with higher concentrations of Cr. Fig. 7b shows that the growth of clusters also happened frequently on grain boundaries.

The first impression from these metastable pits is that they are formed on the surface of the sample due to the concentration inhomogeneity, but, as it is shown in Fig. 8, homogeneous distribution of the different alloying elements is proved by quantitative chemical analysis, performed by energy dispersive X-ray spectroscopy (EDX), at five different places. A known flaw is that the resolution of the EDX is only accurate within a volume of several micrometres, depending on the acceleration voltage. Therefore, any micro-segregation of elements within a volume smaller than a few micrometres is undetected by this method. However, the size and spreading pattern of the metastable pits are far above the EDX resolution and this confirms that the formations of these patterns are not due to the composition variation within the alloy. TEM measurements performed by Stein et al. [39] on several binary and ternary alloys with the same concentration of aluminium, and same history of heat treatment, confirm the existence of D03-ordered, single phase solid solutions at room temperature.

The metastable pit perimeter, as shown in Fig. 7, is irregular and distinct growth regions are formed which propagate in the metal film. Higher density of the metastable pits in Cr doped samples could be due to the effect of Cr on the increment of the transpassive potentials. The initiation, growth and repassivation of the metastable pits happened at the potentials below the pitting potentials in less than a few seconds during the galvanic current application. However, re-passivation of the metastable pits is possible due to their lower current density in compare with the stable pits [40,41]. Fast scanning rate may enhance the initiation of the metastable pit while long-term experiments make a local condition which allows pit stabilization. In crevices, additionally, transformation of the metastable pits into stable pits can happen [30].

3.2. Electrochemical AC measurements

3.2.1. EIS study in borate buffer solution

For all samples, the Bode-phase plots (Fig. 9a and c) show just one time constant and the Nyquist spectra (Fig. 9b) exhibited an unfinished capacitive arc, typical behaviour for a compact passive layer [42]. A mixed single oxide layer composed of Fe–Al or Fe–Al–Cr oxides for binary and ternary alloys is responsible for the corrosion resistance of intermetallics. Additionally, existence of an inhomogeneous electrode surface could be seen in the EIS measurements, where the phase angle minimas are less than 90° [22]. In these cases, the interface between solution and sample does not work like a perfect capacitor. Hence, modelling the interface with a Constant Phase Element (CPE) is often appropriate. Due to this behaviour, we used a modified Randles circuit, with a CPE, instead of a capacitor (Fig. 9d) that exhibits a similar impedance spectrum to the measured spectrum. The impedance of the CPE is defined as [43,44]:

$$I_{CPE} = \frac{1}{Q(j\omega)^m} \quad (2)$$

where Q and m are the CPE constant and exponent respectively, ω is the angular frequency (rad/s) and $j^2 = -1$ is the imaginary number. Fig. 10a and b show the calculated values for solution resistance (R_s) and oxide film resistance (R_p) after fitting the experimental data with the modified Randles circuit. As was expected, the R_s was constant at different potentials and stays in the same range for all the tests. At low potentials, R_p is almost constant for both samples, which suggests that the films' electrical conductivity does not change very much. On the contrary, R_p in sample Fe26Al5Cr showed a peak at 0.94 V_{SHE} (Fig. 10b). This could be due to an increase in the enrichment level of the alloying elements (chromium) in the oxide layer since this characteristic was also observed for Al–4% Cr and Al–9% Cr in the chloride containing solutions [30].

We used two different models (i) Hsu–Mansfeld [45] and (ii) Brug [46] for calculating the effective capacitances of the passive layers ($C_{H\&M}$ and C_B repectively) as a function of potential

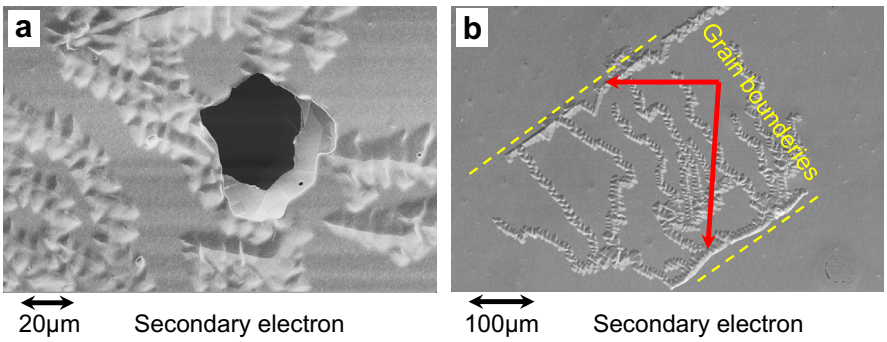

Fig. 7. (a) shows the existence of stable and metastable pits in the Fe26Al5Cr intermetallic after 600 s, application of galvanostatic anodic current of1 mA/cm^2. (b) shows the growth of the metastable pits through the grains boundaries and inside the grains in the Fe26Al5Cr intermetallic after 10 s, application of galvanostatic anodic current of 1 mA/cm^2.

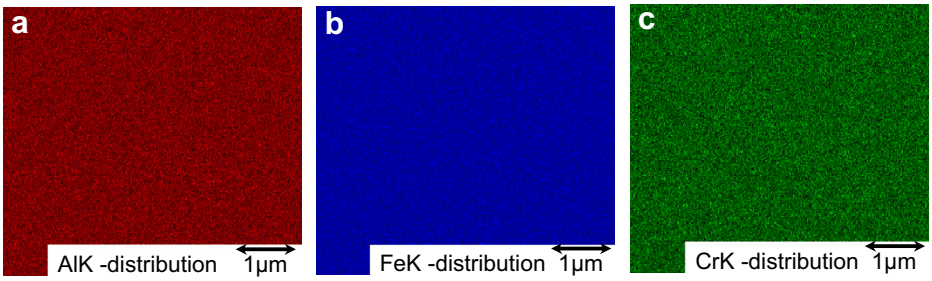

Fig. 8. EDX element mapping of different alloying elements show homogeneous distribution of Al (a), Fe (b) and Cr (c).

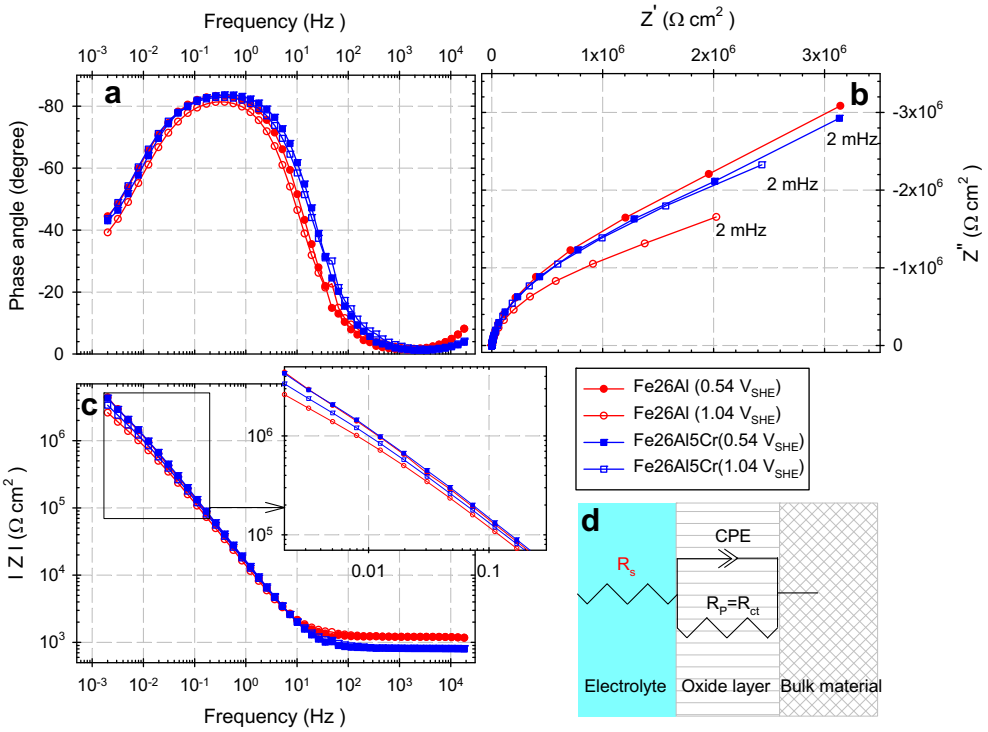

Fig. 9. Phase (a), Nyquist (b) and Bode (c) plots, vs applied potential; and the equivalent electric circuit used to model the EIS data (d). The curves obtained for Fe26Al alloys with different concentration of Cr in the borate buffer solution.

(Appendix A). The calculated capacitances, follow the same trend (Fig. 10c). However, the overestimation of the $C_{H\&M}$ may be because of ignoring the solution resistance in the model; in contrast to the Brug model which considers the effect of both R_s and R_p [45]. Very high values of the capacitance (calculated with both methods) and resistance of the passive layer, in solutions without Cl^-, clearly show that the oxide layers are thin and compact in all different samples. The effective capacitance decreases with the applied

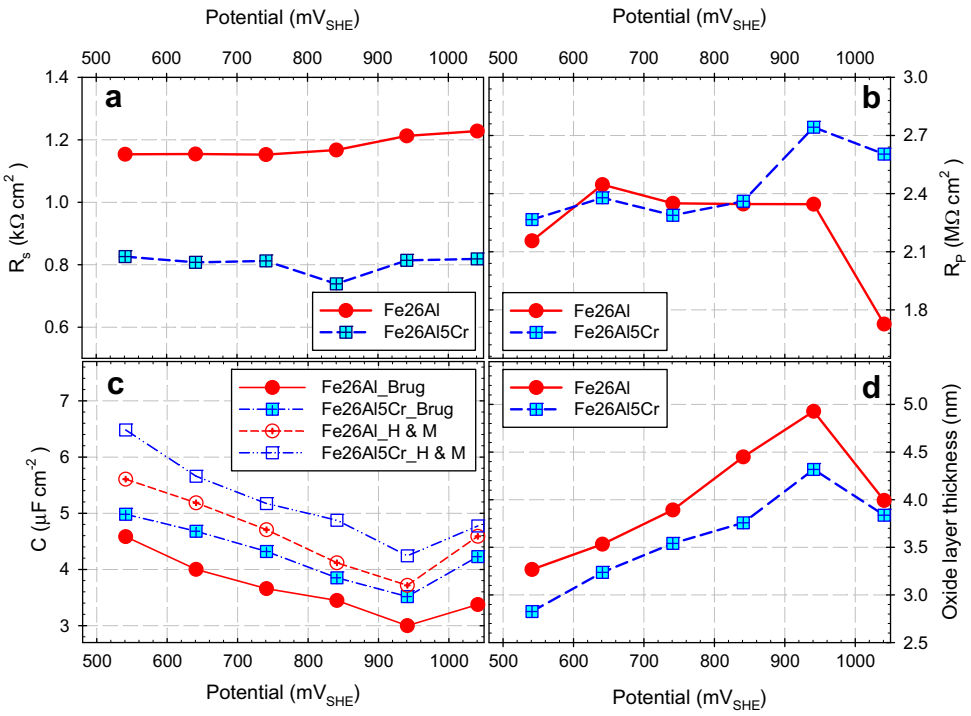

Fig. 10. Show the solution resistance (a), polarization resistance (b), capacitance (c) and passive layer thickness (d), vs applied potential. The curves obtained for Fe26Al alloys with different concentration of Cr in the borate buffer solution.

potential until 0.94 V_{SHE}, but increases as the potentials get close to the oxygen evolution potential. The effective capacitance of the passive layer has a diverse relationship with the thickness of the passive layer (d) [22]:

$$C = \frac{\varepsilon\varepsilon_0}{d}S \tag{3}$$

where S is the surface area of sample exposed to the solution, ε_0 is vacuum permittivity, ε is the relative dielectric constant of the passive layer. Due to the lack of information in the literature about the dielectric constant of passive oxide layer of Fe26AlxCr intermetallics, for the first approximation, we used the average value of the relative dielectric constant for steel [33] and pure aluminium [27] passivated in a borate buffer. Fig. 10d shows the changes of the oxide layer thickness for different samples at different potentials using the capacitance values measured with the Brug model. Addition of Cr increases the capacitance of the passive layer and, hence, decreases the thickness of it. With each increment of the applied potentials, both alloys behave similarly. First, we observed thickening of the passive layer and, afterward, the reduction of the passive layer were observed in both alloys which indicates slight dissolution of the passive layer at potentials higher than 0.94 V_{SHE}.

3.2.2. Mott–Schottky analysis

The Mott–Schottky (MS) analysis was used, in order to evaluate the semiconducting characteristics of the passive layers (Appendix B). The nonstoichiometric nature of the passive layer composition, in addition to its local structural inhomogeneties, is what makes the passive layer semiconductive [47–49]. The localized states in the band gap have different energies and those with low energies have longer time constants for charging and discharging. This may give rise to a frequency dependence of the space-charge capacity. This fact is confirmed from the results of the MS measurements where the measured "double-layer capacities" depend on the applied frequency (Fig. 11). The dispersion of the MS plots, at different frequencies, makes it difficult to measure the flat-band potential (E_{fb}) and the donor density (N_D) of the passive film. To find the proper frequency, we compared the capacitance values measured with the MS method with those calculated based on the Brug (C_B) and Hsu–Mansfeld ($C_{H\&M}$) models. Since the C_B values are very close to the C values measured with the MS method at 1000 Hz, we assumed the existence of capacitance behaviour at this identical frequency and $C_{(1000Hz)}$was used for the measurement of the N_D and E_{fb}. In this high frequency, the charge density in the space-charge region is just the sum of the static positive charge on the ionized donors, and the mobile negative charge of the conduction electrons. This is in contrast to the data points measured at lower frequencies where the low energy defects may also play role on the measured capacitance. Fig. 11 shows that the slop of the MS curves ($C_{sc}^{-2} - E(SHE)$) in the samples with different Cr content is close to zero at the potentials close to OCP, while at more anodic potentials, all curves have positive slope. The positive sign of the slope is an indicator of the n-type behaviour of the passive layers in the applied range of potentials.

The negative sign of the slope at more positive potentials, especially in samples with high concentration of Cr, is an indicator of the p-type behaviour of the passive layers. The n-type transformation into the p-type at higher potentials indicates the increase of the concentration of metal vacancies in the passive film. At the potentials around 0.94, the electro-oxidation of $Cr^{3+}$to Cr^{6+} may happen which causes the p-type characteristic of the passive layer. The formation of Cr^{6+} at higher anodic potentials leads to increased production of metal vacancies in the passive film. However, formation of a p-type passive layer increases pitting resistance by substitution of the oxygen vacancies to the metallic vacancies.

Easy adsorption of chloride ions on the metallic sites makes the n-type passive layers more sensitive to pit nucleation. The effect of the electronic structure on pitting can be explained by a point defect model [50]. This model assumes that the chloride ions are incorporated into the passive film by occupying anion vacancies. This results in a decrease of anion vacancies and an increase in the cation vacancies. When the cation vacancies start to pile

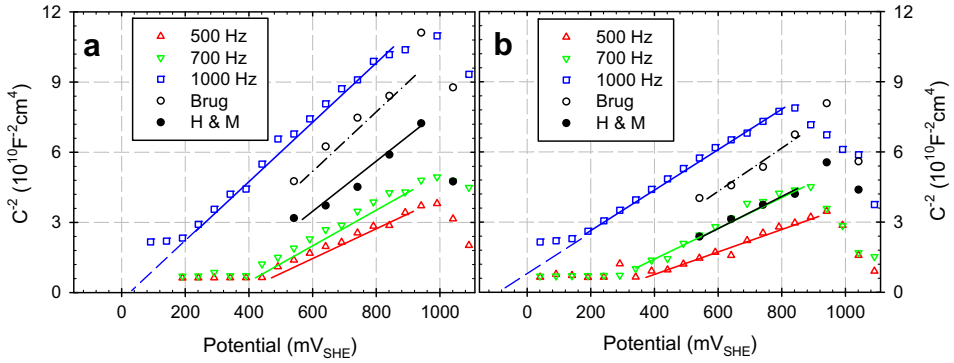

Fig. 11. Frequency dependence of Mott–Schottky plots of passive films formed in borate buffer solution on Fe26Al0.5Cr (a) and Fe26Al5Cr (b).

up at the metal interface, a breakdown of the films occurs [51]. Hence, one possible rate-determining step for the passive film breakdown, in a chloride environment, is the rate of the adsorbed chloride ion's penetration into the passive film. Measurement of the donor densities for samples at 1000 Hz shows an increase from 6×10^{19} for samples with Fe26Al to 7×10^{19} for samples with 5 at.% Cr. Higher donor densities associated with more disordered structures of the passive films may correspond to a higher penetration rate and less stable passive film. Cheng et al. [51] and Morach et al. [52] found that materials with a lower number of localized states have better resistance to localized corrosion. This conclusion is in contrast with the results we found based on the polarization tests, where a longer range of passivation was observed in Fe26Al5Cr alloy, and SEM images showed a lower density of pits in samples with more concentrations of Cr. In agreement with our results, Bockris and Kang [53] observed the enhancement of the pitting resistance of aluminium alloys after addition of Cu, Ta, Mo and W although the slop of the MS curves was decreased in the results (which shows the increment of the donor densities). The reason is that, non-uniform passive layers may have high energy sites (called special "entry sites"), at which the chloride can be more strongly adsorbed, and can subsequently penetrate into the passive film [53]. In other words, the contribution of donors on the penetration of the adsorbed chloride ion's will not be rate-determining step at all. All kinds of surface (grain boundaries) or line (dislocations) defects, for example, could work as an entry site. Especially in the case of aluminium and aluminium alloys, the existence of chain like AlOOH in the aluminium passive film [53] may ease the penetration of the chloride, and thus, the rate of the passive film breakdown would depend upon the chloride ion penetrating through these entry sites. It shows that we cannot relate directly the resistance of the passive layer to the density of donors.

The Cr^{3+} size is 63 pm, slightly bigger than the size of the Al^{3+} ion (51 pm) [54]. This explains why, Cr^{3+} will substitute at the Al^{3+} site. During the formation of the passive film, Cr^{3+} diffuses into the solution/oxide interface. They may segregate at the crystal imperfection sites which act as the entry sites for the chloride ions because of the high surface energy of the defects. Thus, the entry site may be blocked by the alloying oxides. The segregating of atoms to defects in passive layer and reducing their formation energy is similar to that by which surfactants reduce surface energies in solutions. The saturation of the oxide/electrolyte could be seen by the changes of the flat-band potentials where no space charge arises in the passive layer. Our results show the decrease of E_{fb} from -0.010 to -0.125 V_{SHE} with increase of the chromium concentration from 0 to 5 at.% Cr. The shift of E_{fb} to the negative values would imply that the oxide is less defective, more corrosion resistant, and thus, less susceptible to pitting as explained by Menezes et al. [55]. He performed his measurements for pure Al, and AA 7075 and AA 3003 alloys in chloride, molybdate and sulfate solutions using the photoelectrochemical technique.

Furthermore, the flat-band potential is equal to the potential of zero charge (E_{PZC}) when the potential drop across the space charge is zero. In general, the E_{PZC} can be determined by the following equation when the potential drop of the space charge layer due to the specific adsorption is known [53]:

$$E_{PZC} = E_{FB} \pm |\Delta\Phi_{SC}| \tag{4}$$

here $\Delta\Phi_{SC}$ is the potential drop across the space charge layer. The potential at which the chloride starts to adsorb depends on the E_{PZC}. Anodic shift of E_{PZC} moves the critical potential of adsorption to more anodic potentials. Due to the linear dependence of the flat-band potential to the E_{PZC}, the addition of alloying elements which increase the E_{fb} may facilitate the Cl^- adsorption at the passive layer/solution interface [53]. It is the reason that some authors use the influence of alloying elements on E_{fb} as a criterion for studying the susceptibility of different aluminium alloys to the pitting corrosion [53].

However, different features of pitting corrosion should be cleared up to propose a proper model for pitting corrosion of each material. The breakdown of the passive film dependents upon the properties of the film (like semiconductor properties); and the stable pit growth, depends upon the processes occurring within the pit. Pits nucleation or passive layer breakdown is controlled by either Cl^- adsorption/concentration at the passive/solution interface or diffusion of anions through the passive layer. According to our results, the rate-determining step in the mechanism of the protectiveness of the Fe26Al5Cr intermetallics is the penetration of Cl^- (and not the Cl^- concentration at the passive/solution interface). The protectiveness of the chromium enriched intermetallics is enhanced by blocking the entry site of the chloride penetration.

In addition to the E_{fb} effect on the pitting corrosion of alloys, the effect of Cr on the flat-band potential is very important for another reason. A large increase in cathodic current occurs below the flat-band potential [45]. This is very important, especially for iron-aluminium intermetallics, because of very high susceptibility of alloys to hydrogen embrittlement (HE). Films with more negative flat-band potentials are less susceptible to HE due to the decreased reduction kinetics associated with high flat-band potentials. Addition of chromium decreases the flat-band potential, and therefore, reduces the kinetics of the water reduction reaction and hydrogen formation which is believed to be one important reason for the low ductility of alloys in the moist containing environments.

4. Conclusion

With the aid of different electrochemical methods as well as the SEM and EBSD techniques, we tried to characterize the effect of Cr on the passive layer. The results show:

1- Incorporation of Cr as a ternary alloying element into the passive film increases the resistance of the alloys to pitting corrosion and decreases the average density of pits. However, addition of 5 at.% Cr to the binary Fe_3Al intermetallics does not hinder the pitting and crevice corrosion of alloys completely.
2- More metastable pits were observed in samples with higher concentrations of Cr.
3- The pit facets have the {1 1 0} orientation. The grain with the {1 1 0} orientation have slightly higher pit density in comparison with other orientations, but the difference was not significant.
4- Addition of Cr increases the effective capacitance and donor density of the passive layers. The effect of Cr on the polarization resistance was more obvious at high anodic potentials where the strong enrichment of the passivation layer with Cr^{3+} and Cr^{6+} could make a more protective p-type passive layer.
5- Addition of Cr decreases the flat-band potential. It causes less susceptibility of Cr enriched intermetallics to the moisture induced hydrogen embrittlement.

Acknowledgments

The authors wish to thank Prof. Horst Vehoff and Prof. Christian Motz for their advice and help, Dr. M. Palm of Max Planck Institute Eisenforsch GmbH. for supporting the materials, Anna Lynn Maxfield for proofreading, and additionally DFG for financial supports.

Appendix A

Hsu and Mansfeld used a normalization factor ω/ω_c, to enable the use of the parameter $C_{H\&M}$ with the dimension 'Farad'. Where $C_{H\&M}$ is the effective capacitance of a CPE and ω_c could be measured as follows [45]:

$$\omega_c = (1/R_P Q)^{\frac{1}{m}} \tag{5}$$

based on their theory, the maximum in the imaginary component of the impedance occurs at a critical frequency, regardless of the CPE exponent m.

$$C_{H\&M} = Q(\omega_c)^{m-1} \tag{6}$$

The Brug model [46] could be used also for measuring the effective capacitance of the passive layer. It was developed for an irreversible uniform charge transfer and works in the absence of the faradaic processes.

$$C_B = Q^{\frac{1}{m}}\left(R_s^{-1} + R_P^{-1}\right)^{\frac{m-1}{m}} \tag{7}$$

Based on Brúgs model, "CPE is coupled not only to the solution resistance but also to the charge-transfer resistance (or more generally to the faradaic impedance), if it is caused by microscopical or sub-microscopical heterogeneity of the electrode surface." [46].

Appendix B

Under depletion conditions, the MS approximation for an n-type and p-type semiconductor is given by the Eqs. (8) and (9) respectively [51]:

$$\frac{1}{C^2} = \frac{2}{\varepsilon\varepsilon_o e N_D}\left(E - \left(E_{fb} + \frac{kT}{e}\right)\right) \tag{8}$$

$$\frac{1}{C^2} = -\frac{2}{\varepsilon\varepsilon_o e N_D}\left(E - \left(E_{fb} + \frac{kT}{e}\right)\right) \tag{9}$$

where C is the measured capacitance of the film-electrolyte interface, k the Boltzman constant, T is the absolute temperature, E the applied potential, E_{fb} the flat-band potential, e the electron charge, N_D the donor density and C can be described by following equation:

$$\frac{1}{C} = \frac{1}{C_{sc}} + \frac{1}{C_H} \approx \frac{1}{C_{sc}} \tag{10}$$

where C_{sc} and C_H are the space charge and the Helmholtz capacitance, respectively. However, since the capacitance of the space charge layer is very small compared with that of the Helmholtz layer, the measured interfacial capacitance can be regarded as that of the space charge layer when the potentials are applied with a "sufficiently" high frequency. The donor density of passive layer could be measured with calculating the slop of the $C_{sc}^{-2} - E(\mathrm{SHE})$. The $E_{fb} + kT/e$ can be obtained by extrapolating the linear portion of the line to $C_{sc}^{-2} = 0$ where $kT/e = 25.67$ mV at room temperature ($T = 298$).

References

[1] N. DeCristofaro, S. Frangini, A. Mignone, Passivity and passivity breakdown on a beta-FeAl intermetallic compound in sulphate and chloride containing solutions, Corros. Sci. 38 (1996) 307–315.
[2] S. Frangini, N. DeCristofaro, J. Lascovich, A. Mignone, On the passivation characteristics of a beta-FeAl intermetallics compound in sulphate solutions, Corros. Sci. 35 (1993) 153–159.
[3] A. Velon, I. Olefjord, Oxidation behavior of Ni3Al and Fe3Al: II. Early stage of oxide growth, Oxid. Met. 56 (2001) 425–452.
[4] A. Velon, D.-Q. Yi, Influence of Cr on the oxidation of Fe3Al and Ni3Al at 500°C, Oxid. Met. 57 (2002) 13–31.
[5] W.H. Lee, R.Y. Lin, Oxidation, sulfidation and hot corrosion of intermetallic compound Fe3Al at 605 °C and 800 °C, Mater. Chem. Phys. 58 (1999) 231–242.
[6] S. Frangini, R. Giorgi, J. Lascovich, A. Mignone, XPS Study of passive films formed on an iron-aluminium intermetallic compound in acid solution, Surf. Interface Anal. 21 (1994) 435–441.
[7] D.G. Morris, M.A. Munoz-Morris, L.M. Requejo, Work hardening in Fe–Al alloys, Mater. Sci. Eng. A 460–461 (2007) 163–173.
[8] P. Morgand, P. Mouturat, G. Sainfort, Structure and mechanical properties of iron–aluminium alloys, Acta Metall. 16 (1968) 867–875.
[9] J. Herrmann, G. Inden, G. Sauthoff, Deformation behaviour of iron-rich iron–aluminum alloys at low temperatures, Acta Mater. 51 (2003) 2847–2857.
[10] A. Barnoush, J. Dake, N. Kheradmand, H. Vehoff, Examination of hydrogen embrittlement in FeAl by means of in situ electrochemical micropillar compression and nanoindentation techniques, Intermetallics 18 (2010) 1385–1389.
[11] M. Zamanzade, H. Vehoff, A. Barnoush, Cr effect on hydrogen embrittlement of iron aluminide intermetallics: Surface or bulk effect, Acta Mater. (submitted for publication).
[12] N.E. Hakiki, Comparative study of structural and semiconducting properties of passive films and thermally grown oxides on AISI 304 stainless steel, Corros. Sci. 53 (2011) 2688–2699.
[13] M. Salasi, G.B. Stachowiak, G.W. Stachowiak, M.R. Kilburn, Nano SIMS investigation of passive oxide films on high-Cr cast iron, Corros. Sci. 67 (2013) 298–303.
[14] M. Keddam, O.R. Mattos, H. Takenouti, Mechanism of anodic dissolution of iron–chromium alloys investigated by electrode impedances-I. experimental results and reaction model, Electrochim. Acta 31 (1986) 1147–1158.
[15] M. Keddam, O.R. Mattos, H. Takenouti, Mechanism of anodic dissolution of iron–chromium alloys investigated by electrode impedances-II. Elaboration of the reaction model, Electrochim. Acta 31 (1986) 1159–1165.
[16] I. Epelboin, M. Keddam, O.R. Mattos, H. Takenouti, Dissolution and passivation of Fe and Fe–Cr alloys in acidified sulfate medium-influences of pH and Cr content, Corros. Sci. 19 (1979) 1105–1112.
[17] V.S. Rao, A review of the electrochemical corrosion behaviour of iron aluminides, Electrochim. Acta 49 (2004) 4533–4542.

[18] R. Balasubramaniam, On the role of chromium in minimizing room temperature hydrogen embrittlement in iron aluminides, Scr. Mater. 34 (1996) 127–133.
[19] A. Barnoush, M. Zamanzade, Effect of substitutional solid solution on dislocation nucleation in Fe3Al intermetallic alloys, Philos. Mag. 92 (2012) 25–27.
[20] M. Zamanzade, H. Vehoff, A. Barnoush, Effect of Chromium on Elastic and Plastic deformation of Fe3Al Intermetallics, Intermetallics 41 (2013) 28–34.
[21] J.R. Scully, Polarization resistance method for determination of instantaneous corrosion rates, Corrosion 56 (2000) 199–217.
[22] E. Barsoukov, J. Ross Macdonald, Impedance Spectroscopy: Theory, Experiment and Applications, John Wiley & Sons, New Jersey, 2005.
[23] M. Urquidi-Macdonald, S. Real, D.D. Macdonald, Applications of Kramers–Kronig transforms in the analysis of electrochemical impedance data, Electrochim. Acta 35 (1990) 1559–1566.
[24] A.A. Oskuie, T. Shahrabi, A. Shahriari, E. Saebnoori, Electrochemical impedance spectroscopy analysis of X70 pipeline steel stress corrosion cracking in high pH carbonate solution, Corros. Sci. 61 (2012) 111–122.
[25] H. Subramanian, V. Subramanian, P. Chandramohan, M.P. Srinivasan, S. Rangarajan, S.V. Narasimhan, S. Velmurugan, Role of magnesium ions in reducing high temperature aqueous corrosion of carbon steel, Corros. Sci. 70 (2013) 127–139.
[26] V.K. Gupta, S.R. Agnew, Measuring the effect of environment on fatigue crack-wake plasticity in aluminum alloy 2024 using electron backscatter diffraction, Mater. Sci. Eng. A 494 (2008) 36–46.
[27] S. Gudić, J. Radošević, M. Kliškić, Study of passivation of Al and Al–Sn alloys in borate buffer solutions using electrochemical impedance spectroscopy, Electrochim. Acta 47 (2002) 3009–3016.
[28] I.V. Sieber, H. Hildebrand, S. Virtanen, P. Schmuki, Investigations on the passivity of iron in borate and phosphate buffers, pH 8.4, Corros. Sci. 48 (2006) 3472–3488.
[29] S.P. Harrington, F. Wang, T.M. Devine, The structure and electronic properties of passive and prepassive films of iron in borate buffer, Electrochim. Acta 55 (2010) 4092–4102.
[30] Z. Szklarska-Smialowska, Progress in understanding pitting corrosion, in: The Electrochemical Society Proceedings Series, PV2002-13, 2002, pp. 251–265.
[31] S. Frangini, N. De Cristofaro, Analysis of the galvanostatic polarization method for determining reliable pitting potentials on stainless steels in crevice-free conditions, Corros. Sci. 45 (2003) 2769–2786.
[32] D. Tromans, Pitting of passivated cadmium monocrystals, J. Electrochem. Soc. 16 (2009) 203–215.
[33] P. Schmuki, From bacon to barriers: a review on the passivity of metals and alloys, J. Solid State Electrochem. 6 (2002) 145–164.
[34] H. Takahashi, M. Nagayama, Electrochemical behavior and structure of anodic oxide-films formed on aluminum in a neutral borate solution, Electrochim. Acta 23 (1978) 279–286.
[35] K. Azumi, T. Ueno, M. Seo, Cathodic dissolution behavior of an aluminum wire electrode in solutions containing borate and sulfate ions, J. Electroanal. Chem. 567 (2004) 1–7.
[36] M. Yasuda, F. Weinberg, D. Tromans, Pitting Corrosion of Al and Al–Cu Single Crystals, J. Electrochem. Soc. 137 (1990) 3708–3715.
[37] G.M. Treacy, C.B. Breslin, Electrochemical studies on single-crystal aluminium surfaces, Electrochim. Acta 43 (1998) 1715–1720.
[38] S.Y. Yu, W.E. O'Grady, D.E. Ramaker, P.M. Natishan, Chloride ingress into aluminum prior to pitting corrosion – an investigation by XANES and XPS, J. Electrochem. Soc. 147 (2000) 2952–2958.
[39] F. Stein, A. Schneider, G. Frommeyer, Flow stress anomaly and order-disorder transitions in Fe_3Al-based Fe–Al–Ti–X alloys with X = V, Cr, Nb, or Mo, Intermetallics 11 (2003) 71–82.
[40] G.S. Frankel, L. Stockert, F. Hunkeler, H. Boehni, Metastable pitting of stainless steel, Corrosion 43 (1987) 429–436.
[41] S.T. Pride, J.R. Scully, J.L. Hudson, Metastable pitting of aluminum and criteria for the transition to stable pit growth, J. Electrochem. Soc. 141 (1994) 3028–3040.
[42] K. Jüttner, Electrochemical impedance spectroscopy of corrosion processes on inhomogeneous surfaces, Electrochim. Acta 35 (1990) 1501–1508.
[43] A.A. Farag, M.A. Hegazy, Synergistic inhibition effect of potassium iodide and novel Schiff bases on X65 steel corrosion in 0.5 M H_2SO_4, Corros. Sci. 74 (2013) 168–177.
[44] B. Xu, Y. Liu, X. Yina, W. Yang, Y. Chen, Experimental and theoretical study of corrosion inhibition of 3-pyridinecarbozalde thiosemicarbazone for mild steel in hydrochloric acid, Corros. Sci. 74 (2013) 206–213.
[45] S.P. Harrington, M.T. Devine, Relation between the semiconducting properties of a passive film and reduction reaction rates, J. Electrochem. Soc. 156 (2009) C154–C159.
[46] G.J. Brug, A.L.G. Vandeneeden, M. Sluytersrehbach, J.H. Sluyters, The analysis of electrode impedances complicated by the presence of a constant phase element, J. Electroanal. Chem. 176 (1984) 275–295.
[47] Z. Szklarska-Smialowska, Pitting corrosion of aluminum, Corros. Sci. 41 (1999) 1743–1767.
[48] C.A. Della Rovere, J.H. Alano, R. Silva, P.A.P. Nascente, J. Otubo, S.E. Kuri, Characterization of passive films on shape memory stainless steels, Corros. Sci. 57 (2012) 154–161.
[49] M.C.L. de Oliveira, V.S.M. Pereira, O.V. Correa, N.B. de Limac, R.A. Antunes, Correlation between the corrosion resistance and the semiconducting properties of the oxide film formed on AZ91D alloy after solution treatment, Corros. Sci. 69 (2013) 311–321.
[50] C.Y. Chao, L.F. Lin, D.D. Macdonald, A point defect model for anodic passive films. 1. Film growth-kinetics, J. Electrochem. Soc. 128 (1981) 1187–1194.
[51] Y.F. Cheng, J.L. Luo, A comparison of the pitting susceptibility and semiconducting properties of the passive films on carbon steel in chromate and bicarbonate solutions, Appl. Surf. Sci. 167 (2000) 113–121.
[52] R. Morach, P. Schmuki, H. Bohni, Localized corrosion of high alloyed austenitic staineless steel, in: Proceedings of the 4th International Symposium on Electrochemical Methods in Corrosion Research, Helsinki, 1991.
[53] J. Bockris, Y. Kang, The protectivity of aluminum and its alloys with transition metals, J Solid State Electrochem. 1 (1997) 17–35.
[54] K. Sangwal, Additives and Crystallization Processes, John Wiley & Sons, West Sussex, England, 2007. p. 170.
[55] S. Menezes, R. Haak, G. Hagen, M. Kendig, Photoelectrochemical characterization of corrosion inhibiting oxide films on aluminum and its alloys, J. Electrochem. Soc. 136 (1989) 1884–1886.

Paper D

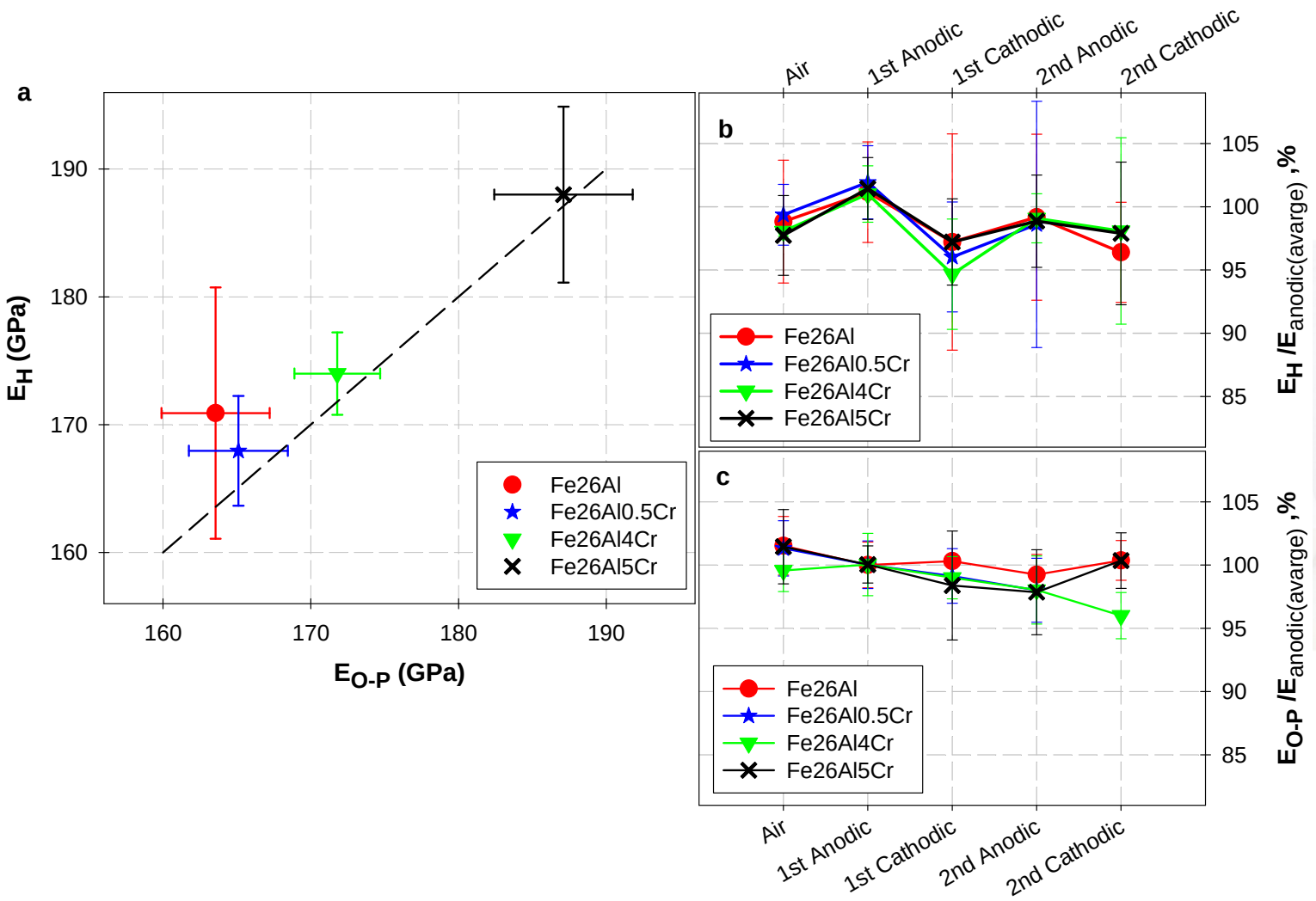
a
190
180
170
160
160
170
180
190
E_H (GPa)
E_{O-P} (GPa)
Fe26Al
Fe26Al0.5Cr
Fe26Al4Cr
Fe26Al5Cr
b
Air
1st Anodic
1st Cathodic
2nd Anodic
2nd Cathodic
105
100
95
90
85
E_H /$E_{anodic(avarge)}$,%
c
E_{O-P} /$E_{anodic(avarge)}$,%

Available online at www.sciencedirect.com

ScienceDirect

Acta Materialia 69 (2014) 210–223

Acta MATERIALIA

www.elsevier.com/locate/actamat

Cr effect on hydrogen embrittlement of Fe_3Al-based iron aluminide intermetallics: Surface or bulk effect

Mohammad Zamanzade [a], Horst Vehoff [a], Afrooz Barnoush [b,*]

[a] Department of Materials Science, Saarland University, D-66041 Saarbrücken, Germany

[b] Department of Engineering Design and Materials, Norwegian University of Science and Technology, No-7491 Trondheim, Norway

Received 17 October 2013; received in revised form 14 January 2014; accepted 19 January 2014

Abstract

The objective of this work is to reduce the susceptibility of binary Fe_3Al intermetallics to hydrogen embrittlement with the addition of chromium as the ternary element. The Young's modulus, Gibbs free energy for homogeneous dislocation nucleation (HDN) and velocity of dislocations were evaluated by an in situ nanoindentation method in air and under cathodic and anodic charging. The results show the influence of hydrogen on the reduction of Young's moduli of alloys, in agreement with the hydrogen-enhanced decohesion model, whereas measurements of the pop-in load indicate a drastic decrease after cathodic charging in samples with low Cr content. This is thought to be due to the decrease of the energy needed for HDN in the dislocation-free samples based on the defect-acting agents concept. Additionally, the effect of hydrogen on the mobility of dislocations and also the influence of Cr on the characteristics of passive oxide layer were analysed in detail.

Keywords: X-ray photoelectron spectroscopy; Electrochemical characterization; Electron backscatter diffraction; Nanoindentation; Dislocation loop

1. Introduction

Emerging new technologies require new materials with better mechanical, thermal and chemical properties. On the other hand, the depletion of natural resources demands the use of raw materials which are available in large quantities. Fe–Al-based intermetallics are good candidates for fulfilling these requests. They have relatively high strength, low density, low cost of production and good corrosion resistance [1–3]. However, with these advantages come disadvantages. Binary iron aluminiums suffer from severe hydrogen embrittlement (HE). Even the presence of a small amount of water vapour at room temperature reduces the ductility of Fe–Al-based intermetallics [4,5], especially those with higher concentrations of Al [6,7]. This is because the Al atoms react with the moisture, creating hydrogen, and it is the resulting hydrogen atoms that are then responsible for the lowered ductility [8,9]. One possible strategy to control this problem is to add ternary alloying elements. McKamey et al. [9] observed an increase in ductility of ~8–10% at room temperature with the addition of 6 at.% chromium. In general, the reasons for the increased ductility are thought to be caused by (i) the influence of Cr on the bulk properties of binary alloys, such as facilitating the dislocation cross-slipping, solid solution softening and an increment in cleavage strength of alloys [9]; and/or (ii) the effect of Cr on the surface properties through a contribution to the passive layers and the decrement of the kinetic of water reduction reactions and hence the reduction of hydrogen formation/adsorption [10]. However, despite these promising results, studies focusing on the exact mechanism of Cr enhancement of the mechanical properties in the presence of the hydrogen are missing.

* Corresponding author. Tel.: +47 735 93807; fax: +47 735 94129.
E-mail address: afrooz.barnoush@ntnu.no (A. Barnoush).

http://dx.doi.org/10.1016/j.actamat.2014.01.042
1359-6454/

The main reason is that in addition to the complex nature of the hydrogen effect on mechanical properties, a discrimination of the Cr effect on the surface or bulk and its interplay with the hydrogen also needs to be carried out.

In addition to studying the effect of hydrogen on the mechanical behaviour of the iron aluminides, the mechanism of hydrogen transport within metals, especially in the presence of microstructural imperfections, was studied as well. Density functional theory–local density approximation calculations [11] in addition to periodic density functional theory calculations within the generalized gradient approximation [12] predicted that hydrogen sits at tetrahedral sites in the bulk FeAl lattice, like its interstitial sites in bulk Fe [13]. Hydrogen diffusivity in iron aluminides is lower than in pure Fe [14–16]; and the activation barrier varies from 0.42 eV [14], 0.22 eV [17] and 0.26 eV [12] for Fe25Al, Fe40Al and Fe50Al, respectively. Electrochemical permeation tests [18–20] found that H diffusivity in Fe–Al alloys decreases with increasing Al content. The diffusion coefficient at room temperature was measured to be 10^{-8} m^2/s [21] for Fe, 10^{-11} m^2/s [15,18] for Fe18Al, 1.45×10^{-13} m^2/s [15] for Fe25Al and 4.4×10^{-13} m^2/s [16] for Fe40Al. More recent measurements at room temperature show an effective diffusion constant of |5.57, 5.07, 4, 46, 3, 62 & 2.25| $\times 10^{-10}$ m^2/s for Fe–|37, 40, 43, 46 & 50|Al, respectively [19]. Reported experimental diffusivity data for Fe–Al alloys vary significantly, presumably due to experimental uncertainties, varying Al concentration, impurities and microstructural differences [12]. Additionally, increasing the chromium content of iron [22] or iron aluminium [15] decreases the diffusion coefficient and increases the solubility of hydrogen, since the heat of absorption decreases, and d-vacancies increase, with substitution of iron with chromium [22].

For the passivated materials, the transport of hydrogen through the passive layer is driven by the electric potential gradient and the hydrogen concentration gradient [23], in contrast to the transport of hydrogen in bulk materials, which is controlled mainly by the concentration gradients. The ionic characteristic of hydrogen atoms (protons) in oxides [24] makes a strong coulombic interaction between hydrogen and oxygen ions. It may cause a very high concentration of hydrogen in the oxide in comparison with bulk metal or the metal/oxide interface. For iron, the ratio of hydrogen in oxide to hydrogen in iron is measured to be $\sim 10^6$ [23]. The transport of hydrogen within the oxide must occur by the activated jumping of a proton from one oxygen ion to another [25] and the necessary breaking of the coulombic bond with the initial oxygen ion causes the mobility of hydrogen in an oxide to be considerably lower than that in the metal phase. Therefore, for example in the case of Fe, the hydrogen diffusivity in the iron oxide layer is much less than that in iron ($\sim 10^{-14}$ m^2/s [23,26]). Based on the density functional theory simulation [27], the existence of an Al_2O_3 layer on the FeAl bulk material suppresses the mobility of hydrogen atoms. Diffusion of the adsorbed hydrogen atoms from the outer part of solution/oxide layer into the $\alpha - Al_2O_3$ layer is thermodynamically unfavourable, endothermic and rate controlling. In contrast, the H diffusion from the inner part of $\alpha - Al_2O_3$ to the oxide/bulk interface as well as from the interface into the bulk of the FeAl is a thermodynamically spontaneous processes and exothermic [27]. It should be mentioned here that the diffusion mechanism through the passive layer and also the passive layer/bulk metal interface is still largely unknown and has so far not been completely explored in published papers. Due to the existence of high donor densities in the passive layers [28], the real thermodynamics and kinetics of hydrogen diffusion may be far from the predicted values based on simulations or the measurements performed on Al-rich coatings [29]. Therefore, an increase in hydrogen diffusivity can be expected with an increase in the density of defects and distortion of the long-range order of the lattice.

For probing the hydrogen effect on the nanomechanical behaviour of metals, we developed a novel method called in situ electrochemical nanoindentation (ECNI). With the aid of this technique, nanoindenting the samples was performed while they were electrochemically charged with hydrogen. Since the ECNI measures the nanomechanical properties just below the surface, hydrogen saturation, after a few minutes, happens although the diffusion rate is very low in iron aluminides. The measured load–penetration depth response of single crystals indented for nanometer-scale depths could be used for calculating the elastic and plastic properties of charged samples using the Hertzian and Oliver–Pharr (O–P) methods [30]. The indenter produces shear stresses underneath the tip contact region. Beyond the elastic limit of a crystal, plastic deformation happens by nucleation, propagation and multiplication of dislocations. The displacement burst, or pop-in, which appears after the initial elastic loading sequence of a nanoindentation experiment, correlates to the homogenous dislocation nucleation (HDN) if the size of the highly stressed zone in the material is smaller than the average dislocation spacing [31]. It is shown in experiments [32], as well as in simulations [33], that the measured maximum shear stress at the pop-in load after HDN approaches the theoretical shear strength [34]. Hence nanoindentation, unlike most of other mechanical testing methods, also allows dislocation nucleation events to be detected on well-prepared surfaces [35–38]. Indentation of samples with high dislocation densities with a blunt tip mainly activates existing sources of dislocations such as Frank–Read sources. In this case, no pop-in occurs [37] or plasticity initiates at the stresses considerably below the theoretical stress needed for HDN [39,40]. Due to the very small volume of deformation during nanoindentation, the dislocation substructure in a bulk sample could be studied prior to, and after, the test with the techniques like orientation gradient mapping [41], transmission electron microscopy (TEM) [42] and electron channelling contrast imaging [43].

The applicability of the ECNI method for studying the hydrogen deformation interaction, and examining the dependence of the pop-in loads on hydrogen charging,

have been demonstrated in Cu [44], Ni [45] and Al [46], 316 and pulsed plasma nitrided alloys [47–50]. In this paper, by applying ECNI after thorough surface and electrochemical examination, we tried to clarify if the enhancement in mechanical properties of the Fe_3Al alloys with Cr addition is a surface or a bulk effect. The passive oxide film formed on the surface is characterized by means of X-ray photoelectron spectroscopy (XPS). Electrochemical cyclic voltammetry (CV) is used to investigate the electrochemical behaviour of the surface, including passivation and hydrogen evolution reactions (HERs) in the electrolyte.

2. Experimental

2.1. Sample preparation

The samples used in these experiments were made using the vacuum induction melt method. In all samples, the Al content was kept constant at 26 at.% while different amounts of Cr were added. As-cast samples, with different concentrations of Cr (0.0, 0.5, 4.0, and 5.0 at.%), were cut by spark erosion into cylinders with a 12 mm diameter. Afterwards, the samples were mechanically polished down to 1 μm, and then marked with a microindenter. The microindents were used later to find the proper crystal orientation for the nanoindentation. Subsequently the samples were electropolished with 1 M sulfuric acid in a methanol solution [34] in order to remove the subsurface damage left behind by mechanical polishing. We estimated the depth of removal by the electropolishing step with the measurement of the diagonal length of micro indents; the depth of indents is ~1/7 of the diagonal length for a Vickers pyramid indenter with an angle of 136° between faces. For all samples the depth of removal was more than 500 nm. The results published in Ref. [34] show the similarities between maximum shear stress at pop-in load and the theoretical shear stress in samples with different Cr contents. It confirms that the homogeneous dislocation nucleation is the likely mechanism of initiation of plasticity rather than inhomogeneous nucleation of dislocations that can arise from surface roughness or the damage below the surface [51].

TEM measurements performed by Stein et al. [52] on several binary and ternary alloys with the same concentration of aluminium, and same history of heat treatment, show the existence of $D0_3$ –ordered, single phase solid solutions at room temperature.

2.2. Electrochemical measurement

The CV technique is used to study the effect of Cr content on the electrochemical behaviour of the Fe_3Al intermetallics. CV measurements were performed on electrochemically polished samples in a borate buffer solution ($H_3BO_3[0.3M]$, $Na_2B_4O_7{\cdot}10H_2O[0.075M]$) with a pH of 8.4. The solutions were made from analytical-grade reagents and double distilled water. A conventional three-electrode electrochemical flat cell inside a Faraday cage was used for performing the electrochemical tests. The surface area of specimens after installation in the cell was 0.92 cm^2. A saturated calomel electrode was connected to the cell through a Luggin capillary to avoid chloride contamination. All potentials were converted and are reported against the standard hydrogen electrode (SHE). A platinum foil with a surface area of 4 cm^2 was used as the counterelectrode. CV was performed with a scan rate of 20 mV/s using a Zahner IM6ex electrochemical testing system. The working electrodes were left to stabilize at its free corrosion potential for ~1 h before starting experiments.

2.3. Surface characterization

2.3.1. XPS

A Physical Electronics Quantum 2000 Scanning ESCA Microprobe was used to perform XPS measurements and analyse the surface composition of the freshly electropolished samples. A penning source was operated with Ar^+ (2 keV) for XPS depth profiling. The sputter rate was calibrated by using an oxidized silicon wafer of known oxide thickness. Quantitative evaluation of spectra was carried out on the basis of standard spectra of oxygen and the alloying components. To reduce the number of figures, original XPS spectra are not shown in this paper.

2.3.2. Microscopy

A Zeiss ΣIGMA™-VP field emission scanning electron microscope was used to perform electron backscatter diffraction (EBSD) measurement. The EBSD measurements were used to characterize the different crystal orientations and grain sizes. The surface quality was characterized, before nanoindentation, with a Zeiss optical microscope equipped with differential interference contrast and also a Bruker dimension 3000® atomic force microscope (AFM). When examined with an AFM, the average root-mean-square roughness was ~1 nm or less, after electropolishing [34]. Additionally, the surface roughness of the samples was studied before indentation at both cathodic and anodic potential using the scanning mode of the triboindenter. In situ images did not show differences in the roughness of the samples.

2.4. Nanoindentation

Nanoindentations were performed with a Hysitron TriboIndenter equipped with Performech controller, nanoDMA III compatible transducer, Stanford Research System (SRS) 830 DSP lock-in amplifier and National Instruments USB-GPIB adaptor. The nanoDMA III software, developed by Hysitron, has been used to perform continuous measurement of the hardness (see Appendix A). This testing method utilizes sinusoidal loading, concurrent with the quasistatic loading, which is varied with each progressive step. The dynamic measurements were performed with a fixed frequency of 220 Hz, and the applied displacement amplitude was always kept between 1 and

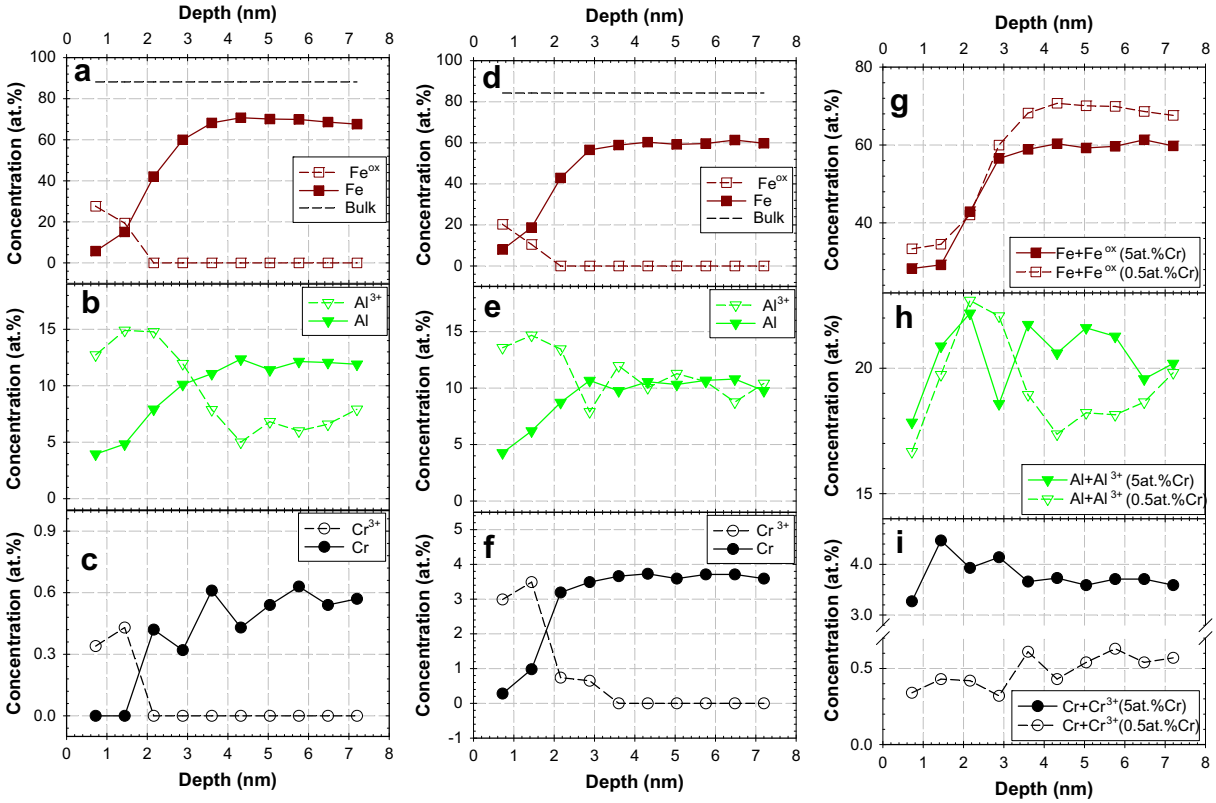

Fig. 1. XPS sputter profiles of Fe–26Al–*x*Cr alloys after electropolishing with a 1 M H_2SO_4/methanol solution. (a–c) Fe26Al0.5Cr. (d–f) Fe26Al5Cr. Sum of ionic and atomic concentrations of iron (g), aluminium (h) and chromium (i) for samples with 0.5 and 5 at.% Cr.

2 nm to ensure the validity of the model used for analysis of the results [53].

We used a Berkovich diamond tip for nanoindentation of different Fe26Al*x*Cr intermetallics at defined anodic or cathodic potentials. In all specimens, the grain sizes were larger than 500 μm in diameter. Considering the very small indentation depth, a grain acts like a single crystal during NI. A selected (0 0 1) grain orientation was marked and all nanoindents were performed in the same grain to eliminate scatter in the data. The presented results are the average of more than 20 indents in each situation, and the distance between the indents was at least three times greater than the average diameter of each indent.

3. Results and discussion

3.1. Surface oxide composition

The distribution of iron (Fe and Fe^{ox}), aluminium (Al and Al^{3+}) and chromium (Cr and Cr^{3+}) after electropolishing were measured by the XPS method for different samples. The reason that we presented the sum of both Fe^{2+} and Fe^{3+} cations as Fe^{ox} is because of the preferential sputtering of oxygen. Fe^{3+} could be reduced to Fe^{2+} and hence the separation between Fe^{2+} and Fe^{3+} is questionable [54]. The metals and their oxidized species are plotted at different depths in Fig. 1a–f. In both samples (samples with 0.5 and 5 at.% Cr), the oxide/solution interface is enriched by the Fe^{ox} and Cr^{3+} ions. The reason for the depletion of the outer side of the passive film from aluminium ions could be the dissolution of the ions in the very low pH of the electropolishing solution. In the sample with higher concentration of chromium, some part of Fe^{ox} is replaced by Cr^{3+} in the passive layer. However, the height of the Al^{3+} maximum does not differ with the addition of chromium concentrations and it remains relatively constant throughout the oxide film thickness. In contrast, the Cr^{3+} and Fe^{ox} concentrations were decreased significantly at higher depths. Fig. 1g–i shows a gradient of the iron ($Fe + Fe^{ox}$), aluminium ($Al + Al^{3+}$) and chromium ($Cr + Cr^{3+}$) distribution through the passive oxide layer; aluminium and chromium enrichment, with respect to the bulk composition, is found at the central part of the passive layer and decreases until the bulk concentration is reached.

In Fig. 2, a schematic model of the oxide layer is represented. In the sample with 0.5 at.% Cr, a very thin passive layer was formed with a thickness of ~3.5 nm ($L1 + L2 \approx 3.5$ nm). A very slight decrease of the oxide layer thickness to values of ~3 nm was observed in samples with 5 at.% chromium. The chromium and aluminium oxide signals show a maximum at a depth of ~1.5 nm ($L1 \approx 1.5$ nm).

3.2. Evolution of the passive film

Electrochemical tests on freshly electropolished iron aluminide samples were performed to study details of the

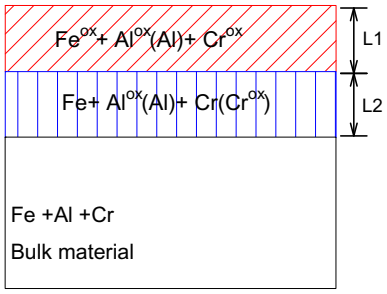

Fig. 2. Schematic model of the passive layer formed on Fe–26Al–*x*Cr alloys after electropolishing with a 1 M H_2SO_4/methanol solution.

electrochemical reactions taking place on the surface of the samples. The voltagramms in Fig. 3 show an increase of the current at the potentials at $\sim -0.5 V_{SHE}$ (A-I). It is due to the oxidation of the remaining metallic aluminium atoms in the passive layer after electropolishing; an identical peak for pure aluminium was seen in borate buffer [55]. Additionally, up to three anodic current increases are obvious on cyclic voltagramms. Similar anodic peaks were observed in the voltammograms for pure iron and steels [56–58]. The anodic peak A-II is due to the activation of the electrochemical reactions 1, 2 and 3 consequently [59].

$$Fe^0(s) \rightarrow Fe^{2+}(aq) + 2e^- \quad (1)$$

$$Fe^0(s) + 2OH^-(aq) \rightarrow Fe(OH)_2(s) + 2e^- \quad (2)$$

$$Fe^{2+}(aq) + 3OH^-(aq) \rightarrow Fe(OH)_3(s) + e^- \quad (3)$$

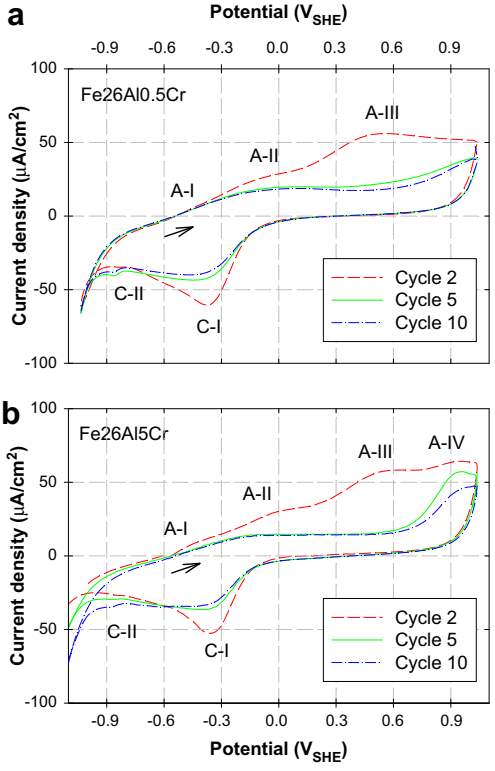

Fig. 3. Cyclic voltammogramms of iron aluminides in a borate buffer solution: (a) Fe–26Al–0.5Cr and (b) Fe–26Al–5Cr.

Eq. (1) causes a material loss, as confirmed with the X-ray absorption near edge structure measurements performed on the pure iron at the same pH [60]. The increase of the $Fe^{2+}(aq)$ concentration in addition to the application of anodic potential may cause the oxidation of Fe^{2+} to Fe^{3+} base on Eq. (3). Due to the low solubility product of $Fe(OH)_3$ [59], it will precipitate on the oxide/solution interface. The rate controlling step in Eq. (3) is the $Fe^{2+}(aq)$ concentration.

There is another broad anodic peak, A-III, which corresponds to the oxidation of the iron(II) oxide/hydroxide layer formed at the first stages of passivation, to an Fe^{2+}/Fe^{3+} oxide film, as described by Eq. (4) [59]:

$$FeO(s) + 2H_2O \rightarrow Fe_3O_4/Fe_2O_3(s) + 4H^+(aq) + 4e^- \quad (4)$$

At anodic potentials greater than 0.6 V_{SHE}, a current plateau is observable, which is due to the conversion of the Fe^{2+} to Fe^{3+}. The addition of chromium to the binary alloys makes a new anodic peak, A-IV, in the alloys with 5 at.% Cr at ~0.9 V. This peak was related to the electrooxidation of Cr^{3+} to Cr^{6+} [61].

The reduction peak appearing between −0.25 and −0.6 V_{SHE} in the voltammograms could be identified with the reduction of Fe_2O_3 and its dissolution as Fe^{2+} (Eqs. (3) and (4)). Another cathodic current peak at the potential of ~ -0.9 V_{SHE} was observed at higher cycles, with the increment of $Fe^{2+}(aq)$ concentration. According to Eq. (1) a part of the dissolved $Fe^{2+}(aq)$ will reduce to Fe^0 and precipitate at the oxide/solution interface.

With increasing the number of cycles the oxidation/reduction peaks, the current in the voltammogram decreased. After the fifth cycle the anodic current peak A-II almost vanished and the current density at the passive range decreased. This observation suggests a dynamic change in the composition of the passive layer. The reduction of the kinetic in Eqs. (1)–(3) is due to the dissolution of iron (hydr)oxide at the passive layer/solution interface. The presence of high concentration of Al results in the formation of a compact dense passive layer, which is responsible for the low current density in the passive range. Since Al (hydr)oxide and also chromium oxide are stable in the pH of the electrolyte [55,62–64], we can expect the aluminium (chromium) enrichment at the oxide–electrolye interface, which is in agreement with the XPS measurements performed by Frangini et al. [65], Schaepers and Strehblow [54]. The Al-rich oxide may have a hexagonal structure, as shown for the oxide layer formed on FeAl [66].

After ten cycles of polarization and stabilization of passive film, the potential was scanned going toward more negative potentials, as shown in Fig. 4. At more negative potentials, the current abruptly increased exponentially due to the hydrogen evolution (Eq. (5)):

$$2H_2O + 2e^- \rightarrow H_2 + 2OH^- \quad (5)$$

The rate of water reduction reaction is controlled by electrolyte composition, the electrochemical potential and the film's semiconducting properties. It was earlier shown

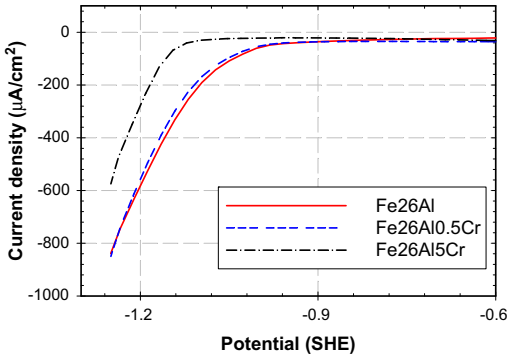

Fig. 4. Rapid polarization scan (20 mV/s) of the Fe_3Al intermetallics with different concentrations of Cr. The increase in cathodic current occurs due to the activation of water reduction reaction.

that the passive layer formed on the iron aluminates has n-type semiconducting behaviour [28]. For n-type semiconducting passive layers, energy-band models predict that at potentials more negative than the film's flatband potential, films exhibit a drastic increase in reduction current with increasing cathodic potential as the semiconductor enters an accumulation mode [67]. In agreement with the results presented earlier by Balasubramaniam [10], the addition of 5 at.% Cr to the binary alloys increases the overpotential of water reduction (up to 100 mV). It could be attributed to the more negative flatband potential of the passive films formed on the Cr-enriched samples [28]. This certainly changes the kinetic of the hydrogen formation and adsorbtion into the Fe_3Al intermetallic alloys and has an enhancing effect on the susceptibility of low Cr content alloys toward the HE.

Like pure aluminium [64], dissolution of Al_2O_3 may happen due to local alkalization induced by the hydrogen evolution reaction at high cathodic current densities. Al(oxide) dissolution reaction under hydrogen evolution is described as follows [64]:

$$Al_2O_3 + 3H_2O + 2OH^- \rightarrow 2Al(OH)_4^- \quad (6)$$

$$Al + 4OH^- \rightarrow Al(OH)_4^- + 3e^- \quad (7)$$

However for our ECNI tests we applied the cathodic current of 100 μA/cm^2. The reduction of the Al_2O_3 cannot happen with the application of low currents [64] due to the buffer capability of the solutions which suppresses the increase in alkalization at low current densities. Hence the pathway of hydrogen, in our experiments, starts with the H_2 molecules at the Al-rich passive layer and ends with hydrogen atoms in Fe_3Al bulk material steel.

3.3. ECNI

We implement ECNI in order to probe the bulk effect of the Cr addition to the Fe_3Al alloys in the presence of hydrogen. However, the XPS and electrochemical CV tests showed that the Cr addition to these alloys may alter some of the surface properties. Since the ECNI measures the nanomechanical properties just below the surface, it is a surface-sensitive technique [68]. Therefore we paid special attention to keeping the surface condition of the samples with different Cr content the same. Also, all other possible parameters, which may affect the nanomechanical response of the surface, are kept constant and unchanged by the following precautions. (i) In all samples, indentation was performed in the grains with the similar (0 0 1) normal orientation and also similar $\langle u,v,w\rangle$ directions. Detailed information about the necessity of the indentation on the grains with the same $\langle h,k,l\rangle$ and $\langle u,v,w\rangle$ is presented in Ref. [69]. (ii) The configuration of the Berkovich tip was kept the same for the ex situ and in situ indentations. (iii) The surface roughness at different polarizations was always checked before performing nanoindentation with the scanning probe microscope mode of our nanoindenter and checked for its consistency with the freshly electropolished surface roughness values. (iv) By selecting the anodic polarization at 500 mV_{SHE} according to the discussion in Section 3.2, the Al^{3+} enriched passive layer was stabilized for all samples and remained stable during the course of the ECNI tests. (v) In order to have a similar hydrogen charging condition (HER and/or hydrogen uptake and transfer through the passive layer) and exclude the Cr effect on hydrogen over potential (Fig. 4), the hydrogen charging was carried out in galvanostatic mode by the application of a 100 μA/cm^2 cathodic current density. By considering these provisions we were able to obtain perfectly reproducible and comparable nanoindentation results with a very low scatter, as shown in Fig. 5 for different studied samples. The load–displacement (L–D) curves start with a fully reversible elastic segment before the displacement burst (pop-in) occurs and followed by an elastoplastic deformation up to the maximum applied load and then fully elastic unloading. In the following sections we will focus on the effects of hydrogen on each of the mentioned segments of load–displacement curves.

3.3.1. Hydrogen effect on elastic properties

Since only the apex of the NI tip is in contact with the material during the initial elastic loading part and the tip at the apex can be approximated with a sphere, the initial elastic interactions between tip and surface could be modelled with the Hertzian contact theory (Eq. (8)) [30]:

$$P = \frac{4}{3}E_r R^{1/2} h^{3/2} \quad (8)$$

where P is the applied load, h is the penetration depth, R is the tip radius and the reduced elastic modulus (E_r) can be converted to the Young's modulus E from $\frac{1}{E_r} = \frac{1-\upsilon^2}{E} + \frac{1-\upsilon_T^2}{E_T}$. Here $E_T = 1140$ GPa and $\upsilon_T = 0.07$ [68] are the Young's modulus and Poisson's ratio of a diamond tip, respectively, and $\upsilon = 0.29$ [69] is the calculated Poisson's ratio of the sample. An accurate measurement of R is the key to a precise measurement of E_r. Using the advantage of the well-defined Young's modulus of fused quartz (69.6 GPa [68]),

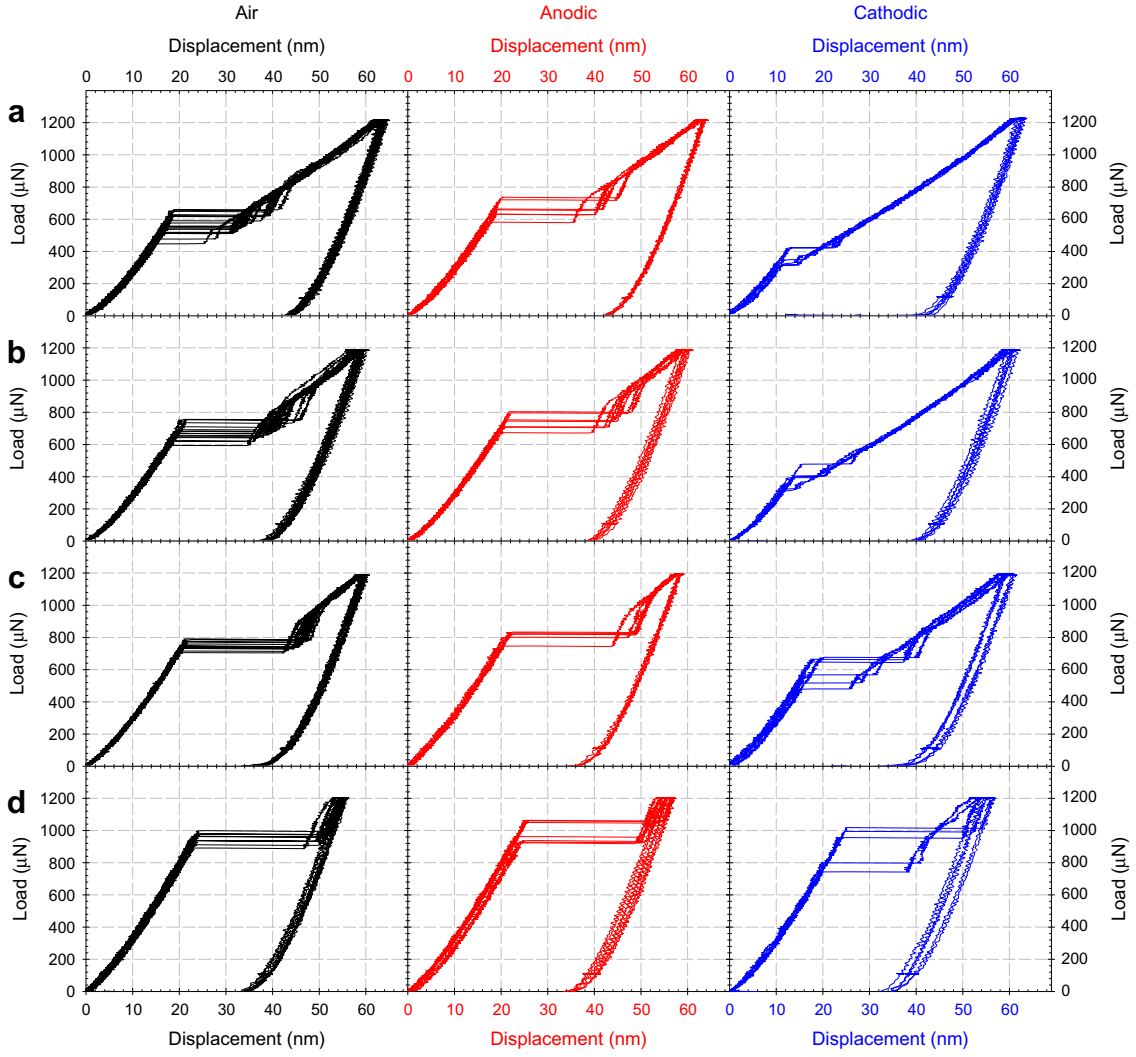

Fig. 5. Typical L-D curves in air (left), under anodic (centre) and cathodic (right) polarization: (a) Fe–26Al, (b) Fe–26Al–0.5Cr, (c) Fe–26Al–4Cr and (d) Fe–26Al–5Cr.

several fully elastic indents were made in fused quartz. Curves were fitted one by one with Eq. (8) to extract R at different maximum displacements (Fig. 6a). Fig. 6b shows that R remains constant at depths between 12 nm and 23 nm ($R = 1.47$ μm). The calculated radius was in agreement with the value measured with the aid of the reverse tip imaging method [69]. The changes of R at higher depths are due to the fact that the pyramidal part of the indenter will begin to penetrate into the sample where the spherical Hertzian contact theory is no longer applicable. For the E_r measurement of different samples, we fitted the first 15 nm of all L–D curves with Eq. (8).

Additionally, the O–P method [70,71] (Eq. (9)) could be used to measure the reduced Young's modulus by analysing the elastic unloaded segment as follows:

$$E_{r(O-P)} = \beta \frac{\sqrt{\pi}}{2\sqrt{A_c}} S \tag{9}$$

where A_c is the projected contact area determined by the O–P method, β is a correction factor depending on the tip geometry (1.034 for a Berkovich indenter) and $S = \partial P/\partial h$ is the slope of the L–D curve at the initial unloading segment. The Young's moduli, measured based on the Hertzian and O–P methods, are presented in Fig. 7a for each of the samples indented in air. The effect of pile-up and sink-in on the measured values of $E_{r(O-P)}$ was corrected based on the method described in Ref. [69]. The effect of hydrogen on the elastic modulus and repeatability of tests was also checked by switching the applied potential from anodic to cathodic, and the results are presented in Fig. 7b and c.

In general, the effect of hydrogen on elastic properties of metal is still under debate. This is due to the lack of experimental verification [37]. Hence, atomic simulation is mainly used to estimate the change in the elastic properties by hydrogen [72–74]. A molecular static simulation done by Taketomi et al. [73] showed a 10% reduction in shear modulus by 1 at.% hydrogen dissolved in Fe, which is in very good agreement with the experimental results of Lunarska et al. [74]. Based on our observations, the nano-indentation technique is capable of measuring the effect of hydrogen on the elastic modulus within the initial elastic loading sequence after using the Hertzian contact model.

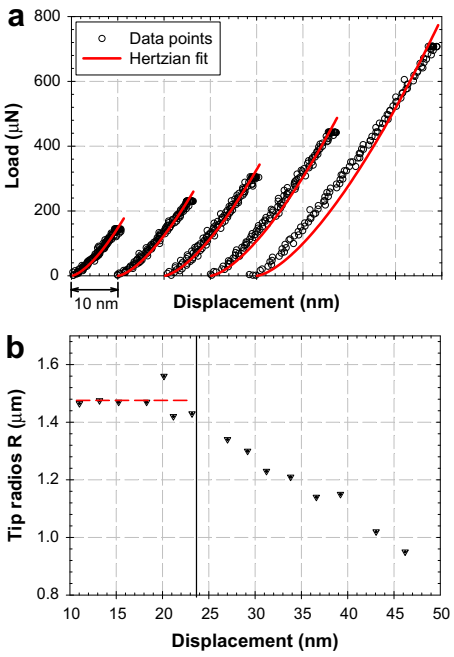

Fig. 6. (a) Elastic indentation on fused quartz. (b) The measured tip radius at different indentation depths.

In contrast, the O–P method, which is based on the final unloading sequence during nanoindentation, is not applicable for probing the effect of hydrogen on elastic properties. This is mainly due to the presence of high compressive stress, which works as driving force for the hydrogen diffusion out of the plastic region below the surface. The fast loading rate (500 μN/s) and the short time within the initial Hertzian elastic regime (1–2 s) are, however, too short for the H escape from the highly stressed region below the surface. Additionally, the large number of dislocations generated within the plastically deformed volume [75] trap and remove the hydrogen from the elastic field of the nanoindenter.

The Young's modulus is proportional to the second derivative of the crystal energy, U_c ($E = \frac{d^2U_c}{da^2}$), where a is the displacement field. According to Rose et al. [76–78] metallic binding-energy–distance curves can be approximately scaled into a single universal relationship for the cohesion of the bulk metals. The universality of cohesive energy in metals relates the reduction in the E to the reduction in cohesive force. In other words, it is possible to relate the reduction of the elastic properties to the reduction of metallic bonding energy; this is in favour of the hydrogen enhanced decohesion (HEDE) model for HE. However, the 3–5% reduction in interatomic binding forces could not be the only responsible mechanism for the HE of the Fe_3Al–xCr alloys.

3.3.2. Hydrogen effect on pop-in load

At the pop-in load, the indenter tip suddenly penetrates into the specimen without the load having to increase. It is shown experimentally [34,79] and through different atomistic and continuum computer simulations [80,81] that the pop-in load ($P_{pop\text{-}in}$) relates to the maximum shear stress ($\tau_{(max)}$) for HDN according to Eq. (10):

$$\tau_{(\max)} = 0.31\left(\frac{6E_r^2}{\pi^3 R^2}P_{pop-in}\right)^{\frac{1}{3}} \tag{10}$$

Dislocation nucleation is a stress-assisted, thermally activated process [82,83]. The critical stress for HDN may be determined by considering the concept of activation energy. At room temperature, where the available

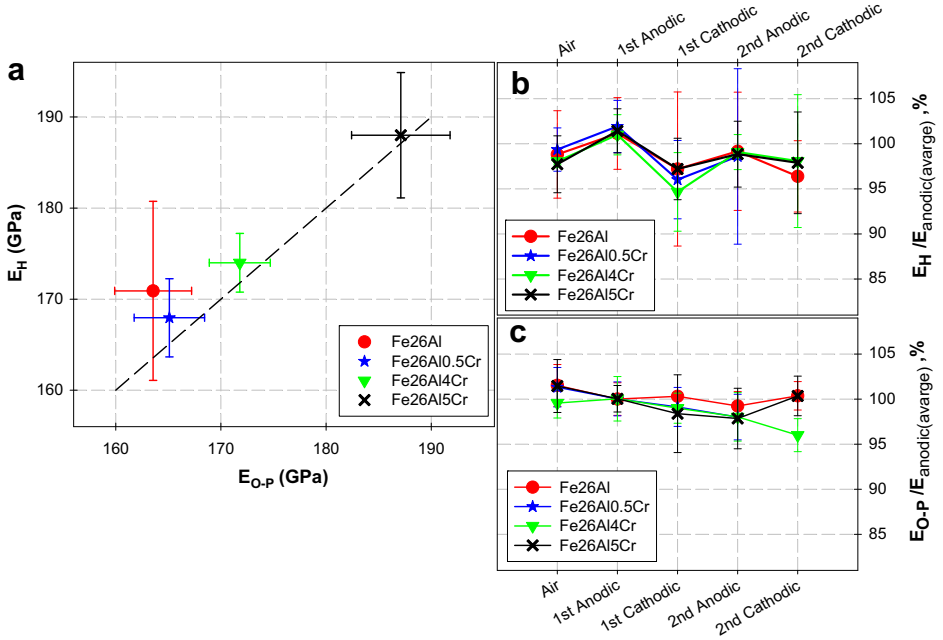

Fig. 7. (a) Elastic modulus of samples in air, measured based on Hertzian and O–P models. Effect of applied potential on the elastic modulus, calculated based on Hertzian (b) and O–P methods (c).

thermal energy is very small, HDN could happen at a critical applied shear stress($\tau_{(max)}$). Fig. 5 clearly shows that both the presence of hydrogen and Cr concentration alter the pop-in load in Fe_3Al intermetallic alloys. It was shown earlier that the change in the cohesive energy of the crystal by the addition of the Cr is responsible for the change in pop-in load [34]. In this paper we will mainly focus on the effect of interstitial hydrogen atoms on the pop-in load and consequently the resolved shear stress required for HDN. To begin, we will look at the effect of the applied potential on the pop-in loads (Fig. 8) to explain the decrease of the resolved shear stress required for HDN after cathodic charging and its recovery after anodic charging. This reproducible behaviour should ensure that the reduction at cathodic potentials is due to the adsorption of interstitial hydrogen atoms and not surface roughening during the nanoindentation. According to Eq. (10), lower values of the $P_{pop\text{-}in}$ after cathodic charging (Fig. 8a) is evidence for the lower $\tau_{(max)}$ needed for HDN (Fig. 8b). The $P_{pop\text{-}in}$ reduction by hydrogen in samples with low Cr content is significant in contrast to the samples with 5 at.% Cr.

The free energy required for HDN can be calculated by considering the line energy of the newly formed dislocation loop W_{dis} and the work for extending the loop $\tau_{(max)}b$ per loop area (πr^2) [84], which in the case of a circular loop could be expressed by the following equation:

$$\Delta G = 2\pi r W_{dis} - \pi r^2 b \tau_{max} \tag{11}$$

where r is the dislocation loop radius. The elastic self-energy for a full circular dislocation loop in an infinite isotropic elastic solid (W_{dis}) is given by:

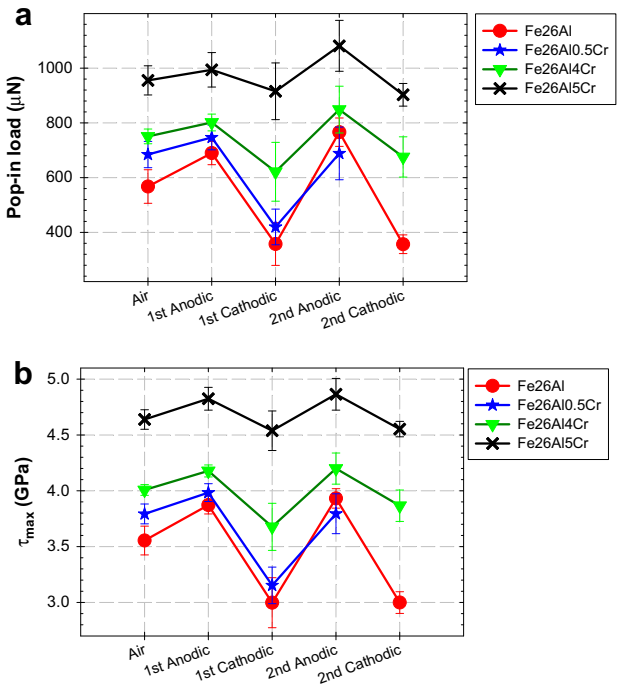

Fig. 8. (a) Effect of applied potential on the pop-in load; and (b) calculated maximum shear stress beneath the tip.

$$W_{dis} = \frac{2-\upsilon}{1-\upsilon}\frac{\mu b^2}{8\pi}\left(\ln\frac{4r}{\psi} - 2\right) \tag{12}$$

where ψ is the dislocation core radius. The effect of Cr content on the dislocation core radius was calculated in Ref. [34]. Considering Eqs. (11) and (12), ΔG can be rewritten as follows:

$$\Delta G = \frac{2-\upsilon}{1-\upsilon}\frac{\mu r b^2}{4}\left(\ln\frac{4r}{\psi} - 2\right) - \pi r^2 b \tau_{max} \tag{13}$$

At the pop-in load, the free energy for the formation of a dislocation loop passes through a maximum free energy (ΔG^*) at a critical loop radius r_c (Fig. 9), which defines the activation energy for the process of dislocation nucleation. ΔG^* can be calculated by setting $\delta\Delta G/\delta r = 0$. At a given applied stress, if the energy from thermal vibrations is sufficient to overcome this activation energy, then a dislocation loop is spontaneously emitted. Obviously, in the H-charged condition, the HDN process (pop-in) occurs in spite of the relatively high activation energy that it requires. The available thermal energy at room temperature is very low. Rice and Beltz [85] estimated that the available energy $\approx 30k_BT$. This value makes thermal activation of the HDN at typical pop-in loads under the H-charged condition impossible; hence, we can assume that H charging changes the material properties in such a manner that HDN at this load becomes possible.

We observed earlier that the hydrogen effect on the elastic modulus is insignificant. Following Eq. (13), the main influence of hydrogen atoms in Fe_3Al–xCr intermetallics is not on shear modulus ($\mu = E/2(1+\nu)$) but on the dislocation core radius ψ. The effects of hydrogen on the other parameters involved in Eq. (13) are either neglected or inapplicable [84]. Our current understanding of the core structure of dislocations is based on computer simulations that show a tendency for vacancy-like defects to form along the dislocation core [86]. Such defects trap hydrogen atoms substantially more than the peripheral strain field of dislocations or the anti-phase boundaries between superpartial dislocations. It is for this reason that the interaction between a dislocation's core and hydrogen is assumed to be so high. The strong hydrogen bonding to dislocation cores reported for Pd [87,88] could also confirm this theory. The core extending to a radius of about one Burgers vector was reported for iron, niobium and tantalum after hydrogen charging [89,90]. The reason for the reduction of the dislocation line energy in Fe_3Al intermetallics could be explained using the defect-acting agents (defactants) model. Segregation of hydrogen atoms to dislocations reduces their formation energy in the way that surfactants reduce surface energies in liquids [91,92]. Consequently, the solute energy is reduced, and this interaction can be described by assigning the decrease in the overall free energy to a decrease in the defect formation energy (defactants concept). Therefore, in the presence of hydrogen, the line energy of the newly formed loop and hence the formation energy of dislocations is reduced.

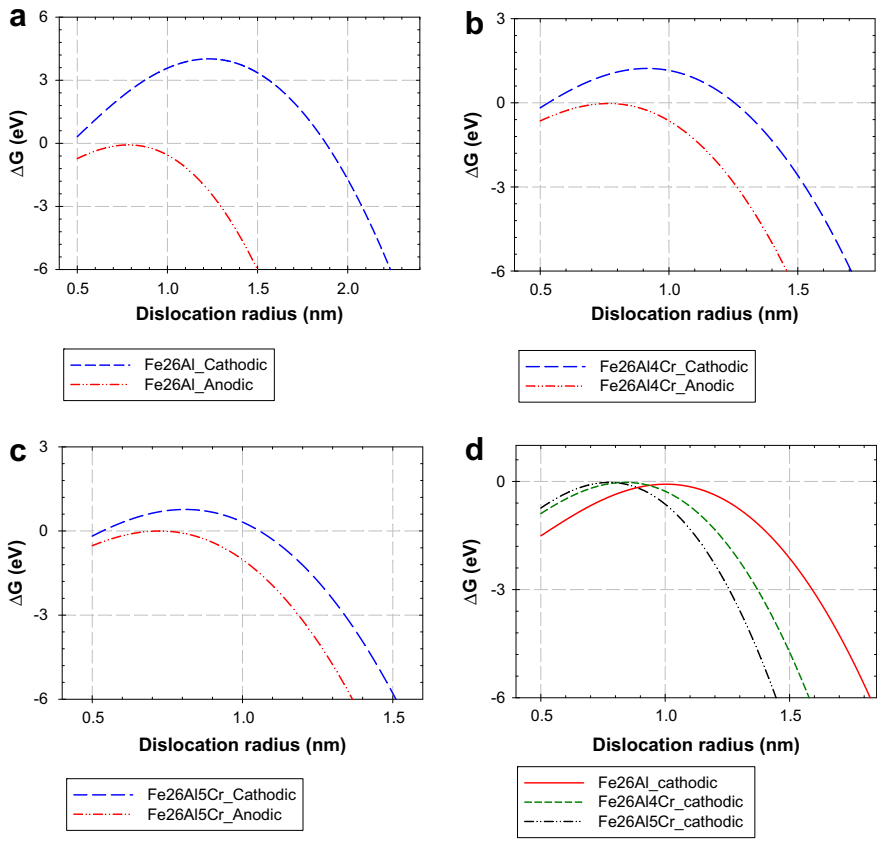

Fig. 9. Free energy curves for (a) Fe–26Al, (b) Fe–26Al–4Cr and (c) Fe–26Al–5Cr. The activation energy for homogeneous dislocation nucleation, ΔG^*, in all samples become zero after correction of the dislocation core radius (d).

If we include the effect of hydrogen on ψ and μ in Eq. (13), Eq. (14) can be rewritten as follows:

$$\Delta G = \frac{2-\upsilon}{1-\upsilon}\frac{\mu^H r b^2}{4}\left(\ln\frac{4r}{\psi^H}-2\right)-\pi r^2 b\tau_{\max} \qquad (14)$$

where ψ^H and μ^H are the hydrogen-affected dislocation core radius and shear modulus, respectively. Eq. (14) shows that the increase of the dislocation core radius with adsorption of hydrogen could decrease the dislocation line energy and ease the dislocation nucleation after adsorption of hydrogen. Based on the elastic constants and the maximum shear stress for HDN (reported earlier in this paper) and lattice constants of the intermetallics reported in Ref. [34], the increase of the dislocation core radius as a result of hydrogen charging was calculated. Fig. 10 shows clearly that the increment of ψ is more in samples without Cr (27%) and less in the sample with 5 at.% Cr (8%). Obviously enough, after correcting the core radius, the critical Gibbs free energy at cathodic potentials shifts to zero for all different samples (Fig. 9d), thereafter ensuring that the HDN will be energetically possible.

3.3.3. Hydrogen effect on the hardness

The physical definition of the hardness is not very straightforward, athough Tabor [93] defines hardness ($H = P/A_c$) as the resistance of a solid to local deformation.

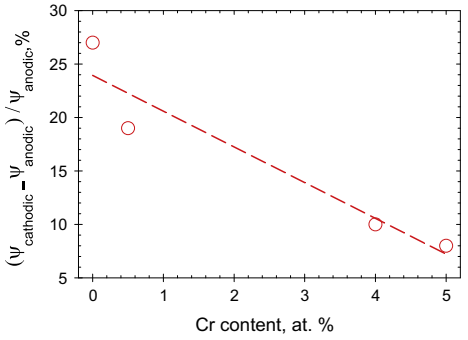

Fig. 10. Effect of hydrogen on the dislocation core radius for samples with different Cr content.

For a self-similar indenter (like a Berkovich) the instantaneous displacement rate of the indenter divided by the plastic depth is typically defined as the indentation strain rate ($\dot{\varepsilon} = \frac{dh}{dt} \times \frac{1}{h(t)}$). Hence, at a defined displacement rate and time of indentation, an increase of the plastic depth ($h(t) \approx A_c$ (see Appendix A)) causes a reduction of H and $\dot{\varepsilon}$. In our tests, the displacement rate was between 8 and 16 $\mu N\ s^{-1}$ in the elastoplastic regime for all samples. Based on the modified version of the Orowan equation [92,94], the effect of hydrogen on the strain rate ($\dot{\varepsilon}$) of a plastically deformed material could be expressed as follows:

$$\dot{\varepsilon} = \frac{b\rho d}{t_g + t_m} \tag{15}$$

where ρ is the density of dislocations, d is the distance a double kink moves the dislocation ahead (for instance the distance between two Peierls valleys), t_g is the time constant for double kink generation and t_m is the time necessary to move the kinks to the ends of a dislocation line. Mobile dissolved hydrogen atoms could influence both parameters t_g and t_m, which depend on the material and hydrogen concentration [92]. It was shown earlier that the adsorption of hydrogen decreases the elastic self-energy of dislocation with the reduction μ^H and increment of ψ^H (Eq. (14)). It caused the reduction of the shear stress needed for HDN; we can also expand it to decrease the kink formation energy within the dislocations. The reduction of t_g may cause softening in the material. In contrast, as is shown in Fig. 11, an increase in the measured hardness values was measured after electrochemical hydrogen charging. It could be due to the contribution of the hydrogen on the t_m. In the following we will explain the effect of hydrogen on the mobility of dislocations in the Fe_3Al iron aluminides.

To describe the dependency of hardness on the indentation depth, we follow the Taylor relation-based approach developed by Nix and Gao [95,96]. We can apply the von Mises flow rule ($\sigma = \sqrt{3}\tau$) and Tabor's relation ($H = 3\sigma$) in order to convert the equivalent flow stress, σ, to the hardness, as follows [97]:

$$H = 3\sqrt{3}\tau \tag{16}$$

During the nanoindentation of a single phase large grain material, other hardening mechanisms, e.g. grain boundaries and precipitates, are absent and the only mechanism which controls the flow stress is the dislocation movement, i.e. lattice friction (τ_{P-N}), and the dislocation–dislocation interaction, i.e. forest hardening, and depends on the densities of statistically stored dislocations (ρ_{SSD}) and the density of geometrically necessary dislocations (ρ_{GND}) [95,96]. Therefore, the shear flow stress (τ) could be formulated as follows:

$$\tau = \tau_{P-N} + \varphi\mu b\sqrt{\rho_{SSD} + \rho_{GND}} \tag{17}$$

where φ is an empirical factor depending on dislocation structures. In the case of a pure metal or ordered intermetallic the Peierls and Nabarro models predict the friction stress of dislocations (τ_{P-N}) as follows [98]:

$$\tau_{P-N} = \frac{\mu(0.15 + 0.03(b/\xi k)}{(1-\upsilon)} \exp\left(\frac{-2\pi\xi k}{b}\right) \tag{18}$$

where k is the distance between slip planes and $\xi = 1/(2(1-\upsilon))$.

The ρ_{SSD} is defined by the so-called depth independent hardness as follows:

$$\rho_{SSD} = \frac{1}{3}\left(\frac{\sigma_{flow}}{\varphi\mu b}\right)^2 \tag{19}$$

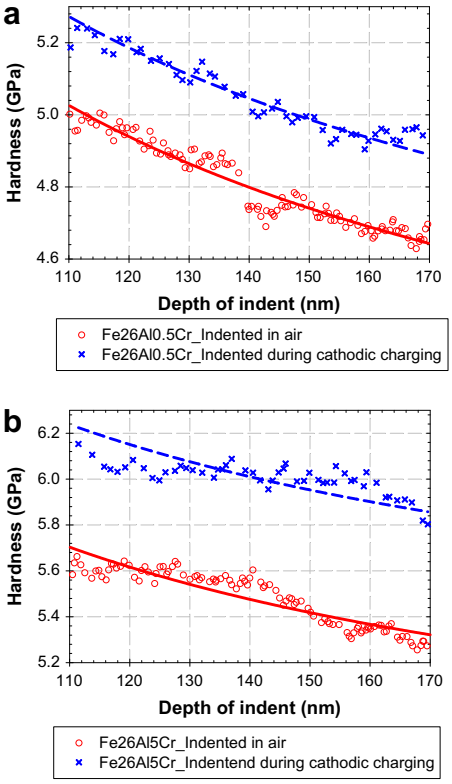

Fig. 11. Effect of hydrogen on the hardness of Fe_3Al intermetallics: (a) Fe–26Al–0.5Cr and (b) Fe–26Al–5Cr.

where σ_{flow} is related to the flow stress in uniaxial tension without accounting for the effect of the intrinsic lattice resistance or microstructural features like grain boundaries. Therefore it is only a function of the SSD density in the material. The density of geometrically necessary dislocations relates to the geometry of the tip and magnitude of the Burgers vector as follows [69]:

$$\rho_{GND} = \frac{3}{2bh}\tan^2\alpha \tag{20}$$

Here α is the angle between the surface of the indenter and the surface plane of the indented material. It could be measured after precise characterization of the tip with the method presented in Ref. [69]. Finally the changes of the hardness at different depths could be formulated as follows:

$$H = 3\left[\sqrt{\sigma_{flow}^2 + \frac{9}{2h}\varphi^2\mu^2 b\tan^2\alpha} + \sqrt{3}\tau_{P-N}\right] \tag{21}$$

Eq. (21) shows that the changes of the hardness could be due to the influence of hydrogen atoms on shear modulus (μ^H) and/or friction stress (τ_{P-N}^H). The flow stress (σ_{flow}) would not change as long as the H-charging condition was kept in such a way as to ensure that there was no increase in the dislocation density due to H charging. This is guaranteed in our test by having the same pop-in statistic before and after H charging, since, if H charging had been been changing the ρ_{SSD} there would be less probability of pop-in observation, and this should remain the same even

after H discharging at anodic polarization. The other parameters in Eq. (21) are constants or geometrical parameters and are not influenced by the hydrogen presence. It was shown that the shear stress decreases after hydrogen charging. Therefore, the increase of the hardness should be due to the increase of the friction stress after hydrogen charging. Because the depth of indents in our test is limited to some nanometers, we can expect the relatively high concentrations of hydrogen. This means that the formation of the Cottrell atmospheres around the kinks will raise the dragging forces, and therefore hydrogen will increase significantly the t_m ($t_m \gg t_g$), causing hardening in the samples. We tried to quantitatively calculate the τ_{P-N}^{H} by fitting the experimental data for the H-charged condition with Eq. (21). The results show that H increases the friction stress by 16.3% and 34.8% in the samples with 0.5 and 5 at.% chromium, respectively. The reason for the larger effect of the H in the samples with higher Cr content is not clear. It could be due to the lower rate of the diffusion of the H in the more highly alloyed sample [15].

3.4. Cr effect on HE in Fe_3Al–xCr

Numerous mechanisms have been proposed to explain the effect of hydrogen on the mechanical properties of various materials [99–101]. Some of the most commonly cited HE mechanisms include (i) reduction of the cohesive strength of the lattice, encouraging cleavage-like failure [102–106], according to the HEDE model; (ii) facilitation of the emission of dislocations from crack tips based on the adsorption induced dislocation emission (AIDE) model [107–109]; (iii) formation of Cottrell atmospheres around dislocation cores and causing embrittlement by reducing the dislocation line energy and easing the dislocation nucleation, according to the defactants theory [91]); (iv) facilitation of the movement of dislocations (hydrogen-enhanced local plasticity (HELP) [110,111]); (v) reduction of the stacking fault energies (RSF) and limiting the cross-slipping of dislocations [100,101,112,113]. Even for materials with identical types of bonds, it is highly unlikely that there is just one mechanism capable of explaining HE. Different mechanisms may operate in different orders, depending on the material, environmental and mechanical parameters.

In general, at a constant temperature, and in the absence of any kind of phase transformation, the energy of the newly formed surfaces (due to the crack growth) is an intrinsic characteristic of material. The hydrogen ingress into the studied intermetallics can influence this new surface energy with the reduction of the shear modulus (μ) and hence the strength of interatomic bonds, as predicted by the HEDE mechanism. On the other hand, the presence of hydrogen controls the multiplication or movement of dislocations (ψ and τ_{P-N}, respectively) in agreement with the defactants, AIDE, HELP and RSF. However, the magnitude of the influence of hydrogen on μ, ψ and τ_{P-N} is different for various intermetallics. Our results show that the alloys with high chromium content exhibit higher friction stress after hydrogen charging, but, in the case of alloys with low chromium contents, the main influence of hydrogen is on the dislocation nucleation process.

Note that all the mentioned parameters (energy of the newly formed surfaces, multiplication or movement of dislocations) are key components of a ductile-to-brittle fracture transition [114]. In the classical theory of dislocation shielding of a singular crack, the effective stress intensity factor K_e at the crack tip is expressed as [114]:

$$K_e = K + K_D \tag{22}$$

where K and K_D are stress intensity factors induced by the externally imposed loading and dislocations, respectively. Fracture takes place when K_e reaches a critical value of K_C. The crack is said to be shielded by dislocations when $K_D \prec 0$ and anti-shielded when $K_D \succ 0$. Therefore, the growth rate of cracks will depend on the mobility of dislocations and the energy for dislocation nucleation. Our results show that the hydrogen decreased:

1. the shear modulus of materials;
2. the energy for dislocation nucleation; and
3. the mobility of dislocations.

In other words, adsorption of hydrogen will ease nucleation of sessile dislocations. Therefore, the shielding effect of dislocations will decrease. Finally, it favours the cleavage fracture of alloys. It shows that the mechanism of dislocation shielding should be considered for analysing the fracture characteristics of Fe_3Al in atmospheres containing hydrogen. Binary alloys, however, are very sensitive to HE because of the strong reduction of the energy needed for HDN after hydrogen charging. The addition of chromium, along with its influence on the reduction of flat-band potential, decreases the susceptibility of binary alloys to the HE because the core radius does not change significantly after hydrogen charging.

4. Conclusion

In this work, the influence of the Cr content on the susceptibility of Fe–26Al–xCr intermetallics to HE was evaluated with the aid of the in situ nanoindentation technique. Our experimental results show that hydrogen decreases the Young's modulus and dislocation mobility. It also affects the Gibbs free energy needs for homogeneous dislocation nucleation. This effect is because the addition of physically adsorbed hydrogen increases the dislocation core radius.

Chromium addition to the intermetallics as a ternary alloying element, while it changes slightly the thickness and protectively of the passive layer, does (i) decrease the flat-band potential; (ii) increase the pop-in load measured in air, showing a strengthening of the interatomic bonds; (iii) decrease the susceptibility of alloys to moisture-induced embrittlement; and (iv) decrease the reduction of the pop-in load after applying a cathodic potential, another sign of decreased sensitivity to HE in Cr-enriched alloys.

Acknowledgments

The authors wish to thank Prof. Christian Motz for his advice and help, Dr. M. Palm, Dr. M. Rohwerder and Dr. S. Merzlikin of Max Planck Institute Eisenforsch GmbH for supporting the materials and performing XPS measurement, A.L. Maxfield for proofreading and additionally DFG for financial support.

Appendix A

The continuous hardness measurement was calculated based on the following formula [53]:

$$H = \frac{P + P_{AC}}{A_c} \tag{A1}$$

where P_{AC} is the dynamic actuation force. The definition of the contact area (A_c) was performed similar to the standard indentation analysis with indentation on a fused quartz with well-defined mechanical properties, little pile-up and indentation size dependency as follows [53]:

$$A_c = C_0 h_c^2 + C_1 h_c + C_2 h_c^{\frac{1}{2}} + C_3 h_c^{\frac{1}{4}} + C_4 h_c^{\frac{1}{8}} + C_5 h_c^{\frac{1}{16}} + B \tag{A2}$$

where the constants $C_0 - C_5$ and also an offset factor (B) are the fitting parameters. The contact displacement (h_c) for the nanoDMA III analysis could be calculated as:

$$h_c = (h + h_{Ac}) - \varepsilon \times \frac{P + P_{AC}}{k_{storage}} \tag{A3}$$

where h is the maximum displacement, h_{AC} is the dynamic displacement, ε is defined as a geometric constant related to the probe, P is the applied quasistatic force, P_{AC} is the dynamic actuation force and $k_{storage}$ is the storage stiffness. $k_{storage}$ is calculated by the following equation:

$$k_{storage} = \frac{P_{AC} \times \cos(\theta) + m_T \times \bar{\omega}}{h_{AC}} - k_T \tag{A4}$$

where θ is phase shift between dynamic force and displacement fluctuations, m_T is defined as the mass of the transducer, $\bar{\omega}$ is the radial frequency and k_T is defined as the stiffness of the transducer.

References

[1] Friák M, Deges J, Krein R, Frommeyer G, Neugebauer J. Intermetallics 2010;18:1310.
[2] Morris DG, Muñoz-Morris MA. Intermetallics 2005;13:1269.
[3] Brinck A, Neuhäuser H. Mater Sci Eng A 2004;387:969.
[4] Liu CT, Lee EH, McKamey CG. Scripta Metall Mater 1989;23:875.
[5] Liu CT, McKamey CG, Lee EH. Scripta Metall Mater 1990;24:385.
[6] Castagna A, Stoloff NS. Mater Sci Eng A 1995;192:399–406.
[7] Alven DA, Stoloff NS. Mater Sci Eng A 1997;239–240:362.
[8] Barnoush A, Dake J, Kheradmand N, Vehoff H. Intermetallics 2010;18:1385.
[9] McKamey CG, Horton JA, Liu CT. J Mater Res 1989;4:1156.
[10] Balasubramaniam R. Scripta Mater 1996;34:127.
[11] Fu CL, Painter GS. J Mater Res 1991;6:719.
[12] Johnson DF, Carter EA. Acta Mater 2010;58:638.
[13] Hirth JP. Metall Trans A – Phys Metall Mater Sci 1980;11:861.
[14] Cheng XY, Wan XJ. Scripta Mater 1998;38:1505.
[15] Banerjee P, Balasubramaniam R. Scripta Mater 1998;39:1215.
[16] Yang Y, Hanada S. Scripta Metall Mater 1995;32:1719.
[17] Kupka M, Stepien K. Corros Sci 2009;51:699.
[18] Luu WC, Wu JK. J Mater Sci 2000;35:4121.
[19] Stepien K, Kupka M. Scripta Mater 2006;55:585.
[20] Prakash U, Parvathavarthini N, Dayal RK. Intermetallics 2007;15:17.
[21] Kimizuka H, Mori H, Ogata S. Phys Rev B 2011;83:094110.
[22] Bockris JOM, Genshaw MA, Fullenwider M. Electrochim Acta 1970;15:47.
[23] Song RH, Pyun SI, Oriani RA. J Electrochem Soc 1990;137:1703.
[24] Ruetschi P, Giovanoli R. J Electrochem Soc 1988;135:2663.
[25] Lee WK, Nowick AS, Boatner LA. Solid State Ion 1986;18–19:989.
[26] Song RH, Pyun SI, Oriani RA. Electrochim Acta 1991;36:825.
[27] Zhang G, Wang X, Yang F, Shi Y, Song J, Lai X. Int J Hydrogen Energy 2013;38:7550.
[28] Zamanzade M, Barnoush A. Corosr Sci 2014;78:223.
[29] Hollenberg WG, Simonen EP, Kalinin G, Terlain A. Fusion Eng Des 1995;28:190.
[30] Fischer-Cripps AC. Nanoindentation. New York: Springer; 2004.
[31] Morris JR, Bei H, Pharr GM, George EP. Phys Rev Lett 2011;106:165502.
[32] Durst K, Backes B, Franke O, Göken M. Acta Mater 2006;54:2547.
[33] Engels P, Ma A, Hartmaier A. Int J Plast 2012;38:159.
[34] Barnoush A, Zamanzade M. Philos Mag 2012;92:25.
[35] Li TL, Gao YF, Bei H, George EP. J Mech Phys Solids 2011;59:1147.
[36] Lodes MA, Hartmaier A, Göken M, Durst K. Acta Mater 2011;59:4264.
[37] Barnoush A. Acta Mater 2012;60:1268.
[38] Salehinia I, Lawrence SK, Bahr DF. Acta Mater 2013;61:1421.
[39] Shim S, Bei H, George EP, Pharr GM. Scripta Mater 2008;59:1095.
[40] Sudharshan Phani P, Johanns KE, George EP, Pharr GM. J Mater Res 2013;28:2728.
[41] Henning M, Vehoff H. Acta Mater 2005;53:1285.
[42] Viswanathan GB, Lee E, Maher DM, Banerjee S, Fraser HL. Mater Sci Eng A 2005;400–401:463.
[43] Barnoush A, Welsch MT, Vehoff H. Scripta Mater 2010;63:465.
[44] Barnoush A, Vehoff H. Corros Sci 2008;50:259.
[45] Barnoush A, Vehoff H. Int J Mater Res 2006;97:1224.
[46] Barnoush A, Vehoff H. Scripta Mater 2008;58:747.
[47] Asgari M, Barnoush A, Johnsen R, Hoel R. Corros Sci 2012;62:51.
[48] Barnoush A, Asgari M, Johnsen R. Scripta Mater 2012;66:414.
[49] Asgari M, Barnoush A, Johnsen R, Hoel R. Tribol Int 2013;61:109.
[50] Asgari M, Barnoush A, Johnsen R, Hoel R. Mater Sci Eng A 2011;529:425–34.
[51] Wang Z, Bei H, George EP, Pharr GM. Scripta Mater 2011;65:469.
[52] Stein F, Schneider A, Frommeyer G. Intermetallics 2003;11:71.
[53] TriboIndenter user manual. Minneapolis: Hysitron Incorporated; 2011.
[54] Schaepers D, Strehblow HH. Corros Sci 1997;39:2193.
[55] Gudic S, Radosevic J, Krpan-Lisica D, Kliskic M. Electrochim Acta 2001;46:2515.
[56] Ramasubramanian H, Preocanin N, Davidson RD. J Electrochem Soc 1986;133:C303.
[57] Flis J, Flis-Kabulska I, Zakroczymski T. Electrochim Acta 2009;54:1810.
[58] Misawa T. Corros Sci 1973;13:659.
[59] Diez-Perez I, Gorostiza P, Sanz F, Muller C. J Electrochem Soc 2001;148:B307.
[60] Oblonsky LJ, Davenport AJ, Ryan MP, Isaacs HS, Newman RC. J Electrochem Soc 1997;144:2398.
[61] Ramasubramanian N, Preocanin N, Davidson RD. J Electrochem Soc 1985;132:793.
[62] Pourbaix M. Lectures on electrochemical corrosion. New York: Plenum; 1973.
[63] Takahashi H, Nagayama M. Electrochim Acta 1978;23:279.
[64] Azumi K, Ueno T, Seo M. J Electroanal Chem 2004;567:1.

[65] Frangini S, Giorgi R, Lascovich J, Mignone A. Surf Interface Anal 1994;21:435.
[66] Franchy R. Surf Sci Rep 2000;38:195.
[67] Harrington SP, Wang F, Devine TM. Electrochim Acta 2010;55:4092.
[68] TriboIndenter User Manual. Minneapolis: Hysitron Inc.; 2006.
[69] Zamanzade M, Vehoff H, Barnoush A. Intermetallics 2013;41:28.
[70] Oliver WC, Pharr GM. J Mater Res 1992;7:1564.
[71] Golovin Y. Phys Solid State 2008;50:2205.
[72] Wen M, Barnoush A, Yokogawa K. Comput Phys Commun 2011;182:1621.
[73] Taketomi S, Matsumoto R, Miyazaki N. Int J Mech Sci 2010;52:334.
[74] Lunarska E, Zielinski A, Smialowski M. Acta Metall 1977;25:305.
[75] Chateau JP, Delafosse D, Magnin T. Acta Mater 2002;50:1507.
[76] Rose JH, Ferrante J, Smith JR. Phys Rev Lett 1981;47:675.
[77] Rose JH, Smith JR, Guinea F, Ferrante J. Phys Rev B 1984;29:2963.
[78] Rose JH, Smith JR, Ferrante J. Phys Rev B 1983;28:1835.
[79] Korte S, Clegg WJ. Acta Mater 2010;58:59.
[80] Begau C, Hartmaier A, George EP, Pharr GM. Acta Mater 2011;59:934.
[81] Wen M, Li Z. Comput Phys Commun 2012;54:28.
[82] Bei H, Gao YF, Shim S, George EP, Pharr GM. Phys Rev B 2008;77. 060103-1.
[83] Schuh CA, Lund AC. J Mater Res 2004;19:2152.
[84] Barnoush A. Acta Mater 2010;58:5274.
[85] Rice R, Beltz GE. J Mech Phys Solids 1994;42:333.
[86] Hakkinen H, Makinen HS, Manninen M. Phys Rev B 1990;41:12441.
[87] Kirchheim R. Acta Metall 1981;29:835.
[88] Rodrigues JA, Kirchheim R. Scripta Metall Mater 1983;17:159.
[89] Kumnick A, Johnson H. Acta Metall Mater 1980;28:33.
[90] Funk G, Schultz H. Z Metallkd 1985;76:311.
[91] Kirchheim R. Scripta Mater 2010;62:67.
[92] Kirchheim R. Scripta Mater 2012;67:767.
[93] Tabor D. The hardness of metals. New York: Oxford University Press; 1951.
[94] Argon AS. Strengthening mechanisms in crystal plasticity. Oxford: Oxford University Press; 2006.
[95] Qiu X, Huang Y, Nix WD, Hwang KC, Gao HJ. Acta Mater 2001;49:3949.
[96] Feng G, Nix WD. Scripta Mater 2004;51:599.
[97] Nix WD, Gao HJ. J Mech Phys Solids 1998;46:411.
[98] Nabarro FRN. Philos Mag A 1997;75:703.
[99] Robertson IM. Eng Fract Mech 2001;68:671.
[100] Ferreira PJ, Robertson IM, Birnbaum HK. Influence of hydrogen on the stacking-fault energy of an austenitic stainless steel. Material science forum. Zurich: TransTech Publications; 1996.
[101] Tang XG, Thompson A. Mater Sci Eng A 1994;186:113.
[102] Johnson HH, Morlet JG, Troiano AR. Trans Am Inst Min Met Eng 1958;212:528.
[103] Whiteman MB, Troiano AR. Corrosion 1965;21:53.
[104] Wriedt HA, Oriani RA. Acta Metall 1970;18:753.
[105] Oriani RA. Acta Metall 1970;18:147.
[106] Oriani RA, Josephic PH. Acta Metall 1979;27:997.
[107] Lynch SP. Scripta Mater 2009;61:331.
[108] Gangloff RP, Somerday BP. Gaseous hydrogen embrittlement of materials in energy technology, vol. 1. Cambridge: Woodhead; 2012.
[109] Gangloff RP, Somerday BP. Gaseous hydrogen embrittlement of materials in energy technologies, vol. 2. Cambridge: Woodhead; 2012.
[110] Ferreira PJ, Robertson IM, Birnbaum HK. Acta Mater 1998;46:1749.
[111] Ferreira PJ, Robertson IM, Birnbaum HK. Acta Mater 1999;47:2991.
[112] Cornet M, Trichet MF, Talbotbesnard S. Mem Etud Sci Rev Met 1977;74:307.
[113] Ulmer DG, Altstetter CJ. Acta Metall Mater 1991;39:1237.
[114] Hirsch PB, Roberts SG. Philos Mag A 1991;64:55.

Paper E

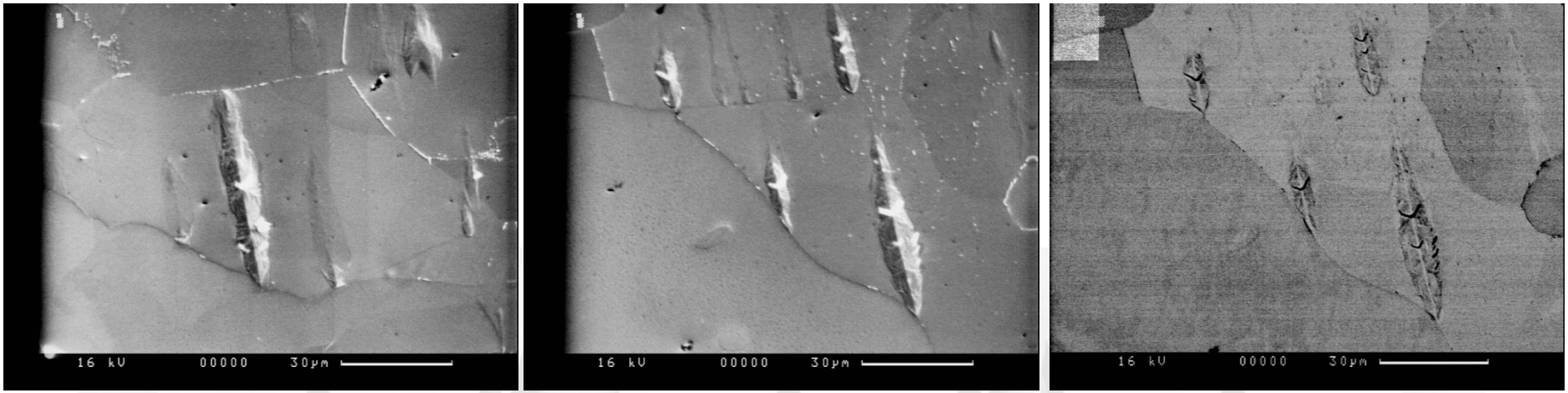
16 kV 00000 30µm
16 kV 00000 30µm
16 kV 00000 30µm

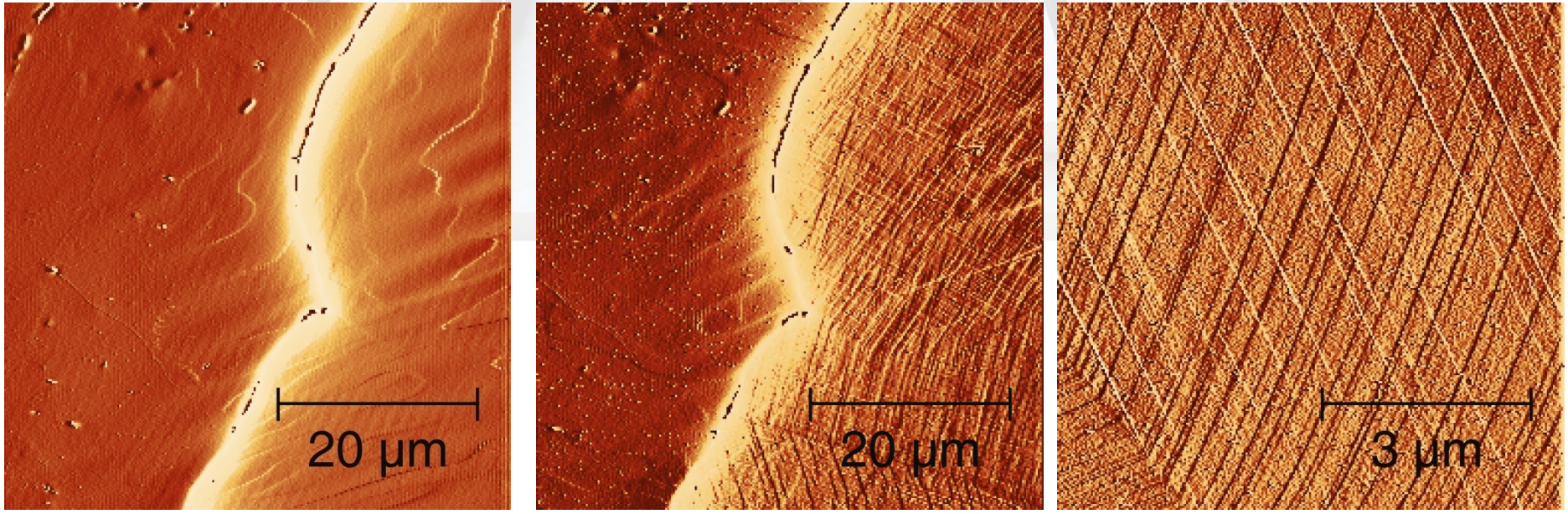
20 µm
20 µm
3 µm

Available online at www.sciencedirect.com
ScienceDirect
Scripta Materialia 62 (2010) 242–245
Scripta MATERIALIA
www.elsevier.com/locate/scriptamat

Direct observation of hydrogen-enhanced plasticity in super duplex stainless steel by means of in situ electrochemical methods

Afrooz Barnoush,* Mohammad Zamanzade and Horst Vehoff

Saarland University, Department of Materials Science, Bldg. D22, P.O. Box 151150, D-66041 Saarbruecken, Germany

Received 6 August 2009; revised 5 November 2009; accepted 6 November 2009
Available online 11 November 2009

In situ electrochemical hydrogen charging in combination with atomic force microscopy and optical microscopy has been used to study the effect of hydrogen on the austenite phase in super duplex stainless steel. Observations showed that hydrogen charging results in an irreversible deformation of austenite. High residual tensile stresses form in austenite during quench annealing. These stresses, in combination with the activation of dislocation sources by hydrogen, result in formation of slip lines on the austenite surface during in situ hydrogen charging.

Keywords: Hydrogen embrittlement; Dislocation; Residual stress; Magnetic force microscopy; Atomic force microscopy

Super duplex stainless steels (SDSS) are highly alloyed two-phase steels with excellent resistance against localized corrosion. They are used in especially demanding environments found in the chemical, oil and gas industries. The very favorable properties of SDSS fail due to hydrogen embrittlement (HE) [1]. In spite of the vast study of HE in SDSS, the mechanism of HE in this alloy is still not completely understood [2]. This is mainly because SDSS consist of two phases with different physical properties, specifically from the view point of HE. For example, austenite (γ) and ferrite (α) phases in SDSS have different solubilities and diffusivities for hydrogen. Therefore it is necessary to study HE on the scale of the individual phases. Previously it has been shown that local mechanical testing methods like nanoindentation in combination with in situ hydrogen charging (H-charging) can be successfully used for examination of HE [3–6]. In the case of SDSS, due to their complex microstructure, primary nanoindentation experiments [7,8] showed continuous microstructural changes in austenite when moderate H-charging was applied which made the nanoindentation measurements unreliable. The purpose of this paper is to examine and understand the effect of H-charging alone on austenite in SDSS.

The SDSS cylindrical sample (∅12 mm and 5 mm thickness) was cut from an SAF 2507® slab provided by OUTOKUMPU. The composition provided by the supplier is given in Table 1. The sample was in the solution annealed condition, having been heat treated at 1120 °C for 45 min and quenched in water. The ferrite content was 46% according to the supplier's test results.

Standard surface preparation, including mechanical polishing to 1 μm with diamond paste followed by electropolishing in H_2SO_4/methanol, was used. Because of the different surface binding energies of α and γ, the connected grains of both phases can be distinguished easily from each other by their shape. The austenite grain clusters are preferentially convex, whereas the ferrite grains fill the space between these grain clusters and are elevated (Fig. 1a).

A Zeiss optical microscope with a differential interference contrast was used to study the microstructural evolution on the surface during in situ electrochemical charging of the sample inside a specially designed cell. For the electrochemical cell, a three-electrode electrochemical setup with a platinum counter electrode and an Ag/AgCl reference electrode was developed. Details of the electrochemical cell are given elsewhere [3,4]. All potentials are reported against the Ag/AgCl reference electrode. The electrochemical H-charging was performed in 0.1 M Na_2SO_4 aqueous solution (pH 6) without the addition of any promoter. The same electrochemical setup was used in combination with a Digital Instruments Dimension 3000® atomic force microscope (AFM) with a special tip holder for imaging in fluids. The in situ imaging was performed in contact mode with an ultrasharp tip. In order to observe the changes in the topography the images were taken in deflection mode.

* Corresponding author. E-mail: a.barnoush@matsci.uni-sb.de

1359-6462/$ - see front matter © 2009 Acta Materialia Inc. Published by Elsevier Ltd. All rights reserved.
doi:10.1016/j.scriptamat.2009.11.007

Table 1. Composition of SDSS used in this study as provided by the supplier.

Element	C	Si	Mn	P	S	Cr	Ni	Mo	N
wt.%	0.016	0.23	0.79	0.021	0.001	25	6.98	3.82	0.27

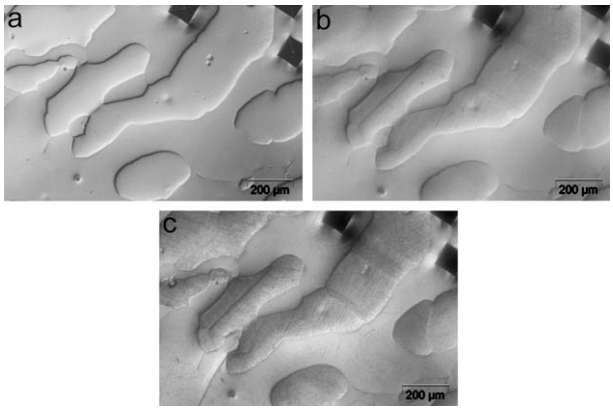

Figure 1. In situ OM shows the formation of slip lines on austenite due to H-charging. (a) Electropolished surface before H-charging. (b) After H-charging for 1 h at −1300 mV. (c) After H-charging for 5 h at −1300 mV.

The same AFM was used for magnetic force microscopy (MFM). For X-ray diffraction (XRD) measurements, a PANalytical X'Pert MRD diffractometer with a Cu X-ray source was used.

Figure 1a shows the optical micrographs of the sample before in situ electrochemical H-charging. The sample was then covered with a 2 mm thick layer of electrolyte and polarized to −1300 mV (~ 10 mA/cm^2), which resulted in moderate hydrogen evolution on the surface that did not disturb the image. The microstructural evolutions on the surface were observed continuously. Figure 1b shows the surface of the sample in exactly the same position as in Figure 1a (microindents as reference) after 1 h of charging. The evolution of slip lines on the surface of the austenite can be easily seen, while there was no change in the ferrite grains. The optical microscope's large field of view proved that the similar slip lines evolved all around the sample in the austenite phase. Examination of the ferrite phase did not reveal any slip line formation. This is worth mentioning because there were no external forces applied to the surface during in situ charging. Furthermore, during installation of the sample in the electrochemical cell, special care was taken to ensure that no stresses would be applied to the sample [8]. By increasing the charging time, the density of slip lines increased. Figure 1c shows the same position as in Figure 1a after 5 h of charging. The whole process of in situ H-charging can be seen online in the Supplementary video data. A large field of view and fast real time observation ability within OM were useful in revealing the hydrogen-induced plasticity in all austenite grains of the sample surface. In order to improve the spatial resolution, the same in situ experiments were performed with the AFM. While the sample was immersed in solution and H-charged, changes in the surface topography (deflection) were studied. Figure 2a

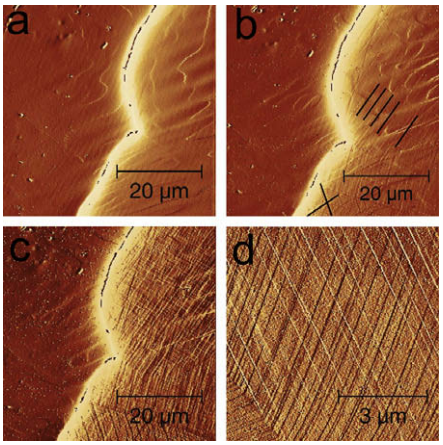

Figure 2. EC-AFM deflection mode images form the surface of the sample during in situ electrochemical H-charging. (a) Before H-charging at the OCP; on the left is a ferrite grain and on the right is an austenite grain which can be easily distinguished by its convex grain boundary. (b) The image of the same position after 1 h of in situ H-charging. (c) The image of the same position after 2.5 h of in situ H-charging. (d) Higher magnification image from the surface of the austenite grain.

shows the surface of the sample before H-charging at open circuit potential (OCP). In Figure 2a the austenite grain with its convex grain boundary on the right-hand side can be easily distinguished. Figure 2b was taken after 1 h of H-charging at −1200 mV (a lower potential in order to inhibit bubble formation). While there were no observable changes in ferrite, formation of slip lines on the surface of austenite can be seen (some of the slip lines are marked). After H-charging for 2.5 h, the density of slip lines had increased further. This is shown in Figure 2c and d at higher magnification. The evolution of the slip lines seemed to stop or slow down after a few hours of charging, and this was not resolved within the time scale of our experiments. The kinetics (i.e. potential and time dependence) of slip lines evolution can be studied with quantitative information about the height of the slip lines provided by the electrochemical (EC)-AFM. In this paper we are focused on mechanism of hydrogen induced slip line formation.

Austenitic stainless steels that contain less than about 18 wt.%Ni are known to transform to ϵ and α' martensites under the influence of strain or subzero cooling [9]. It has been reported that this transformation can be triggered by H-charging as well [10,11]. Although the charging condition in our experiment was more moderate than the condition required for triggering martensitic transformation [9,11], we used MFM and XRD to check the formation of any martensite. Figure 3 shows the MFM and atomic force microscopy images of an austenite grain in the sample after H-charging and formation of slip lines. Figure 3a shows the topography image (height mode) with hydrogen induced slip lines in austenite. In the upper left corner can be seen a ferrite grain. Figure 3b shows the MFM image of Figure 3a where no magnetic domain in austenite region can be detected, while the magnetic domains in the ferrite grain resulted in obvious contrast. As shown in Figure 4, the diffraction pattern of the sample after H-charging and

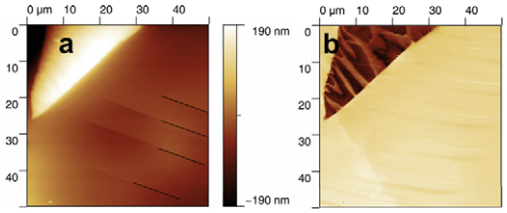

Figure 3. (a) AFM image of an austenitic region where slip lines formed during electrochemical H-charging. A ferrite grain can be seen at the top left. (b) MFM image of the same region where no magnetic domain formation in austenite were observed. The magnetic domains of the ferrite grain can be seen.

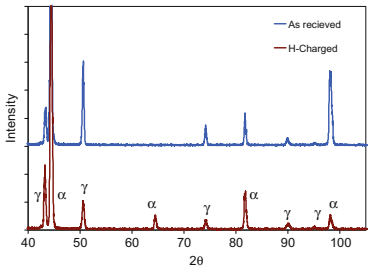

Figure 4. X-ray diffraction pattern of the sample before and after electrochemical H-charging. After H-charging there was a clear slip line formation on the sample surface but no ϵ or α' martensite phase was detected.

the slip line formation had not changed. Also, no ϵ or α' martensite peaks were revealed. Therefore, a hydrogen-induced martensitic phase transformation [9,11] cannot explain the formation of the slip lines by H-charging of our sample.

When a multi-phase alloy is heat-treated, internal stresses form due to differences in the thermal expansion coefficients between the constituent phases. The distribution of such internal stresses in SDSS after quenching in water from an elevated temperature has been discussed in the literature [12–14]. These stresses can be divided into residual macroscopic and microscopic stresses. The macroscopic residual stress, σ_{ij}^{M}, is due to the temperature gradient between the surface and the internal region of the specimen. If the elastic moduli of the constituent phases are not too different, as in the case of SDSS, then σ_{ij}^{M} can be neglected [12]. The microscopic residual stresses arise due to misfit strains among grains of the constituent phases with different thermal expansion coefficients. These stresses may vary from grain to grain, and their averaged value over each constituent phase is called thermal phase-stress, σ_{ij}^{ph}, [14]. During the production of SDSS it is water quenched from 1120 °C, in order to have an equal amount of γ and α phases in the microstructure. This stabilizes the metastable γ phase and results in phase-stresses and so called eigenstrains, ϵ_{ij}^{*}, which can be calculated as follows [15]:

$$\epsilon_{ij}^{*} = \delta_{ij}(\alpha_A - \alpha_F)\Delta T \tag{1}$$

where δ_{ij} is Kronecker's delta, α_A and α_F are linear thermal expansion coefficients of γ and α, and ΔT is the temperature change. ϵ_{ij}^{*} of an ellipsoidal inclusion inside an infinite medium with the same elastic moduli can be related to the stress in inclusion by using Eshelby's inclusion theory [15]

$$\sigma_{ij} = C_{ijkl}(S_{klmn}\epsilon_{mn}^{*} - \epsilon_{kl}^{*}) \tag{2}$$

where C_{ijkl} are the components of the elasticity tensor of the matrix and S_{klmn} are the components of the Eshelby's tensor. Eshelby's inclusion theory coupled with the Mori–Tanaka mean field theory [15] can then predict the average stress in the matrix and in the randomly distributed inclusions. In the present case, austenite grains can be considered as inclusions, with uniform ϵ_{ij}^{*}, randomly distributed inside a ferritic matrix. Assuming that elastic moduli for both phases are identical, the mean phase-stresses in the ferrite phase, σ_{ij}^{F}, and austenite phase, σ_{ij}^{A}, formed by quenching are calculated as follows:

$$\sigma_{ij}^{A} = x_F C_{ijkl}^{F}(S_{klmn}\epsilon_{mn}^{*} - \epsilon_{kl}^{*}) \tag{3}$$

$$\sigma_{ij}^{F} = (x_F - 1)C_{ijkl}^{F}(S_{klmn}\epsilon_{mn}^{*} - \epsilon_{kl}^{*}) \tag{4}$$

where C_{ijkl}^{F} are the components of the elasticity tensor of ferrite. For simplicity, the shape of grains can be assumed to be spherical. Then $S_{1111} = S_{2222} = S_{3333} = (7-5\nu)/15(1-\nu)$, $S_{1122} = S_{2233} = S_{3311} = -1(1-5\nu)/15(1-\nu)$, $S_{1212} = S_{2323} = S_{3131} = (4-5\nu)/15(1-\nu)$ and others are zero. Unfortunately, no data are available for exact values of α_A and α_F. This is due to the difficulty of preparation of a completely austenitic or ferritic reference alloy having a chemical composition identical to that of a constituent phase in SDSS. Typical coefficients of thermal expansion for γ and α are $\alpha_A = 12.5 \times 10^{-6}\ \mathrm{K}^{-1}$ and $\alpha_F = 17.1 \times 10^{-6}\ \mathrm{K}^{-1}$, respectively [16]. Inputting α_A, α_F and $\Delta T = 1000$ K into Eq. (1), $\epsilon_{ij}^{*} = 5.5 \times 10^{-3}\delta_{ij}$ is obtained. Then, by using a Young's modulus of $E = 200$ GPa and a Poisson's ratio of $\nu = 0.3$ equally for γ and α in Eqs. (3) and (4), $\sigma_{ij}^{F} = 470$ MPa (compressive) and $\sigma_{ij}^{A} = 400$ MPa (tensile) are obtained. These values are in very good agreement with the reported values in the literature calculated with the constitutive material law [16] (~400 MPa), measured by neutron diffraction [12] (~500 MPa) and X-ray diffraction [14] (~280–500 MPa). The good agreement between the calculated and measured residual stress shows that the relaxation due to dislocation punch out from the surface under ambient conditions is negligible. In order to understand the effect of this relatively high internal stress on austenite it is necessary to compare it with its yield stress, which again is not accessible, again due to the unavailability of a completely austenitic reference alloy with an identical chemical composition. A relation for the yield stress, σ_y^A, of high nitrogen alloyed austenitic steels has been experimentally established by Werner [17]:

$$\sigma_y^A = \sqrt{\left(\sigma_r^A\right)^2 + \left(\Delta\sigma_r^A\right)^2} + \frac{K_y^A}{\sqrt{\bar{L}^A}} \tag{5}$$

where $\Delta\sigma_r^A$ is the change in friction stress as a function of the nitrogen concentration in the austenite, c_N^A, and is equal to $486(c_N^A)^{0.5}$ MPa/$\sqrt{wt.\%}$. K_y^A is the grain size coefficient, and is equal to $7 + 39.4c_N^A$ Nmm$^{-3/2}$/wt.% The friction stress of nitrogen-free austenite, $\sigma_r^A = 220$ MPa

[16], and the partitioning coefficient for nitrogen, $c_N^F/c_N^A = 0.18$ [18], are used with the metallographically determined mean γ grain size, $\overline{L}^A = 100\ \mu m$ [7], to calculate $\sigma_y^A = 470$ MPa from Eq. (5). Comparing $\sigma_{ij}^A = 400$ MPa with $\sigma_y^A = 470$ MPa proves that the residual stress in austenite is near to its yield stress but not near enough to plastically deform it and relax by dislocation punch out. This relatively high residual stress plays a crucial role during the H-charging of SDSS, primarily increasing the solubility of hydrogen in austenite according to the following equation [19]:

$$C_\sigma = C_0 e^{-\sigma \overline{V}_H / RT} \tag{6}$$

in which C_σ and C_0 are the concentration of the interstitial solute in the stressed and unstressed body, respectively, and $\overline{V}_H$ is the partial molal volume of the hydrogen with a typical value of $\overline{V}_H \approx 2\ cm^3\ mol^{-1}$. For tensile stress, σ is negative, and so the solubility increases. With the calculated σ_{ij}^{ph} values in our SDSS this means an $\sim 50\%$ increase in the solubility of hydrogen for austenite and an $\sim 50\%$ decrease in solubility for ferrite. In the next step, this stress-enhanced concentration of hydrogen in austenite results in the activation of existing dislocation sources which are already stretched under the existing stress field. This should not be confused, however, with the well-known hydrogen-enhanced local plasticity (HELP) model [20]. HELP has been explained in terms of a hydrogen shielding model in which the presence of hydrogen atmospheres around dislocations and elastic obstacles decreases the interaction energy between them [20]. Since the dislocation density in our sample after quench annealing is very low [18], an increase in the mobility of existing dislocation due to hydrogen cannot explain large amounts of slip formation (see Fig. 2) without the activation of new dislocation sources. Therefore, it is necessary to have regenerative multiplication of dislocations. If we assume a Frank–Read-type source in the sample, the relation used to calculate τ_c, the critical shear stress required to activate the source, is:

$$\tau_c = \kappa \frac{2Gb}{\ell} \tag{7}$$

where G is the shear modulus, ℓ is the length of segment and κ includes the line energy of dislocation. Due to the existing residual stress in the austenite, the Frank–Read source is already bowed out, but the stress is not enough to activate the source. It has been shown that hydrogen reduces the shear modulus [21–23], which, according to Eq. (7), results in the activation of the source under the existing residual stress. Additionally, as proposed by Kirchheim et al. [24,25], a reduction in the dislocation line energy by the segregation of hydrogen on it (i.e. a reduction of κ) contributes further to the activation of the Frank–Read source according to Eq. (7).

We reported a uniformly spreading and continuously increasing hydrogen-induced plasticity in austenite grains of SDSS. This happened under moderate H-charging which could not trigger any phase transformation in austenite, as reported elsewhere [2]. This was proved by XRD and MFM examinations. Hydrogen reduces the required stress for activation of dislocation sources which are already under tension due to residual stresses formed during quench annealing. This initiates dislocation punch out from the surface and relaxation of the microstructure. This shows how hydrogen in combination with a complex microstructure results in microstructural changes which can play a crucial role in hydrogen embrittlement of industrially important alloys. To our knowledge, the effect of residual stresses on hydrogen uptake and microstructural changes has not been considered before in any study of the HE of SDSS. However, the findings presented here clearly show the effect of the residual stresses in combination with hydrogen on the microstructure. Therefore, it is necessary to consider their effect on HE and corrosion in future experiments and simulations. Further experiments are planned to study the effect of hydrogen on ferrite and stress-free austenite in SDSS.

The authors thank Prof. M. Pohl for helpful discussions, and are grateful to Jules Dake for proofreading.

Supplementary data associated with this article can be found, in the online version, at doi:10.1016/j.scriptamat.2009.11.007.

[1] V. Olden, C. Thaulow, R. Johnsen, Mater. Design 29 (2008) 1934.
[2] K. Lo, C. Shek, J. Lai, Mater. Sci. Eng. R 65 (2009) 39.
[3] A. Barnoush, C. Bies, H. Vehoff, J. Mater. Res. 24 (3) (2009) 1105.
[4] A. Barnoush, H. Vehoff, Scripta Mater. 58 (2008) 747.
[5] K. Nibur, D. Bahr, B. Somerday, Acta Mater. 54 (2006) 2677.
[6] A. Barnoush, H. Vehoff, Int. J. Mater. Res. 97 (2006) 1224.
[7] M. Øverland, Master's thesis, NTNU, 2007.
[8] A. Barnoush, Hydrogen Embrittlement Revisited by In Situ Electrochemical Nanoindentation, Shaker Verlag, Aachen, 2009.
[9] Q. Yang, L.J. Qiao, S. Chiovelli, J.L. Luo, Scripta Mater. 40 (1999) 1209.
[10] P. Rozenak, R. Bergman, Mater. Sci. Eng. A 437 (2006) 366.
[11] Q. Yang, J. Luo, Mater. Sci. Eng. A 288 (2000) 75.
[12] S. Harjo, Y. Tomota, M. Ono, Acta Mater. 47 (1998) 353.
[13] M. Pohl, A. Bracke, Z. Metallkd. 90 (1999) 551.
[14] J. Johansson, M. Odén, X. Zeng, Acta Mater. 47 (1999) 2669.
[15] T. Mura, Micromechanics of Defects in Solids, Kluwer, Dordrecht, 1987.
[16] T. Siegmund, E. Werner, F.D. Fischer, J. Mech. Phys. Solids 43 (1995) 495.
[17] E. Werner, Mater. Sci. Eng. A 101 (1988) 93.
[18] W. Horvath, W. Prantl, H. Stroisznigg, E. Werner, Mater. Sci. Eng. A 256 (1998) 227.
[19] J. Bockris, Modern Electrochemistry: An Introduction to an Interdisciplinary Area, Plenum Press, New York, 2000.
[20] H.K. Birnbaum, P. Sofronis, Mater. Sci. Eng. A A176 (1–2) (1994) 191.
[21] A. Barnoush, H. Vehoff, Corros. Sci. 50 (2008) 259.
[22] D. Bahr, N. Overman, C.S. Marchi, K. Nibur, Effects of Hydrogen on Materials, ASM International, Materials Park, OH, 2008, pp. 179.
[23] A. Barnoush, B. Yang, H. Vehoff, Advances in Solid State Physics, Springer, Berlin, 2008.
[24] R. Kirchheim, Acta Mater. 55 (2007) 5139.
[25] A. Pundt, R. Kirchheim, Annu. Rev. Mater. Res. 36 (2006) 555.